Università deghi Studi di Padova

Dipartimento di Scienze Chimiche

Scuola di Dottorato in Scienze Molecolari

CICLO XXXI

Monolayer Protected Gold Nanoparticles: Application in Molecular Recognition

Direttore della Scuola: Ch.mo. Prof. Leonard J. Prins

Supervisore: Ch.mo. Prof. Fabrizio Mancin

Dottoranda: Xiaohuan Sun

Table of contents

Abbreviations

MPGN	Monolayer protected gold nanoparticle
NMR	Nuclear magnetic resonance
MD	Molecular dynamic
EPR	Electron paramagnetic resonance
TOABr	Tetraoctylammonium bromide
$NaBH_4$	Sodium borohydride
NOE	Nuclear Overhauser effect
DOSY	Diffusion-ordered spectroscopy
STD	Saturation transfer difference
FRET	Fluorescence resonance energy transfer
Ig M	Immunoglobulin M
DLS	Dynamic light scattering
IDA	Indicator displacement assay
PPE	Poly(paraphenyleneethynylene)
Con A	Concanavalin A
STM	Scanning tunnelling microscopy
AFM	Atomic force microscopy
DPT	Diphenyl thiol
DDT	Dodecanethiol
DMOT	3,7-dimethyloctanethiol
PRE	Paramagnetic relaxation enhancement
PEG	Polyethylene glycol
rdf	Radial distribution functions
NSAIDs	Nonsteroidal anti-inflammatory drugs
FTIR	Fourier-transform infrared spectroscopy
UV-Vis	Ultraviolet-visible spectroscopy
SANS	Small angle neutron scattering
SERS	Surface enhanced Raman spectroscopy
PELDOR	Pulsed electron-electron double resonance

Abstract

In the last years, a relevant attention has been paid to monolayer protected gold nanoparticles (AuNPs), which are nanometer-sized gold colloids coated with a monolayer of organic molecules. Indeed, they have several interesting features. The first one is the easiness to synthesize gold cores with various sizes. Second, the versatile chemistry of AuNPs allows the grafting of functional groups and co-factors onto their surface. Taking advantage of different kinds of non-covalent interactions (namely hydrophobic, ion pairing, and metal-ligand coordination), such functional groups can in turn provide tailored binding sites for virtually any class of substrates. The variety of monolayers that can be potentially assembled endows a fine-tuning of these interactions not only in terms of selectivity, but also in terms of their strength. Therefore, AuNPs were emerging as great scaffolds for molecular recognition.

In this thesis, chapter 1, the introductive chapter, will present the methods for the preparation of AuNPs, the recent progress of AuNPs as chemosensors and the approaches that have been developed to investigate the monolayer morphology of mixed AuNPs. In chapter 2, the aims and objectives of this thesis will be addressed. In chapter 3 and 4, a series of water soluble AuNPs were prepared and investigated as nanoreceptors and chemosensors using nuclear magnetic resonance (NMR) protocols. The results of chapter 3 indicated that by appropriate design of the coating ligands, the spontaneous formation of the sensing pockets in the monolayer of the gold nanoparticles can be achieved. The results in chapter 4 confirmed the possibility that the rational design of AuNPs with intrinsic binding cavities and controlled sensing ability can be aided by molecular dynamic (MD) simulations. In chapter 5, three kinds of positive charged AuNPs were prepared and they were able to detect and discriminate nonsteroidal anti-inflammatory drugs in a quantitative manner. In the field of molecular recognition, unique properties can also be obtained by the preparation of mixed AuNPs. Previous studies have already demonstrated that the morphology of the mixed monolayer is closely related to their properties. For this reason, in chapter 6, we will describe a method which combines NMR and electron paramagnetic resonance (EPR) techniques to investigate the morphology of mixed AuNPs. Furthermore, in chapter 7 we demonstrated that the morphology of the mixed monolayer can be transformed when in the presence of proper interacting analytes.

Chapter 1. Introduction

"Molecular recognition" has become a popular term since 1980s.[1] It covers the specific interactions between two or more molecules through noncovalent bondings such as hydrogen bonding, hydrophilic/hydrophobic interaction, van der Waals forces, π-π interactions, metal coordination and so on. Even though molecular recognition was extensively investigated in the past years,[2, 3] the controlled and predictable design still remains a significant problem, especially when using dynamic large supramoleuclar scaffold, for example, monolayer protected gold nanoparticle (AuNP in the rest of the thesis), as receptors.

AuNPs are spherical clusters of gold atoms coated by a monolayer of organic molecules, in most of the cases thiols, called ligands. Size of the metal core may range from 1 to 100 nm, which means that the number of gold atoms ranges from a dozen to hundreds of thousands, and the number of coating molecules spans from few units to several thousands.

Beside several possible applications, AuNP are emerging as an excellent scaffold for the design and preparation of novel chemosensors due to their intrinsic chemical and physical properties.[4-6] First, by tailored design of the coating ligands, the functionalized AuNP can possess specific binding sites, which can bind various targets through non-covalent interactions. In addition, proper design of multifunctional AuNP can obtain synergistic effect in binding with the targets.[7] Second, the AuNP are endowed with unique optoelectronic properties, such as fluorescence,[8] surface plasmon resonance,[9] redox potential,[10] conductivity[11] and so on.[12] All of these properties can be taken as signal generating elements when in the presence of analytes. Third, the self-assembled nature of AuNP makes their synthesis, modification and optimization relatively easy. Of course, such advantages may be counterbalanced by drawbacks, which include the effects of size dispersion (with the exception of molecularly precise clusters), the conformational flexibility of the coating molecules, which may create different local environments and different binding sites for molecular accommodation. In addition, the uncertainty about the morphology of mixed monolayers makes the investigation of the monolayer distribution of mixed AuNP meaningful.
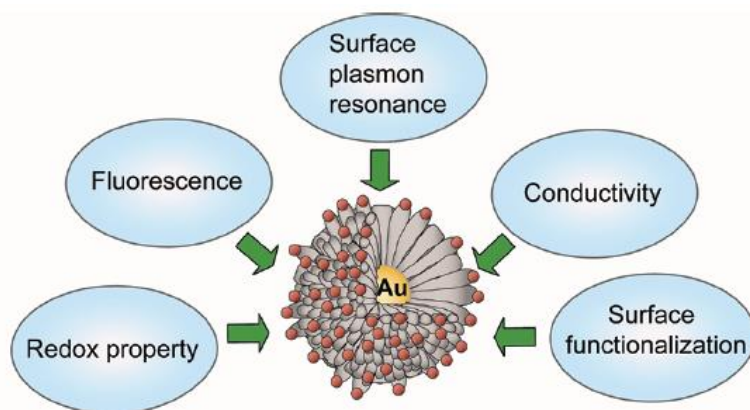
Figure 1-1. Optoelectronic properties of AuNP.

In this introductive chapter, I will show different methods for the preparation of AuNP and mixed AuNP. In addition, the progress of AuNP-based chemosensors using different signal generation methods will be discussed. Finally, also protocols that were used to study the morphology of mixed AuNPs will be addressed.

1.1 Synthesis of AuNPs

Many methods have been reported for the preparation of AuNPs. The development of different preparative methods was mainly focused on the control of the shape, size, stability and functionalization of the gold nanoparticles. When a specific route to prepare gold nanoparticles is considered, several factors, such as the category of the reducing agent, the coating molecules, the solvent and the temperature need to be clearly addressed. In this part, I will introduce the classical methods for the preparation of AuNPs and the advantages and disadvantages of different methods will be discussed.

As a general remark, it must be recalled that nanoparticles are thermodynamically unstable because of their high volume to surface ratio. Surface stabilizing agents are then required to prevent coalescence either by electrostatic or steric repulsion. Any synthetic protocols needs hence to consider both the production of the nanoparticle precursors, i.e. gold atoms, and the stabilization of the growing particles.

1.1.1 Turkevich method

One of the earliest methods for the preparation of gold nanoparticles (with size >5 nm) was published by Hauser and Lynn [13] in 1940. They reported the formation of gold nanoparticles by reducing the tetrachloroauric acid with trisodium citrate. In this method, besides being the reducing regent, trisodium citrate also acts as the stabilizing agent providing a negative charge to

the nanoparticles. Moreover, by varying the feeding ratio of citrate salt to gold, nanoparticles with a wide range of sizes can be prepared. Later, this result was redescribed by Turkevich and coworkers[14] in 1951, which made the method well known. Until now, many modified approaches have been explored according to the original one.
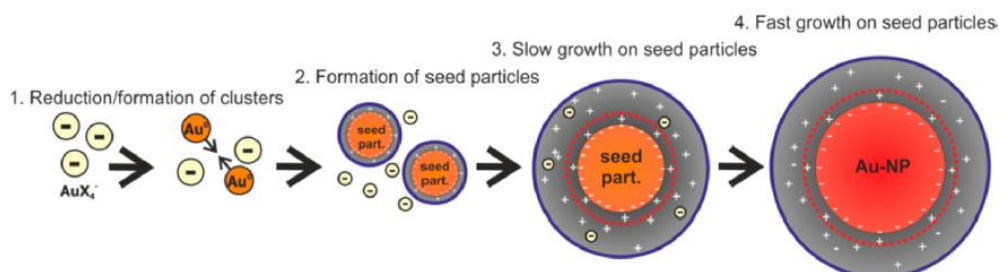
Figure 1-2. Schematic representation of the gold nanoparticle growth using the Turkevich Method.

The nanoparticles growth mechanism using this method is also widely studied. According to Polte *et al*,[15] this process includes four steps. First, the Au^{3+} is partially reduced to Au^0 by citrate salts and form small clusters. In the second step, the small clusters grow and aggregate to become seed particles. The remaining Au^{3+} is then attracted and attached on the electrical double layer of the seed particle as co-ions. In the third and fourth step, the remaining Au^{3+} was reduced to Au^0, first slowly and then fast. In this way it only deposits on the surface of the available seed particles until all the gold precursors are consumed.

Even if this method has been widely applied and extensively studied, it has limitations.[16] Nanoparticles with size smaller than 5 nm cannot be prepared. Relatively high dilutions are required, so that only relatively small amounts of nanoparticles can be prepared. The reaction has to be performed at high temperature (boiling) since the thermal degradation of the citrate salts is the key step in formation and stabilization of the AuNPs. However, at high temperature is difficult to control accurately the concentration of the gold solution or citrate, and consequently the final size of the gold nanoparticles.

1.1.2 Brust–Schiffrin method

The Brust-Schiffrin method is another widely applied approach to prepare gold nanoparticles.[17] When introduced, this method represented a real breakthrough since it allowed for the first time to prepare gold nanoparticle stable, amenable to be dried and redispersed and usable as stable compounds. The reason of this different behavior is the use of thiols as ligands, since the Au-S interaction is much stronger than the Au-COO$^-$ one. Since at that time most of the thiols

commercially available were soluble only in low polarity solvent, tetraoctylammonium bromide (TOABr) was used as phase transfer regent to transfer $HAuCl_4$ from aqueous phase to toluene. Then the Au^{3+} was reduced by sodium borohydride ($NaBH_4$) in the presence of dodecanethiol. The mechanism proposed involves as first step the reduction of Au(III) to Au(I) by the thiols. This induces the formation of $[Au(SR)]_n$ polymers. Subsequently, the addition of sodium borohydride completes the reduction of Au(I) to Au(O). In this method, the conditions employed are mild. The reaction is performed at room temperature or at 0 °C. In addition, the size of the nanoparticles can be roughly controlled in the range of 1.5-5 nm, by the use of different feeding ratio of thiol to gold salt. As expected, the AuNPs obtained using hydrocarbon thiols are mostly soluble only in low polarity solvent.[18]

Later on, modifications of this method that avoid the use of two phases and of the phase transfer agent were introduced. They may use organic solvents capable to solubilize tetrachloauric acid (THF, methanol, etc.), gold salts soluble in organic solvents ($AuClPPh_3$) or reducing agents soluble in organic solvents. The mechanism of nanoparticles formations is similar to the Brust-Schiffrin one and size is essentially controlled by feeding ratio of thiol to gold salt. Generally, larger particles (4-8 nm) are obtained with respect to the Brust-Schiffrin protocol.
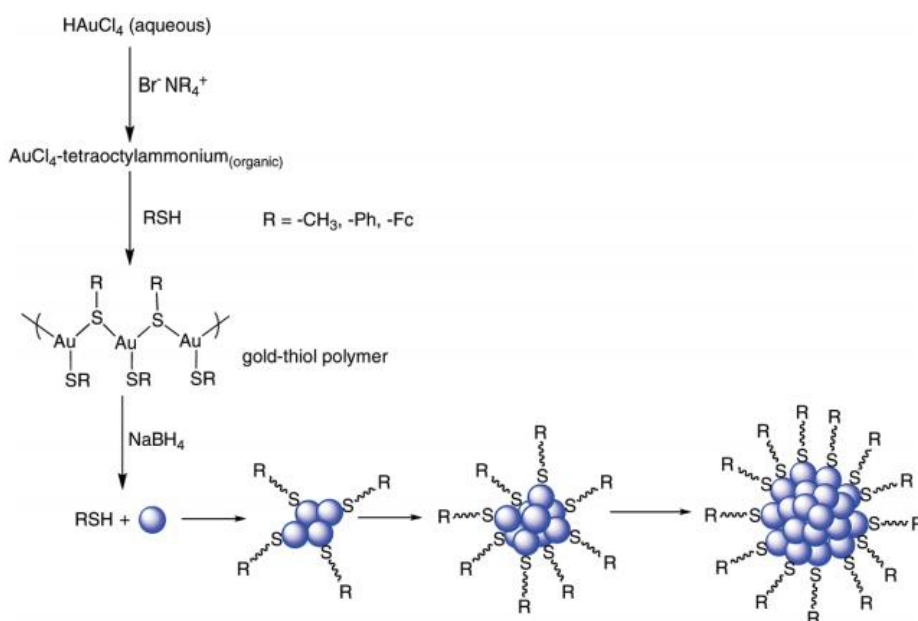

Figure 1-3. Schematic representation of the gold nanoparticle preparation using the Brust-Schiffrin method.

1.1.3 Peng-Scrimin method

Considering the limitations of the Brust-Schiffrin protocol,[18] Scrimin *et al.* developed a new method based on the modification of the Brust-Schiffrin one. In Peng-Scrimin method, TOABr was

also used as phase transfer regent and sodium borohydride as reducing regent. What is different is that in this method dioctylamine was employed as stabilizing regent. The introduction of dioctylamine leads to two advantages. First, the amount of dioctylamine can be used to control the size of the AuNPs. Second, the thiol-protected gold nanoparticles can be easily obtained by exchanging the dioctylamine, avoiding in this way the exposure of the thiols to harsh conditions. The size of the AuNPs obtained using this method is well controlled by the amount of dioctylamine added and the preparation of water soluble AuNPs is possible, which largely promotes the development of AuNPs. Other similar methods, which avoid the two phases using reducing agents soluble in organic solvents were introduced later on.
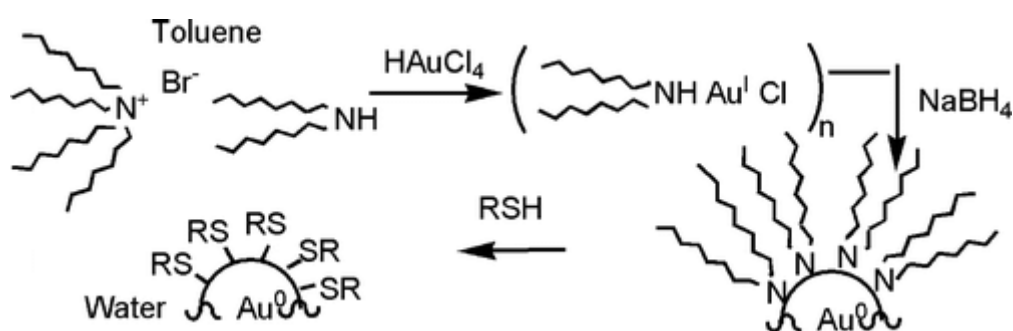
Figure 1-4. Schematic representation of AuNPs preparation using the Peng-Scrimin method.

1.1.4 Synthesis of mixed AuNP

Mixed monolayer gold nanoparticles are becoming more and more appealing to scientists as they allow increasing the chemical complexity of the monolayer.[19, 20] To prepare mixed AuNPs, three methods can be employed. It is relevant to note that quite the very same methods, when pushed to the extreme conversion, can be used for the synthesis of homogenously coated nanoparticles.

Direct synthesis. Direct synthesis is a very simple and fast way to prepare mixed AuNPs. It used the same procedures described above using mixtures of coating molecules instead of pure ones. The main limitation is that the composition of the mixed AuNPs is difficult to control. Usually, the ratio of the coating ligands obtained from the resulting AuNPs is not the same as the ratio of the feeding ligands. This can be due to the difference in the solubility, the steric hindrance effect and the supramolecular nature of the two ligands.[7, 21, 22]

Thiol exchange method. Thiol exchange method,[23, 24] which was first reported by Murray *et al*, is the substitution of thiol ligands from the surface of AuNP with a different kind of thiol. Taking

advantage of this method, new functionalities can be introduced to the monolayer of gold nanoparticles. The exchange efficiency depends on the nature of the feeding thiol, the ratio of the feeding thiol, the reaction time, the solvent and the temperature. Using this method, the mixed monolayer protected gold nanoparticles with intrinsic features can be easily obtained. Though this method provides an easy way to obtain controlled composition of the mixed AuNPs, still, it has limitations, such as time consuming or the possibility to induce the nanoparticles etching.
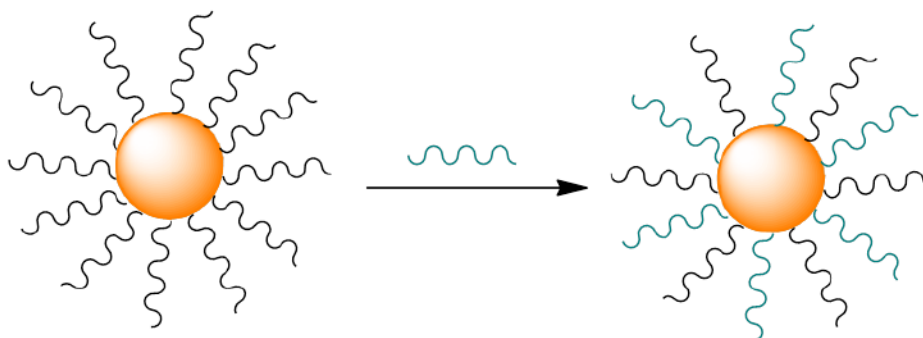
Figure 1-5. Schematic representation of the thiol exchange.

Post-Synthetic modification. Post-synthetic modification method[25, 26] is based on the fact that the functional groups which are anchored on the surface of the AuNPs can further undergo synthetic transformation. This method can be a better choice in several cases. When the synthesis of the functionalized thiol results in a really low yield, post-synthetic method can optimize the synthesis route. In addition, the further functionalization efficiency highly depends on the reaction activity. Therefore, quantitative modification of the monolayer of the gold nanoparticle can be achieved. However, this method requires a mild reaction condition.

1.2 Chemosensors based on monolayer protected nanoreceptors

Reliable and precise methods capable of identifying specific compounds in mixture have attracted increasing interest in the last decades.[27-30] Among the various materials have been developed for molecular recognition, AuNPs have a huge potential for the development of innovative receptors sensing applications due to peculiar distinct physical and chemical properties.[31-33] Here, we will discuss the approaches that were recently developed by using AuNPs as nanoreceptors for chemosensing. The discussion will be mainly focused on NMR and fluorescence methods, which are the most widely used ones, but some other methods will also be described.

1.2.1 NMR methods

NMR is probably one of the most powerful techniques to monitor recognition events.[34-36] The undisputed advantage of NMR spectroscopy over other techniques in molecular recognition studies is the wealth of information on the formed complex that can be obtained, both regarding the binding affinity and the structure. The provided information includes the chemical shift, the signal intensity, the diffusion coefficient, the relaxation and so on.[37, 38] For this reason, NMR spectroscopy is the method of choice for most molecule-based recognition studies. Recently, NMR spectroscopy is also rapidly gaining attraction as a promising tool for studying the interaction between small molecules and AuNPs favored by some important features. Firstly, when passivated with a proper monolayer, nanoparticles are stable and form homogeneous solutions, which allow the use of solution-state NMR spectrometers. Secondly, because of their small size, diamagnetic nanoparticles do not perturb significantly the magnetic field homogeneity and are hence compatible with high-resolution NMR experiments. Due to such properties, NMR spectroscopy would also allow, in principle, to use any molecular receptor as chemosensor. Indeed, molecular recognition results almost always in a change of some NMR observable (chemical shift, relaxation time, NOE, diffusion rate). Yet, in most of the cases signal crowding prevents practical use.

For the above reasons, ^{19}F NMR spectroscopy is used in multianalyte detection. Indeed, it conjugates a sensitivity similar to that of ^{1}H NMR with the general absence of background signals and the large chemical shift range. Consequently, fluoride containing receptors are frequently employed to design chemosensors based on the perturbation of ^{19}F NMR chemical shifts.[39-41]

Recently, this idea was also applied to AuNPs using a displacement assay.[42] Fluoride-containing arylboronic acids can bind with the thioundecyl-D-glucopyranoside-protected gold nanoparticles. In the AuNP-bound state, the relaxation rate of the fluoride-containing arylboronic acids was significantly increased because of the low flexibility and tumbling rate of the nanoparticle. Therefore, the NMR signals of the fluoride atoms experienced a substantial broadening. Then, when dopamine, which is known to have a high affinity for arylboronic acids, was added to the system, the fluoride compound could be displaced from the monolayer of AuNPs. The resulting ^{19}F NMR spectrum was then featured with sharp signals. Taking advantage of the relaxation-modulating property of the AuNPs, dopamine can be detected with a limit of detection of 20 μM. Imaging-based detection is also possible. Finally, the chemical shift of the sharp signal appearing after analyte detection are different for any analyte, allowing is identification.
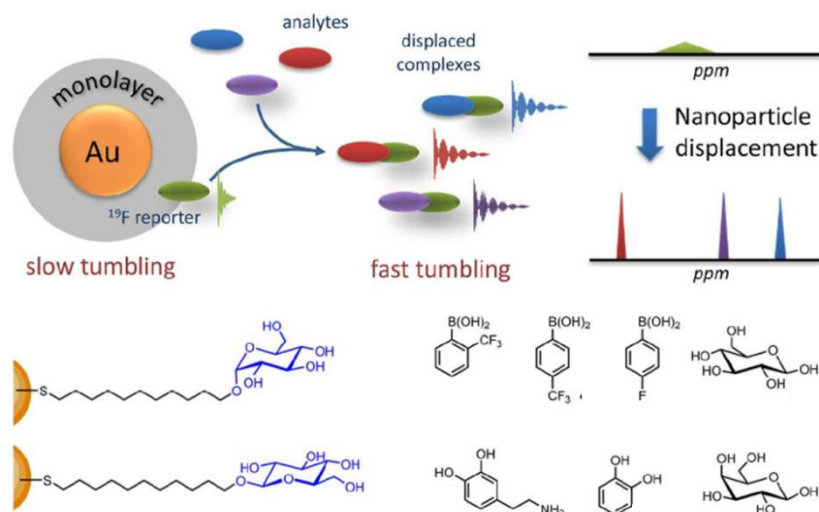
Figure 1-6. Upper: the schematic representation of the ^{19}F NMR-based sensing mechanism. Lower: the structure of the coating ligands, the fluoride compounds and analytes used.

A different chemosensing strategy is based on the selective transfer of magnetization from the nanoparticles to the interacting analytes via nuclear Overhauser effect (NOE) (Figure 1-7). Based on this principle, our group recently developed a NMR sensing protocol called NOE-pumping.[43-45] This method requires the use of nanoparticles with receptor ability and a combination of different NMR experiments. The first is a diffusion filter experiment, which cancels all the signals of the small, fast diffusing species in the sample (by dephasing their magnetization). On the other hand, the nanoparticles diffuse slowly, thanks to their relative largeness, and hence their magnetization survives this step. In the second experiment the retained magnetization is transferred to analytes interacting with the nanoparticles via NOE. Finally, the re-magnetized analyte relax producing the NMR spectrum which is recorded. In this way, the signal produced by the sensing system is the NMR spectrum of the analyte and its identity can be clearly recognized even when it is an unknown molecule. Because of the use of nanoparticle-based receptors this method was called "nanoparticle-assisted NMR chemosensing", and it may be considered a general method for direct detection and identification of broad analyte classes via ^{1}H NMR.
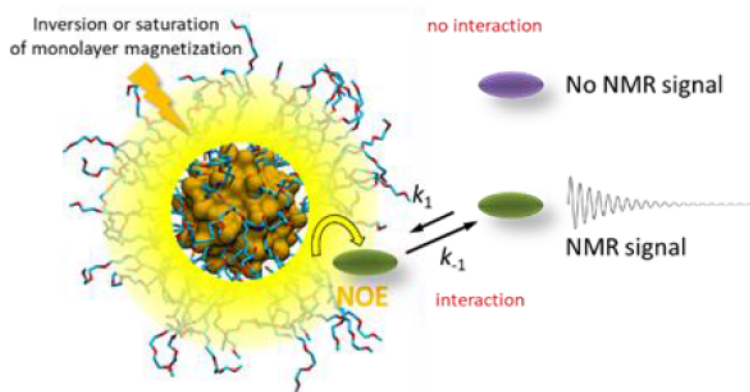
Figure 1-7. Outline of the NOE pumping experiment used for NMR chemosensing.
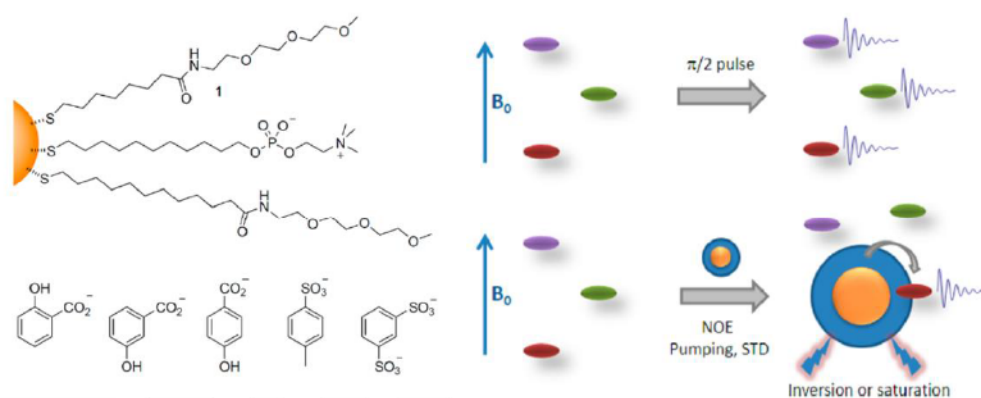
Figure 1-8. (Left) the structure of the coating ligands and analytes used. (Right) schematic representation of the NOE-pumping protocol.

In the first example (Figure 1-8),[43] sodium salicylate was mixed with water soluble gold nanoparticles (1-AuNP). Using the NOE-pumping sequence, the signals arising from the sodium salicylate was observed in the NOE-pumping spectrum, indicating the binding event occurred between 1-AuNP and sodium salicylate. What is more interesting, when NOE-pumping experiment was performed with a aqueous solution containing sodium salicylate, 3-hydroxybenzoate, 4-hydroxybenzoate, sodium *p*-toluenesulfonate, disodium benzene-1,3-disulfonate, whose chemical structures are quite similar, and AuNP-1, the presence of the sole sodium salicylate was observed, indicating the excellent selectivity of this system. In addition, the ability to detect sodium salicylate in human urine was also confirmed. This approach features several advantages. First, the NOE-pumping spectrum can provide structural information which leads to the unambiguous identification of the analytes. Second, both the operating and processing are simple and can be implemented to standard NMR spectrometer. Last but not the least, the features of the AuNPs can be easily modified by tuning the structure of the coating ligands. This makes the tailored design for the detection of different types of analytes possible.

Figure 1-9. The structure of the coating ligands.

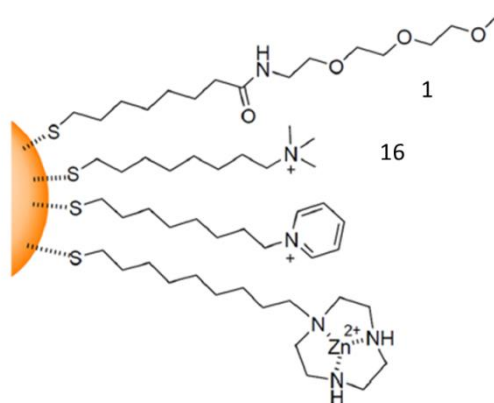   To demonstrate this point, AuNPs coated with molecules featuring different kinds of non-covalent interactions were subsequently designed.[44] It was found that the binding constant between sodium salicylate and 1-AuNP, whose driving force was supposed to be mainly hydrophobic interaction, is 120 M^{-1}. While for 16-AuNP, which was endowed with both hydrophobic and electrostatic interactions, the binding constant with sodium salicylate is 4×10^4 M^{-1}. The modulation of the strength of the binding affinity can be confirmed by NOE-pumping method, through the integration of the resulting signals of the analyte from the NOE-pumping spectra.

    NOE pumping requires a week interaction between the nanoparticle and the analyte. Indeed the spectrum is collected from the analyte molecules free in solution after their interaction with the AuNP and the magnetization transfer. Weak and fast exchange interaction ensures a significant fraction of free analytes as well as a turnover of the analytes molecules in the binding sites such to produce relevant signal amplification. When the interaction between the AuNPs and analyte is strong, like in the case of 16-AuNP and sodium salicylate mentioned above, the occurrence of the binding event can also be demonstrated by diffusion-ordered spectroscopy (DOSY). This method based on the fact that AuNPs have a larger diffusion coefficient than organic compounds due to their large size. When the analyte were bound to AuNPs, its diffusion coefficient will increase in different degrees corresponding to the fraction of molecules bound to the nanoparticles (Figure 1-10). By measuring the changing of the diffusion coefficient, the binding affinity between the AuNPs and analyte can be directly evaluated.
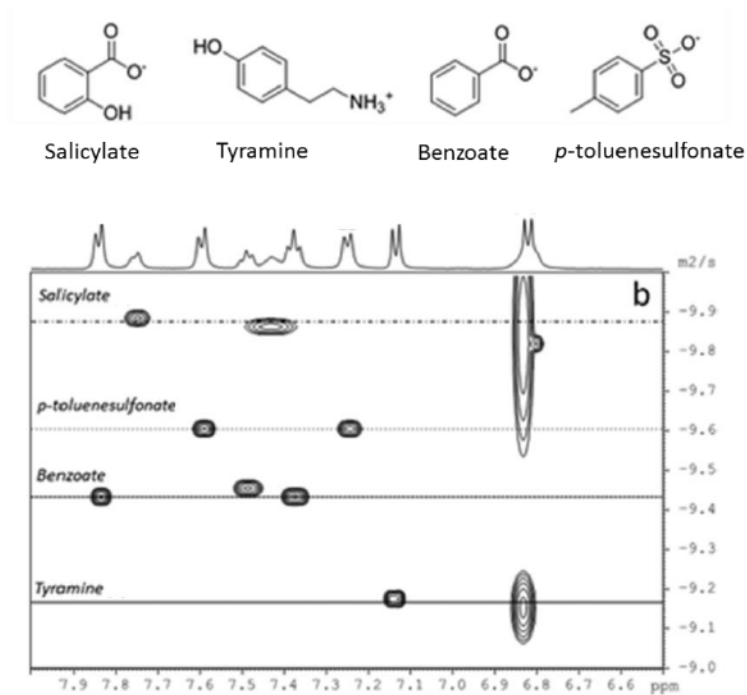
Figure 1-10. (Upper) the structure of salicylate, tyramine, benzoate and *p*-toluenesulfonate. (Lower) the DOSY spectrum of a mixture of salicylate, tyramine, benzoate and *p*-toluenesulfonate in the presence of 16-AuNP.

The NOE magnetization transfer implemented in NMR chemosensing is based on population inversion, but a similar result can be reached by saturating, rather than inverting, the populations of the spins in the monolayer. In fact, nanoparticles with a 2 nm core possess a rather efficient spin-diffusion mechanism, which opens the pathway to saturation transfer difference (STD, Figure 1-11) experiments.[46] While conceptually similar to a NOE experiment, the STD experiment provides stronger signals because saturation is effective for longer periods compared with transient NOE. However, to perform STD experiment, the signals of the analyte and AuNPs have to be clearly separated.

In our recently reported study, we found that with a negative charged coating monolayer, the AuNPs can be used to detect analytes with primary amine groups.[47] When the signals of AuNP have no overlap with the signals of the analyte, STD experiment could be implemented and the results showed that the phenethylamine derivatives can be detected with a limit of detection as low as 30 μM (Figure 1-12).

Figure 1-11. Schematic explanation of STD experiment.

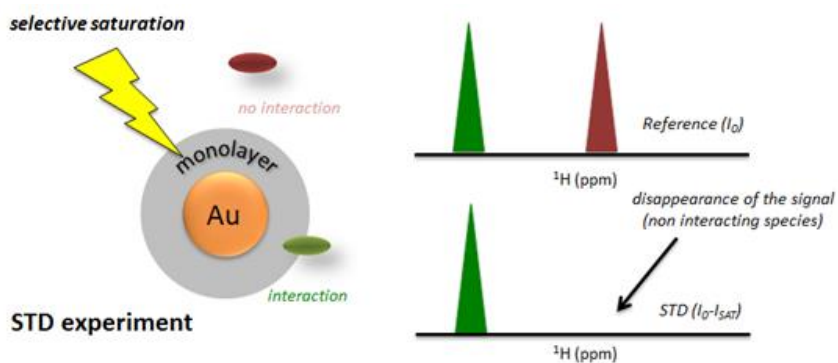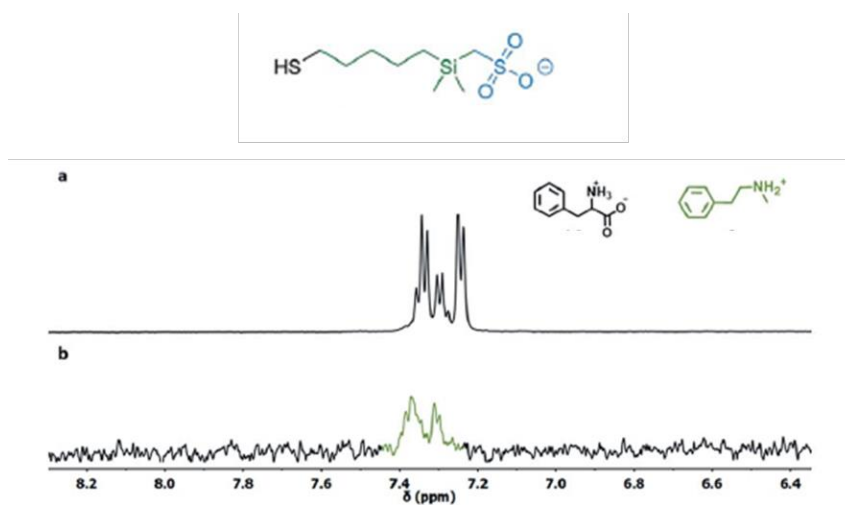**Figure 1-12.** The a: ^{1}H NMR, b: STD subspectrum of a mixture of phenethylamine derivatives and the negatively charged AuNPs.

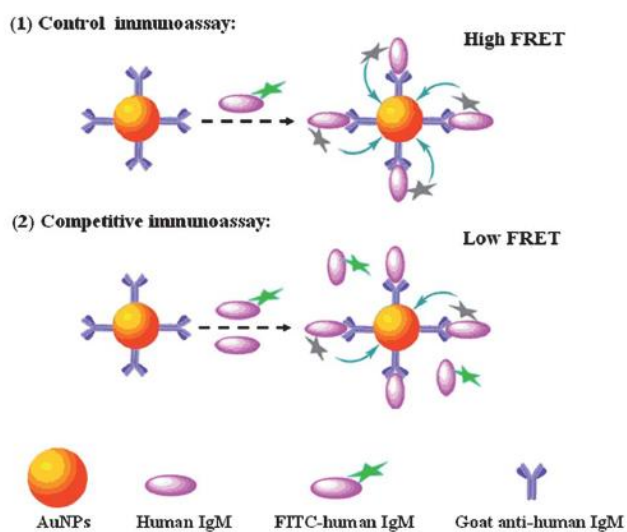## 1.2.2 Fluorescence methods

Figure 1-13. Schematic representation of the antibody-based AuNPs for the detection of IgM.

Metal nanoparticles are very efficient fluorescence quenchers,[48-50] via excitation energy transfer, due to their extraordinary high molar extinction coefficients and broad energy bandwidth. Because of this property, AuNPs were frequently used as fluorescence resonance energy transfer (FRET) acceptors. In this FRET-based method, the fluorescence of the donor will be quenched when complexed with the AuNPs. When the analyte, which can also bind with the AuNPs, is added to the system, the donor gets displaced to the solution and the fluorescence recovers. Therefore, the fluorescence intensity can be used to detect and quantify the analyte. Taking advantage of this strategy, Chen and coworkers[51] reported a AuNPs-based chemosensor (Figure 1-13). In their study, the gold nanoparticles were functionalized with immunoglobulin M (IgM) antibody, which enables the binding between the AuNPs and antigen-labeled fluorescein isothiocyanate. When the binding event occurred, the fluorescence of the fluorescein isothiocyanate was quenched. By adding an increased concentration of IgM, the antigen-labeled fluorescein isothiocyanate was displaced from the surface of AuNPs and its fluorescence was recovered. Based on the calibration curve, this immunoassay was demonstrated to have a limit of detection for Ig M as low as 42 pM.

Carbon dots received a great number of attention recently because they feature intrinsic fluorescence, high photostability, superior biocompatibility and low cost for the synthesis.[52] Recently, carbon dots have also been used as fluorophores to develop FRET-based nanosensors. Taking advantage of the same fluorescence turn-on principle, Das and coworkers[53] reported a anionic carbon dot-AuNP system for the detection of glutathione (Figure 1-14). The results demonstrated that this nanosystem can detect glutathione with a limit of detection of 6 nM.
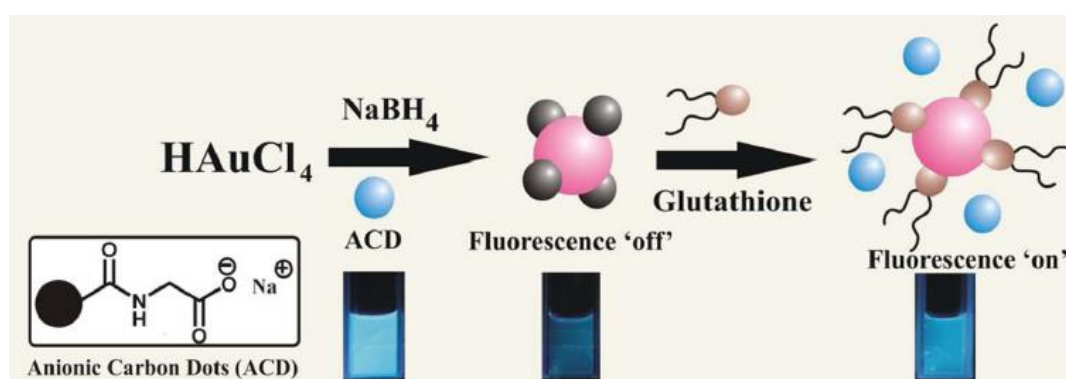
Figure 1-14. Carbon dots-based nanosystem for the detection of glutathione.

Since the FRET phenomenon is highly dependent on the distance between the fluorescence donor and acceptor, the FRET-based sensors can also be designed by modulating the spatial between the donor and acceptor. Dubertret et al[54] reported a hairpin FRET-based nanosystem for the detection of DNA (Figure 1-15). In their study, the nucleic acid was conjugated with both

AuNPs and organic dyes at its two ends. Because of the self-complementary of the nucleic acid, hairpin shaped nucleic acid was formed. This brought the close proximity of the AuNPs and organic dyes and led to the occurrence of FRET. When in the presence of the target DNA, which is complementary to the nucleic acid, the hairpin shape was destroyed and the AuNPs and organic dyes were separated, resulting in the increase of the fluorescence intensity.
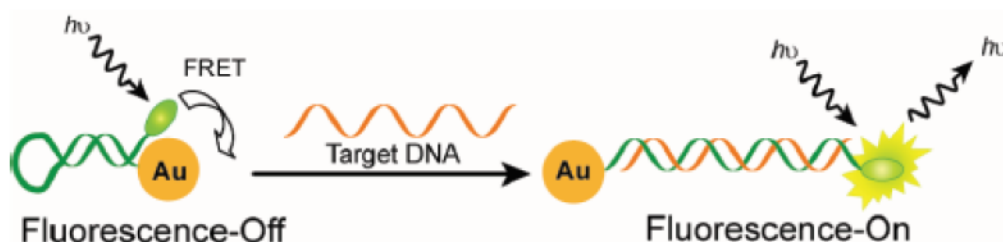
Figure 1-15. Schematic illustration of the mechanism for NDA detection.
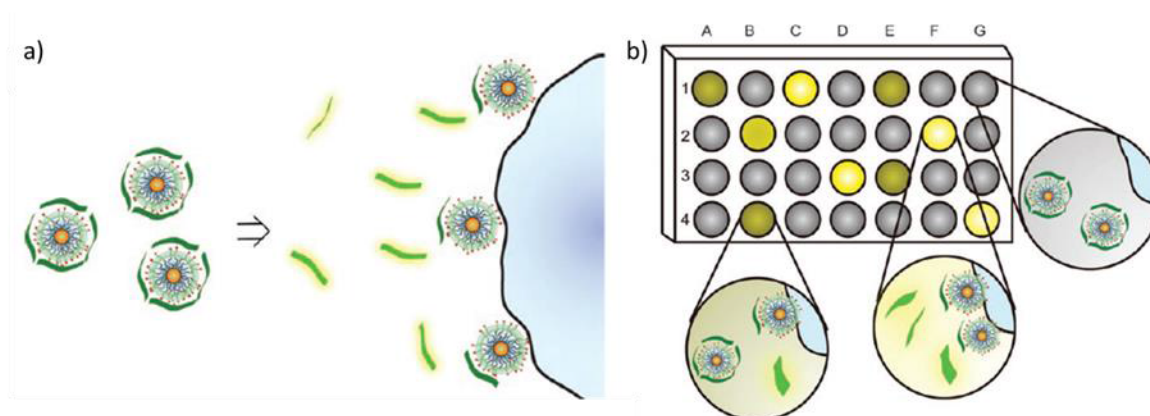
Figure 1-16. Representation of the mechanism of IDA-based sensing array.

The fluorescence quenching ability of the AuNPs also allowed the straightforward design of indicator displacement assay (IDA) based sensing arrays.[55-57] The IDA based sensing array exploits different sensing acceptors to generate signaling patterns that can be used to identify and discriminate various types of analytes. Taking advantage of this strategy, by simply varying the structure of the coating molecules one can create a large number of nanoparticle receptors and develop array-based differential sensing systems.[58-60] This approach was pioneered and elegantly exploited by Rotello and Bunz[61, 62] (Figure 1-16). They used cationic gold nanoparticles coated with different ammonium-thiol derivatives to generate the sensor arrays and polyanionic fluorescent poly(paraphenyleneethynylene) (PPE) polymers or proteins as indicators. By disrupting the nanoparticle-polymer interaction, distinct fluorescence response patterns can be produced for

specific proteins, cells and bacteria. In this way, various proteins, cells or bacterial were detected and discriminated.

Figure 1-17. The IDA approach for the detection of nucleotides.

This approach was later expanded by the Prins group to the sensing of small molecules (Figure 1-17).[63] They created a sensor array by using 1,4,7-triazacyclononane terminated gold nanoparticles, loaded with two different metal ions (Zn^{2+} and Cu^{2+}) in combination with three polyanionic fluorescent dyes. They found that di- and tri- nucleotides NDP and NTP (N = A, T, G, C) interacted differently with the (3x2) sensor array, allowing the disc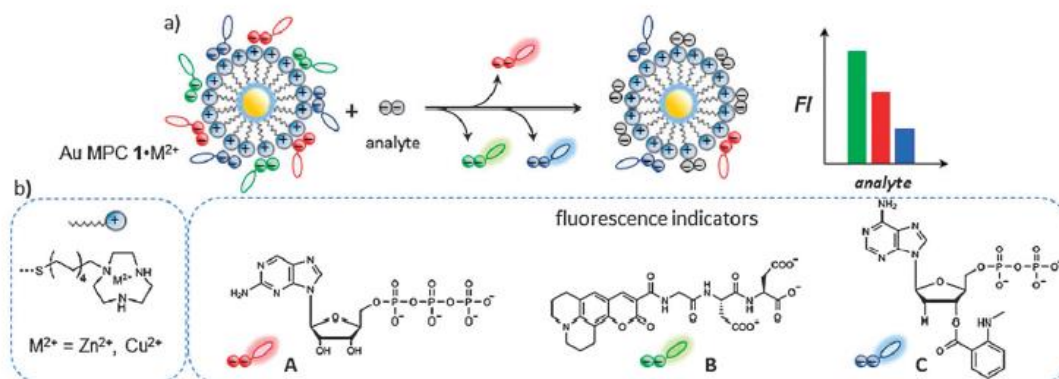rimination of the eight analytes in a quantitative manner. Interestingly, this work showed that the selectivity diversity needed for differential sensing can be created in the case of nanoparticles receptor arrays not only by changing the chemical structure of the nanoparticle coating molecules, but also by using different reporters and metals.

1.2.3 Other methods

Besides NMR and fluorescence methods, there are still some other methods available for the design of AuNPs-based chemosensors. One of the examples is based on EPR spectroscopy. EPR has been extensively employed to investigate the interactions between stable free radicals (such as nitroxides) and the monolayer of gold nanoparticles. Taking advantage of this technique, evidence of interactions are generally revealed by perturbations in the EPR nitrogen hyperfine splitting and by incomplete averaging of the anisotropic components of the hyperfine and g-tensors (resulting in systematic line widths broadening).

One of the earliest works in this context was reported by Pasquato *et al* (Figure 1-18).[64] They utilized water soluble 1-AuNP to study its interaction with para-substituted benzyl hydroxyalkyl nitroxides. The results determined that the EPR spectra of the nitroxide was featured with two

additional signals (new signals) when in the presence of 1-AuNP. Several evidences indicated that the presence of the new signals is due to the accommodation of the nitroxide into the gold nanoparticle monolayer. First, the decreasing of the nitrogen hyperfine splitting α(N) of the new signals compared to the free radical suggested that the nitroxide which generated the new signals were located in a less polar environment. In addition, the line broadening occurred to the new signals, indicating the low flexibility of the radicals. Moreover, the changing of the molar ratio of 1-AuNP and nitroxide directly related to the intensity ratio of the new and free radical signals. All of these evidences supported the long-standing idea that proper ligands grafted onto the AuNPs can generate ''hydrophobic pockets'' inside the monolayer, where organic solutes can be accommodated. Note that even if in this example no sensing was performed, the modification of the EPR spectra of the radical probe suggests the possibility to develop a nanoparticle-assisted EPR chemosensing strategy.
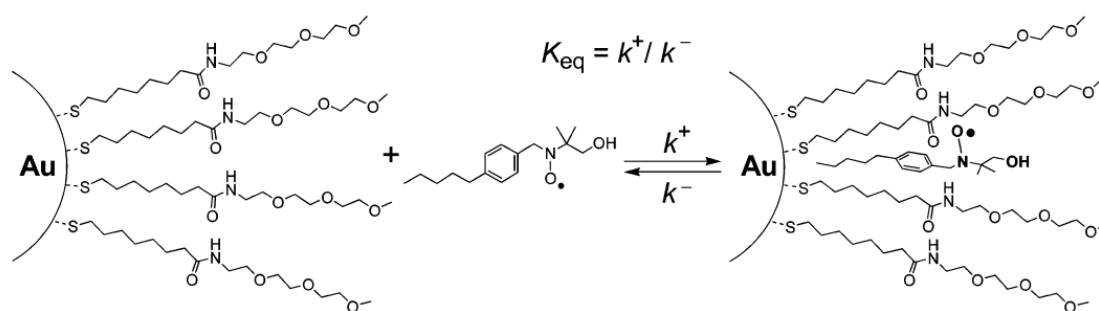
Figure 1-18. Schematic representation of the radical accommodation to the gold nanoparticle monolayer.

AuNPs are also widely used to develop colorimetric sensors for the detection of ions, anions, DNA and even proteins. The design of AuNPs-based colorimetric sensors is based on the fact that the aggregation and disaggregation of AuNPs of a proper size can lead to the dramatic change of the surface plasmon resonance property. Kim and coworkers[32] reported a dithioerythritol-protected gold nanoparticle which can bind Hg^{2+} through sulfur-Hg-sulfur interaction, resulting in the red shift of the absorbance spectra. Mirkin and coworkers[65] reported a nanosystem with two types of DNA-protected gold nanoparticles (Figure 1-19). The base sequence of the coating DNAs is designed to be complementary to the two ends of the target DNA. When in the presence of the target DNA, the interparticle aggregation occurred and the resulting color change makes the detection of DNA possible.

Figure 1-19. (A) The illustration of the aggregation of the AuNPs. (B) The color change induced by the aggregation. (C) The absorbance of DNA (modified with or without AuNP) at different temperature.

Figure 1-20. Schematic representation of the aggregation and dissociation of the AuNPs induced by Con A and glucose.

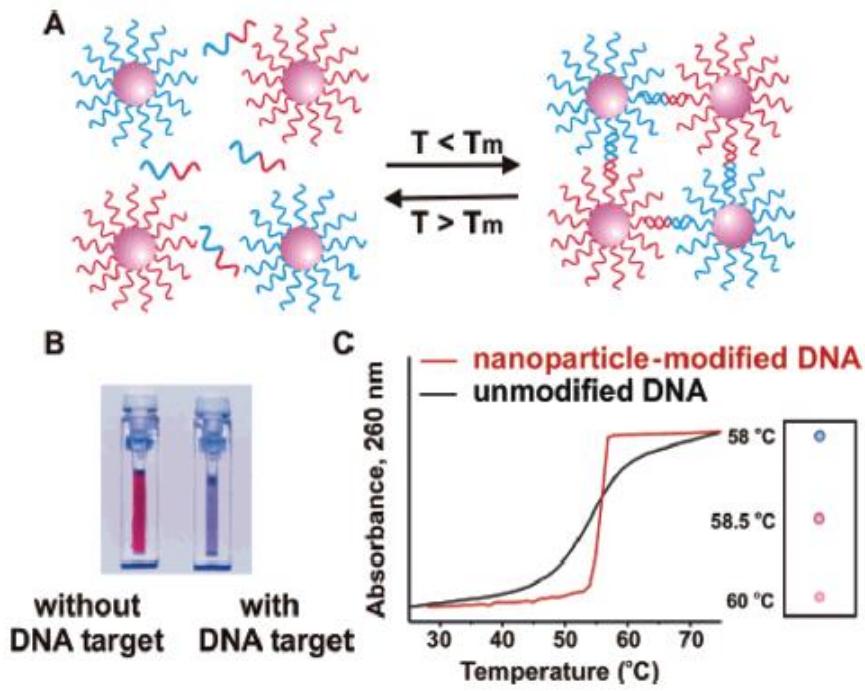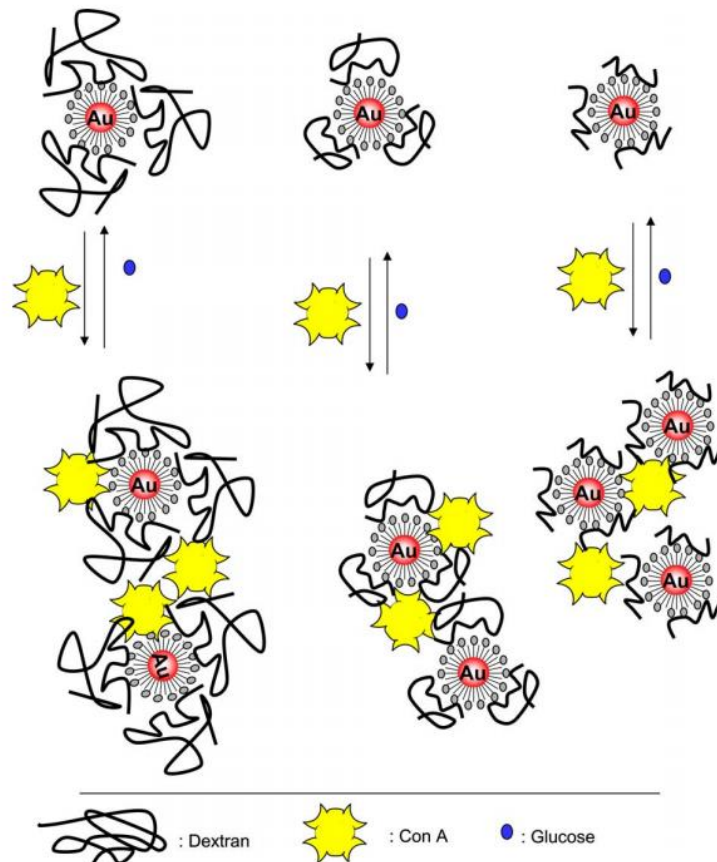Using the same concept, the detection can also be realized by the disaggregation of the AuNPs (Figure 1-20). In this case, a blue shift of absorbance band will be observed. Geddes and coworkers[66] reported the detection of glucose based on the competitive binding induced dissociation of AuNPs. In their study, dextran-coated gold nanoparticles were first employed to interact with concanavalin A (Con A), which led to the aggregation of the AuNPs and the broadening and redshifts of the absorbance band. Then when glucose, which can competitively binds with Con A, was added to the system, the Con A was released from the monolayer of the gold nanoparticles and the dissociation of the AuNPs happened. This process was demonstrated by the recovering of the UV-Vis spectrum.

1.3 Morphology determination of mixed AuNPs

It is accepted that the gold nanoparticles functionalized with diverse coating molecules can significantly contributed to the field of both chemistry and biology.[67, 68] Already proved by the literature, the monolayer distribution of the mixed AuNP can affect the particles' properties such as wettability,[69] solubility,[70] protein nonspecific adsorption,[71] cell penetration,[72] catalysis,[73] and ion/molecular recognition.[74] Therefore the determination of the morphology of the mixed AuNP is becoming a key procedure to well characterize the nanoparticles. Until now, several approaches taking advantage of various techniques, such as microscopy, spectroscopy and so on, have already been reported. Herein we will discuss the progress of this area and clarify the advantages and limitations of the available methods.

1.3.1 Microscopy

To determine the morphology of mixed gold nanoparticles, one of the best methods would be without doubts the use of microscopy. This is not only because of the advantage of direct visualization, but also because this method can provide information about one single AuNP instead of general average data. However, due to the small size of the gold core and the dimension of the coating ligands, not many microscopy tools are available for this goal. So far, the most used technique is scanning tunneling microscopy (STM).[75]
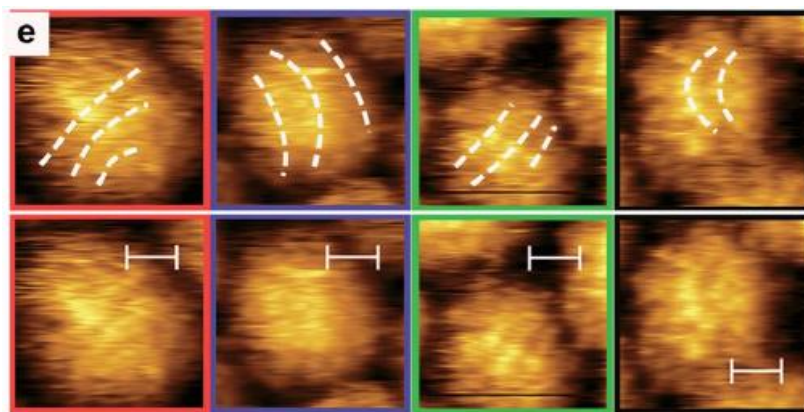
Figure 1-21. The STM images of stripe distributed mixed AuNPs coated with dodecanethiol and hexanethiol.

Stellacci group[76] reported the first STM image of striped AuNPs coated with dodecanethiol-hexanethiol (C12 : C6) 2 : 1. As revealed from the STM images (Figure 1-21), the coating ligands with different length appear to be organized into strip-like domains in 1-phenyloctane. In their study, they also demonstrated that when recorded with the same sample in air, the STM images obtained were either Janus distributed or featureless due to the collapse of the C12 thiol. This no doubt indicated one of the limitations of using microscopy technique, which is that extra attention must be paid to the sample preparation to acquire the real morphology of the AuNP. Moreover, to get a good resolution of the STM image of the mixed AuNP, first the AuNPs need to be clean enough to avoid the contaminate of the scanning tips by the impurities. Second the AuNP has to be firmly attached to the conductive flat surface, so the AuNPs will not move during the measurement, which can significantly affect the resolution of the image.[77] Finally, ligands must be sufficiently different, in length or other features, to be distinguishable in the image, and their conformation must be such to allow the clear discrimination.

1.3.2 NMR spectroscopy

NMR is a powerful technique for the characterization of the morphology of mixed AuNPs. Recently, several methods have been developed to determine the structure information of the mixed monolayer of gold nanoparticle based on NMR. Stellacci et al.[78] studied AuNPs coated with diphenyl thiol (DPT) together with aliphatic ligand dodecanethiol (DDT) or 3,7-dimethyloctanethiol (DMOT), by the combination of 1D ^{1}H NMR and 2D NOESY techniques. NOESY allows for the determination of average proximity between nuclei. It is a 2D NMR technique that exhibits cross-peaks arising from dipole–dipole interaction between nuclear spins that are close enough in proximity (typically <0.4nm). The intensity of a NOESY cross-peak depends inversely on the sixth

power of the distance of protons, so this technique can be exploited for an estimation of internuclear distance. For mixed AuNP samples, the presence of cross-peaks can be used as a proof that the distance between two ligands is <0.4nm. Moreover, the intensity of the cross-peaks can be used to confirm the possible morphologies. In Stellacci's study, they found that when the AuNPs were coated with DPT and DMOT or DDT, they can obtain random, Janus and stripe-like distributed gold nanoparticles. This was firstly confirmed by the structure features arising from the STM images. In addition, NOESY showed the corresponding presence or absence of the cross-peaks, which indicated the relative distance of the two kinds of coating ligands. They further studied the relationship between ^{1}H NMR of the mixed AuNPs and the ratios of the coating molecules. The results demonstrated that when the composition of the mixed AuNPs is different, the chemical shift of the DPT varies based on the packing density and neighboring environment. For randomly distributed AuNPs, the ^{1}H NMR chemical shift of the DPT experienced a linear unfiled shifting with the increasing of the composition of DPT. For Janus AuNPs, the ^{1}H NMR chemical shift of DPT against the composition of DPT gave a downcurved tendency. While for stripe-like AuNPs when the ratio of DPT is between 20%-60%, the chemical shift of DPT kept constant. With the further increasing of DPT composition, the ^{1}H NMR chemical shift of DPT decreased lineally. This method can differentiate the various morphologies of the mixed AuNPs with high accuracy. However, the requirement of a series of AuNPs with different composition largely limits its application.
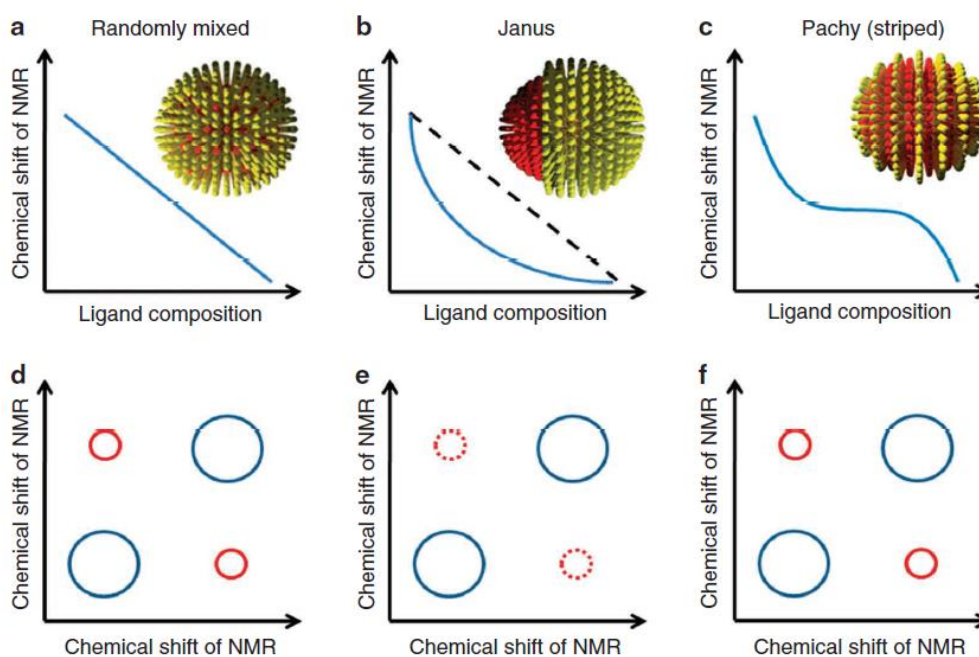

Figure 1-22. Idealized ^{1}H NMR and NOESY plots for mixed AuNPs with various morphologies.

Another NMR approach developed to study the morphology of mixed AuNP was reported by our group (Figure 1-23).[79] In this method, the strategy employed is based on the paramagnetic relaxation enhancement (PRE)[80] induced by lanthanide ions. This PRE effect causes the signals of the resonant spins surrounding (within a defined distance) the metal ions to broaden and eventually disappear from the ^{1}H NMR spectrum. Therefore, the different broadening patterns observed for the coating molecules might provide the direct information on the morphology of the AuNP. In the study, mixed AuNPs coated with alkyl thiol and polyethylene glycol (PEG) derivative in 50: 50 ratio were investigated. The chosen of the coating ligands is based on the fact that they possess different binding affinity to lanthanide ions, in this case Gd^{3+}. As revealed from NMR spectra, they found that with the addition of Gd^{3+} to the solution of the AuNPs, the signals arising from the PEG broadened and eventually disappeared. On the other hand, the signals of the alkyl thiols, while experiencing some broadening, where still present at 60% of the original intensity when the PEG signals disappeared. With this information and geometrical calculations, one can assume that this mixed AuNP is Janus distributed.
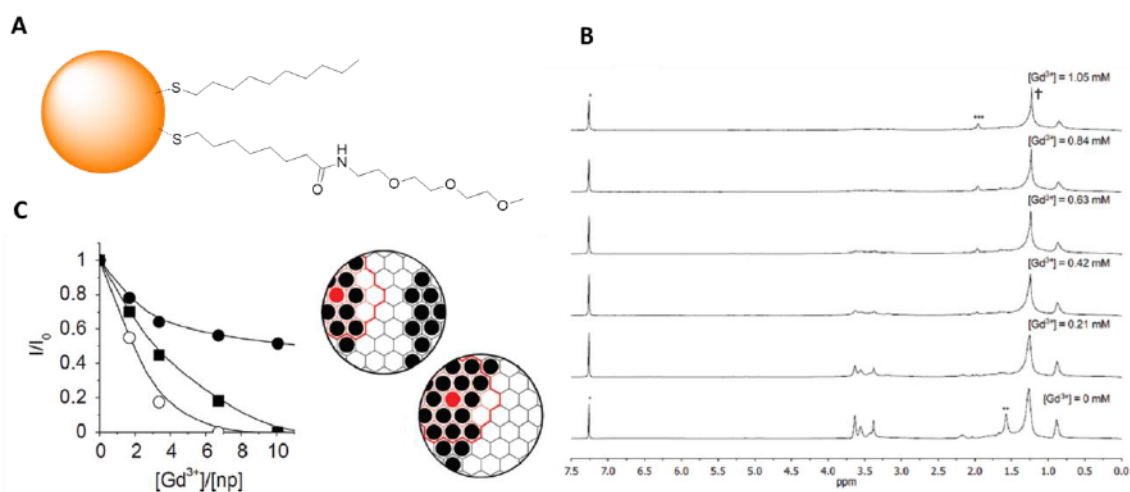
Figure 1-23. (A) the structure of the coating ligands used for the preparation of AuNPs. (B) the NMR spectra of the mixed AuNPs in the presence of various amount of Gd3+. (C) Relative intensity of signals from alkyl thiol (●, peak at 0.8 ppm) and PEG thiol (○, peak at 2.1 ppm) as a function of the Gd^{3+} ions/particles ratio (lines, data trend; ■, data from 100% PEG-coated AuNPs).

1.3.3 Matrix assisted laser desorption/ionization (MALDI) mass spectroscopy

It has been demonstrated that the morphology of mixed AuNPs can be determined by MALDI, which was reported by Cliffel et al (Figure 1-24).[81] The development of this method was based on the fact that Au_4L_4 is the most abundant species within the ionized fragments of AuNPs.[82] Hence

the distribution of $Au_4L_xL'_{4-x}$ can be exploited to investigate the ligands arrangement on the surface of the AuNPs. If the fragments of $Au_4L_xL'_{4-x}$ follow a binominal distribution, this indicates the AuNPs is randomly distributed. The larger the fragments deviate from the binominal distribution, the higher degree of phase separation occurs. This approach by no doubt provides a simple way to characterize the monolayer morphology of mixed AuNPs, however, the requirement of the similar ionization capability of the coating ligands is needed.
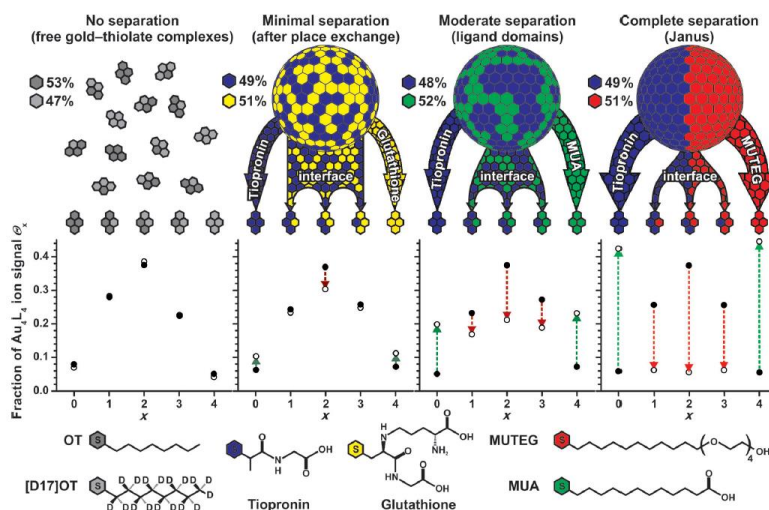

Figure 1-24. Morphology dependent distribution of $Au_4L_xL'_{4-x}$ fragments.

1.3.4 EPR spectroscopy

An EPR spectroscopy study aimed to demonstrate the morphology of mixed AuNPs was presented by Pasquato *et al*.[83] The authors make use of the fact that the field separation (G) of the radical probe is very sensitive to the local surrounding environment. They studied a wide range of mixed AuNPs which coated with HS-C8-TEG and HS-F8-PEG in different ratios. The investigation of the EPR spectrum showed that when the ratio of HS-C8-TEG/HS-F8-PEG is less than 2.5, the ΔG of the radical probe is 2.05, which is the same as they observed when the group was partitioned in the monolayer of HS-F8-PEG. This suggested the occurrence of phase separation. As the increasing of the ratio of HS-C8-TEG/HS-F8-PEG, the island formed by HS-F8-PEG is becoming smaller until the local environment experienced by the probe was disordered by HS-C8-TEG. In this case, the ΔG of the EPR spectra of the probe changed.
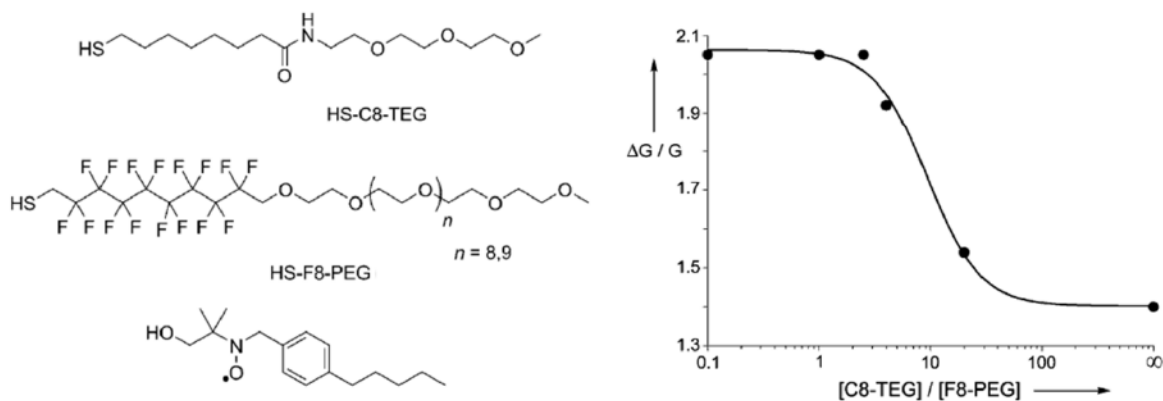
Figure 1-25. (Left) the structure of the coating ligands and radical probe used. (Right) the EPR spectra of AuNPs coated with HS-C8-TEG and HS-F8-PEG in different ratio in the presence of the radical probe.

1.3.5 Other methods

Besides the examples mentioned above, there are other methods have been studied to demonstrate the morphology of mixed AuNPs, such as fourier-transform infrared spectroscopy (FTIR),[21] Ultraviolet–visible spectroscopy (UV-Vis),[84] small angle neutron scattering (SANS),[76] adsorption-based fluorescence spectroscopy,[22] surface-enhanced Raman spectroscopy (SERS) or simulation.[85] For all these approaches developed, there are still several limitations. For microscopy method, expensive instrument, well preparation of the samples and image interpretation are needed. In addition, it is difficult to prove the presence of randomly distributed AuNPs. For NMR method, either a series of mixed AuNPs were needed or one of the ligands has to be functionalized to interact with the paramagnetic lanthanide ions to induce PRE effect. For MALDI method, it is necessary for the two ligands to have similar ionization efficiency. Overall, new methods are still demanding to progress this field.

In summary, AuNPs have received considerate research interest due to its easiness to prepare, unique physical and chemical properties and functionalization. The development of various signal transducing strategies largely promoted the blossoming of the AuNP-based molecular recognition. Undoubtedly, the intrinsic features of the AuNPs will continue to revolutionize the chemosensing area.

Chapter 2. Aims and objectives

Monolayer protected gold nanoparticles have emerged as molecular systems with promising applications in the field of biology, medicine, and chemistry. This PhD thesis aims to study the potential of AuNPs as self-organized chemosensors.

This PhD thesis has been focused on the following aspects:

1) The tailored design of NMR chemosensors based on monolayer protected gold nanoparticles.

2) The construction of IDA based sensor arrays made by self-organized nanoreceptors for detection and discrimination of carboxylate drugs.

3) The investigation of monolayer morphology of mixed AuNPs.

As discussed in the previous chapter, recently our group has developed a NMR chemosensing protocol, which named "NOE Pumping". This method is based on the use of nanoparticles as receptors capable, thanks to their relative "largeness", to label the analyte by NOE magnetization transfer. The receptor ability of the nanoparticles is granted by the presence of multiple coating molecules on the surface of the nanoparticles. If the thiol end group is not taken into account, such molecules have essentially a surfactant structure: an alkyl chain long 6-12 carbon atoms, essential to ensure the stability of the coating layer, and a functional head group responsible for solubility and also providing sites of interaction with the target molecules. The somehow ordered alignment of the coating molecules, as well as their spatial proximity, favors their cooperation in the target recognition. The alkyl chains, as demonstrated by the work of Pasquato and coworkers[64], provide a hydrophobic pseudophase capable of accommodating hydrophobic species, the head groups, as well as other functional groups inserted along the coating molecule, can provide multiple interactions.

Taking inspiration from such considerations, we aimed to study in better detail what kind of role the coating ligands played in the process of molecular recognition. Indeed, size, molecular weight and complexity of a 2-nm gold nanoparticle are similar to that of a protein. On the other hand, while in the latter substrate recognition arise from a precise structural organization resulting into the formation of well-defined binding sites, in the case of nanoparticles the monolayer organization and the factors controlling molecular recognition are largely unexplored. To this aim, beside the investigation of the properties of different monolayer prepared by "naive" design on

the basis on tentative or ipersemplified interaction models, we were also interested to understand if computational simulations can be employed to enable the rational design of AuNPs based macromolecular receptors with controlled recognition and sensing performance.

A further increase of the complexity of nanoparticle-based receptors could be provided by the use of mixed monolayer nanoparticles. However, if the advantage brought about is the possibility of easily multiply the possible interactions, in the same way Nature does by using 20 different amino acids, the drawback is in the further decrease of the degree of control over the monolayer structure. In this case indeed, uncertainty not only attains the conformation of the coating molecules, but also their spatial distribution and the nanoparticle composition itself. For this reason, previously established NMR methods, newly developed NMR methods, EPR and MALDI based method were exploited to investigate the morphology of the mixed AuNP. Moreover, we also aimed to study the morphology transformation induced by the interacting analytes.

Finally we studied different sensing applications of the nanoreceptors generated. We already mentioned as gold nanoparticles are very efficient fluorescence quenchers and such ability has allowed the straightforward development of IDA and array based sensing approaches. Based on this IDA strategy, we aimed to apply nanoreceptors capable to recognize organic anions to the design AuNPs-based sensor arrays for the detection and discrimination of structure similar carboxylate drugs.

In summary, this PhD thesis investigated the promising potential of AuNPs as self-organized nanoreceptors taking advantage of various techniques (NMR, fluorescence and EPR). The obtained results, which were shown in the following chapters, paved a way to the better understanding of the unique features of AuNPs and enabled the tailored design of AuNP-based chemosensors.

Chapter 3. Nanoparticle-based receptors mimic protein-ligand recognition

Receptors are cavity-like molecular structures capable to recognize, i.e. selectively bind, a target through convergent interactions. In biochemistry, they play a fundamental role in many relevant processes as rapid chemical transformations in catalysis,[86] selective transportation across cell membranes,[87] and modulation of key cellular signal processing.[88] Nature evolved a synthetically cost-effective strategy for the realization, modification and optimization of such functionalized cavities. These are formed by the controlled synthesis and folding of multifunctional biopolymers as proteins and nucleic acids.

Inspired by the power of Nature, the desire and ambition of engineering artificial receptors,[89] and control chemical processes through molecular recognition, is at the origin of Supramolecular Chemistry. The realization of suitable molecular scaffolds, however, must face several drawbacks arising mainly from the rigidity of the starting structural frame, the difficulties in introducing and positioning binding sites in it and, eventually, in its synthetic accessibility. Indeed, design of artificial receptors usually requires the implementation of suitable binding sites into a more or less rigid scaffold featuring a cavity-like, or at least concave, shape. Such a structure ensures the optimization of the dispersion interaction, the convergent arrangement of the binding sites, shape selectivity and, in water, the presence of high energy solvent molecules[90] that will be released upon substrate binding.

An approach to the realization of artificial receptors, which might be considered reminiscent of the Nature's one, is provided by AuNPs.[91] AuNPs form spontaneously by reduction of gold salts in presence of suitable coating molecules (usually thiols) and appropriate reaction conditions. The coating monolayer can be considered as a semi-flexible three-dimensional array of radially ordered organic molecules. As a consequence, binding sites inserted in the coating molecules are clustered and partially pre-organized, while maintaining enough flexibility to allow position adjustments and conformational reorganization.[92] Such an organization has been exploited by several groups to realize self-organized macromolecular receptors.[7, 93] In addition, functional group inserted in the monolayer may act cooperatively to perform other specific tasks besides recognition.[94-96] This has been exploited as an instance to endow AuNPs with the ability to catalyze reactions.[12, 97] The range of potential applications of such AuNP is therefore huge, and ranges from materials science and electronics, to bioimaging, nanomedicine, and even catalysis.[98, 99] Thus, a

quite relevant goal is now the rational design of nanoparticle-based receptors with programmed selectivity and affinity.[100] To accomplish this, however, several crucial steps must still be taken. In particular, a deeper understanding of the process of molecular recognition within the nanoparticle coating monolayer and of the parameters that control it is need.

We recently focused our attention on nanoparticles coated by the amide-bearing thiol **1**. As discussed in Chapter 1, Pasquato and coworkers[64] had already demonstrated that these nanoparticles can bind organic molecules in water, with a mechanism that was considered to be similar to the partition of hydrophobic specie between water and the lipophilic pseudophase of surfactant aggregates. However, also in this case monolayer organization may affect the binding. Indeed, Pasquato and Lucarini reported that bulky substrates have a smaller affinity than linear ones, and that affinity for the same substrate decreased by increasing the nanoparticles size.

Later on, studying the very same nanoparticles (1-AuNP),[43] again as discussed in chapter 1, we reported that they are capable to bind salicylate in water with an association constant (Kass, 25 °C) about 120 M^{-1}. Most remarkably they are selective for salycilate over molecules with similar structure, included the two isomers 3-hydroxysalycilate (4) and 4-hydroxysalicilate (5). However, when the sensing performance of 2-AuNP was investigated, we found that substrate preference does not perfectly follow the lipophilicity scale, and the substrate structure also plays a relevant role. Such evidences confirmed that substrate binding to the nanoparticles is the result of a more complex event than simple partition.

In this chapter, we report a detailed investigation on the recognition abilities of **1**-AuNPs compared with a series of new AuNPs (Chart 3-1) featuring different coating monolayers and selectivity for analytes. NMR-based experiments combined with extensive MD simulations indicate that molecular recognition at the monolayer of these selected AuNPs requires the pre-formation of specific, although transient, protein-like binding pockets in the nanoparticle-coating monolayer. We found that the presence of these pockets is, in turn, the result of a delicate and somehow counterintuitive balance of interactions within the monolayer itself and with the solvent. Taken together, these findings represent the basis for the rational design of tailored coating groups that can form selective recognition sites on monolayer-protected AuNPs, which are thus able to operate with programmed recognition ability.[101]

3.1. AuNPs design

The chemical structure of the original ligand **1** (Chart 3-1) can be divided into four parts: 1) the thiol (gray), which ensures the grafting to the monolayer surface; 2) the hydrophobic alkyl chain (blue); 3) an amide group (green), originally inserted for synthetic accessibility;[102] and 4) a hydrophilic oligo(ethylene glycol) (OEG) moiety (red), which ensures water solubility. At first glance, the alkyl part of thiol **1** should be the portion providing relevant interactions with salicylate. In the nanoparticle's coating monolayer, this alkyl part forms a hydrophobic pseudo-phase that may accommodate hydrophobic substrates, in a similar manner to surfactant aggregates. On the other hand, the amide group and also the OEG chain may form additional H-bonds with the substrate. To better understand these points, we designed a series of analogues where the two relevant parts of the ligand were systematically modified. In all ligands **7-10**, the amide group was removed. In **7**, it was substituted with an ether group (CH$_2$O). In this way, the removal of the amide did not substantially affect the size of the alkyl portion, while the ligand maintained the same length as **1**. In ligands **8-10**, on the other hand, removal of the amide groups was accompanied by an increase in length of the alkyl and/or the OEG portion.
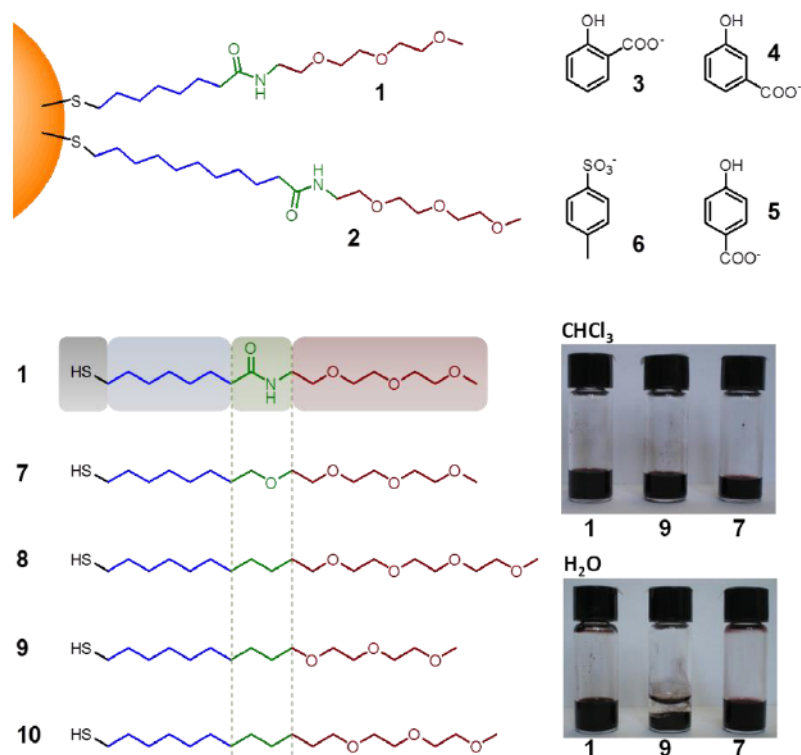

Chart 3-1. (Upper): The NMR chemosensing machinery for salycilate detection, monolayer protected nanoparticles used in early studies and analytes investigated. (Lower): Nanoparticle-coating thiols used in this study and solubility of representative samples in CHCl$_3$ and water.

3.2 Organization of the nanoparticle's coating monolayer

Ligands **7**-**10** and the corresponding AuNPs (1.5-1.7 nm gold core diameter) were prepared by standard protocols (Experimental section). Notwithstanding the similar structure of the coating thiols, nanoparticles revealed different solubility properties (Chart 3-1), intended here as the ability to form stable mixtures with the solvent that do not settle upon prolonged storage. Indeed, **1**-AuNP was very soluble in water (up to 300 μM, or 15 mg/mL) and in organic solvents with high and moderate polarity (from methanol to chloroform).[43, 103] **7**- and **8**-AuNPs were also soluble in water and organic solvents, but saturation concentration in water was lower (about 60 μM, or 3 mg/mL) than those of **1**-AuNP. Finally, **9**- and **10**-AuNPs, which contain shorter OEG chains, were soluble only in organic solvents. Based on such results, we decided to further investigate the dispersion state of nanoparticles **1**-, **7**-, and **8**-AuNPs in water by TEM, dynamic light scattering (DLS) and NMR. TEM micrograph obtained by depositing nanoparticle water solutions on the grids showed nanoparticles homogenously distributed over the substrate, without apparent aggregation (Figure 3-1). DLS measurements in water (at 15 μM nanoparticles concentration) revealed the presence in each case of a unimodal nanoparticles distribution with average diameters of 8, 16, and 21 nm for **1**-, **7**-, and **8**-AuNPs, respectively (Figure 3-2). Similar results were obtained by DOSY-NMR experiments, which detected again the presence of a unimodal nanoparticles distribution with average diameters of 5, 15, and 18 nm, respectively (Figure 3-3). These results indicated that **1**-AuNPs are present in water solution mainly as isolated nanoparticles while **7**- and **8**-AuNPs may form small aggregates. However, both DLS and DOSY-NMR hardly discriminate entities with similar sizes and consequently cannot provide precise information on the amount of aggregates present in the solutions with respect to isolated nanoparticles. Furthermore, if isolated and aggregated nanoparticles were involved into multiple exchange equilibria (a likely possibility), the interpretation of their apparent diffusivities would be even more complicated. Deeper insight into this point came from ^{1}H NMR investigations (Figure 3-4).
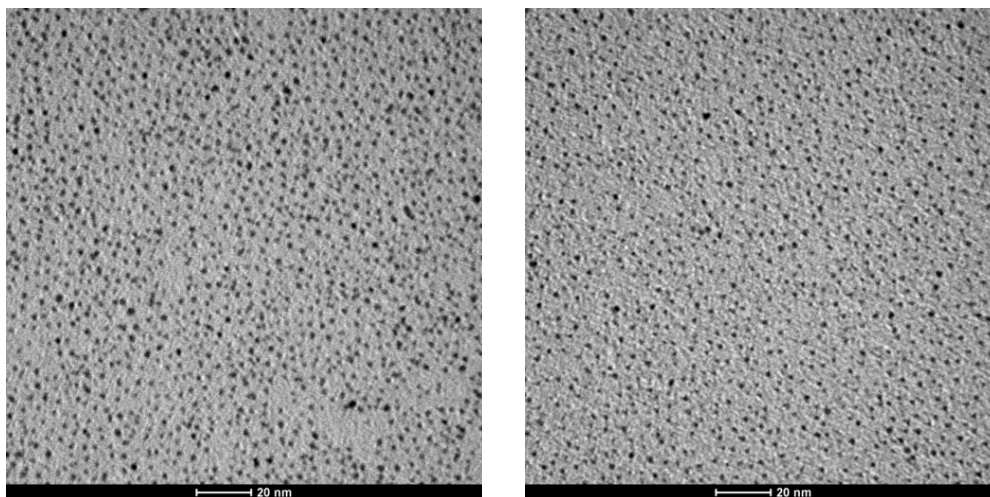
Figure 3-1. TEM images of **7**-AuNP (left) and **8**-AuNP (right) acquired after deposition of 15 μM (0.7 mg/mL) solution of nanoparticles in water.
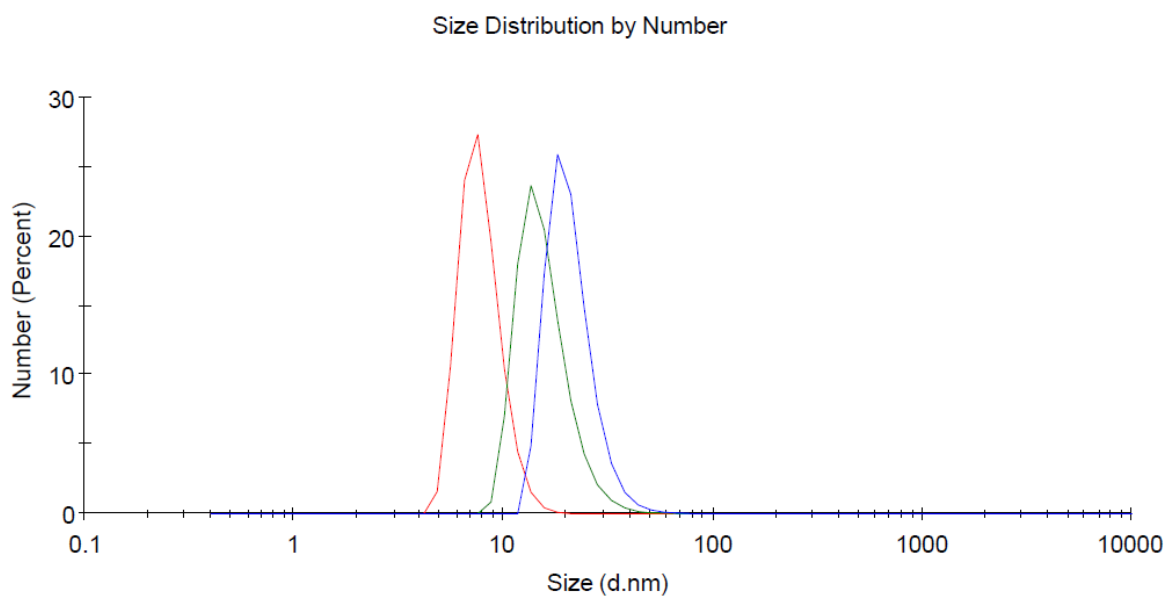

Figure 3-2. Number weighted size distribution obtained by DLS analysis for **1**-AuNP (red, 8±2 nm), **7**-AuNP (green, 16±5 nm) and **8**-AuNP (blue, 21±5 nm) in water at 15 μM (0.7 mg/mL) concentration (confidence intervals represent the half-widths of the size distribution curves).
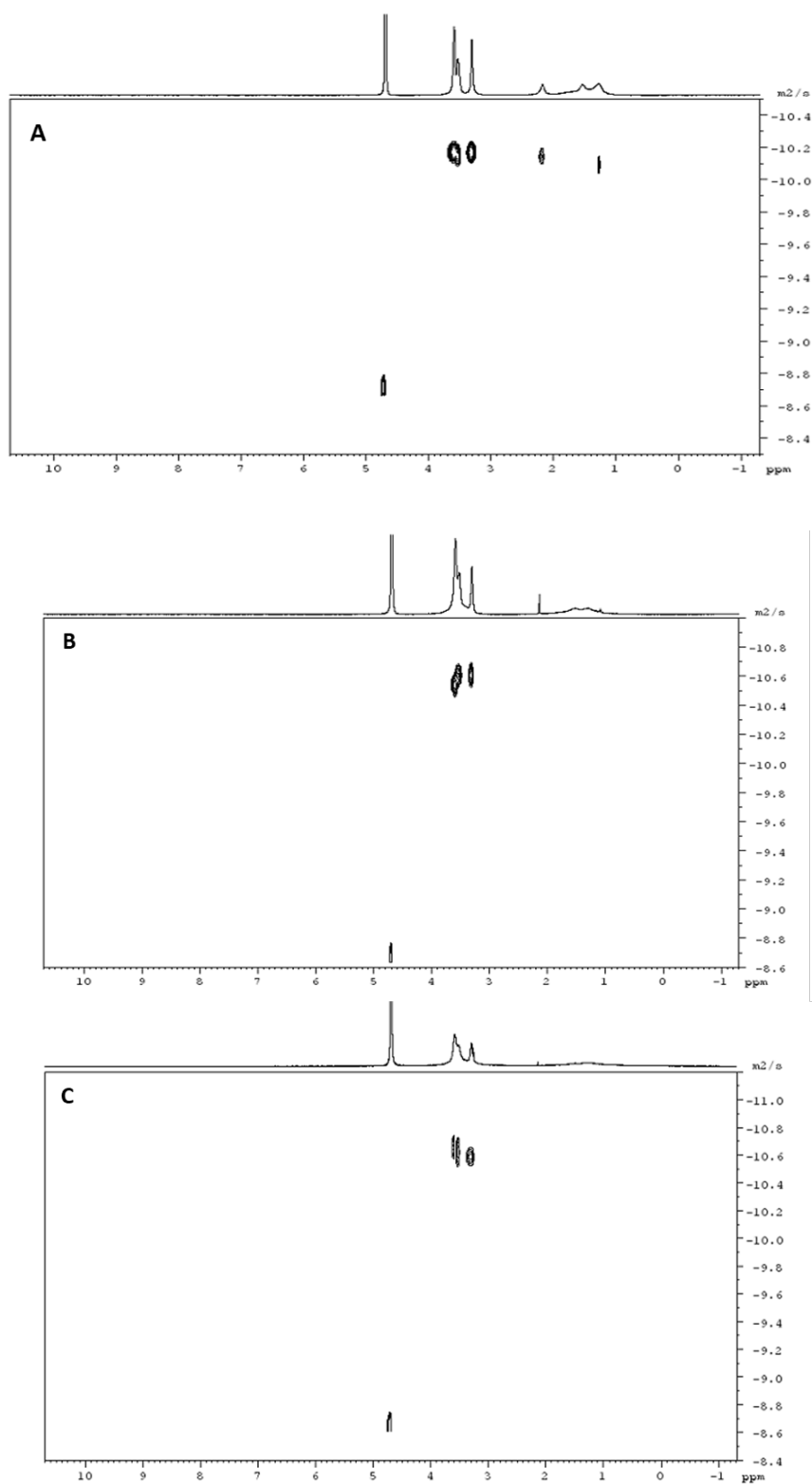
Figure 3-3. DOSY spectrum of AuNPs in water at 15 uM (0.7 mg/mL) concentration. A) 1-AuNPs, $D = (6.43 \pm 0.06) \times 10^{-11}$ m^{2}s^{-1}, B) 7-AuNPs $D = (2.14 \pm 0.06) \times 10^{-11}$ m^{2}s^{-1}, C) 8-AuNPs, $D = (2.0 \pm 0.2) \times 10^{-11}$ m^{2}s^{-1}.
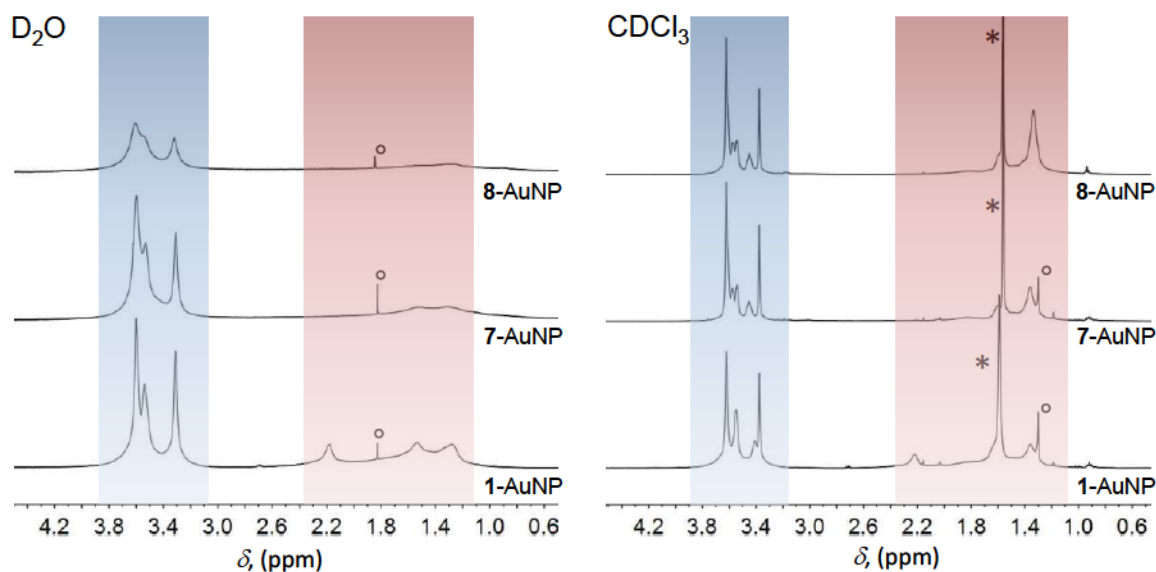
Figure 3-4. NMR spectra of **1**-, **7**- and **8**-AuNP in D_2O (left) and $CDCl_3$ (right), signals from the OEG portion of the coating thiols are highlighted in blue, signals from the alkyl portions are highlighted in red. *: residual water signal. °: impurities.

As expected, due to the nanoparticle grafting, all the ^{1}H signals arising from the coating thiols are relatively broad and the hyperfine structure is not resolved.[104] However, a striking difference becomes evident when comparing the spectra recorded in deuterated water for **1**-, **7**-, and **8**-AuNPs (Figure 3-4). In fact, the signals arising from the OEG portion, between 3.3 and 3.8 ppm, and in particular from the terminal methoxy residue at 3.35 ppm, have similar linewidths for **1**-AuNP (13.3 Hz) and **7**-AuNP (16.6 Hz) but are significantly broader for **8**-AuNP (24.5 Hz). Linewidth of signals arising from terminal groups have been shown to strongly depend on nanoparticle size.[105] Indeed, neglecting magnetic field in homogeneities, NMR signal broadening depends on the transverse relaxation time T_2. This is determined mainly by the dipolar interactions between the spins in the monolayer, as modulated by the nanoparticle tumbling rate and by the internal mobility of the ligands within the monolayer. Since the dynamics of the OEG portions of the coating ligands should be independent from the ligand packing in the monolayer, broadening of **8**-AuNP signals indicates a slower tumbling rate (or chains rigidification) as expected in the case of aggregates. We hence concluded that **7**-AuNP are dispersed in water mainly as isolated nanoparticles that coexist with a small fraction of aggregates, while in the case of **8**-AuNP the population of aggregates is more pronounced.

Values for ^{1}H relaxation times T_1 and T_2 are reported in Table 3-1. As expected, T_2 values increase with the distance from the Au core since protons farther from the core are less packed and consequently have larger degrees of freedom with respect to those closer to the nanoparticle core.[105] In $CDCl_3$, T_2 values for the signals of the different regions (alkyl, OEG, CH_3, Table 3-1) are

similar for all AuNPs, confirming that all nanoparticles have a similar mobility of the coating ligands, similar sizes and are present as isolated entities. In water, the behavior is different: all spins of **1**-AuNP relax more slowly than those of **7**- and **8**-AuNPs. In addition, as revealed from Table 3-1, the T_2 values of the terminal methyl groups are about two times larger with respect to the OEG groups in both $CDCl_3$ and D_2O. This is because the terminal methyl groups experience the internal rotation effect.

Solvent	Signals	min-max T_2 (sec)[b]			min-max T_1 (sec)[b]		
		7-AuNp	**8**-AuNp	**1**-AuNp	**7**-AuNp	**8**-AuNp	**1**-AuNp
$CDCl_3$	Alkyl[c]	0.504-0.694	0.429-0.537	0.711-0.766	0.660-0.989	0.667-0.69	1.04-1.30
	OEG[d]	1.13-1.41	1.13-1.49	0.626-0.744	0.748-1.59	0.847-1.64	0.923-0.986
	CH_3[e]	2.61	2.52	1.67	2.84	2.83	1.81
D_2O	Alkyl[c]	0.006**-0.016*	0.024*-0.05*	0.07*-0.11*	0.67-0.7*	0.6**-0.7**	0.596-0.62
	OEG[d]	0.061-0.065	0.031*-0.038*	0.222-0.279	0.648-0.681	0.64-0.64	0.638-0.638
	CH_3[e]	0.101	0.07**	0.52	0.912	0.70	1.13

[a] Errors within 10% unless indicated: * errors within 25%, ** errors within 50%; detailed error values are reported in the Supporting Information. [b] For each spectral region the higher and smaller relaxation times are reported. [c] Signals in the 1.2-2.3 ppm range. [d] Signals in the 3.4-3.8 ppm range. [e] Broad signal at 3.3 ppm, relaxation parameters for the terminal methyl group are reported separately because they are affected by internal rotation.

Table 3-1. [1]H T_1 and T_2 relaxation times for 1-, 7- and 8-AuNPs in $CDCl_3$ and D_2O.[a]

In the case of **8**-AuNP such an effect may be ascribed to aggregation that reduces both the nanoparticles tumbling rate and the mobility of the chains (because of their interlocking). However, when **1**- and **7**-AuNP are compared, one can note that the decrease of the T_2 values for the latter is much more relevant for the signals arising from the alkyl chains (~10-fold decrease) with respect to the ones from the outer OEG chains (~4-fold decrease). This suggests that, besides a possible reduction of the tumbling rate, faster relaxation of the alkyl signals in **7**-AuNP may also arise from a decrease of their internal mobility. In other words, when in water, the nanoparticles coated with ligands devoid of the amide unit, as **7**-AuNPs, feature substantially more rigid alkyl chains than those of **1**-AuNP, which contain the amide moiety.

Subsequently, we investigated the ability of water-soluble **1**-, **7**-, and **8**-AuNPs to detect organic molecules with the NMR chemosensing protocol (Figure 3-5). The NOE pumping sequence was used to analyze samples containing the nanoparticles (15 μM) and salicylate at increasing concentrations (1-10 mM) in carbonate buffered D_2O solution at pD = 10.0. **1**-AuNP confirmed their reported ability to detect salicylate in water.[43] Analyte signals appeared in the NOE pumping

spectra at substrate concentrations as low as 2 mM and increased in both intensity and signal-to-noise ratio by increasing concentration. On the other hand, and surprisingly enough, analyte signals were never detected with a signal-to-noise ratio above 3 (which we usually set as a detection limit) in the experiments performed using **7**- and **8**-AuNPs, even in the presence of high (10 mM) concentrations of the substrate. All the nanoparticles have the same size and a very similar structure of the coating thiols, which leads to similar longitudinal relaxation rates (T_1) of protons within the same moieties (Table 3-1). Thus, the different signal enhancements observed in NOE-pumping experiments (Figure 3-5) should rather arise from different cross relaxation rates, which depend on the affinity on the analytes for the substrate. This indicates that **7**- and **8**-AuNPs have an affinity for salicylate that is sensibly lower than that of **1**-AuNP and confirms that partition into the hydrophobic pseudo-phase formed by the alkyl portions of the nanoparticles coating thiols cannot explain the observed substrate recognition.
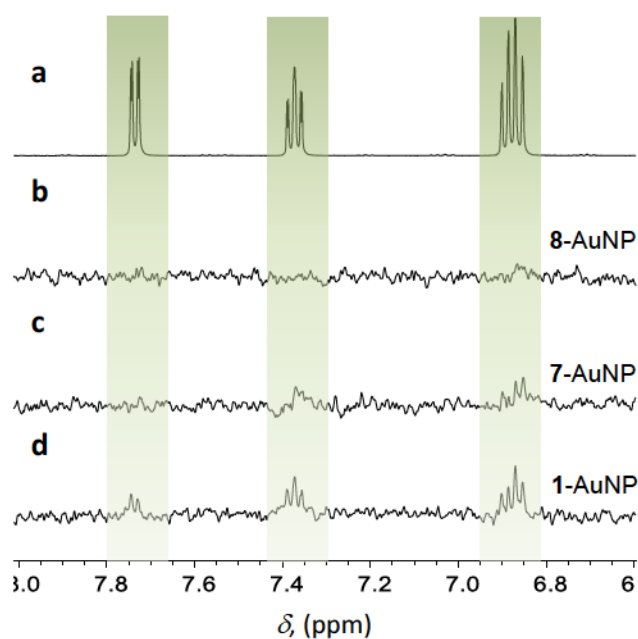
Figure 3-5. a) ^{1}H-NMR subspectrum of 5 mM sodium salicylate (**5**) in D_2O. b) NOE-pumping subspectrum of the same sample in the presence of **8**-AuNP. c) NOE-pumping subspectrum of the same sample in the presence of **7**-AuNP. d) NOE-pumping subspectrum of the same sample in the presence of **1**-AuNP. Conditions: [AuNP]= 15 μM, carbonate buffer 20 mM, pD = 10, 28 °C.
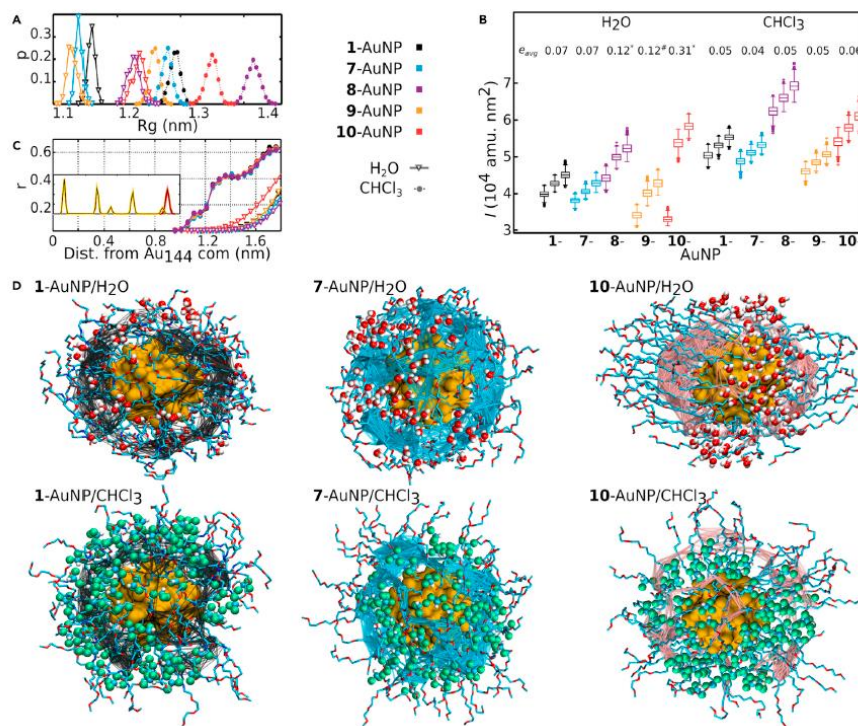
3.3 Morphology and dynamics

Figure 3-6. Shape and solvation of AuNPs. Probability distributions of: A) radius of gyration (R_g) and B) moments of inertia (I, shown as box-and-whisker plots) of **1**-, **7**-, **8**-, **9**-, and **10**-AuNPs in water and chloroform. The average nanoparticle eccentricity $e=\langle 1-I_{min}/I_{avg}\rangle$, where e = 0 for a sphere and 1 for a prolate spheroid, is also reported (st.dev. = 0.2 except for * and #, where it is 0.3 and 0.4, respectively). C) Distribution of the solvent molecules and the gold and sulfur atoms (in the inset in yellow and orange, respectively) from the center of mass of the Au_{144} core. D) Representative snapshots of the AuNPs and solvent molecules within 1 nm of the gold atoms (wires connect carbon atoms C^4-C^7 closer than 0.8 nm).

To obtain more insight on this behavior, we started a collaboration with the group of Dr. Marco De Vivo at the Italian Institute of Technology (Genova). They performed a series of extended MD simulations of all the AuNPs immersed in either explicit water or chloroform. The first problem to address was the starting structure of the nanoparticle to be used for the simulations. Nanoparticles samples prepared by standard solution methods are usually composed by clusters of different sizes. In our case, the average Au core diameter (1.7 nm) is close to that of the $Au_{144}(SR)_{60}$ cluster (~1.6 nm). Indeed, it has already been shown that $Au_{144}(SR)_{60}$ is the main component in nanoparticles batches with average diameter around 2 nm. In addition, we previously demonstrated that computational simulations performed using the $Au_{144}(SR)_{60}$ nicely predict the properties of nanoparticles samples with similar size distribution.[106] We hence considered the $Au_{144}(SR)_{60}$ structure as single nanoparticle model to analyze the dynamical

properties and interactions of the different coating ligands. Classical MD simulations in explicit solvents >200 ns for each AuNP/solvent system (~3.2 μs in total) were performed hence at IIT.

The picture emerging from such simulations provided relevant information. First, we noticed that all the monolayer-protected AuNPs were more compact in water, as reflected by a decrease of ~10% of their radius of gyration compared to that in chloroform (Figure 3-6A). In chloroform, the relative distribution of the three moments of inertia and the eccentricity, which are shape descriptors, indicate that all the AuNPs adopted a spherical shape (Figure 3-6B). On the contrary, monolayer conformational preferences in water were quite different. **1**- and **7**-AuNP appeared relatively spherical in this solvent too, but we observed progressively broader relative distributions of moments of inertia, causing an increase of the eccentricity values, for **8**-, **9**-, and in particular **10**-AuNPs, suggesting a less spherical shape (Figure 3-6B). In **10**-AuNP, sphericity deviation can be clearly ascribed to the collapse of the coating molecules into bundles, featuring aligned alkyl chains located at opposite poles of the nanoparticle (Figure 3-6D).[107] For **7**-, **8**-, and **9**-AuNPs, on the other hand, alkyl-chain bundles were not clearly detected but simulations again indicated a similar level of conformational rigidity for the alkyl portion of these nanoparticles, in line with the broad NMR signals and short transverse relaxation times observed for **7**-AuNP in the NMR experiments (Figure 3-4 and Table 3-1). In chloroform, all AuNPs were more flexible than in water, and the OEG of **7**- and **8**-AuNPs was less constrained than that of **1**-AuNP, in agreement with the NMR experiments discussed above.

The elongated spheroid shape of **8**-, **9**- and **10**-AuNPs in water resulted in the exposure of the ligand's alkyl chains to the solvent. This is particularly evident in **10**-AuNPs. Here, the bundling of the coating ligands created a structure with a wide, ring-shaped, equatorial region where alkyl chains were poorly shielded from water by few OEG chains. Indeed, the water molecules closest to the gold core were almost exclusively found in this ring-shaped region (Figure 3-6D). The number of ligand/water hydrogen bonds (HBs) is reported in Figure 3-7 and provides interesting information. **1**-AuNP formed the larger number of HBs with the solvent (~150), followed by **7**- and **8**-AuNPs (~86-88), and, finally, by **9**- and **10**-AuNPs (~76-79).

Figure 3-7. H-bond interactions. Average number of ligand/ligand and ligand/water HBs during MD simulations and decomposition of this number for the different coating thiol atoms (ordered top to bottom from the outer to the inner part of the coating ligand). [a]NH is present in **1**-AuNP while O in **7**- and **8**-AuNPs.

Interestingly, the trends of the computed eccentricity values in water and of the number of H-bonds with the solvent well correlate with the observed nanoparticles solubility and aggregation tendency. That is, nanoparticles showing a more spherical shape, with a consequent better shielding of the inner alkyl chains and a better solvation in our simulations, correspond to those present in solution as individual entities. Still, subtle differences found for quite similar nanoparticles, as **7**- and **8**-AuNP, indicate that a full explanation of nanoparticles stability in solution will require additional investigations.

The substantially greater number of HBs made by **1**-AuNP is due to the amide group, particularly its carbonyl oxygen, which was responsible for ~50% (~60% considering the NH, too) of the interactions with water. The OEG portion accounts for the remaining 40% of HBs, with the number of interactions decreasing from the terminal and more exposed oxygen to the inner ones. The same trend was observed in **7**-, **8**-, **9**-, and **10**-AuNPs. Here, however, the total number of HBs formed by the three outer oxygens was larger than in **1**-AuNPs (~73-79 *vs* ~61).

The additional oxygen atom in **7**- and **8**-AuNP, compared to **9**- and **10**-AuNPs, formed only a few (~13-15) HBs with water. This is because the extra HB acceptor site in **7**- and **8**-AuNP is buried inside the monolayer and thus poorly exposed to the solvent. In this view, it is striking that the insertion of the carbonyl group in **1**-AuNP increased the number of HBs from ~76-79 to ~150. This implies that the amide groups not only provide an additional site of interaction with the solvent,

but also substantially affect the conformation of the ligands, which in turn modulate solvation of the monolayer.

Another relevant feature revealed by HBs analysis regards the interligand interactions in **1**-AuNP. In this case, the amide NH group formed 22±4 HBs with acceptors on neighboring ligands. This is quite close to the average number of interactions established with water molecules (19±4). Interestingly, half of the interligand HBs formed by NH are with neighboring carbonyl oxygens, while the remaining ones are formed with the OEG, decreasing from the outer to the inner oxygen (Figure 3-7). Importantly, these results revealed that: 1) the number of interaligand HBs is relatively small (the theoretical maximum being about 60); 2) the formation of HBs between the amide groups and the OEG oxygens is favored by the significant bending of the coating ligands. On the other hand, we found ~90 HBs with intercalated water, which are thus favored compared to interligand HBs. Likely, HBs with intercalated waters helped maintain the amide groups of **1**-AuNP in being spaced and distributed homogeneously, preventing the massive bundling observed with the other AuNPs. Instead, the bending of some ligands of **1**-AuNP, which favors rigidification through interligand HBs with the amide group (Figure 3-7), explains the smaller average number of interactions that OEG oxygens establish with water, with respect to those formed by **7**-, **8**-, **9**-, and **10**-AuNPs.

In chloroform, where HBs with the solvent are not possible, the number of interligand HBs in **1**-AuNP almost doubled to 43±3 (Figure 3-7), compared to water. At the same time, and in contrast to water, OEG headgroups were rarely involved in these interactions, preferring extended conformations toward the solvent. The interligand HB network generated highly structured HB-chains (Figure 3-8). Such interactions modified the preferred monolayer conformation in these nanoparticles, from the homogeneously distributed structure observed for the simulations in water to a more inhomogeneous structure characterized by the presence of large "canyons" filled by solvent molecules (Figure 3-6C, 3-6D).
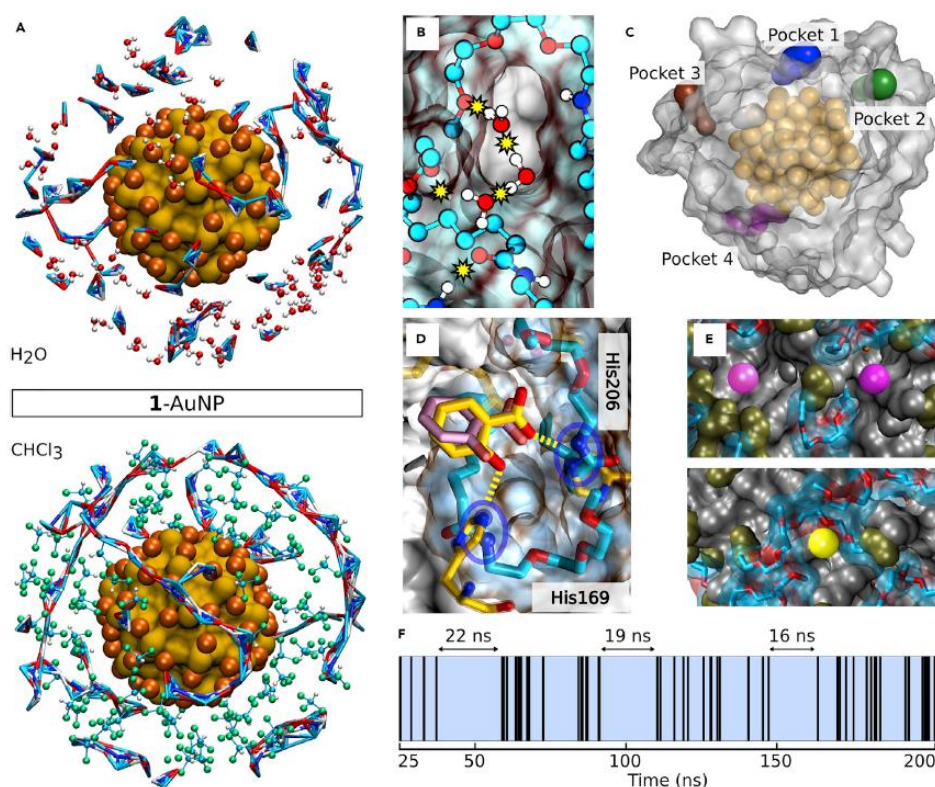
Figure 3-8. Structure of the monolayer A) Amide group atoms closer than 0.4 nm are connected by wires, and solvent molecules within 1 nm of the Au_{144} core are shown. Au_{144} core is shown as gold surface, while sulfur atoms as orange spheres. B) Example of HB network for **1**-AuNP in water. C) Identification of pockets on one snapshot of **1**-AuNP in water. D) Superposition of docking pose of salicylate in **1**-AuNP and in the LysR-type transcription factor (PDBid: 2Y7K). E) Characterization of pockets for **1**-AuNP in water. Magenta spheres indicate the "deep cavity" pockets (upper panel), while yellow spheres indicate the "OEG sinking" pockets (bottom panel). Gray, green, and cyan surfaces identify the alkyl, amide, and OEG region, respectively. F) Time-evolution and life-time of a stable pocket formed in **1**-AuNP in water. Blue color for the open-pocket and black for the closed-pocket.

Taken together, these data show that the compactness, shape, and surface arrangement of the AuNPs' coating ligands are strongly affected by both the ligand structure and the solvent. In chloroform, ligands prefer a disordered conformation that results in an overall spherical nanoparticle shape. Only for **1**-AuNP, the formation of interligand HBs induce the clustering of the ligands in small bundles separated by deep "canyons". Such a behavior is in full agreement with the early observation by Rotello *et al.*[108] who detected relatively strong interligand HBs in nanoparticles coated with amide bearing thiols in organic solvents. Based on chemical oxidation experiments, such interligand interactions were supposed to generate ligand bundling, and the resulting "canyons" to cause the lower resistance of the gold core to decomposition.[108] In water, it is the dispersive/hydrophobic interaction between the alkyl chains that induces the aggregation of the ligands to form bundles. It appears that such structures may favor aggregation and even prevent the nanoparticle's dissolution in water, depending on the length of the OEG chains.

The effect of the amide groups in **1**-AuNP in water is therefore somehow intriguingly counterintuitive. Amide groups do not reinforce the bundling, as in chloroform where they provide an additional interligand interaction.[109] Instead, amide groups favor the intercalation of water molecules, which act as spacers between the ligands, inducing a more disordered and spherical monolayer conformation in water.

3.4 Molecular basis for recognition

Importantly, for **1**-, **7**-, and **8**-AuNP, the simulations in water revealed the formation of transient pockets in the monolayer structure (Figure 3-8). The pockets showed different sizes and shapes. The observed average number was ~5±2 for each AuNP, and an average volume of ~0.15±0.04 nm^3, which is enough to accommodate a few waters, but also small organic molecules such as salicylate. The pockets lifetime ranged from hundreds of ps to tens of ns, revealing their transient nature. While some pockets were very flexible, i.e., they had a high frequency of transitions between short-lived open/closed conformations, other pockets were more structured and able to remain open for the majority of the simulation time (see Figure 3-8F, this pocket was open for > 90% of the time). Closer inspection revealed that such pockets could be classified into two different topological classes. The first class, found in all the nanoparticles, was essentially characterized by the sinking of the OEG layer, and only fragments of such moieties composed the pocket walls. The second class, present only in **1**-AuNP, was deeper and penetrated down into the alkyl layer (Figure 3-8B). Notably, in this case, water molecules were often found to form bridges either between distant parts of the same coating ligand (i.e. amide and OEG) or between distinct ligands, creating a complex HB network topology (Figure 3-8B).

The occurrence of the latter transient cavities only on the surface of **1**-AuNP helps rationalize the recognition ability of these nanosystems in NMR chemosensing experiments. To further investigate **1**-AuNP's interaction with the bound analytes, we reversed the NOE-pumping approach by transferring magnetization from the analyte to the monolayer with a selective 1D-NOESY pulse scheme.[110] From a qualitative viewpoint, the larger the number of close contacts between the monolayer and the analyte, the stronger the nanoparticles' NOE signals in this experiment. The 1D-NOESY spectrum in Figure 3-9 clearly shows that NOE enhancements on the alkyl portion of the coating monolayer are larger than those on the oxo-methylene moieties. This suggests that the salicylate molecule arranges in such a way as to place its protons in close proximity to the inner alkyl portion of the monolayer. However, its position in the monolayer is

not deep enough to prevent contacts with the OEG portion, as evidenced by the weak NOE signals observed.
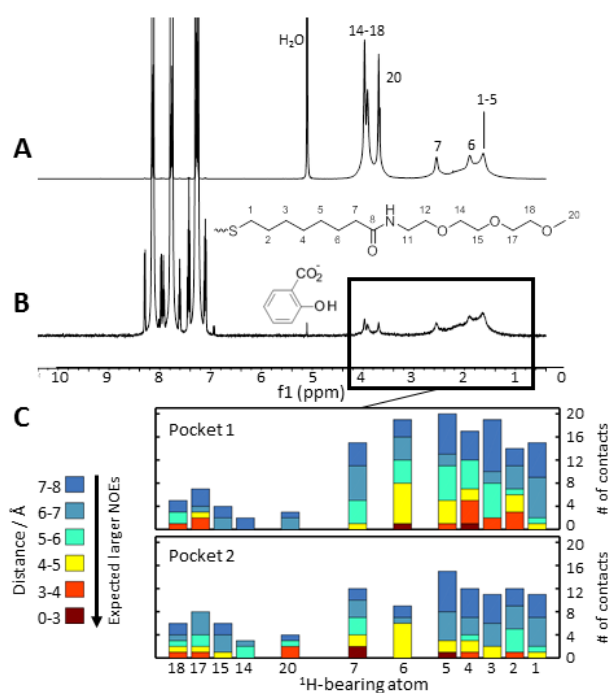

Figure 3-9. A) ^{1}H reference spectrum of 20 mM sodium salicylate and 10 mM **1**-AuNP in D_2O carbonate buffer (pD = 10). B) 1D NOESY spectrum of the same sample obtained with selective excitation of the salicylate resonances (6-9 ppm) and 300 ms mixing time. Signals of the nanoparticle highlight a negative NOE regime (slow tumbling). C) Number of total ^{1}H-^{1}H contacts, colour-coded in intervals of 1 Å, between docked salicylate and ^{1}H bearing atoms of **1**-AuNP (exchangeable NH omitted). The bars have been sorted according to the chemical shifts of the parent atoms.

This result was compared with molecular docking calculations of salicylate to the four pockets detected on the monolayer of a representative equilibrated MD snapshot (Figure 3-8). In particular, pockets 1 and 2 were of the "deep cavity" type, while pockets 3 and 4 were of the "OEG sinking" type. Interestingly, we found that the interaction network of the salicylate's docking pose into pockets 1 and 2 gave rise to a large number of contacts with the alkyl portion of the coating ligand (Figure 3-9C), in agreement with the results of the selective NOESY experiment. On the other hand, docking in pockets 3 and 4 resulted in predominant contacts with the OEG groups. There is thus a good qualitative agreement between the NMR data and the docking of salicylate to the "deep cavity" pockets that are present in **1**-AuNPs. In addition, the predicted docking pose into pocket 2 well-matched that of salicylate co-crystallized with LysR-type transcription factors (Figure 3-8D).[111] This corroborates the idea that AuNPs can form protein-like pockets on the surface, as here in **1**-AuNP, and suggests that cavities with the proper topology are essential for the specific

interaction with selected analytes. Nicely enough, Lucarini *et al.*[112] have reported that gold nanoparticles coated with thiol **1** undergo a decrease of affinity for hydrophobic organic molecules as their size increases. Indeed, formation of binding pockets in the monolayer would be more difficult in large nanoparticles, as the decreased curvature should induce a stronger packing of the thiols, which in turn may hamper pockets opening.
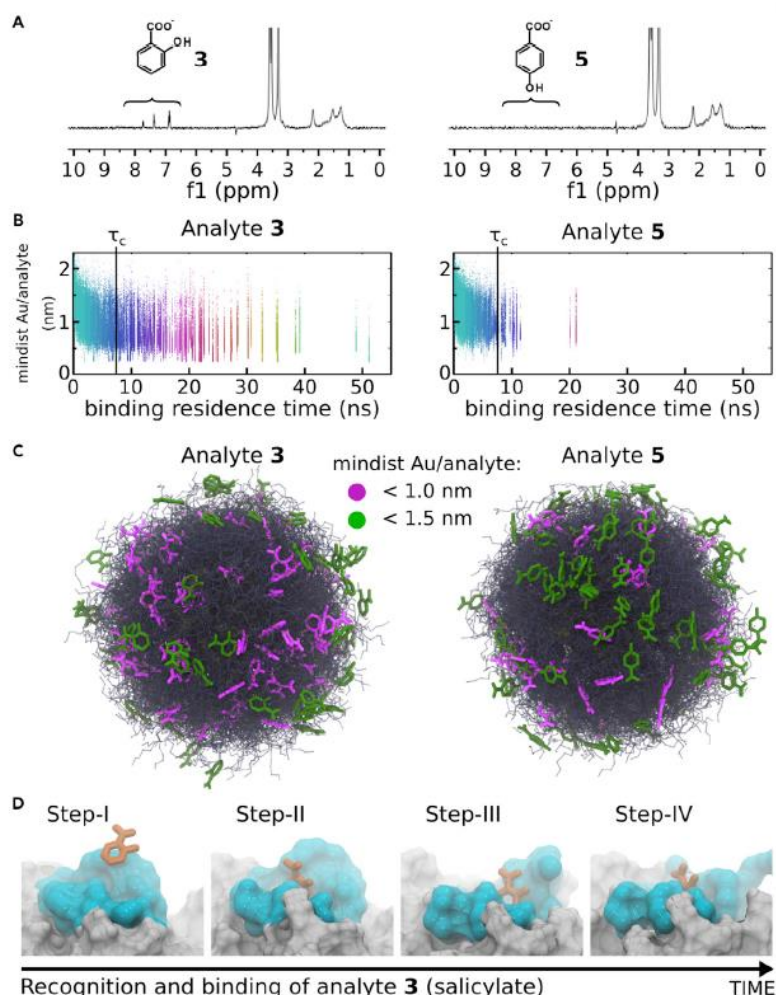
Figure 3-10. 1-AuNP/analyte interactions. A) NOE pumping spectra resulting from a solution of 15 μM **1**-AuNP with either 5 mM salicylate (left) or 5 mM 4-hydroxybenzoate (right). Mixing time is 1.2 s. The emergence of a signal only for salicylate is well rationalized by the MD results outlined in panel B (see text for details). B) During MD simulations, **1**-AuNP/analyte binding events were defined when the minimum intermolecular proton-proton distance was less than 0.4 nm. The binding events were sorted by their binding residence time (x-coordinate) and plotted against the minimum distance between the analyte and the Au_{144} core (depth of penetration in the monolayer, y-coordinate). The rotational correlation time (τ_c) of **1**-AuNP is also reported as a visual guideline. C) Distribution of the analytes in the monolayer taken from MD snapshots every 25 ns. Purple analytes lay at max 1 nm from the gold core, while green lay between 1 and 1.5 nm. D) Binding event of salicylate to **1**-AuNP.

Accommodation of the substrate inside pockets in the nanoparticle-coating monolayer may be somewhat expected. The different efficiency of **1**- and **7**-AuNP in the NOE pumping experiments, however, indicates that pockets opening may be a prerequisite for an efficient recognition.

To clarify these relevant points and define the molecular basis for the AuNP/analyte recognition process, IIT collaborators run two 1 μs long MD simulations of **1**-AuNP, with either salicylate or 4-hydroxybenzoate (**3** and **5** in Chart 3-1, respectively) in solution. Results obtained showed that salicylate, which is selectively detected by **1**-AuNP in chemosensing experiments (Figure 3-10A), spent ~48% of the simulation time bound to the monolayer (i.e., conformations where the distance between protons of the analyte and of the monolayer was less than 0.4 nm). In addition, residence time related to each recognition event is quite long, lasting tens of ns (Figure 3-10B). In NOE pumping experiments, a sizeable magnetization transfer between the spins of the monolayer and those of the analyte is detected only when the residence time of the analyte in the monolayer is comparable, or longer, than the rotational correlation time (T_c) of the nanoparticle. Inspection of Figure 3-10B, where the binding events are sorted according to their binding residence time, reveals that many binding events of salicylate visibly exceed T_c of the nanoparticle. Moreover, in agreement with NOE experiments, MD simulations indicated that salicylate was mostly sinking into the inner part of the monolayer, with the aromatic ring pointing toward the gold core and the carboxylate group remaining exposed to the water solution. We also detected the formation of HBs between the substrate's carboxylate and hydroxyl groups and the monolayer amides, which were formed during 6% of the total simulation time.

On the other hand, 4-hydroxybenzoate, which is not experimentally detected by NOE pumping experiments with **1**-AuNP (Figure 3-10A), was in the bound state only for 27% of the overall simulation time. Moreover, the observed binding events of 4-hydroxybenzoate were on a short time scale (a few ns), thus rarely above T_c. Indeed, our MD simulations show that this analyte was mostly floating on the outer OEG surface when compared to salicylate. Orientation of 4-hydroxybenzoate inside the monolayer was similar to that observed for salicylate, with the carboxylate group pointing toward the water phase. In this configuration, the 4-hydroxy group is located deep inside the hydrophobic portion of the cavity. Such unfavorable condition likely justifies the shorter permanence of the substrate into the cavities.

Noticeably, the time of residence into the cavities is not only correlated with magnetization transfer, but also with binding affinity, since it directly depends on the rate of dissociation (k_{off}) of the analytes form the monolayer. A longer residence time hence suggests a higher thermodynamic affinity of the substrate for the monolayer.

Ultimately, these simulations allowed us to decipher the binding mechanism of salicylate to **1**-AuNP, which occurred through four main steps (Figure 3-10D): I) formation of transient pockets in

the monolayer; II) binding of salicylate into one of these transient pockets; III) conformational changes of the pocket in response to analyte binding; IV) sinking of the analyte into the inner shell of the monolayer. Such a sequence confirms our early hypothesis that the opening of the pocket is the essential prerequisite for ligand binding. Consequently, as here found, nanoparticles recognition ability is crucially related to their ability to form pockets with the proper structure and lifetime. Fascinatingly, the above listed series of events suggests also an interplay between conformational selection and induced fit,[113] well mimicking the recognition and binding process for protein-ligand complex formation.

3.5 Conclusions

Overall, this combined computational–experimental study shows that functionalized coating ligands can self-organize through a delicate and somehow counterintuitive balance of interactions within the monolayer itself and with the solvent. These complex interactions can also favor the formation of transient, protein-like binding pockets in monolayer-protected AuNPs.[114] These findings imply that nanoparticle-based recognition operates through a process that is similar to that for protein-ligand complex formation. The results here reported also open new questions that merit further investigation, like on which structural and physiochemical parameters predominantly control monolayer organization and pocket formation, similarly to what established for binding pockets in proteins. The next goal will be the rational design of thiols capable of favoring the formation of selective pockets and receptors in the nanoparticle coating monolayer.

3.6 Experiment section

3.6.1 Synthesis of 8-mercapto-N-(2-(2-(2-methoxyethoxy)ethoxy)ethyl)octanamide (thiol 1)

Thiol **1** was prepared according to the following scheme:
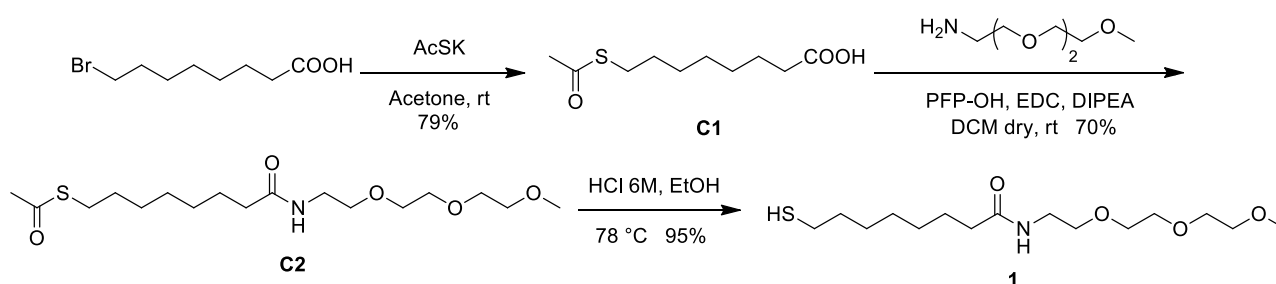
Scheme 3-1. Synthesis of the thiol **1.**

Synthesis of 8-(acetylthio)octanoic acid (C1). 8-bromooctanoic acid (4.00 g, 17.9 mmol, 1.0 equiv) was dissolved in acetone (100 mL) and potassium thioacetate (2.50 g, 21.9 mmol, 1.2 equiv) was added. The mixture was stirred for 24 hours at room temperature. After solvent evaporation, the crude product was purified by flash chromatography (Petroleum Ether/ EtOAc 8:2). 3.11 g (79%) of 8-(acetylthio)octanoic acid (**C1**) were obtained.

^{1}H NMR (500 MHz, CDCl$_3$) δ 2.87 (t, 2H, CH$_2$S), 2.36 (t, 2H, CH$_2$CO), 2.33 (s, 3H, CH$_3$CO), 1.63 (m, 2H, CH$_2$), 1.61 – 1.53 (m, 2H, CH$_2$), 1.36 (m, 6H, CH$_2$).

^{13}C NMR (126 MHz, CDCl$_3$) δ 196.14 (1C, COS), 179.96 (1C, COOH), 33.98 (1C, CH$_2$), 30.63 (1C, CH$_2$), 29.41 (1C, CH$_2$), 29.07 (1C, CH$_2$), 28.84 (1C, CH$_2$), 28.70 (1C, CH$_2$), 28.54 (1C, CH$_2$), 24.55 (1C, CH$_2$).

ESI-MS (m/z): 219.2 [M+H$^+$], 241.3 [M+Na$^+$].

Synthesis of S-(12-oxo-2,5,8-trioxa-11-azanonadecan-19-yl) ethanethioate (C2). C1 (1.03 g, 4.72 mmol, 1.0 equiv) and pentafluorophenol (1.13 g, 6.13 mmol, 1.3 equiv) were dissolved in dry CH$_2$Cl$_2$ (20 mL) and N-(3-Dimethylaminopropyl)-N-ethyl-carbodiimide hydrochloride (EDC, 1.18 g, 6.13 mmol, 1.3 equiv) was added. The mixture was stirred for 12 hours under nitrogen. Then N,N-diisopropylethylamine (DIPEA, 0.800 g, 6.13 mmol, 1.3 equiv) and 2-(2-(2-methoxyethoxy)-ethoxy)ethanamine (1.01 g, 6.13 mmol, 1.3 equiv) were added. The mixture was stirred at room temperature for another 12 hours. After solvent evaporation, the crude product was purified by flash chromatography (EtOAc/CH$_3$OH 9.5:0.5), giving 1.20 g (70%) of **C2**.

^{1}H NMR (500 MHz, CDCl$_3$) δ 6.18 (br, 1H, NH), 3.68 – 3.62 (m, 6H, CH$_2$O), 3.57 (m, 4H, CH$_2$O), 3.45 (q, 2H, CH$_2$O), 3.40 (s, 3H, CH$_3$O), 2.86 (t, 2H, CH$_2$CO), 2.31 (s, 3H, CH$_3$CO), 2.22 – 2.14 (t, 2H, CH$_2$), 1.67 – 1.59 (m, 2H, CH$_2$), 1.59 – 1.52 (m, 2H, CH$_2$), 1.41 – 1.27 (m, 6H, CH$_2$).

^{13}C NMR (126 MHz, CDCl$_3$) δ 195.93 (1C, COS), 173.13 (1C, CON), 71.86 (1C, CH$_2$O), 70.43 (1C, CH$_2$O), 70.39(1C, CH$_2$O) , 70.09 (1C, CH$_2$O), 69.83 (1C, CH$_2$O), 58.93 (1C, CH$_2$O), 39.05 (1C, CH$_2$), 36.48 (1C, CH$_2$), 29.38 (1C, CH$_2$), 29.05 (1C, CH$_2$), 28.99 (1C, CH$_2$), 28.76 (1C, CH$_2$), 28.54 (1C, CH$_2$), 25.55 (1C, CH$_2$).

ESI-MS (m/z): 364.3 [M+H$^+$], 386.2 [M+Na$^+$].

Synthesis of 8-mercapto-N-(2-(2-(2-methoxyethoxy)ethoxy)ethyl)octanamide (1). C2 (0.0359 g, 0.0988 mmol) was dissolved in ethanol (2 mL). A 6 M HCl solution in water (2 mL) was added and the mixture was stirred at 78 °C for 2 hours under nitrogen atmosphere. The reaction mixture was allowed to cool and the solvent was evaporated obtaining 0.0302 g (quantitative) of **1**.

^{1}H NMR (500 MHz, MeOD) δ 3.67 – 3.60 (m, 8H, CH$_2$O), 3.56 (m, 2H, CH$_2$N), 3.50 (t, 2H,CH$_2$O), 3.38 (s, 3H, CH$_3$O), 2.52 (t, 2H, CH$_2$S), 2.43 (t, 2H, CH$_2$CO), 1.72 – 1.57 (m, 4H, CH$_2$), 1.48 – 1.33 (m, 6H, CH$_2$).

^{13}C NMR (126 MHz, MeOD) δ 176.90 (1C, CO), 71.53 (1C, CH$_2$O), 70.16 (1C, CH$_2$O), 69.97 (1C, CH$_2$O), 69.90 (1C, CH$_2$O), 68.28 (1C, CH$_2$O), 57.76 (1C, CH$_3$O), 40.34 (1C, CH$_2$N), 34.34 (1C, CH$_2$), 33.68 (1C, CH$_2$), 28.59 (1C, CH$_2$), 28.35 (1C, CH$_2$), 27.78 (1C, CH$_2$), 25.73 (1C, CH$_2$), 23.56 (1C, CH$_2$S).

TOF ES+ HRMS: [M+H$^+$] calcd. for C$_{21}$H$_{28}$BrN$_2$O$_2$ = 419.1329; found = 419.1334.

3.6.2 Synthesis of 2,5,8,11-tetraoxanonadecane-19-thiol (thiol 7)

Thiol **7** was prepared according to the following scheme:
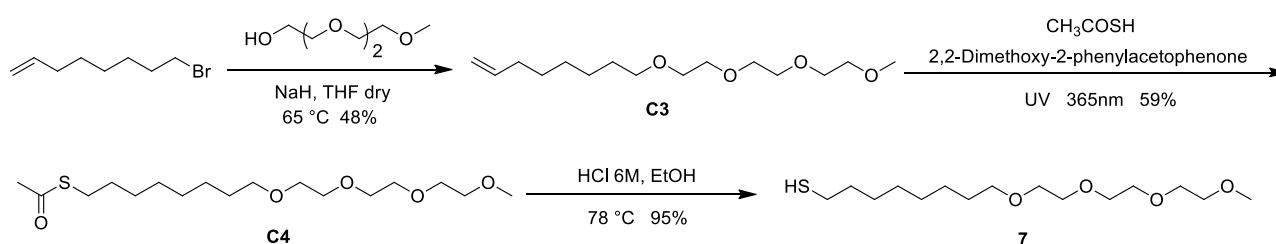
Scheme 3-2. Synthesis of the thiol **7**.

Synthesis of 2,5,8,11-tetraoxanonadec-18-ene (C3). 2-(2-(2-methoxyethoxy)ethoxy)ethanol (0.516 g, 3.14 mmol, 1.2 equiv) and NaH (0.220 g, 9.16 mmol, 3.5 equiv) were dissolved in dry THF (10 mL). After 15 min stirring, 8-bromooct-1-ene (0.500 g, 2.62 mmol, 1.0 equiv) was added. The mixture was stirred for 12 hours under nitrogen at 65 °C. After solvent evaporation, the crude product was purified by flash chromatography (Petroleum Ether/ EtOAc 8:2). 0.317 g (48%) of **C3** were obtained.

^{1}H NMR (500 MHz, CDCl$_3$) δ 5.88 – 5.69 (m, 1H, CH), 5.06 – 4.82 (dd, 2H, CH$_2$), 3.67 – 3.60 (m, 8H, CH$_2$O), 3.56 (m, 2H, CH$_2$O), 3.53 (m, 2H, CH$_2$O), 3.43 (t, 2H, CH$_2$O), 3.36 (s, 3H, CH$_3$O), 2.07 – 1.98 (m, 2H, CH$_2$), 1.60 – 1.51 (m, 2H, CH$_2$), 1.41 – 1.25 (m, 6H, CH$_2$).

^{13}C NMR (126 MHz, CDCl$_3$) δ 139.20 (1C, CH$_2$), 114.08 (1C, CH), 71.91 (1C, CH$_2$O), 71.42 (1C, CH$_2$O), 70.60 (1C, CH$_2$O), 70.57 (1C, CH$_2$O), 70.49 (1C, CH$_2$O), 70.03 (1C, CH$_2$O), 58.99 (1C, CH$_3$O), 33.68 (1C, CH$_2$), 29.55 (1C, CH$_2$), 28.91 (1C, CH$_2$), 28.82 (1C, CH$_2$), 25.91 (1C, CH$_2$).

ESI-MS (m/z): 275.2 [M+H$^+$], 297.2 [M+Na$^+$].

Synthesis of S-2,5,8,11-tetraoxanonadecan-19-yl ethanethioate (C4). C3 (0.230 g, 0.838 mmol, 1.0 equiv) was dissolved in methanol (3 mL) and the solution was degassed for 10 min under nitrogen. Afterwards, 2,2-Dimethoxy-2-phenylacetophenone (0.0110 g, 0.0419 mmol, 0.05 equiv) and ethanethioic S-acid (0.255 g, 3.35 mmol, 4.0 equiv) were added and the mixture was stirrend

under irradiation (365 nm) for 2 hours. After solvent evaporation, the crude product was purified by flash chromatography (Petroleum Ether / EtOAc 7:3). 0.173 g (59%) of **C4** were obtained.

^{1}H NMR (500 MHz, CDCl$_3$) δ 3.70 – 3.63 (m, 8H, CH$_2$O), 3.60 – 3.57 (m, 2H, CH$_2$O), 3.57 (m, 2H, CH$_2$O), 3.45 (t, 2H, CH$_2$O), 3.39 (s, 3H, CH$_3$O), 2.86 (t, 2H, CHO), 2.33 (s, 3H, CH$_3$CO), 1.62 – 1.51 (m, 4H, CH$_2$), 1.41 – 1.25 (m, 8H, CH$_2$).

^{13}C NMR (126 MHz, CDCl$_3$) δ 195.94 (1C, CO), 71.92 (1C, CH$_2$O), 71.43 (1C, CH$_2$O), 70.60 (1C, CH$_2$O), 70.57 (1C, CH$_2$O), 70.50 (1C, CH$_2$O), 70.03 (1C, CH$_2$O), 59.00 (1C, CH$_2$O), 30.61 (1C, CH$_2$), 29.56 (1C, CH$_2$), 29.46 (1C, CH$_2$), 29.26 (1C, CH$_2$), 29.09 (1C, CH$_2$), 29.02(1C, CH$_2$), 28.71 (1C, CH$_2$), 25.98 (1C, CH$_2$S).

ESI-MS (m/z): 351.3 [M+H$^+$], 373.2 [M+Na$^+$].

Synthesis 2,5,8,11-tetraoxanonadecane-19-thiol (7). C4 (0.0351 g, 0.0987 mmol) was dissolved in ethanol (2 mL). A 6 M HCl solution in water (2 mL) was added and the mixture was stirred at 78 °C for 2 hours under nitrogen atmosphere. The reaction mixture was allowed to cool and the solvent was evaporated to obtain 0.0289 g (quantitative) of **7**.

^{1}H NMR (500 MHz, MeOD) δ 3.67 – 3.62 (m, 8H, CH$_2$O), 3.59 (t, 2H, CH$_2$O), 3.56 (t, 2H, CH$_2$O), 3.49 (t, 2H, CH$_2$O), 3.38 (s, 3H, CH$_3$O), 2.51 (t, 2H, CH$_2$O), 1.66 – 1.54 (m, 4H, CH$_2$), 1.47 – 1.29 (m, 8H, CH$_2$).

^{13}C NMR (126 MHz, MeOD) δ 71.59 (1C, CH$_2$O), 70.94 (1C, CH$_2$O), 70.19 (1C, CH$_2$O), 69.99 (1C, CH$_2$O), 69.78 (1C, CH$_2$O), 57.73 (1C, CH$_3$O), 33.83 (1C, CH$_2$), 29.32 (1C, CH$_2$), 29.09 (1C, CH$_2$), 28.80 (1C, CH$_2$), 27.97 (1C, CH$_2$), 25.77 (1C, CH$_2$), 23.59 (1C, CH$_2$S).

TOF ES+ HRMS: [M+H$^+$] calcd. for C$_{21}$H$_{28}$BrN$_2$O$_2$ = 419.1329. Found = 419.1334.

3.6.3 Synthesis of 2,5,8,11-tetraoxadocosane-22-thiol (thiol 8)

Thiol **8** was prepared according the following scheme:
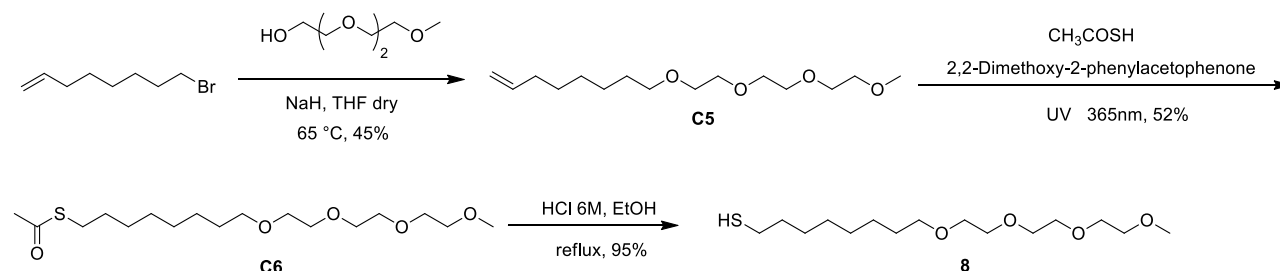
Scheme 3-3. Synthesis of the thiol **8**.

Synthesis of 2,5,8,11-tetraoxadocos-21-ene (C5). 2-(2-(2-methoxyethoxy)ethoxy)ethanol (0.845 g, 5.15 mmol, 1.2 equiv) and NaH (0.360 g, 15.0 mmol, 3.5 equiv) were dissolved in dry THF (10 mL). After 15 min stirring, 11-bromoundec-1-ene (1.00 g, 4.29 mmol, 1.0 equiv) was added. The mixture was stirred for 12 hours under nitrogen at 65 °C. After solvent evaporation, the crude product was purified by flash chromatography (PE/ EtOAc 8:2) giving 0.609 g (45%) of **C5**.

^{1}H NMR (500 MHz, CDCl$_3$) δ 5.86 – 5.75 (m, 1H, CH), 4.96 (dd, 2H, CH$_2$), 3.69 – 3.62 (m, 8H, CH$_2$O), 3.60 – 3.57 (t, 2H, CH$_2$O), 3.56 – 3.53 (t, 2H, CH$_2$O), 3.44 (t, 2H, CH$_2$O), 3.38 (s, 3H, CH$_3$O), 2.03 (q, 2H, CH$_2$), 1.61 – 1.53 (m, 2H, CH$_2$), 1.41 – 1.24 (m, 12H, CH$_2$).

^{13}C NMR (126 MHz, CDCl$_3$) δ 139.23 (1C, CH$_2$), 114.26 (1C, CH), 72.11 (1C, CH$_2$O), 71.62 (1C, CH$_2$O), 70.79 (1C, CH$_2$O), 70.67 (1C, CH$_2$O), 70.23 (1C, CH$_2$O), 59.11 (1C, CH$_3$O), 33.93 (1C, CH$_2$), 29.80 (1C, CH$_2$), 29.67 (1C, CH$_2$), 29.60 (1C, CH$_2$), 29.25 (1C, CH$_2$), 29.06 (1C, CH$_2$), 26.24 (1C, CH$_2$).

ESI-MS (m/z): 317.3 [M+H$^+$], 339.3 [M+Na$^+$].

Synthesis of S-2,5,8,11-tetraoxadocosan-22-yl ethanethioate (C6). **C5** (0.300 g, 0.948 mmol, 1.0 equiv) was dissolved in methanol (3 mL) and the solution was degassed for 10 min under nitrogen. Afterwards, 2,2-Dimethoxy-2-phenylacetophenone (0.0123 g, 0.0474 mmol, 0.05 equiv) and ethanethioic S-acid (0.289 g, 3.79 mmol, 4.0 equiv) were added. The mixture was stirred under irradiation (365 nm) for 2 hours. After solvent evaporation, the crude product was purified by flash chromatography (PE/ EtOAc 7:3). 0.193 g (52%) of **C6** were obtained.

^{1}H NMR (500 MHz, CDCl$_3$) δ 3.67 – 3.61 (m, 8H, CH$_2$O), 3.56 (m, 2H, CH$_2$O), 3.55 – 3.52 (m, 2H, CH$_2$O), 3.43 (t, 2H, CH$_2$O), 3.36 (s, 3H, CH$_3$O), 2.84 (t, 2H, CH$_2$), 2.30 (s, 3H, CH$_3$CO), 1.59 – 1.50 (m, 4H, CH$_2$), 1.37 – 1.21 (m, 14H, CH$_2$).

^{13}C NMR (126 MHz, CDCl$_3$) δ 195.96 (1C, CO), 71.92 (1C, CH$_2$O), 71.49 (1C, CH$_2$O), 70.60 (1C, CH$_2$O), 70.57 (1C, CH$_2$O), 70.49 (1C, CH$_2$O), 70.02 (1C, CH$_2$O), 59.00 (1C, CH$_3$O), 30.60 (1C, CH$_2$), 29.61 (1C, CH$_2$), 29.52 (1C, CH$_2$), 29.47 (1C, CH$_2$), 29.43 (1C, CH$_2$), 29.11 (1C, CH$_2$), 29.08 (1C, CH$_2$), 28.78 (1C, CH$_2$), 26.06 (1C, CH$_2$S).

ESI-MS (m/z): 393.3 [M+H$^+$], 415.3 [M+Na$^+$].

Synthesis of 2,5,8,11-tetraoxadocosane-22-thiol (8). **C6** (0.0393 g, 0.0987 mmol) was dissolved in ethanol (2 mL). A 6 M HCl solution in water (2 mL) was added and the mixture was stirred at 78 °C for 2 hours under nitrogen atmosphere. The reaction mixture was allowed to cool and the solvent was evaporated to obtain 0.0329 g (quantitative) of **8**.

**¹H NMR** (500 MHz, MeOD) δ 3.66 – 3.62 (m, 8H, CH₂O), 3.61 – 3.57 (m, 2H, CH₂O), 3.56 (m, 2H, CH₂O), 3.48 (t, 2H, CH₂O), 3.38 (s, 3H, CH₃O), 2.55 – 2.47 (t, 2H, CH₂O), 1.67 – 1.51 (m, 4H, CH₂), 1.46 – 1.25 (m, 14H, CH₂).

¹³C NMR (126 MHz, MeOD) δ 71.58 (1C, CH₂O), 70.97 (1C, CH₂O), 70.17 (1C, CH₂O), 69.98 (1C, CH₂O), 69.77 (1C, CH₂O), 57.81 (1C, CH₃O), 33.85 (1C, CH₂), 29.33 (1C, CH₂), 29.27 (1C, CH₂), 29.19 (1C, CH₂), 28.83 (1C, CH₂), 28.03 (1C, CH₂), 25.82 (1C, CH₂), 23.59 (1C, CH₂S).

TOF ES⁺ HRMS: [M+H⁺] calcd. for $C_{21}H_{28}BrN_2O_2$ = 419.1329. Found = 419.1334.

3.6.4 Synthesis of 10-(2-(2-methoxyethoxy)ethoxy)decane-1-thiol (thiol 9)

Thiol **9** was prepared according to the following scheme:
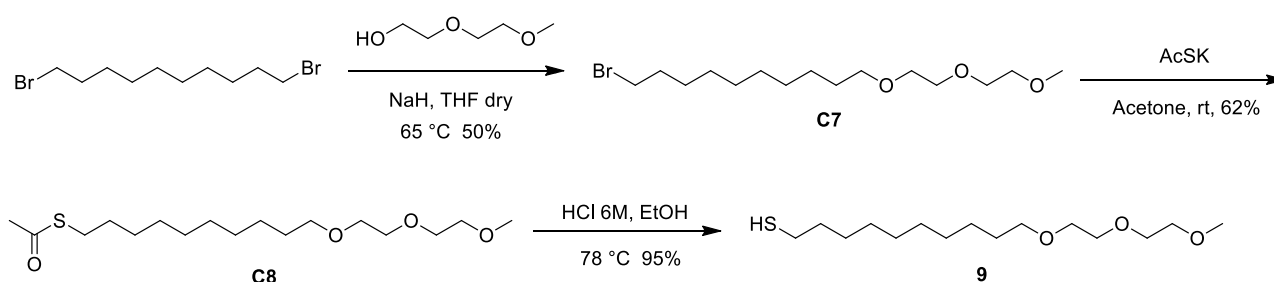
Scheme 3-4. Synthesis of the thiol 9.

Synthesis of 1-bromo-10-(2-(2-methoxyethoxy)ethoxy)decane (C7). 2-(2-methoxyethoxy)ethanol (0.200 g, 1.67 mmol, 1.0 equiv) and NaH (0.267 g, 6.67 mmol, 4.0 equiv) were dissolved in dry THF (10 mL). After 15 min stirring, 1,10-dibromodecane (1.00 g, 3.33 mmol, 2.0 equiv) was added. The mixture was stirred for 12 hours under nitrogen at 65 °C. After solvent evaporation, the crude product was purified by flash chromatography (PE/ EtOAc 8:2). 0.283 g (50%) of **C7** were obtained.

¹H NMR (500 MHz, MeOD) δ 3.67 – 3.62 (m, 4H, CH₂O), 3.61 – 3.58 (m, 2H, CH₂0), 3.57 – 3.54 (m, 2H, CH₂O), 3.47 (m, 4H, CH₂O CH₂Br), 3.38 (s, 3H, CH₃O), 1.90 – 1.82 (m, 2H, CH₂), 1.62 – 1.54 (m, 2H, CH₂), 1.46 (m, 2H, CH₂), 1.41 – 1.31 (m, 10H, CH₂).

¹³C NMR (126 MHz, MeOD) δ 71.58 (1C, CH₂O), 70.96(1C, CH₂O), 70.17 (1C, CH₂O), 69.99 (1C, CH₂O), 69.76 (1C, CH₂O), 57.72 (1C, CH₃O), 29.33 (1C, CH₂Br), 29.23 (1C, CH₂), 29.14 (1C, CH₂), 28.46 (1C, CH₂), 27.80 (1C, CH₂), 25.81 (1C, CH₂).

ESI-MS (m/z): 339.2 [M+H⁺], 361.2 [M+Na⁺].

Synthesis of S-(10-(2-(2-methoxyethoxy)ethoxy)decyl) ethanethioate (C8). C7 (0.200 g, 0.589 mmol, 1.0 equiv) was dissolved in acetone (4 mL) and potassium thioacetate (0.135 g, 1.18 mmol, 2.0 equiv) was added. The mixture was stirred for 24 hours at room temperature. After solvent

evaporation, the crude product was purified by flash chromatography (Petroleum Ether/ EtOAc 8:2), giving 0.122 g (62%) of **C8**.

^{1}H NMR (500 MHz, MeOD) δ 3.66 – 3.62 (m, 4H, CH$_2$O), 3.61 – 3.57 (m, 2H, CH$_2$O), 3.56 (m, J = 5.7, 3.7 Hz, 2H, CH$_2$O), 3.48 (t, J = 6.6 Hz, 2H, CH$_2$O), 3.38 (s, 3H, CH$_3$O), 2.89 (t, J = 14.5, 7.2 Hz, 2H, CH$_2$O), 2.36 – 2.28 (s, 3H, CH$_3$CO), 1.63 – 1.51 (m, 4H, CH$_2$), 1.43 – 1.28 (m, 12H, CH$_2$).

^{13}C NMR (126 MHz, MeOD) δ 195.94 (1C, CO), 71.61 (1C, CH$_2$O), 70.98 (1C, CH$_2$O), 70.20 (1C, CH$_2$O), 70.03 (1C, CH$_2$O), 69.79 (1C, CH$_2$O), 57.76 1C, CH$_3$O), 29.41 (1C, CH$_2$), 29.37 (1C, CH$_2$), 29.29 (1C, CH$_2$), 29.19 (1C, CH$_2$), 28.85 (1C, CH$_2$), 28.49 (1C, CH$_2$), 28.46 (1C, CH$_2$), 25.84 (1C, CH$_2$S).

ESI-MS (m/z): 335.3 [M+H$^+$], 357.2 [M+Na$^+$]

Synthesis of 10-(2-(2-methoxyethoxy)ethoxy)decane-1-thiol (9). C8 (0.0330 g, 0.0987 mmol) was dissolved in ethanol (2 mL). A 6 M HCl solution in water (2 mL) was added and the mixture was stirred at 78 °C for 2 hours under nitrogen. The reaction mixture was allowed to cool and the solvent was evaporated giving 0.0274 g (quantitative) of **9**.

^{1}H NMR (500 MHz, MeOD) δ 3.66 – 3.62 (m, 4H, CH$_2$O), 3.61 – 3.57 (m, 2H, CH$_2$O), 3.56 (m, 2H,CH$_2$O), 3.49 (t, 2H, CH$_2$O), 3.38 (s, 3H, CH$_3$O), 2.55 – 2.46 (t, 2H, CH$_2$), 1.66 – 1.53 (m, 4H, CH$_2$), 1.47 – 1.27 (m, 12H, CH$_2$).

^{13}C NMR (126 MHz, MeOD) δ 71.57 (1C, CH$_2$O), 70.96 (1C, CH$_2$O), 70.16 (1C, CH$_2$O), 69.98 (1C, CH$_2$O), 69.75 (1C, CH$_2$O), 57.70 (1C, CH$_3$O), 33.84 (1C, CH$_2$), 29.31 (1C, CH$_2$), 29.26 (1C, CH$_2$), 29.21 (1C, CH$_2$), 29.15 (1C, CH$_2$), 28.81 (1C, CH$_2$), 28.01 (1C, CH$_2$), 25.80 (1C, CH$_2$), 23.57 (1C, CH$_2$S).

TOF ES$^+$ HRMS: [M+H$^+$] calcd. for C$_{21}$H$_{28}$BrN$_2$O$_2$ = 419.1329. Found = 419.1334.

3.6.5 Synthesis of 12-(2-(2-methoxyethoxy)ethoxy)dodecane-1-thiol (thiol 10)

Thiol **10** was prepared according to the following scheme:
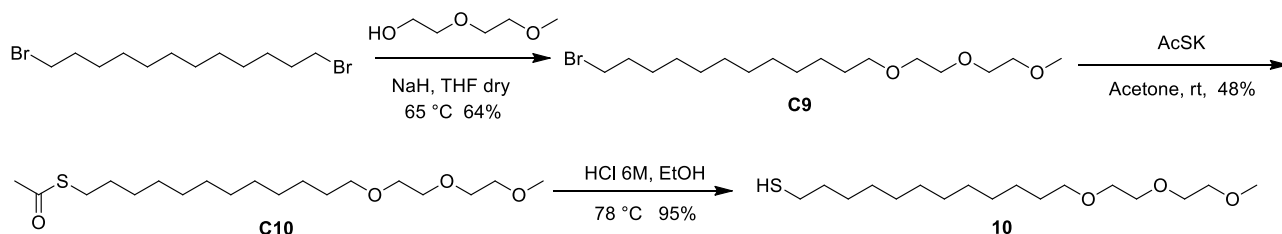
Scheme 3-5. Synthesis of the thiol 10.

Synthesis of 1-bromo-12-(2-(2-methoxyethoxy)ethoxy)dodecane (C9). 2-(2-methoxyethoxy)-ethanol (0.183 g, 1.52 mmol, 1.0 equiv) and NaH (0.146 g, 6.10 mmol, 4.0 equiv) were dissolved in

dry THF (10 mL). After 15 min stirring, 1,12-dibromododecane (1.00 g, 3.05 mmol, 2.0 equiv) was added. The mixture was stirred for 12 hours under nitrogen at 65 °C. After solvent evaporation, the crude product was purified by flash chromatography (PE/ EtOAc 8:2), giving 0.356 g (64%) of **C9**.

^{1}H NMR (500 MHz, MeOD) δ 3.67 – 3.62 (m, 4H, CH$_2$O), 3.61 – 3.57 (m, 2H, CH$_2$O), 3.56 (m, 2H, CH$_2$O), 3.47 (m, 2H, CH$_2$O), 3.38 (s, 3H, CH$_3$O), 1.90 – 1.82 (m, 2H, CH$_2$), 1.63 – 1.55 (m, 2H, CH$_2$), 1.46 (m, 2H, CH$_2$), 1.36 (m, 14H, CH$_2$).

^{13}C NMR (126 MHz, MeOD) δ 71.59 (1C, CH$_2$O), 70.98 (1C, CH$_2$O), 70.18 (1C, CH$_2$O), 70.00 (1C, CH$_2$O), 69.77 (1C, CH$_2$O), 57.73 (1C, CH$_3$O), 33.06 (1C, CH$_2$Br), 32.65 (1C, CH$_2$), 29.36 (1C, CH$_2$), 29.29 (1C, CH$_2$), 29.21 (1C, CH$_2$), 28.50 (1C, CH$_2$), 27.82 (1C, CH$_2$), 25.83 (1C, CH$_2$).

ESI-MS (m/z): 389.2 [M+Na$^+$].

Synthesis of S-(12-(2-(2-methoxyethoxy)ethoxy)dodecyl) ethanethioate (C10). C9 (0.263 g, 0.716 mmol, 1.0 equiv) was dissolved in acetone (4 mL) and potassium thioacetate (0.164 g, 1.43 mmol, 2.0 equiv) was added. The mixture was stirred for 24 hours at room temperature. After solvent evaporation, the crude product was purified by flash chromatography (PE/EtOAc 8:2). 0.240 g (48%) of **C10** were obtained.

^{1}H NMR (500 MHz, MeOD) δ 3.66 – 3.62 (m, 4H, CH$_2$O), 3.61 – 3.57 (m, 2H, CH$_2$O), 3.56 (m, 2H, CH$_2$O), 3.48 (t, 2H, CH$_2$O), 3.30 (s, 3H, CH$_3$O), 2.88 (t, 2H, CH$_2$O), 2.32 (s, 3H, CH$_3$CO), 1.63 – 1.53 (m, 4H, CH$_2$), 1.43 – 1.28 (m, 16H, CH$_2$).

^{13}C NMR (126 MHz, MeOD) δ 196.14 (1C, CO), 71.59 (1C, CH$_2$O), 70.98 (1C, CH$_2$O), 70.18 (1C, CH$_2$O), 70.01 (1C, CH$_2$O), 69.78 (1C, CH$_2$O), 57.73 (1C, CH$_3$O), 29.39 (1C, CH$_2$), 29.36 (1C, CH$_2$), 29.30 (1C, CH$_2$), 29.21 (1C, CH$_2$), 29.16 (1C, CH$_2$), 28.84 (1C, CH$_2$), 28.48 (1C, CH$_2$), 28.44 (1C, CH$_2$), 25.84 (1C, CH$_2$S).

ESI-MS (m/z): 363.3 [M+H$^+$], 385.3 [M+Na$^+$].

Synthesis of 12-(2-(2-methoxyethoxy)ethoxy)dodecane-1-thiol (10). C10 (0.0358 g, 0.0987 mmol) was dissolved in ethanol (2 mL). A 6 M HCl solution in water (2 mL) was added and the mixture was stirred at 78 °C for 2 hours under nitrogen atmosphere. The reaction mixture was allowed to cool and the solvent was evaporated obtaining 0.0301 g (quantitative) of **10**.

^{1}H NMR (500 MHz, MeOD) δ 3.64 (m, 4H, CH$_2$O), 3.60 – 3.57 (m, 2H, CH$_2$O), 3.56 (m, 2H, CH$_2$O), 3.48 (t, 2H, CH$_2$O), 3.38 (s, 3H, CH$_3$O), 2.51 (t, 2H, CH$_2$), 1.65 – 1.54 (m, 4H, CH$_2$), 1.44 – 1.29 (m, 16H, CH$_2$).

13C NMR (126 MHz, MeOD) δ 71.57 (1C, CH_2O), 70.96 (1C, CH_2O), 70.15 (1C, CH_2O), 69.98 (1C, CH_2O), 69.75 (1C, CH_2O), 57.70 (1C, CH_3O), 33.84 (1C, CH_2), 29.32 (1C, CH_2), 29.29 (1C, CH_2), 29.17 (1C, CH_2), 28.82 (1C, CH_2), 28.02 (1C, CH_2), 25.80 (1C, CH_2), 23.57 (1C, CH_2S).

TOF ES+ HRMS: $[M+H^+]$ calcd. for $C_{21}H_{28}BrN_2O_2$ = 419.1329. Found = 419.1334.

3.6.6 Preparation of **1**, **7**, **8**, **9** and **10**-AuNP.

Monolayer protected gold nanoparticles (**1, 7, 8, 9, 10**-AuNPs) were prepared modifying a previously reported two-step procedure.[18] A solution of $HAuCl_4 \cdot 3H_2O$ (50.0 mg, 0.127 mmol, 1.0 equiv) in water (2 mL) was extracted with a solution of tetraoctylammonium bromide (0.175 g, 0.318 mmol, 2.5 equiv) in N_2 purged toluene (125 mL). To the resulting reddish-orange organic solution dioctylamine (0.613 g, 2.54 mmol, 20.0 equiv) was added (the amount of dioctylamine was calculated[2] in order to obtain 2 nm nanoparticles). The mixture is vigorously stirred under N_2 for 1.5 hours. During this period of time the color of the mixture fades. Then the solution is cooled at 0 °C and a $NaBH_4$ solution (48.0 mg, 1.27 mmol, 10.0 equiv) in H_2O (1 mL) is then rapidly added. The color of the solution turns rapidly to black and after 1.5 hours of stirring at 0°C, the aqueous layer is removed. To the obtained nanoparticle solution, the desired thiol (0.254 mmol, 2.0 equiv) dissolved in 3 mL of ethyl acetate was rapidly added. The reaction mixture was stirred for 3 hours at 0°C. Then the solvent was evaporated and the resulting crude was purified. 1-AuNPs were dissolved in 5 ml of milliQ water and then washed 7 times with EtOAc. Then water was evaporated under reduced pressure and the resulting nanoparticles were purified by gel permeation chromatography with Sephadex G25. On the other hand 7, 8, 9, 10-AuNPs were dissolved in the minimum amount of AcOEt and then precipitated with diethyl ether (2 times) and subsequently with petroleum ether (5 times). The resulting NPs were finally purified by gel permeation chromatography with Sephadex LH-20.

3.6.7 Characterization of **1**, **7**, **8**, **9** and **10**-AuNP.

Characterization of 1-AuNPs. TEM analysis of the different samples of small nanoparticles (Figure 3-11) yields an average diameter for the AuNP of 1.7±0.5 nm. Formula for **1**-AuNPs calculated on the basis of TEM diameter and TGA analysis is $Au_{152}RS_{51}$. TGA analysis of a sample of **1**-AuNPs under air atmosphere is shown in Figure 3-12. UV-Vis spectrum of a sample of **1**-AuNPs is shown in Figure 3-13. NMR analysis (Figure 3-14, 3-15, 3-16) indicates monolayer formation (broadening of all signals), as confirmed by diffusion-filtered experiments (not shown).
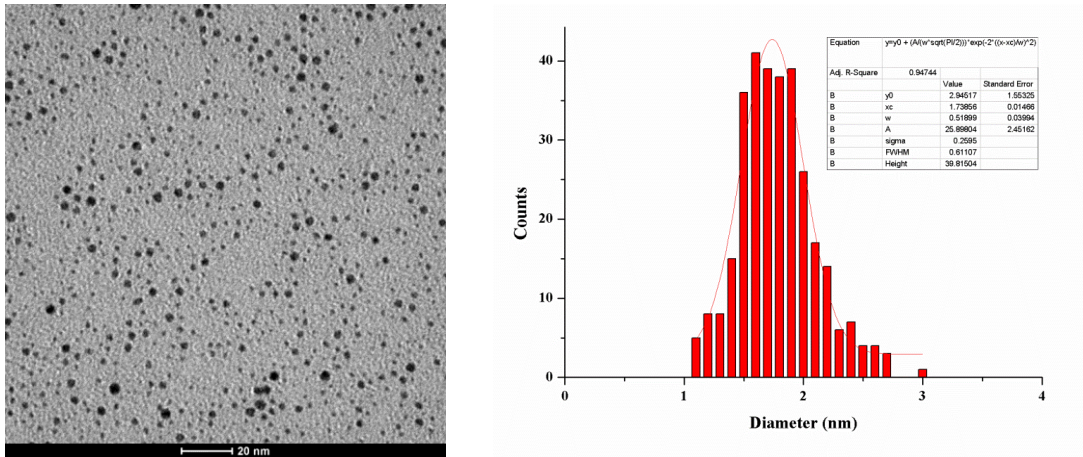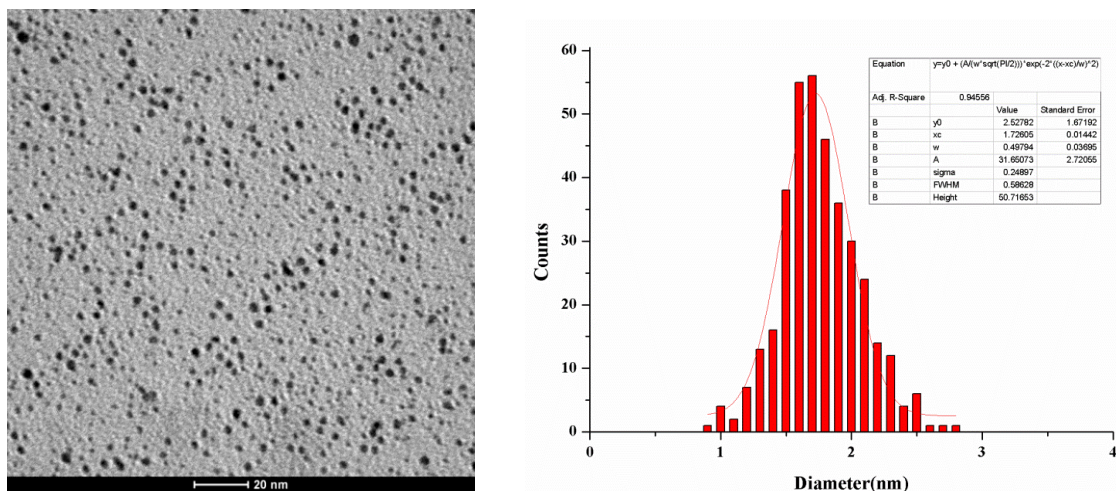
Figure 3-11. TEM image of **1**-AuNPs and size distribution: average diameter = 1.7 ±0.2 nm.
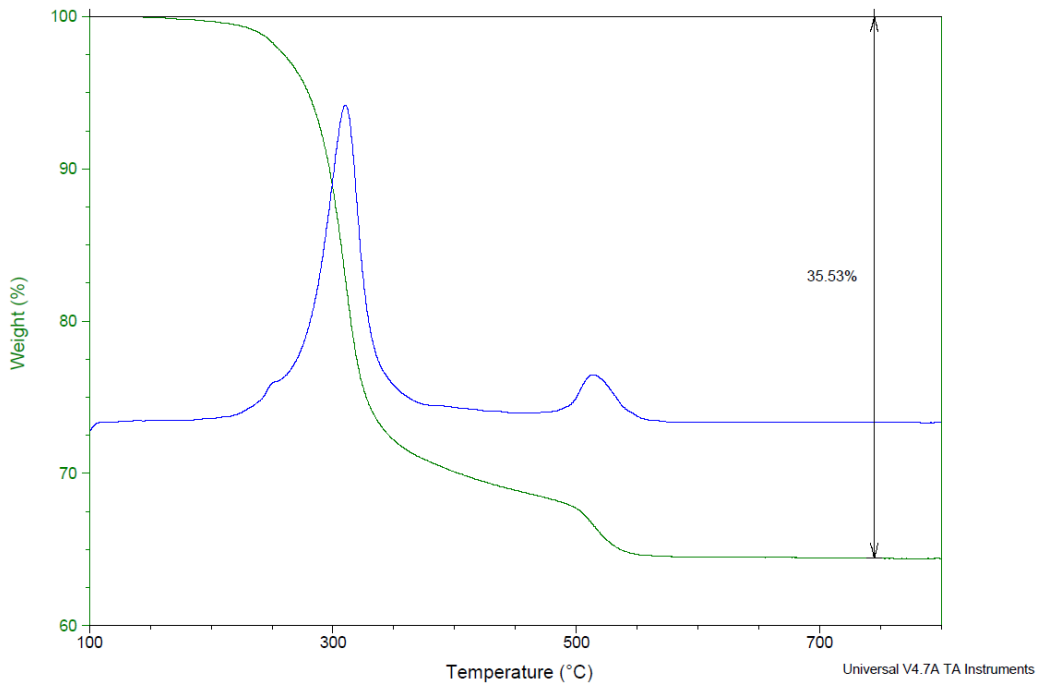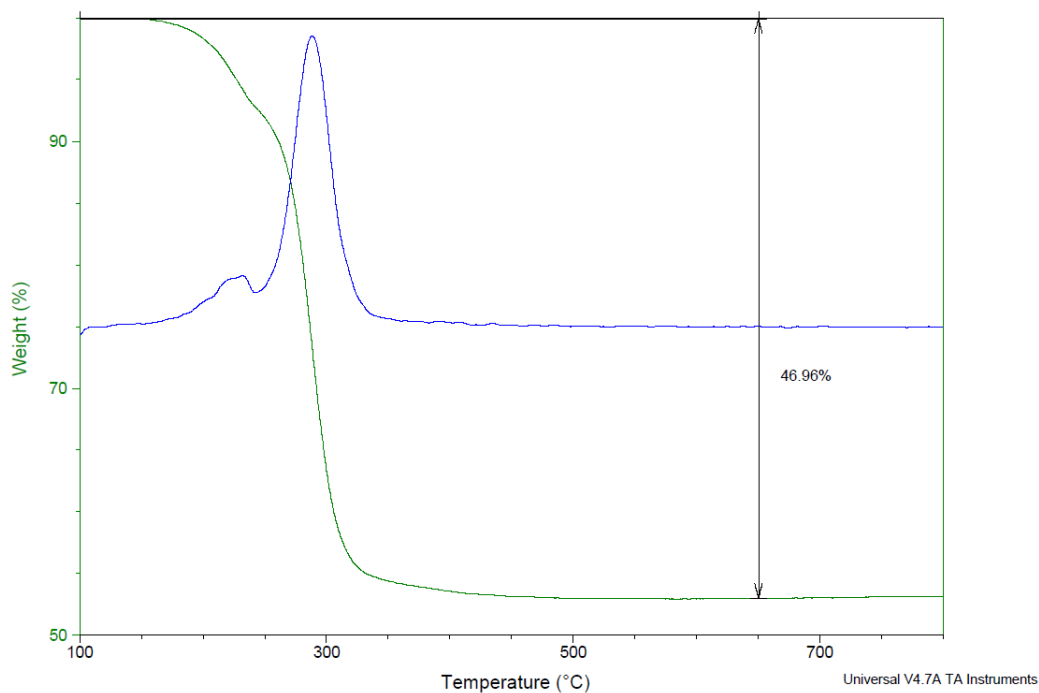

**Figure 3-12.** TGA analysis of a sample of **1**-AuNPs under air atmosphere.
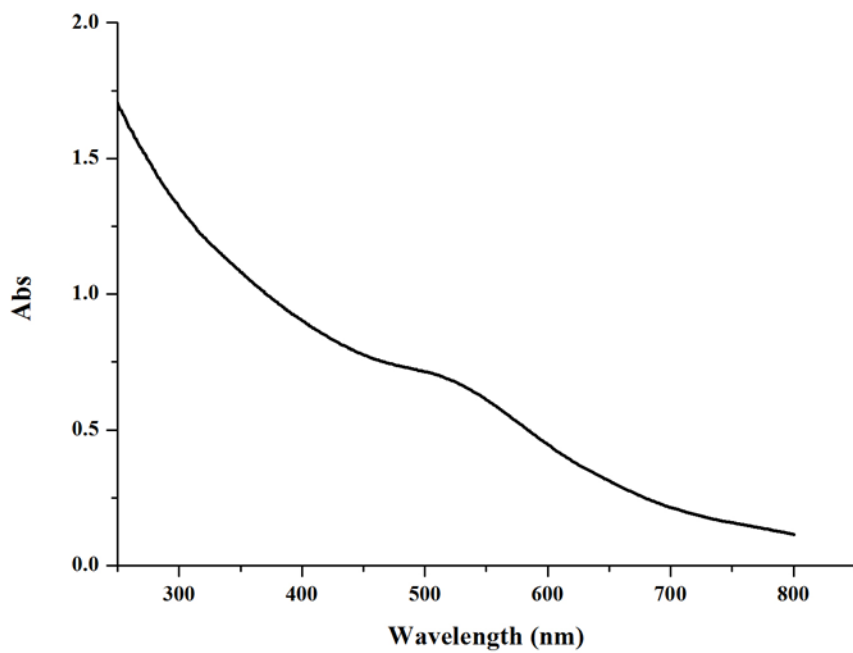
**Figure 3-13.** UV-Vis spectrum of **1**-AuNPs (0.1 mg/mL) at 25°C in water.
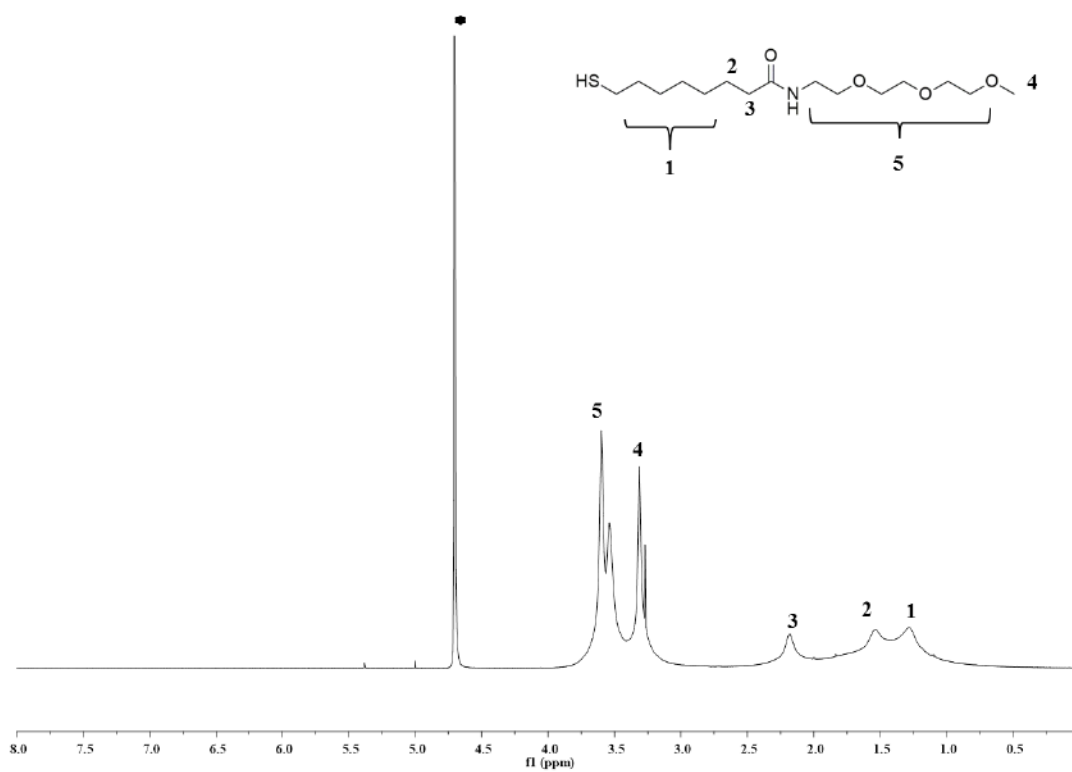
Figure 3-14. ^{1}HNMR spectrum of **1**-AuNPs in D_2O (⬢ indicates the residual solvents and impurities).
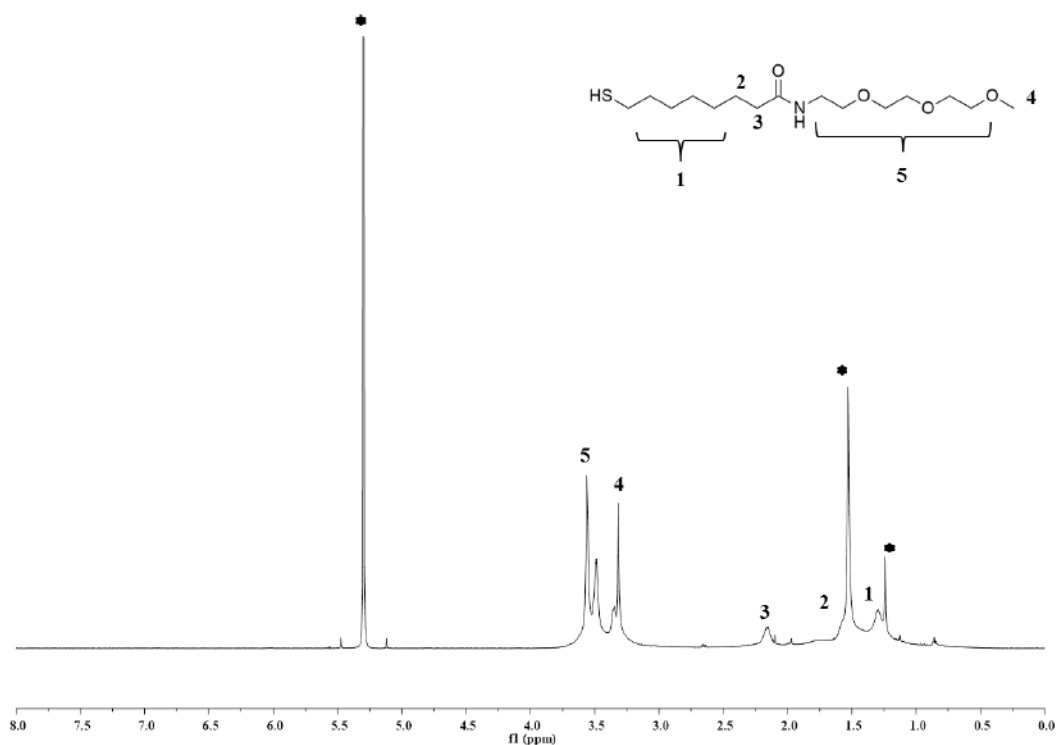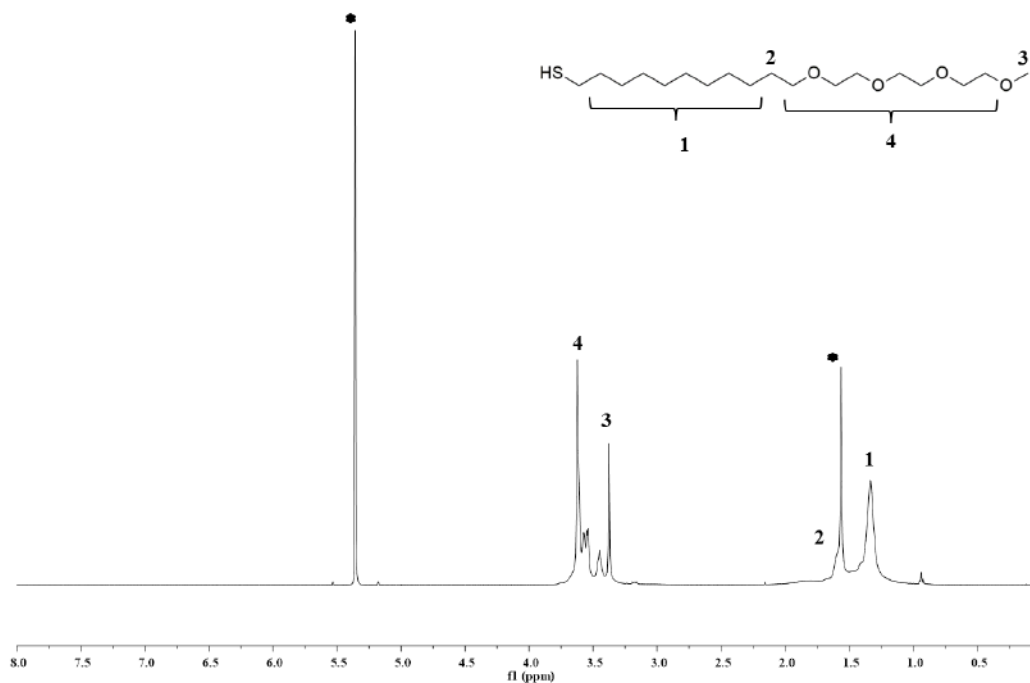
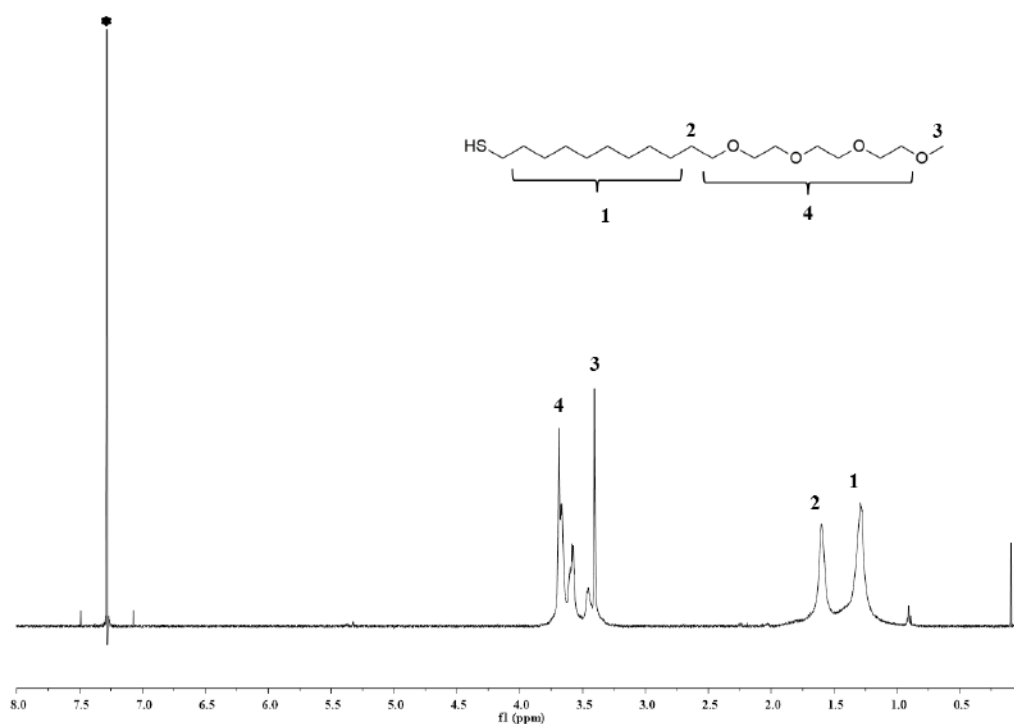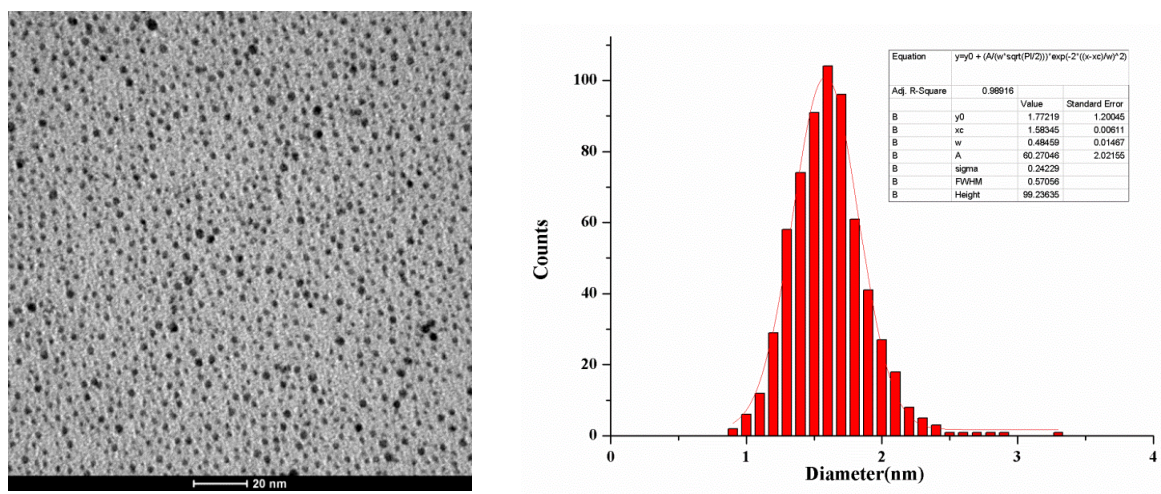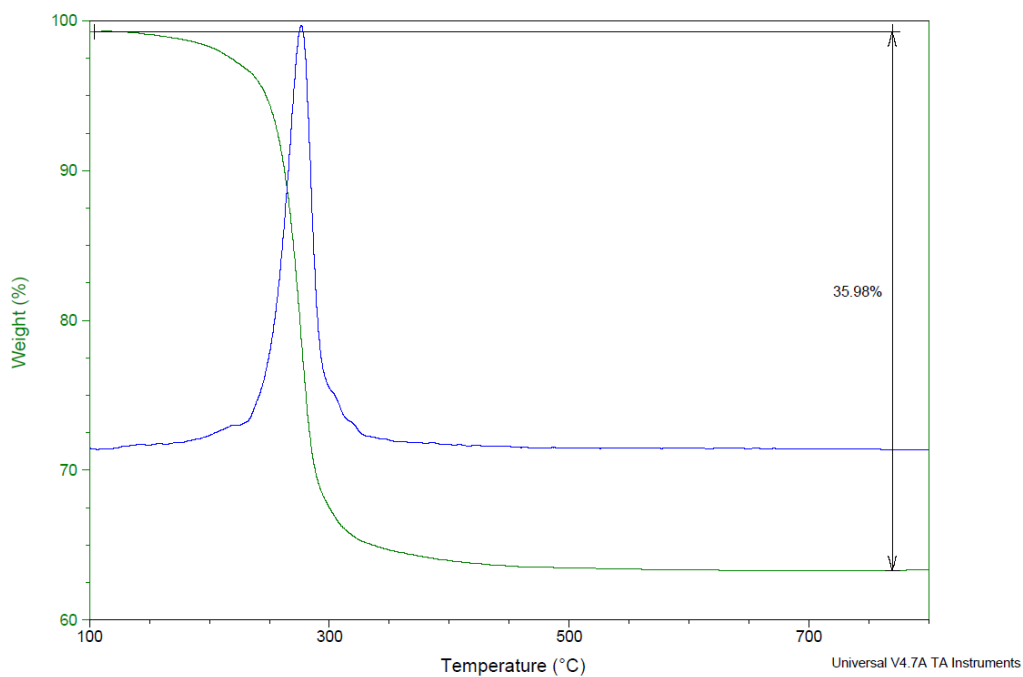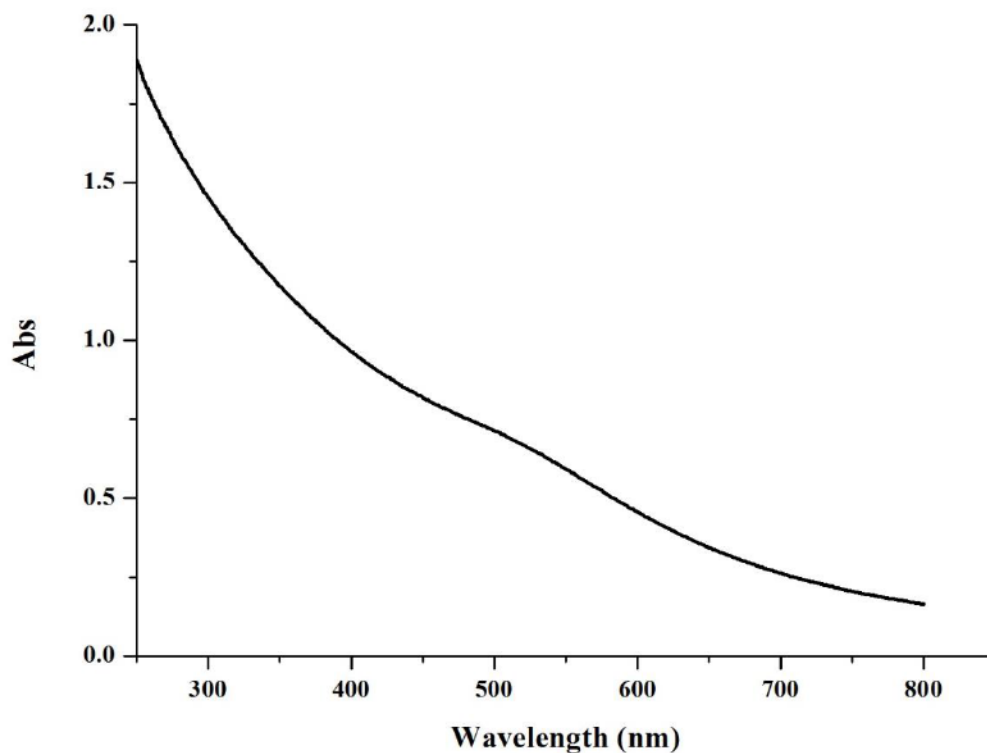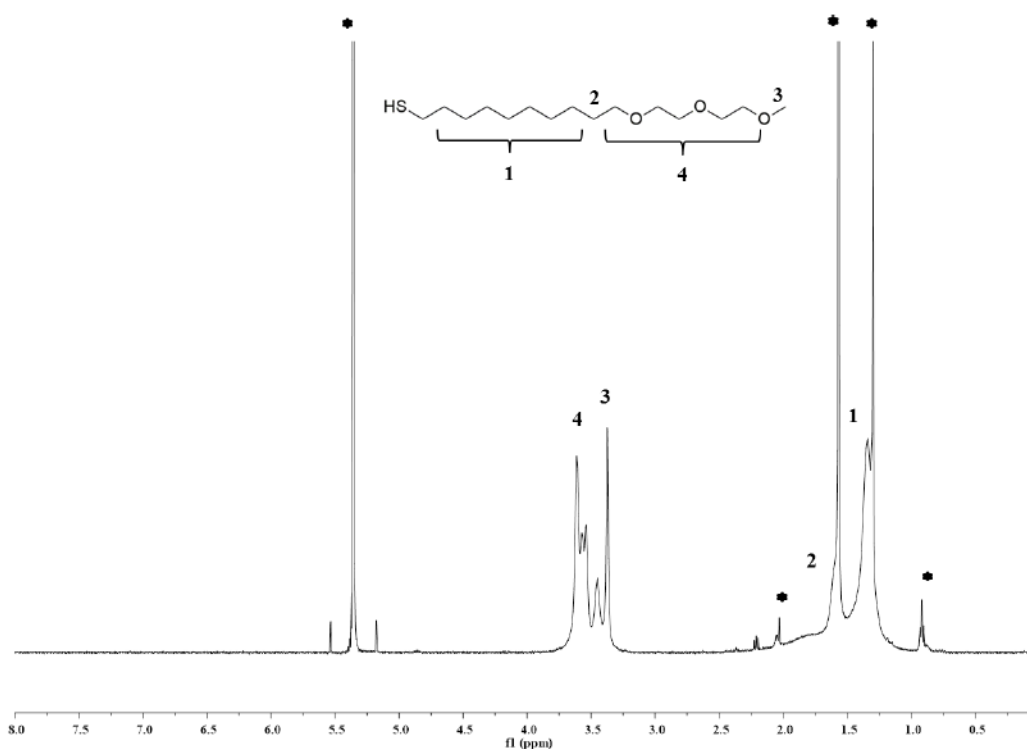**Figure 3-15.** ^{1}HNMR spectrum of **1-AuNPs** in CD_2Cl_2 (◆ indicates the residual solvents and impurities).
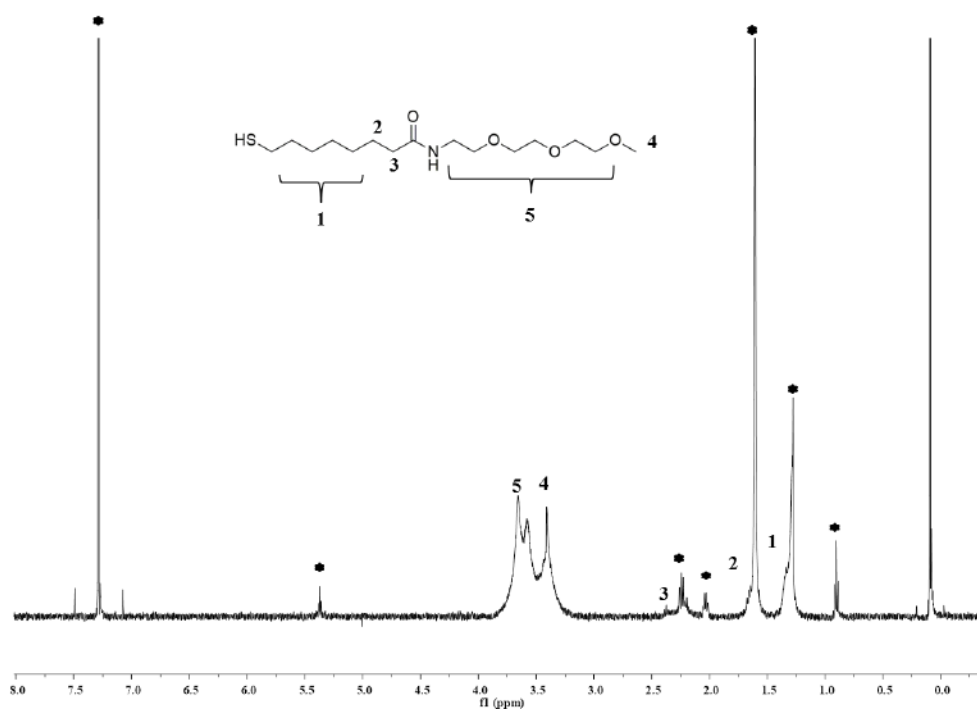
Figure 3-16. ^{1}HNMR spectrum of **1-AuNPs** in $CDCl_3$ (◆ indicates the residual solvents and impurities).

Characterization of 7-AuNPs. TEM analysis of the different samples of small nanoparticles (Figure 3-17) yields an average diameter for the AuNP of 1.5±0.4 nm. Formula for **7-AuNPs** calculated on the basis of TEM diameter and TGA analysis is $Au_{104}RS_{47}$. TGA analysis of a sample of **7-AuNPs** under air atmosphere is shown in Figure 3-18. UV-Vis spectrum of a sample of **7-AuNPs** is

shown in Figure 3-19. NMR analysis (Figure 3-20, 3-21, 3-22) indicates monolayer formation (broadening of all signals), as confirmed by diffusion-filtered experiments.
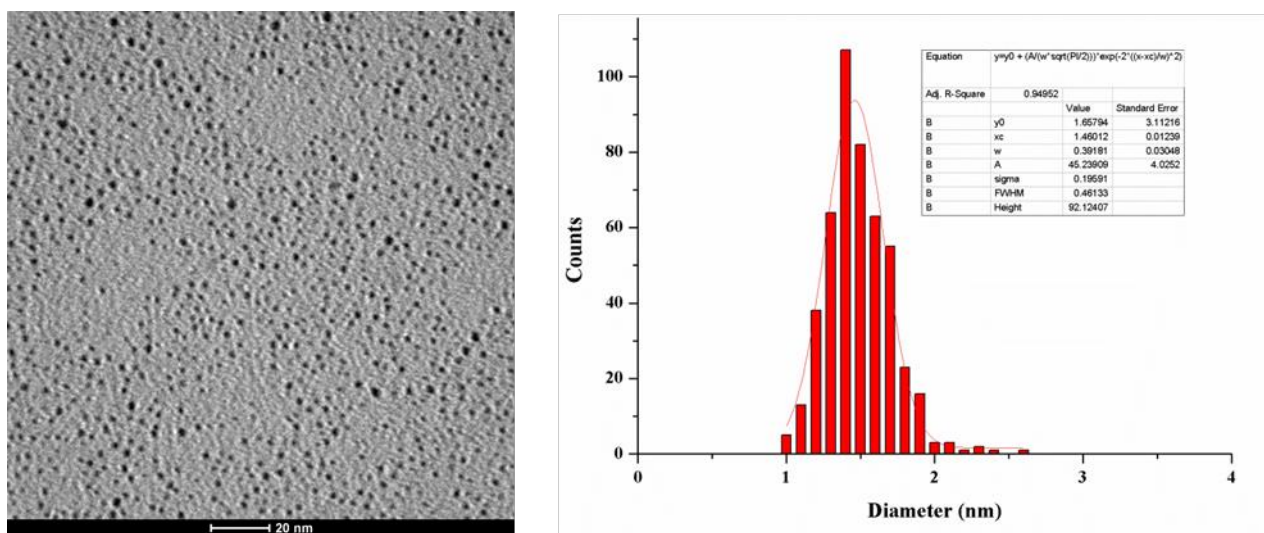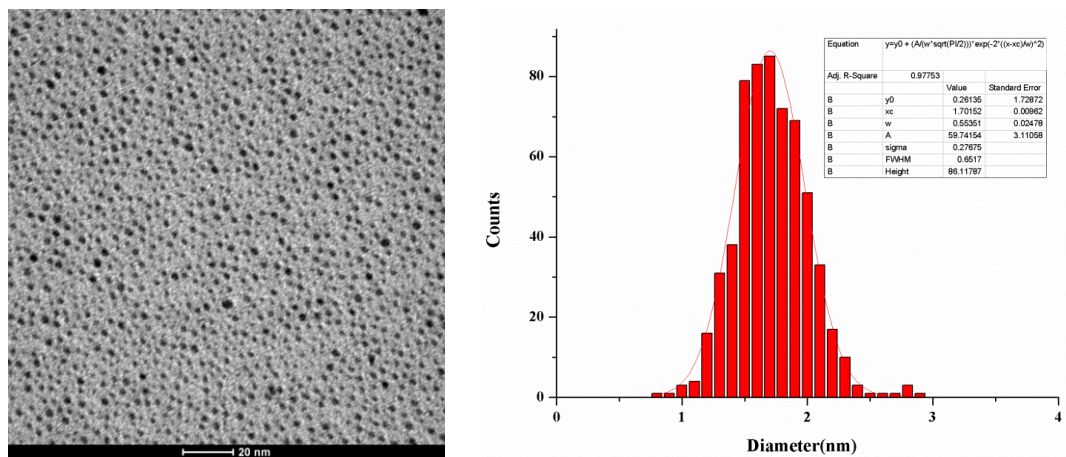

Figure 3-17. Sample TEM image of **7**-AuNPs and size distribution: average diameter = 1.5 ±0.2 nm.
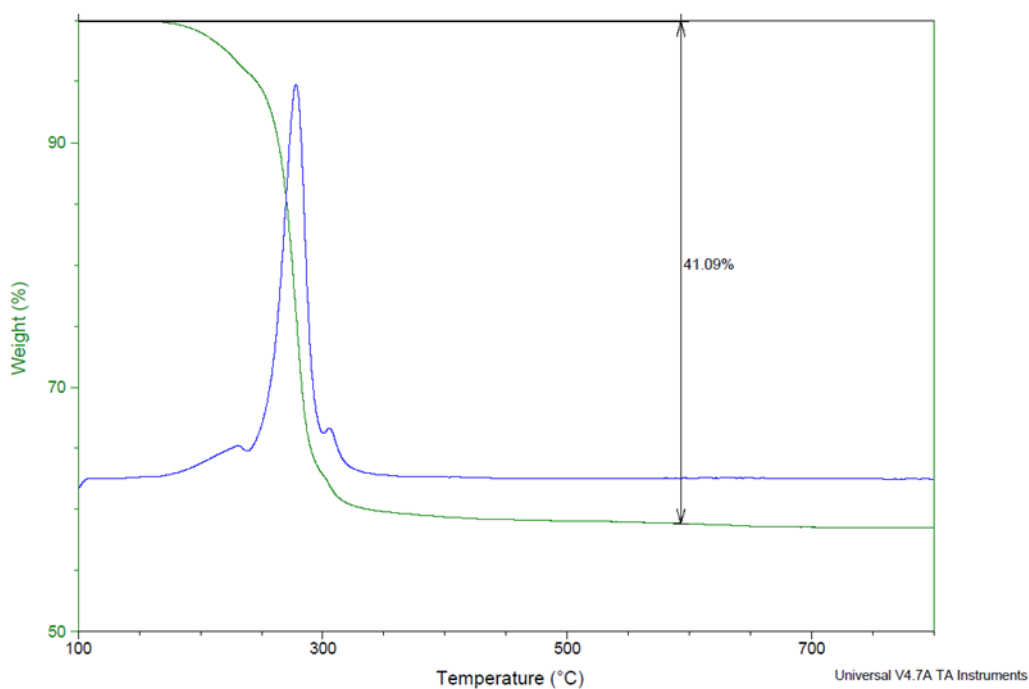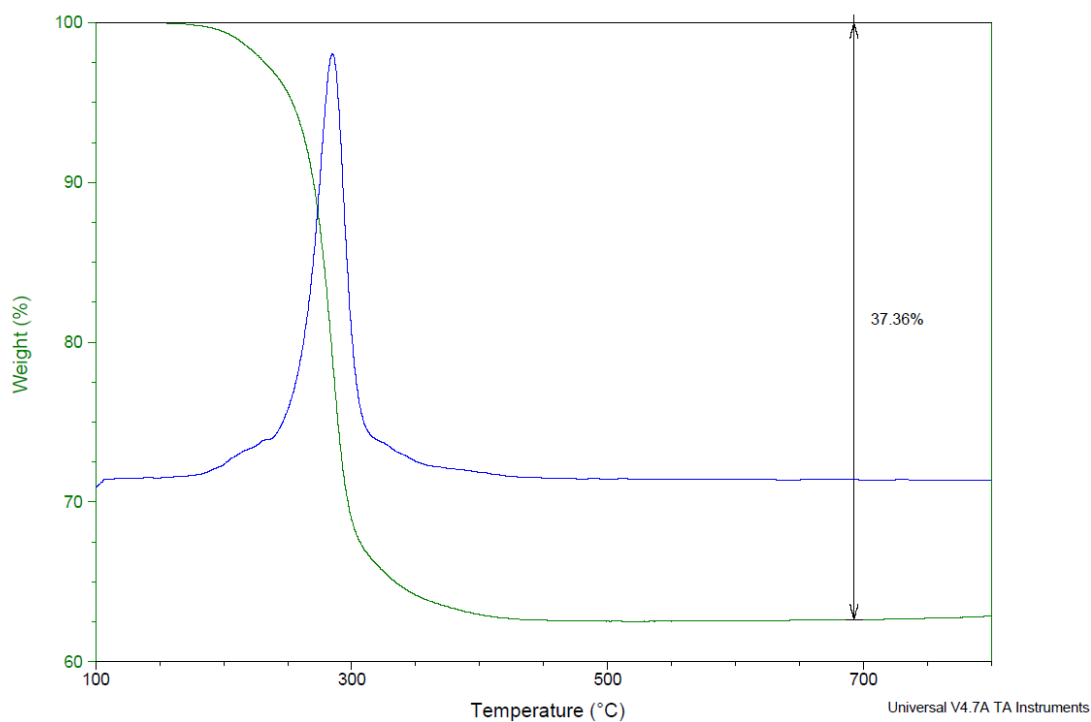

Figure 3-18. TGA analysis of a sample of **7**-AuNPs under air atmosphere.
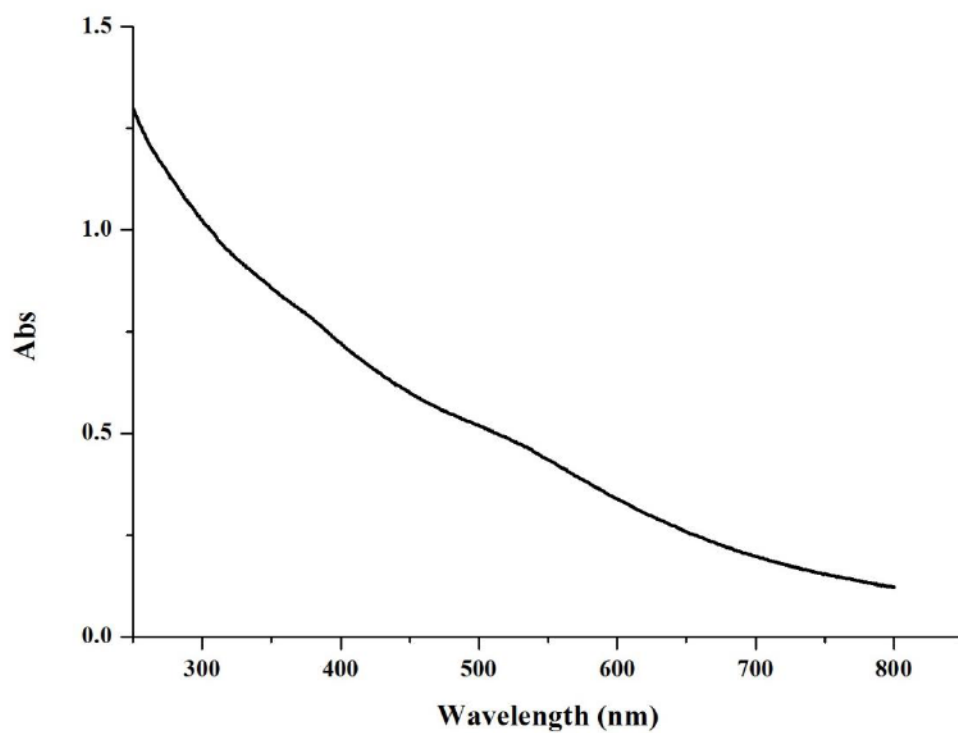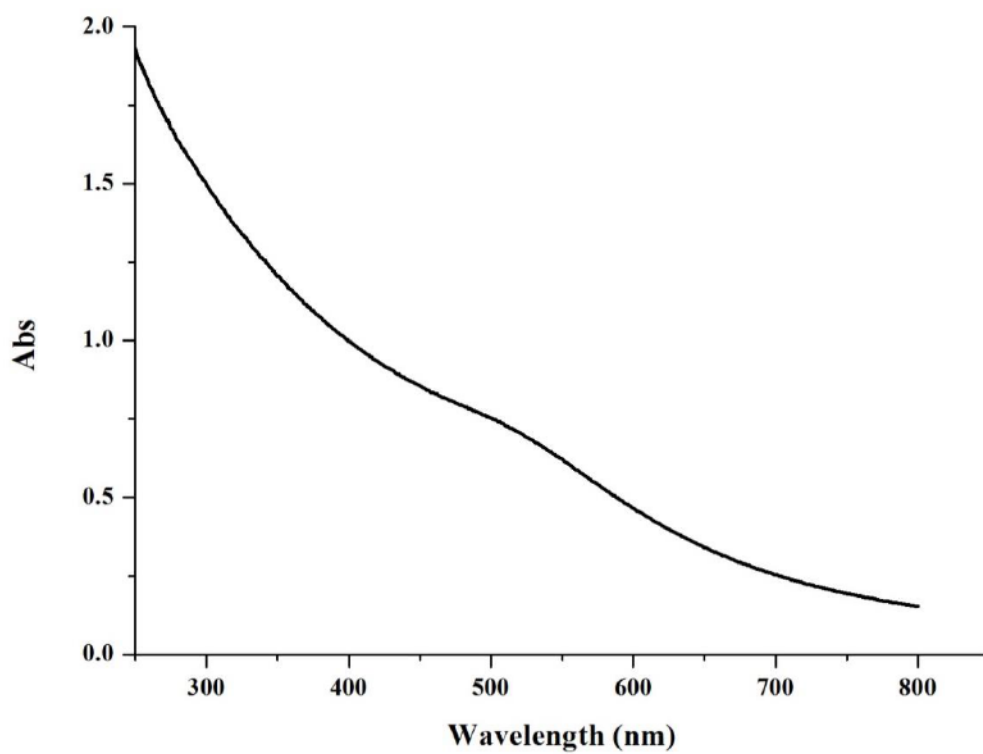
**Figure 3-19.** UV-Vis spectrum of **7**-AuNPs (0.1 mg/mL) at 25°C in water.
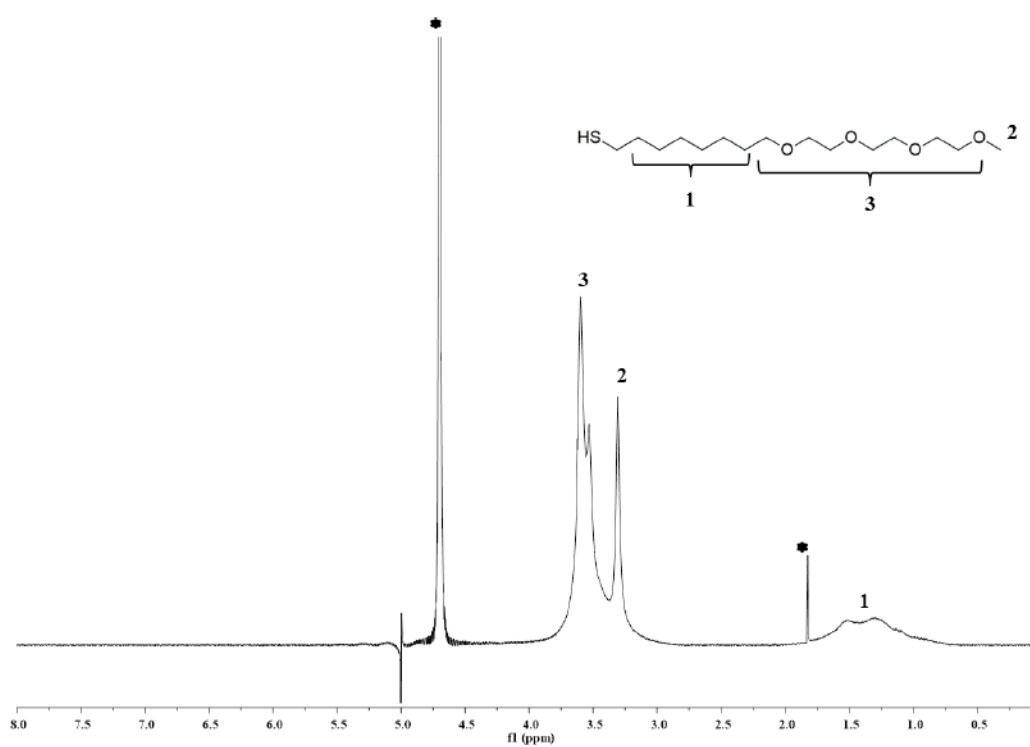
Figure 3-20. ^{1}HNMR spectrum of **7**-AuNPs in D$_2$O (● indicates the residual solvents and impurities).
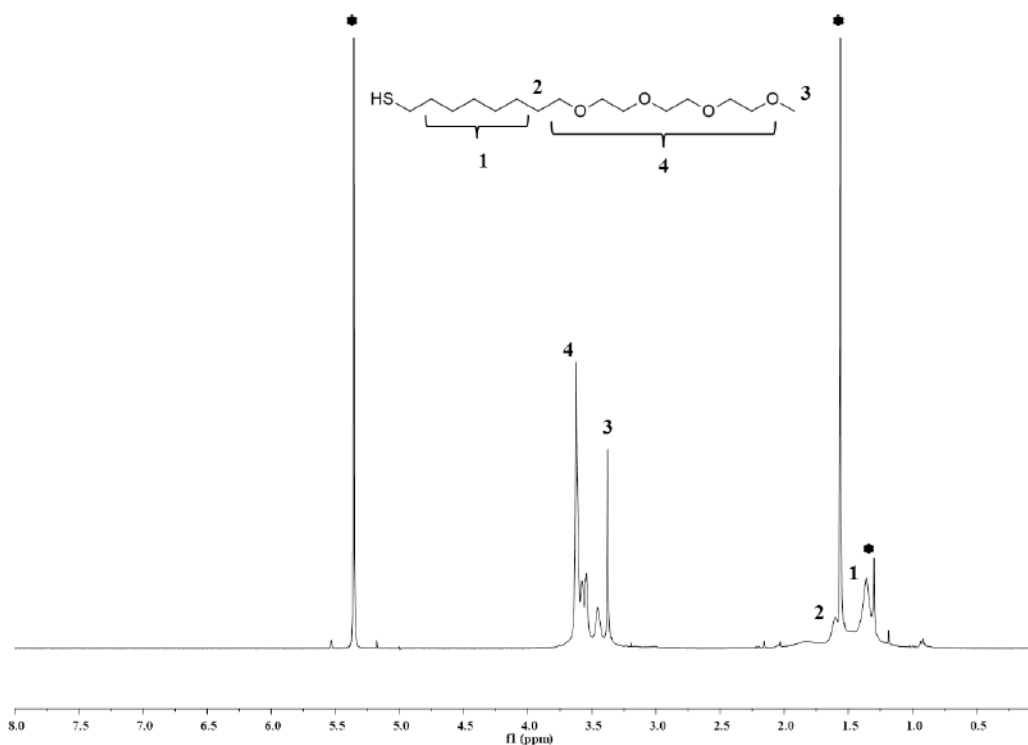
Figure 3-21. ^{1}HNMR spectrum of **7**-AuNPs in CD$_2$Cl$_2$ (◆ indicates the residual solvents and impurities).
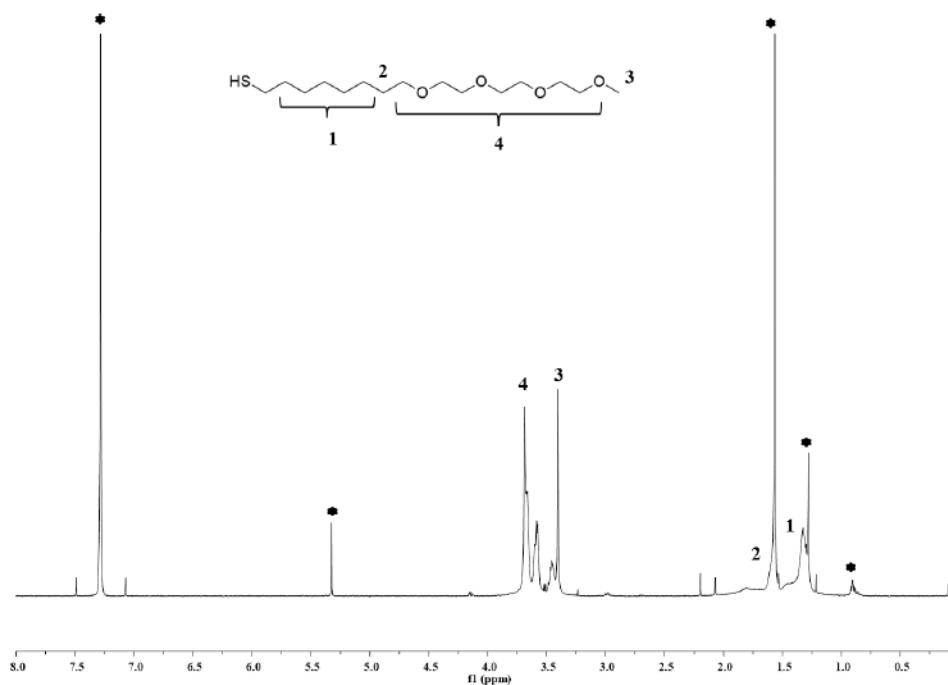
Figure 3-22. ^{1}HNMR spectrum of **7**-AuNPs in CDCl$_3$ (◆ indicates the residual solvents and impurities).

Characterization of 8-AuNPs. TEM analysis of the different samples of small nanoparticles (Figure 3-23) yields an average diameter for the AuNP of 1.7±0.5 nm. Formula for **8**-AuNPs

calculated on the basis of TEM diameter and TGA analysis is $Au_{152}RS_{76}$. TGA analysis of a sample of **8**-AuNPs under air atmosphere is shown in Figure 3-24. UV-Vis spectrum of a sample of **8**-AuNPs is shown in Figure 3-25. NMR analysis (Figure 3-26, 3-27, 3-28) indicates monolayer formation (broadening of all signals), as confirmed by diffusion-filtered experiments.

Figure 3-23. Sample TEM image of **8**-AuNPs and size distribution: average diameter = 1.7 ±0.2 nm.

Figure 3-24. TGA analysis of a sample of **8**-AuNPs under air atmosphere.
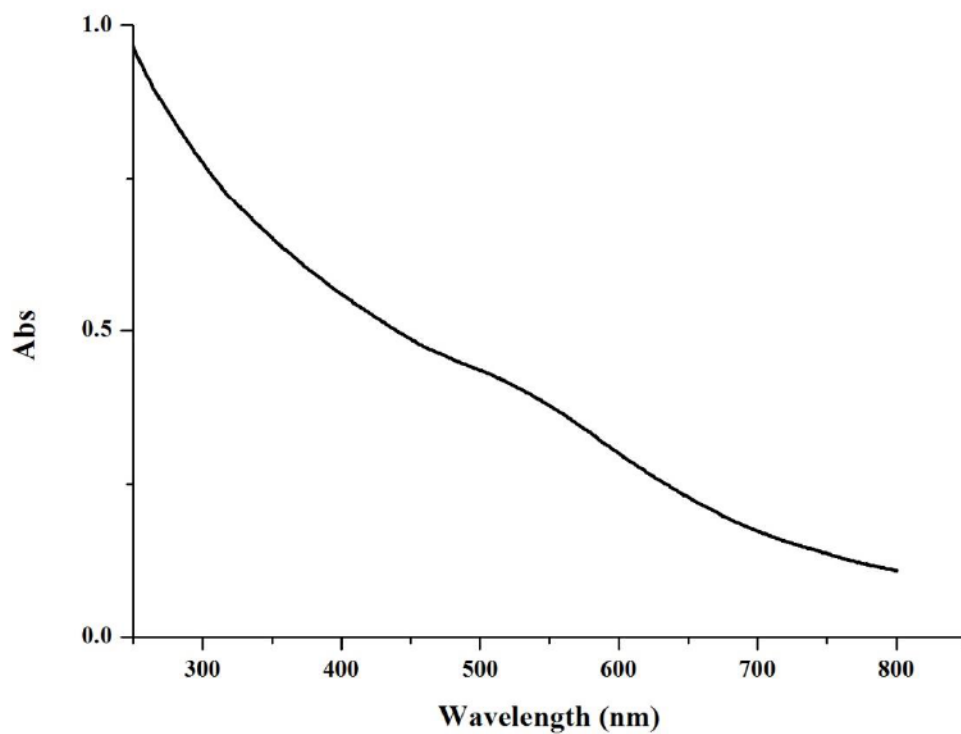
Figure 3-25. UV-Vis spectrum of **8**-AuNPs (0.1 mg/mL) at 25°C in water.
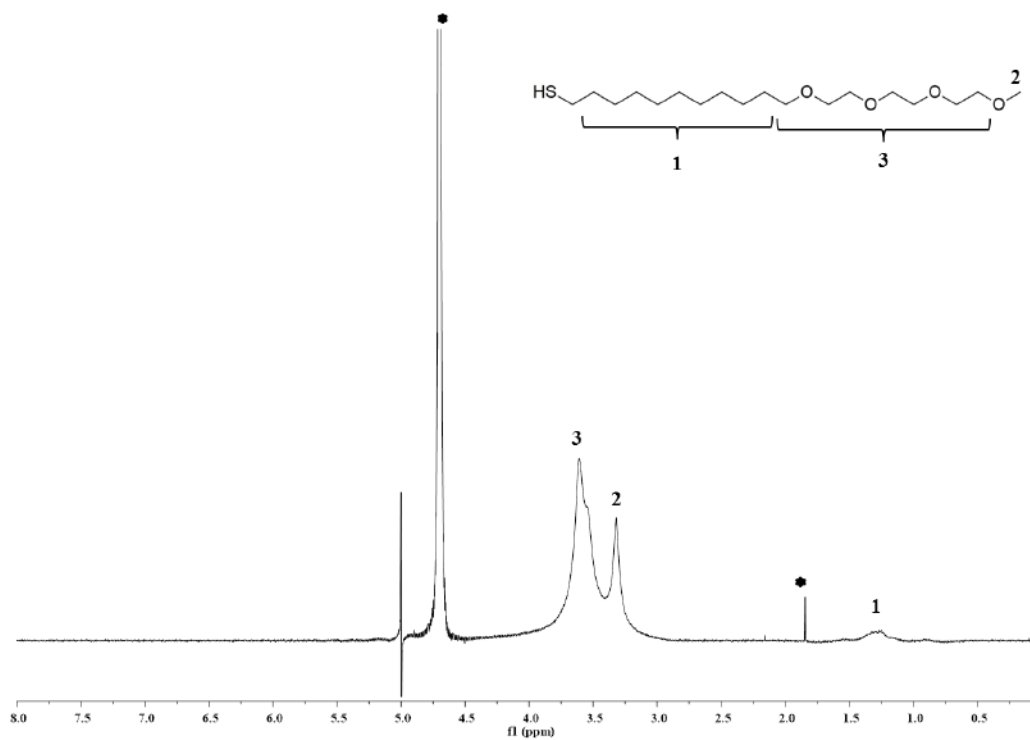
Figure 3-26. ^{1}HNMR spectrum of **8**-AuNPs in D$_2$O (● indicates the residual solvents and impurities).

Figure 3-27. ^{1}HNMR spectrum of **8**-AuNPs in CD$_2$Cl$_2$ (● indicates the residual solvents and impurities).

Figure 3-28. ^{1}HNMR spectrum of **8**-AuNPs in CDCl$_3$ (● indicates the residual solvents and impurities).

Characterization of 9-AuNPs. TEM analysis of the different samples of small nanoparticles (Figure 3-29) yields an average diameter for the AuNP of 1.6±0.5 nm. Formula for **9**-AuNPs calculated on the basis of TEM diameter and TGA analysis is Au$_{127}$RS$_{58}$. TGA analysis of a sample of **9**-AuNPs under air

atmosphere is shown in Figure 3-30. UV-Vis spectrum of a sample of **9**-AuNPs is shown in Figure 3-31. NMR analysis (Figure 3-32) indicates monolayer formation (broadening of all signals), as confirmed by diffusion-filtered experiments.

Figure 3-29. Sample TEM image of **9**-AuNPs and size distribution: average diameter = 1.6 ±0.2 nm.

Figure 3-30. TGA analysis of a sample of **9**-AuNPs under air atmosphere.

Figure 3-31. UV-Vis spectrum of **9**-AuNPs (0.1 mg/mL) at 25°C in CH_2Cl_2.

Figure 3-32. ^{1}HNMR spectrum of **9**-AuNPs in CD_2Cl_2 (◆ indicates the residual solvents and impurities).

Characterization of 10-AuNPs. TEM analysis of the different samples of small nanoparticles (Figure 3-33) yields an average diameter for the AuNP of 1.7±0.5 nm. Formula for **10**-AuNPs calculated on the basis of TEM diameter and TGA analysis is $Au_{152}RS_{56}$. TGA analysis of a sample of

10-AuNPs under air atmosphere is shown in Figure 3-34. UV-Vis spectrum of a sample of **10**-AuNPs is shown in Figure 3-35. NMR analysis (Figure 3-36) indicates monolayer formation (broadening of all signals), as confirmed by diffusion-filtered experiments.

Figure 3-33. Sample TEM image of **10**-AuNPs and size distribution: average diameter = 1.7 ±0.3 nm.

Figure 3-34.TGA analysis of a sample of **10**-AuNPs under air atmosphere.

Figure 3-35. UV-Vis spectrum of **10**-AuNPs (0.1 mg/mL) at 25°C in CH_2Cl_2.
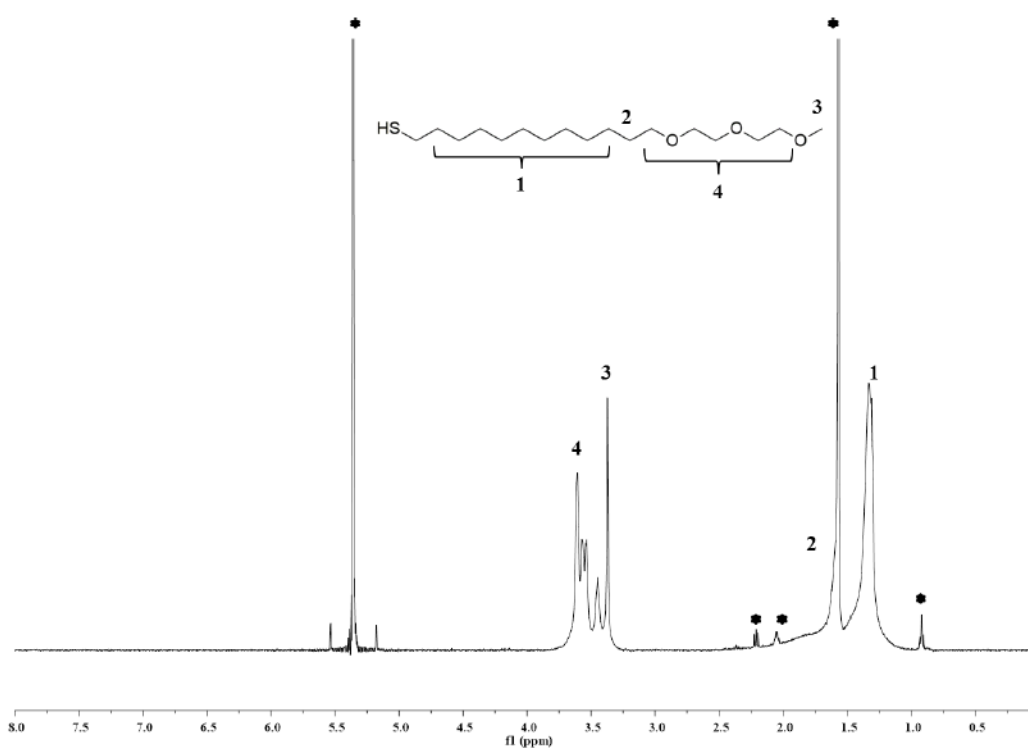
Figure 3-36. ^{1}HNMR spectrum of **10**-AuNPs in CD_2Cl_2(◆ indicates the residual solvents and impurities).

Chapter 4. Molecular dynamics simulation guided rational design of nanoreceptors with targeted selectivity

4.1 Introduction

In the previous chapter we showed as extensive MD simulation led to discover that the receptor ability of **1**-AuNP is due to the spontaneous formation of deep pockets in the monolayer.[92] Such pockets have a cavity shape, with a hydrophobic bottom and a hydrophilic rim formed by the amide groups and the oligo(ethylene glycol) moieties. The opening of the pocket precedes the binding and the selectivity observed (2-hydroxybenzoate versus 4-hydroxybenzoate) arises from its complementarity with the substrate structure. Finally, docking experiments resulted into salicylate binding poses very similar to those observed in salicylate-binding proteins. The formation of the transient pockets is strongly related to the presence of the amide group in the chemical structure of thiol **1**. Indeed, the nanoparticle coating monolayer revealed to be more flexible, in water, than those formed by thiols devoid of the amide group. Water molecules, bridging the amide residues in **1**, prevented the hydrophobic packing of the alkyl moieties of the coating molecules to form rigid bundles, which in turn prevented pocket opening.

Such results suggest the intriguing possibility to rationally design binding cavities in the nanoparticle coating monolayer using molecular dynamics simulations. With this in mind, still in collaboration with the group of M. De Vivo, we undertook a detailed investigation aimed to get a deep understanding of the pocket formation in the monolayer and of the mode of binding of salicylate and to evaluate the effect of selected modification of the binding sites present in the monolayer, toward the possibility of tune the interaction between the analyte and the nanoparticle. In this chapter, we will show that, in an approach similar to those used for protein modification, MD simulations can guide the design of new nanoreceptors with tailored affinity for the substrate.

4.2 Structural determinants for binding of salicylate to 1-AuNP.

The starting point of this investigation was the computational simulations on the interaction between **1**-AuNP and salicylate discussed in the previous chapter. Indeed, we realized that the rational modification of the nanoparticles affinity for this substrate requires a more detailed understanding of the analyte binding modes and of the interactions at play. A crucial point to address is the identification of the bound state of the substrate to the nanoparticle. Indeed, in the

absence of clearly defined binding sites (due to the transient nature of the pockets) the simple "contact distance" between coating molecules and the substrate may be misleading. MD investigations described in the previous chapter revealed that the interaction of salicylate with **1**-AuNP, with respect to the non-binding 4-hydroxybenzoate, was characterized by an increase of both the contact time and the depth of penetration of the analyte in the monolayer (Figure 3-10). In agreement, reversed NOE experiments demonstrated that the alkyl region of the particle coating monolayer is responsible for the transfer of magnetization from the nanoparticle to the salicylate protons (Figure 3-10). According to the NOE theory, effective magnetization transfer requires indeed close distance (within 0.4 nm) and prolonged contact time between the interacting species.

Starting from these considerations, the IIT group extended their microsecond-long MD simulations on **1**-AuNP in the presence of salicylate to get further details on analyte recognition and binding. Radial distribution functions (rdf, Figure 4-1), centered on the nanoparticle core, revealed that salicylate distribution around the nanoparticles is quite broad, covering the whole region between 1.2 and 2.2 nm from the center of the nanoparticle. However, such a broad distribution is divided in two populations, as well revealed by the shape of the rdf of C4. This features a relatively sharp inner distribution region at 1.25 nm from the center (which finds a correspondence in less pronounced shoulders, at smaller distances form the center, in the rdf of the oxygen atoms) and a second, outer and much broader, distribution around 1.5 nm. Another relevant information that comes from the analysis of the rdf for salicylate, is that the phenolic oxygen is generally closer to the particle surface than the two carboxylic oxygens, which in turn have an identical radial distribution. This suggests that there is a favorite orientation of salicylate in the monolayer, with the ideal axis connecting the C4 and the carboxylic carbon perpendicular to the particle surface. Such an orientation results indeed in the exposure of the charged carboxylate residue to the outer water phase.

When we turned the attention on the distribution functions of the coating thiols (Figure 4-1C), we found as expected a radial structure centered on the metal core, with the atoms from the alkyl portion in the inner region of the monolayer, followed by the atoms of the amide group and finally by those belonging to the oligo(ethylene) portion (OEG). In detail, carbon atoms belonging to the alkyl chains are found up to 1.7 nm far from the center. Their distributions are quite narrow for the carbons close to the nanoparticle surface and become broader and broader as they move from the core to the periphery. Atoms from the amide group are found, again with relatively broad

distributions, between 1.6 and 1.9 nm from the center. Finally, atoms from OEG have a very broad and complex distribution, with the ones of the inner portion located between 1.7 and 2.2 nm from the center and those of the outer portion covering a large distances range that extends down to 1.2 nm, penetrating both the amide and the alkyl regions.
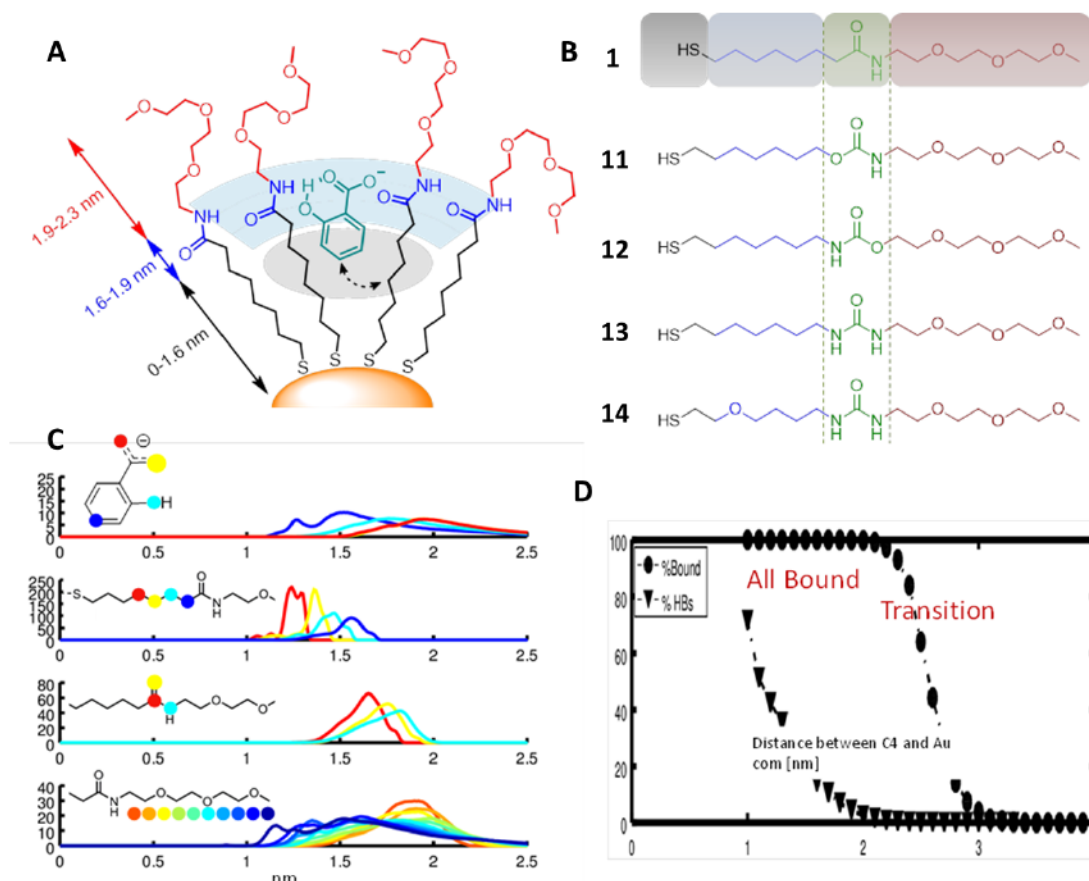
Figure 4-1. (A) salicylate orientation in the monolayer of **1**-AuNP, (B) the structure of the coating ligands used in this study, (C) radical distribution function of salicylate and coating thiol **1**, (D) the occurrence of the binding event and formation of HBs against the distance between C4 and Au core.

Such distributions indicate that the alkyl portion of the coating thiols is relatively rigid and likely prefers an extended conformation. Conformational flexibility increases with the distance from the particle surface and eventually the PEG chains substantially fold toward the amide region. As previously evidenced, such conformation is related, at least partially, by the formation of H-bonds between the outer OEG oxygens and the amide group, or by bridging water molecules.

When the distributions of the atoms belonging to salicylate and **1**-AuNP are compared, it appears quite evident that the MD simulations individuate two potential binding modes. In the first one, salicylate is essentially trapped in the OEG region with a wide range of possible orientations. In the second one, it penetrates deeper in the alkyl region, with a precise localization

of the hydrophobic benzene moiety and a more defined, albeit still broad, orientation of the hydrophilic region corresponding to the carboxylate and hydroxyl groups. The oxygen atoms of these two residues are also found to be close to the NH and the first OEG oxygens of the coating, confirming the possibility of H-bond interactions as already suggested by the earlier simulations.
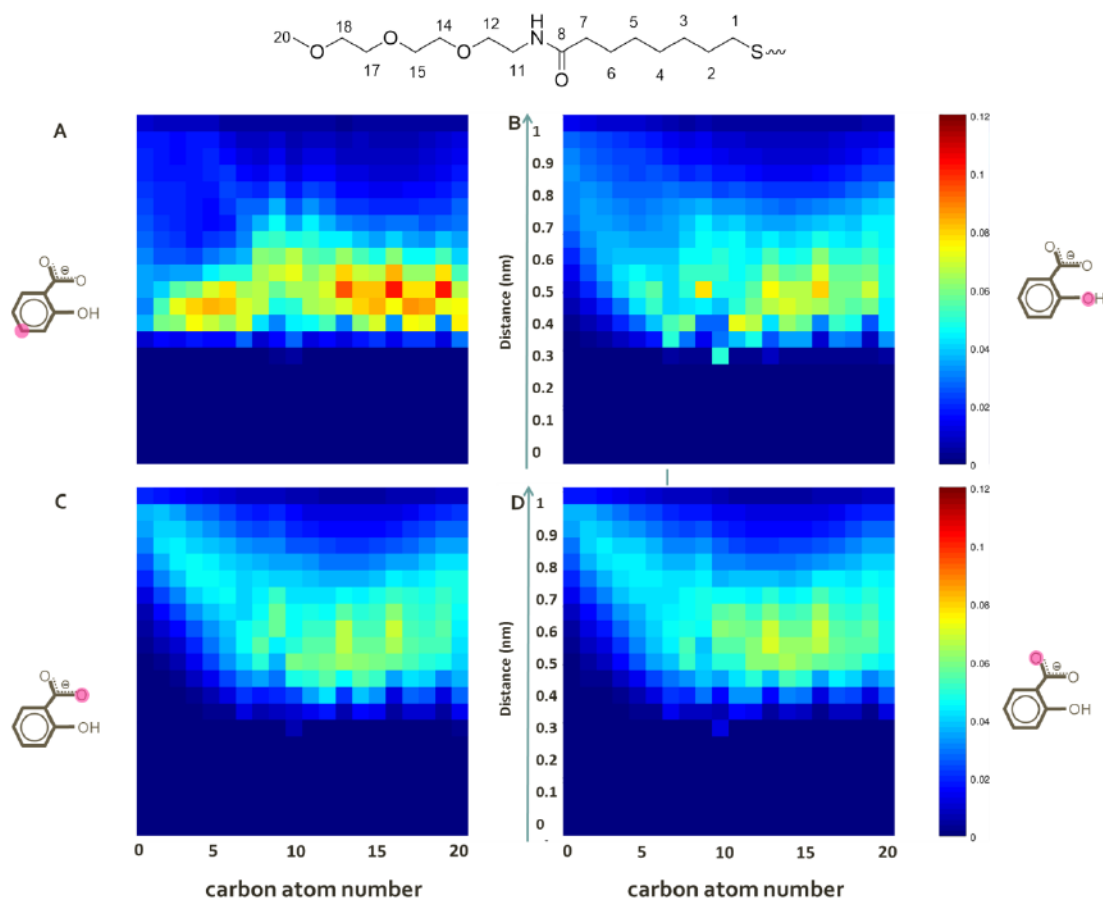
Figure 4-2. The probability of contacts between the (A) C4 atom, (B) phenolic hydroxyl, (C) and (D) carboxylate oxygens of docking salicylate and the coating thiol.

Contact mapping (Figure 4-2) confirmed this picture. Indeed, two regions of close contacts were found for the salicylate C4, the first with the atoms 4-6 of the alkyl chain of **1-AuNP**, and the second with the OEG portion. In a similar way, the phenolic hydroxyl is found close to the amide residue, or in the OEG portion, while the carboxylate oxygens are found in contact only with the OEG portion.

Having in our hands a better description of the possible binding modes, we performed a detailed analysis of H-bonding between the analyte and the monolayer (figure 4-1D). When we focused the attention on the long-lived binding events, we found that in 21% of such events an H-bond is present between the amide group of the coating and the substrate, mainly involving the

NH group as donor and the phenolic oxygen as acceptor. On the other hand, turning the attention on the deep binding events, i.e. those associated to the sharp inner distribution region of salicylate's C4, we found that H-bonding is present in 43% of the cases.

Taken together, all the information available suggests that effective salicylate recognition and binding occur via its deep insertion in the monolayer. This is characterized by a relatively precise orientation of the substrate, suggesting quite a defined structure of the binding pocket and the presence of relevant interactions. Contact maps and H-bonding analysis indicate that such interactions are likely the hydrophobic/dispersion interaction between the substrate arylic portion and the alkyl region of the nanoparticle coating thiols and the H-bonding between the phenolic oxygen and the amide group of the thiols hydrophobic. Remarkably, this binding mode is quite similar with that observed in salicylate binding proteins. On the other hand, the second area of salicylate localization in the outer region of the monolayer, corresponding to the OEG moieties, likely represents just a short lived state preliminary to the deep binging mode.

4.3 Rational modifications of the coating ligands

On the basis of the above analysis, we started a program of rational modification of the nanoparticle affinity for salicylate based on a binding site design strategy. Modifications were planned in order to affect both the main interactions at play, discussed in the previous paragraph. Coating molecules **11**-**14** (Figure 4-1B) were hence designed. In thiols **11**-**13**, the H-bonding interaction with the substrate is modulated. Indeed, urethane residues are weaker H-bond donors with respect to amide, and urea is a stronger and symmetric donor. In thiol **14**, in turn, the hydrophobic/dispersion interaction is modulated by inserting a polar oxygen atom in the alkyl chain.

To evaluate the effect of such modifications, an additional series of extended MD simulations (>200 ns each) of **11-14** AuNPs immersed in explicit water were performed by the IIT Group. Analysis of the MD simulations provided once again interesting information. Solvent distribution functions (Figure 4-3) are similar for all the nanoparticles (included **1**-AuNP) and the first water molecules are found at about 1.5 nm from the center nanoparticles, a region corresponding to the amide/urethane/urea group. On the basis of previous results, spherical shape and limited solvent penetration indicate a good shielding of the inner alkyl chains from the solvent, suggesting that the nanoparticles have a small tendency to aggregate and are present in solution as individual entities.
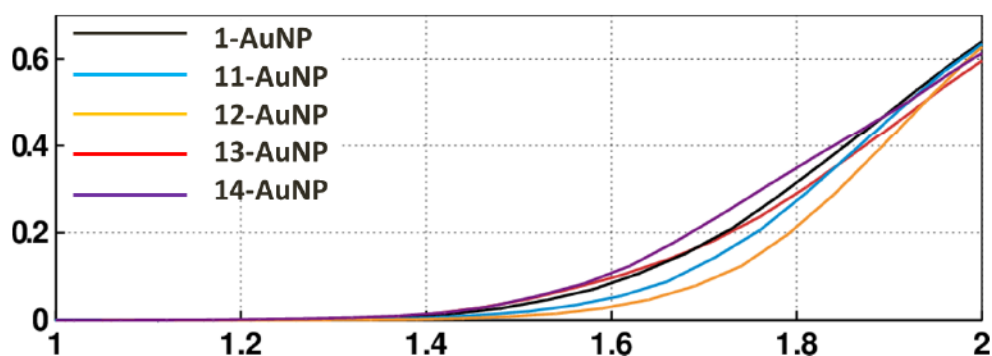
Figure 4-3. The distribution functions of water in the monolayer of **1**, **11**, **12**, **13** and **14**-AuNP.

Solvation is an important parameter affecting both intra-particle interactions and their receptor ability. The number of ligand/water hydrogen bonds (HBs) is reported in Figure 4-4. All the AuNP formed a similar number of HBs with the solvent (~135 to ~165). However, **11**- and **12**-AuNP showed a smaller tendency to solvation (~135 to ~140 HBs) than **1**-AuNP (~150) and **13**- and **14**-AuNPs (~155 to ~165) respectively. Such figures well reflect in the water distribution functions that show a larger amount of water within the coating monolayer in the case of **1**-, **13**- and **14**-AuNP.

	1-AuNP		11-AuNP		12-AuNP		13-AuNP		14-AuNP	
	NP	H_2O	NP	H_2O	NP	H_2O	NP	H_2O	NP	H_2O
O	5±2	26±4	4±2	24±4	3±1	21±4	16±4	26±4	11±4	30±5
O	4±2	19±4	4±2	15±4	3±1	14±3	10±3	19±4	9±3	19±4
O	2±2	16±4	4±2	13±3	3±1	10±3	4±2	15±3	4±3	15±3
	22±4	19±4	1±1	2±1	16±3	4±2	34±4	19±4	36±4	16±4
=O	12±3	69±5	8±2	79±5	4±2	85±5	38±5	68±5	43±6	61±5
			21±3	6±2	3±2	1±1	36±4	17±3	39±4	14±4
									7±3	1±1
Tot	22 ±4	149 ±10	22 ±3	140 ±8	16 ±3	134 ±7	69 ±7	164 ±12	75 ±7	156 ±14

Figure 4-4. Average number of ligand-ligand and ligand-H_2O interactions during MD simulations.

Most of the interactions with water are due to the amide, urethane or urea residues, where the carbonyl oxygen accounts for ~40% (urea) to ~60% (urethane) of the interactions with water. NH residues are on the other hand less effective in forming HB with the solvent when they belong to urethane (forming only ~1 to ~6 HBs), and more effective when they belong to urea (~14 to ~19 HBs). The OEG portions account for the remaining HBs from the solvent, with the number of interactions decreasing from the terminal and more solvent-exposed oxygen to the inner ones.

Similar trends were observed in all the AuNPs with urethane containing nanoparticles forming a somewhat smaller number of HBs (~45-52 *vs* ~61-64). Interestingly, a quite small number of H-bonds are formed with the oxygen atom located in the inner alkyl portion of **14**-AuNPs (~7).

The chemical modifications of the coating ligands had a much more pronounced effect on the intra-monolayer interactions. Here, we noted that the number of HBs formed by the urea groups in **13**- and **14**-AuNPs is much larger than that formed by amide group in **1**-AuNP (~69 to ~75 versus ~22). In particular, the urea NH groups formed ~36 to ~39 HBs versus the ~22 formed by the amide NHs. This number is substantially larger than the average number of interactions established with water molecules (~14 to ~19 HBs independently of the chemical nature of the NH group). Most of the interligand HBs formed by urea NH groups are with neighboring carbonyl oxygens, while the remaining ones are formed with the OEG, in decreasing amount from the outer to the inner oxygen (Figure 4-4). Notably, the effect of the urethane groups in **11**- and **12**-AuNPs is significantly different. The number of interligand interactions is similar to that of **1**-AuNP (~16 to ~22 versus ~22) and also the NH groups form a similar number of HBs (~16 to ~21 versus ~22). On the other hand, the carbonyl oxygen is accepting much fewer HBs in **11**- and **12**-AuNPs than in **1**-AuNPs (~4 to ~8 versus ~12) only partially compensated by those accepted by the urethane oxygen (~1 to ~3). HBs to the OEG oxygens are similar in all the three particles (~9 to ~12 versus ~11). As a result of the different extent of intramonolayer H-bonding, the autocorrelation functions of the CH bonds indicated an increase of the rigidity of the inner alkyl portion in nanoparticles **13**- and **14**-AuNP with respect to **1**-AuNP.

These results revealed that: 1) the number of intramonolayer HBs is significantly affected by the chemical structure of the central moiety, with the urea group that considerably increases it, while urethane slightly decreases it. Such structural effect is apparently correlated with the rigidity increase evidenced by the CH autocorrelation functions; 2) quite surprisingly, intramonolayer interactions and solvation are correlated. In other words, more extensive interactions between the coating molecules do not prevent the interaction with the solvent, at least in the cases here studied.

Having elucidated the effects of the chemical modification of the coating molecules on the monolayer structure, we turned our attention to the interaction with salicylate. The IIT Group run three 1 μs long MD simulations of **11**-, **13**- and **14**-AuNPs with salicylate in solution, which were compared with those performed with **1**-AuNP and already discussed.

Analysis of the radial distribution profiles (Figure 4-5) show that a larger amount of salicylate is found closer to the surface of **13**-AuNP with respect to the other nanoparticles, suggesting a stronger affinity of these nanoparticles for the analyte. A more detailed inspection of the plots reveals the distribution profiles follow different behaviors for the different nanoparticles. For distances smaller than 1.3 nm from the gold surface, a distance corresponding to the alkyl region, the amount of analyte found is in the order **13**-AuNP > **1**-AuNP > **11**-AuNP $\approx$ **14**-AuNP. On the other hand, when distances smaller than 2.0 nm from the surface are considered, corresponding to almost the whole monolayer region, the abundance order changes to **13**-AuNP > **11**- AuNP > **1**-AuNP >> **14**-AuNP.
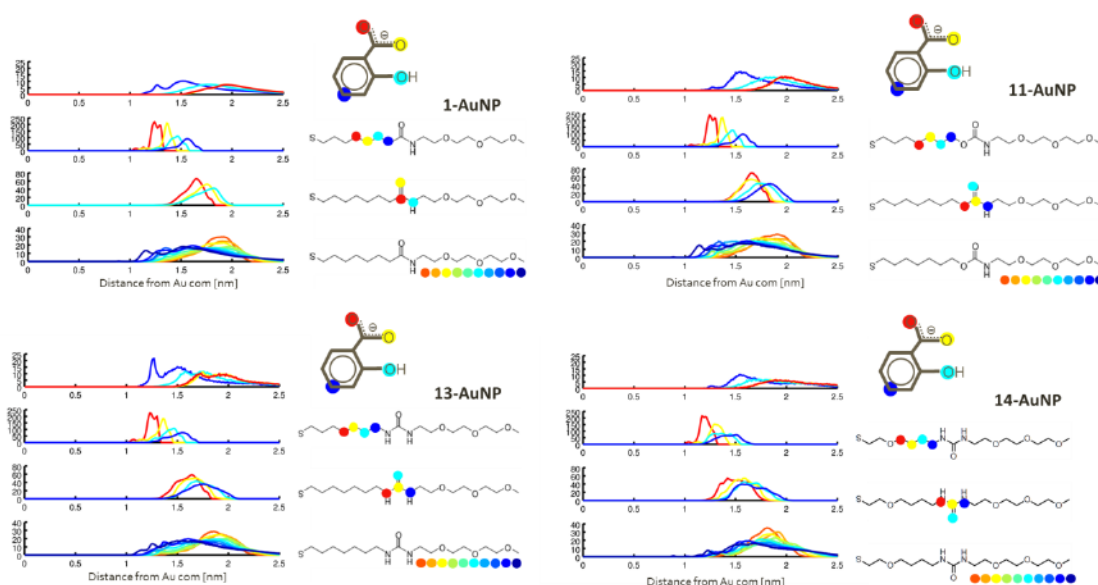
Figure 4-5. The radical distribution profile of salicylate (in the monolayer of **1**, **11**, **13** and **14**-AuNP) and coating ligands.

The reason of such a behavior can be found by inspecting the distribution profiles (Figure 4-5). A first sight to the plots immediately highlights that only in the case of **1**- and **13**-AuNPs, the analyte is distributed over a bi-modal profile. A first population of distances is found at 1.2 nm form the gold surface. Salicylate spends about 5 % and 2 % of the computation time in this position in the case of **13**- and **1**-AuNP respectively, while it is not found at such a low distance in the case of **11**- and **14**-AuNP. The second population is centered at 1.5 nm for all the nanoparticles. Such bimodal behavior is clearly related to the two binding states previously discussed, i.e. deep binding in the alkyl region and pre-binding in the OEG region. This hypothesis is confirmed by the radial distribution functions of the individual salicylate atoms. As in the case of **1**-AuNP, rdf for the salicylate C4 atom features a sharp distribution region at 1.25 nm from the center, but its intensity and area are substantially greater than in the case of **1**-AuNP. A second broader distribution is

around 1.5 nm. In this case, the bimodal distribution of distances is well-visible also for the analyte's oxygen atoms. As with **1**-AuNP, the phenolic oxygen is on average closer to the particle surface than the two carboxylic oxygens, suggesting that a similar binding mode is at play with **13**- and **1**-AuNP. However, the more defined localization of such atoms suggests quite a tight binding with a precise orientation of the substrate in the monolayer and relatively strong interactions. Remarkably, such low-distance population distributions are not found with both **11**- and **14**-AuNP, suggesting a smaller affinity of these nanoparticles for the analyte.
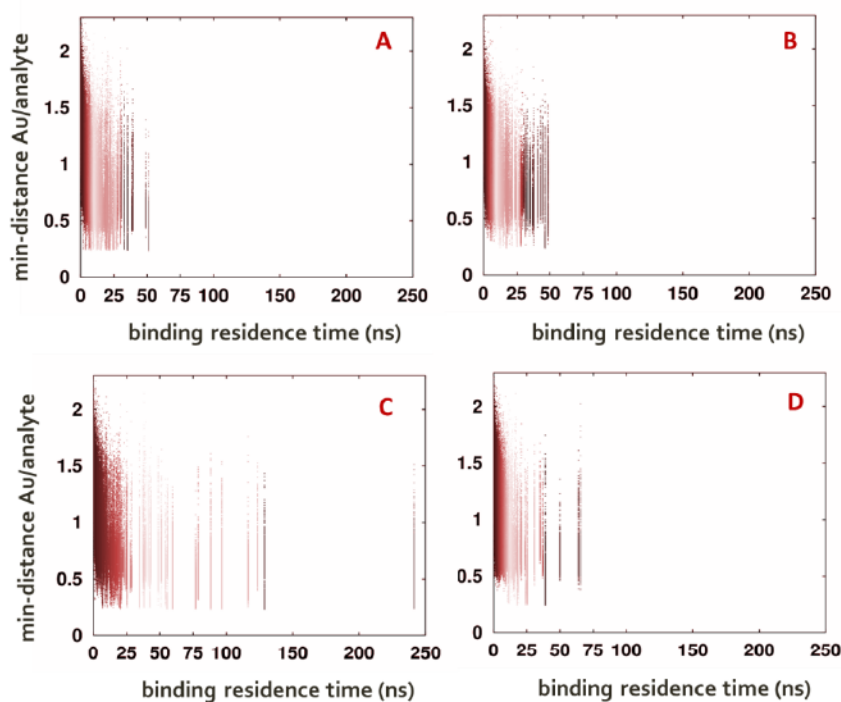
Figure 4-6. The plot of the minimum distance between the salicylate and the core of (A)**1**-AuNP, (B) **11**-AuNP, (C) **13**-AuNP and (D) **14**-AuNP against the binding residence time.

Residence time classification of the contact events (Figure 4-6) reveals that, in the case of **13**-AuNP, deep binding events remain numerous and experience a significant increase of their duration. With **11**-AuNP both lifetime and degree of penetration of the contact event significantly decrease. Finally, in the case of **14**-AuNP, while the duration of the contact events is apparently similar to that observed with **1**-AuNPs, the degree of penetration in the monolayer is sensibly smaller.

On the basis of this results, we predicted the affinity of **13**-AuNP for salicylate to be larger than that of **1**-AuNP, and that of **11**- and **14**-AuNP to be smaller. The clear correlation between deep penetration and H-bonding suggests a relevant role of this interaction in the substrate recognition. However, the results obtained for **14**-AuNP indicate that such interaction produces effective

binding only when complemented with another attractive interaction (either hydrophobic or dispersive) in the monolayer alky region.

4.4 Experimental testing and validation of nanoreceptor/analyte affinity
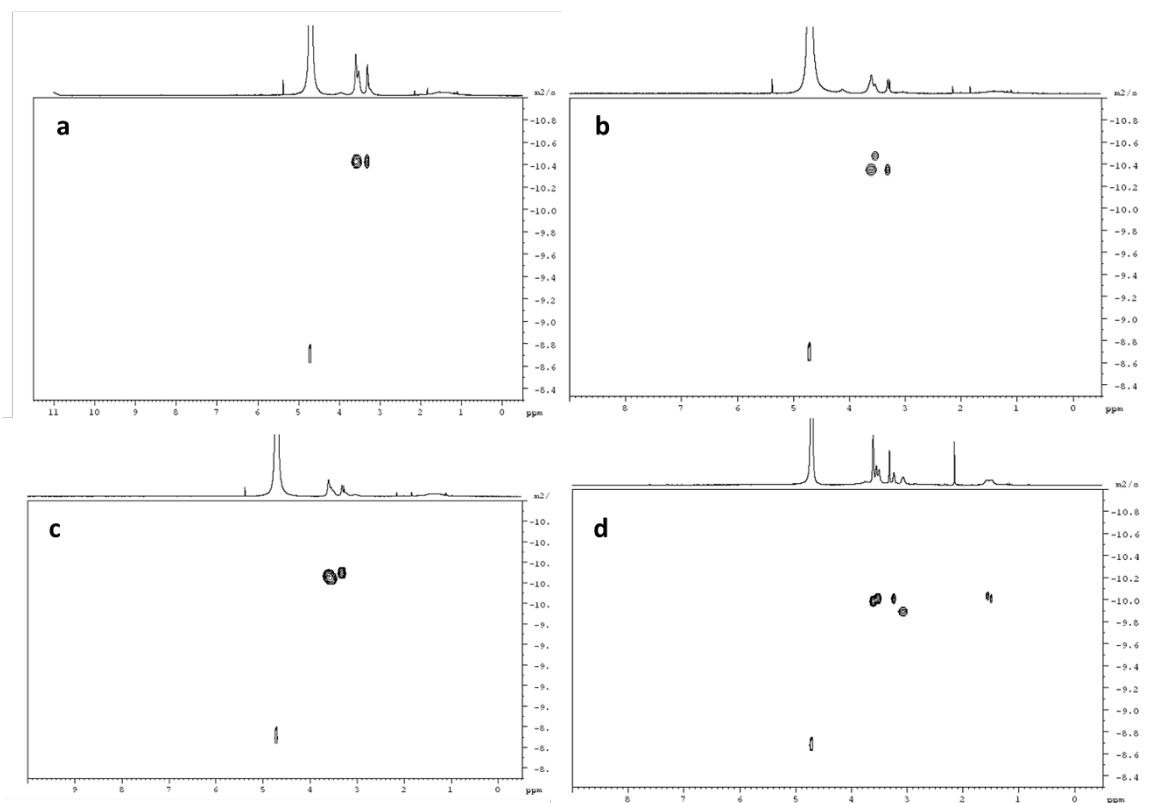
Figure 4-7. DOSY spectrum of AuNPs in water at 15 uM concentration. a) 11-AuNPs, D=3.12×10^{-11}. b)12-AuNP, D=4.09×10^{-11}. c) 13-AuNP, 4.55×10^{-11}. d)14-AuNP, 8.62×10^{-11}.

The ability of MD simulations to effectively anticipate the nanoparticles affinity for salicylate was investigated using the NMR chemosensing protocol. Coating molecules **11**-**14** (Figure 4-1), and the corresponding nanoparticle 11-14-AuNP were synthetized following standard procedures. All the nanoparticles resulted to be well soluble in water. ^{1}H-NMR and DOSY experiment (Figure 4-7, average diameter of 7.1 nm for 11-AuNP, 5.7 nm for 12-AuNP, 5.1 nm for 13-AuNP and 3.5 nm for 14-AuNP) confirmed the absence of aggregation in this solvent. The NOE pumping sequence was used to analyze samples containing the nanoparticles (1mM in thiol) and salicylate at 5 mM concentration in carbonate buffered D$_2$O solution at pD = 10.0. The results are reported in Figure 4-8. **1**-AuNP confirmed their already reported ability to detect salicylate in water. Analyte signals appeared in the NOE pumping spectra with a signal to noise ratio of ~3. In the case of **13**-AuNP, significantly more intense salicylate signals (S/N ~ 9) were obtained in the same conditions. A titration experiment where NOE pumping experiments were run on a series of samples containing **13**-AuNP and increasing concentrations of salicylate revealed that the integrated intensities of the

salicylate signals increase with the concentration, almost reaching a plateau value at about 5 mM. Further inspection of Figure 4-8B showed that the titration plot is close to linear at concentrations lower than 1 mM. Considering that the thiols arising from 13-AuNP at this experimental condition is also 1 mM, a 1:1 binding model was employed to fit the integrated intensities versus the analyte concentration and an apparent association constant (K_{ass}) of $1.1 \times 10^3 \, M^{-1}$ was obtained. This figure is one order of magnitude greater than the value of $120 \, M^{-1}$ previously obtained with **1**-coated nanoparticles. At 25 °C, a 10-fold affinity increase corresponds to a ~6 KJ/mol decrease of the ΔG for the binding process, a figure that is quite in agreement with the formation of one additional H-bond in water.

On the other hand, analyte signals were never detected with a signal-to-noise ratio above 3 (which we usually set as a detection limit) in the experiments performed using **11**- and **14**-AuNPs, even in the presence of high (10 mM) concentrations of the substrate. This confirms that **11**- and **14**-AuNPs have an affinity for salicylate that is sensibly lower than that of **1**-AuNP, as predicted by the molecular dynamic simulations.
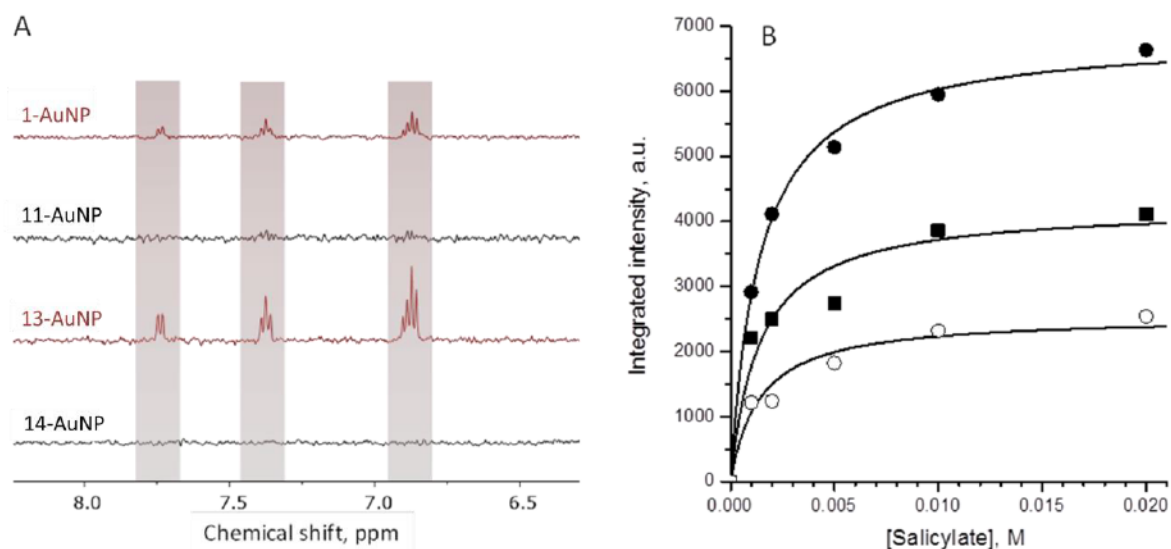
Figure 4-8. (A) The NOE-pumping spectra of 1, 11, 13 and 14-AuNPs in the presence of salicylate. Experimental condition: AuNPs (1mM in thiol), carbonate buffer (20 mM, pD=10.0), salicylate (5 mM). (B) Relative integrated intensity of NMR signals of salicylate (●6.8 ppm, ■7.4 ppm, ○7.8 ppm) from NOE-pumping spectra against its concentration.
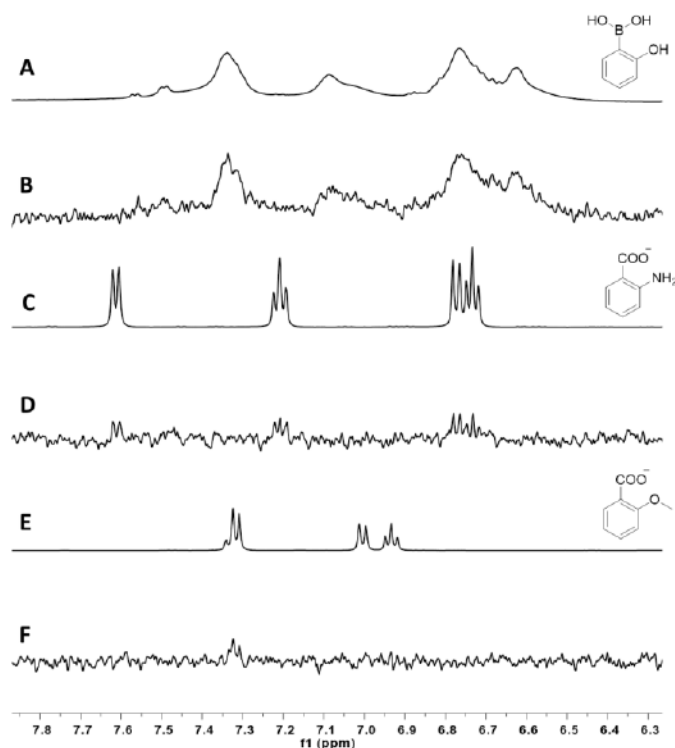
Figure 4-9. (A) ^{1}H NMR spectrum of 2-hydroxy-phenylboronate. (B) NOE-pumping spectrum of 2-hydroxy-phenylboronate in the presence of **13**-AuNP. (C) ^{1}H NMR spectrum of 2-amino-benzoate. (D) NOE-pumping spectrum of 2-amino-benzoate in the presence of **13**-AuNP. (E) ^{1}H NMR spectrum of 2-methoxy-benzoate. (F) NOE-pumping spectrum of 2-methoxy-benzoate in the presence of **13**-AuNP. Experimental conditions: AuNPs, 15 μM. Carbonate buffer, 20 mM, pD=10. Analytes, 5 mM.

To further validate the information obtained from the computational investigations, we focused our attention on the relationship between binding affinity and substrate structure. According to calculations, the most relevant H-bonding interaction occurs between the phenolic oxygen of salicylate and the NH residues in the monolayer. We hence tested analytes featuring a similar structure but a different H-bonding ability (Figure 4-9). We found that, at 15 μM nanoparticles and 5 mM salicylate concentration (in carbonate buffered D$_2$O solution at pD=10.0), 2-hydroxy-phenylboronate is detected by **13**-AuNPs via NOE-pumping experiments with a S/N ratio (≈8) comparable to that found with salicylate. On the other hand, 2-amino-benzoate is detected with a sensibly lower S/N ratio (≈3) and 2-methoxy-benzoate is not detected at all. A peculiar feature of salicylate and some of his analogues is the possibility to form a highly stable, RAHB-type, H-bond between the phenolic OH and the neighbouring group. Such a possibility is prevented only in 2-mehoxy-benzoate and apparently is very relevant in controlling the H-bonds accepting properties of the substrate. In 2-amino-benzoate the internal H-bonding is still possible but the group in position 2 on the benzene ring cannot accept H-bonds. This results in a lower affinity for the

monolayer. Finally, in 2-hydroxy-phenylboronic acid the whole intramolecular network of H-bonds is maintained and detection ability of **13**-AuNP is similar to that observed with salicylate.

4.5 Conclusions

In conclusion, the experiments here reported confirm the exciting opportunity to prospectively apply computational simulations to investigate the recognition ability of monolayer protected nanoparticles toward selected molecular species. As in protein studies, in silico calculations allow to analyze the binding mode of the target to the monolayer in order to individuate the most relevant interactions at play. The computer-aided rational design of such interactions allowed to evaluate the effect of systematic modifications of the nanoparticle coating ligands and to estimate the affinity for salicylate, which was nicely confirmed by experiments. At the end, a 10-fold affinity increase was obtained by rational reinforcement of the H-bonding interaction emerged as relevant in MD simulation, as well as an at least 10-fold affinity decrease was obtained by perturbing the hydrophobic/dispersion interaction.

Difficulties to overcome are similar, if not larger, to those encountered in protein engineering efforts. The highly dynamic nature of the monolayer, only partially attenuated by the grafting of the coating molecules to the gold core, prevents the precise definition of the structure of the binding site. Indeed, the binding pockets that open in the monolayer have a transient and poorly defined nature that prevents the punctual identification of the binding interactions with the analyte. In addition, also the definition of the "bound" state is elusive, as the simple contact of the analyte with the monolayer atoms is not sufficient to define a binding interaction. We addressed such problems by running extensive MD simulations in the presence of explicit analytes and analyzing the resulting trajectories with respect to several parameters included distances, contacts, H-bonding and residence times. Interestingly, the results of such simulations indicated that strong binding requires the concurrence of different interactions, in the present case H-bonding and hydrophobic/dispersion interactions. Such a binding mode is confirmed also by the results reported by several groups on the behavior of nanoreceptors.[93, 115] In addition, it is also reminiscent of several examples of binding of small molecules to natural receptors. Less obviously, if one considers the still high dynamic nature of the monolayer, we found that strong binding correlates to a quite precise positioning of the analyte in the nanoparticle coating monolayer, at least in the cases here studied.

The next problem to address will be the simplification of the computational protocol, which now requires running extended MD simulations in the presence of explicit analytes in order to estimate the binding mode and the affinity of each analyte for a given ligand. Indeed, given the highly flexible nature of the coating thiols, MD simulations seem necessary to estimate recognition and binding of any given analyte for the coating ligand of interest. This is at the moment the main bottleneck toward and efficient computer-aided nanoreceptors design, although more basic protocols based on static molecular docking have shown to be at least qualitatively informative, when targeting selected pockets that act mostly via conformational selection for binding. This relates to another relevant point, which is the reduction of the monolayer flexibility to achieve the formation of permanent, partially rigid, binding pockets. Results reported here, as well as in previous works, suggest that increasing the extent of intramolecular interactions could effectively lead to more rigid monolayers. However, in the case of linear coating molecules, as those here reported, rigidification may result into massive bundling of the coating molecules without the formation of pockets. Possibly, the use of bulkier or branched coating molecules, with better space filling factors, may provide the desired solution.

4.6 Experimental section

4.6.1 Synthesis of 8-mercapto-N-(2-(2-(2-methoxyethoxy)ethoxy)ethyl)octanamide (thiol 1)

Thiol 1 was synthesized according to Chapter 3.

4.6.2 Synthesis of 7-mercaptoheptyl (2-(2-(2-methoxyethoxy)ethoxy)ethyl)carbamate (thiol 11)

Thiol **11** was prepared according to the following scheme:
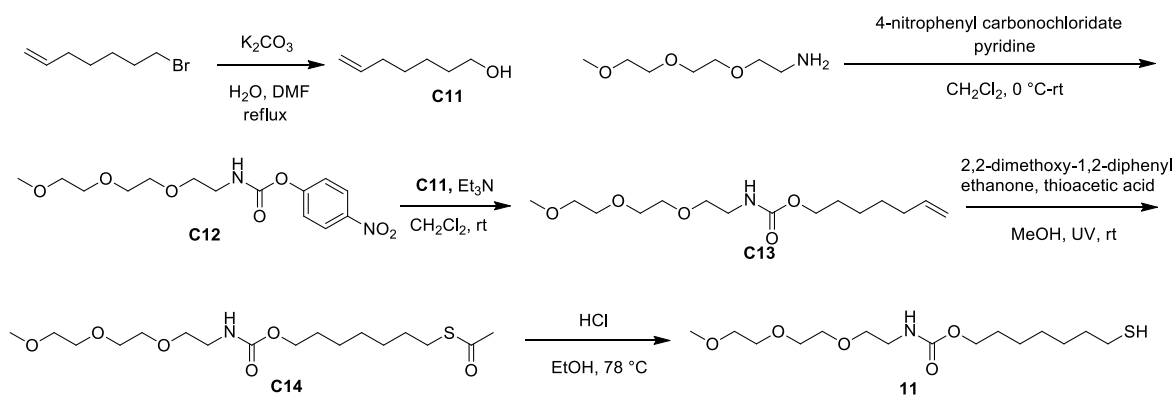
Scheme 4-1. Synthesis of the thiol **11.**

Synthesis of hept-6-en-1-ol (C11). 7-bromohept-1-ene (0.600 g, 3.39 mmol, 1.0 equiv) was dissolved in H_2O (4.0 mL) and DMF (8 mL), then potassium carbonate (1.03 g, 6.78 mmol, 2.2 equiv) were added to the solution. The mixture was stirred for 12 hours at 100 °C. Then the mixture was extracted with CH_2Cl_2 and washed with H_2O. After dried with sodium sulfate, the solution was concentrated and the crude product was purified by flash chromatography (silica gel, eluent: PE/ EtOAc 8:2). 0.142 g (37%) of hept-6-en-1-ol (**C11**) were obtained.

^{1}H-NMR (500 MHz, $CDCl_3$) δ 5.86-5.75 (m, 1H, CH), 5.08 – 4.90 (dd, 2H, CH_2), 3.58 – 3.68 (t, 2H, CH_2O), 2.12-2.03 (q, 2H, CH_2), 1.62 – 1.53 (m, 2H, CH_2), 1.49 – 1.33 (m, 4H, CH_2).

^{13}C-NMR (126 MHz, $CDCl_3$) δ 138.86 (1C, CH), 114.37 (1C, CH_2), 62.86 (1C, CH_2O), 33.71 (1C, CH_2), 32.57(1C, CH_2), 28.67 (1C, CH_2), 25.22 (1C, CH_2).

ESI-MS (m/z): 115.2 [M+H$^+$].

Synthesis of 4-nitrophenyl (2-(2-(2-methoxyethoxy)ethoxy)ethyl)carbamate (C12). 2-(2-(2-methoxyethoxy)ethoxy)ethanamine (0.250 g, 1.67 mmol, 1.0 equiv) was dissolved in anhydrous CH_2Cl_2 (10 mL), then 4-nitrophenyl carbonochloridate (2.22 g, 11.0 mmol, 1.5 equiv) pyridine (0.872 g, 11.0 mmol, 1.5 equiv) were added to the above solution at 0 °C. The mixture was stirred for 12 hours at room temperature. After solvent evaporation, the crude product was purified by flash chromatography (silica gel, eluent: PE/EtOAc 5:5). 1.04 g (43%) of (**C12**) were obtained.

^{1}H-NMR (500 MHz, $CDCl_3$) δ 8.27-8.18 (d, 2H, CH), 7.36-7.28 (d, 2H, CH), 3.71-3.62 (m, 8H, CH_2O), 3.59-3.55 (t, 2H, CH_2O), 3.50-3.43 (t, 2H, CH_2O), 3.38 (s, 3H, CH_3O).

^{13}C-NMR (126 MHz, $CDCl_3$) δ 156.09 (1C, C), 153.30 (1C, COO), 144.62 (1C, CN), 125.06 (2C, CH), 121.99 (2C, CH), 71.86 (1C, CH_2O), 70.49 (1C, CH_2O), 70.43 (1C, CH_2O), 70.18 (1C, CH_2O), 69.58 (1C, CH_2O), 58.99 (1C, CH_3O), 41.09 (1C, CH_2N).

ESI-MS (m/z): 329.1 [M+H$^+$], 351.1 [M+Na$^+$].

Synthesis of hept-6-en-1-yl (2-(2-(2-methoxyethoxy)ethoxy)ethyl)carbamate (C13). C11 (0.110 g, 0.963 mmol, 1.0 equiv) was dissolved in anhydrous CH2Cl2 (2 mL), then **C12** (0.380 g, 1.16 mmol, 1.2 equiv) and triethylamine (0.390 g, 3.85 mmol, 4.0 equiv) were added to the above solution at 0 °C. The mixture was stirred for 12 hours at room temperature. After solvent evaporation, the crude product was purified by flash chromatography (silica gel, eluent: DCM/ MeOH 10:0.2). 0.120 g (41%) of (**C13**) were obtained.

^{1}H-NMR (500 MHz, CDCl$_3$) δ 5.88-5.71 (m, 1H, CH), 5.04 – 4.90 (dd, 2H, CH$_2$), 4.10 – 4.00 (t, 2H, CH$_2$O), 3.69-3.62 (m, 6H, CH$_2$O), 3.59-3.53 (m, 4H, CH$_2$O), 3.39 (s, 3H, CH$_3$O), 3.39-3.34 (m, 2H, CH$_2$N), 2.09-2.03 (q, 2H, CH$_2$), 1.66-1.58 (qn, 2H, CH$_2$), 1.46-1.32 (m, 4H, CH$_2$).

^{13}C-NMR (126 MHz, CDCl$_3$) δ 156.84 (1C, CO), 138.76 (1C, CH$_2$), 114.42 (1C, CH$_2$), 71.91 (1C, CH$_2$O), 70.51 (1C, CH$_2$O), 70.21 (1C, CH$_2$O), 70.10 (1C, CH$_2$O), 64.85 (1C, CH$_2$O), 59.02 (1C, CH$_2$O), 40.73 (1C, CH$_3$O), 33.63 (1C, CH$_2$N), 30.92 (1C, CH$_2$), 28.91 (1C, CH$_2$), 28.53 (1C, CH$_2$), 25.36 (1C, CH$_2$).

ESI-MS (m/z): 304.3 [M+H$^+$], 326.3 [M+Na$^+$].

S-(12-oxo-2,5,8,13-tetraoxa-11-azaicosan-20-yl) ethanethioate (C14). **C13** (0.120 g, 0.396 mmol, 1.0 equiv) was dissolved in methanol (3 mL). Nitrogen was injected into the solution for 20 min to remove oxygen. Afterwards, 2, 2-Dimethoxy-2-phenylacetophenone (5.13 mg, 0.0200 mmol, 0.05 equiv) and ethanethioic S-acid (0.120 g, 1.58 mmol, 4.0 equiv) were added. The mixture was left under irradiation (UV, 365 nm) for 2 hours. After solvent evaporation, the crude product was purified by flash chromatography (silica gel, eluent: DCM/ MeOH 10:0.2). 0.0810 g (54%) of (**C14**) were obtained.

^{1}H-NMR (500 MHz, MeOD) δ 4.08-3.99 (t, 2H, CH$_2$O), 3.67 – 3.60 (m, 6H, CH$_2$O), 3.59 – 3.50 (m, 4H, CH$_2$O), 3.38(s,3H, CH$_3$O), 3.32-3.26 (t, 2H, CH$_2$S), 2.93-2.84 (t, 2H, CH$_2$N), 2.32 (s, 3H, CH$_3$O), 1.68-1.53 (m, 4H, CH$_2$), 1.46-1.31 (m, 6H, CH$_2$).

^{13}C-NMR (126 MHz, CDCl$_3$) δ 196.11 (1C, COS), 157.83 (1C, CON), 71.53 (1C, CH$_2$O), 70.15 (1C, CH$_2$O), 69.97 (1C, CH$_2$O), 69.84 (1C, CH$_2$O), 69.58(1C, CH$_2$O), 64.43 (1C, CH$_2$O), 57.70 (1C, CH$_3$O), 40.24 (1C, CH$_2$N), 29.28 (1C, CH$_3$O), 29.11 (1C, CH$_2$S), 28.72 (1C, CH$_2$), 28.41 (1C, CH$_2$), 28.40 (1C, CH$_2$), 28.28 (1C, CH$_2$), 25.42 (1C, CH$_2$).

ESI-MS (m/z): 380.3 [M+H$^+$], 402.2 [M+Na$^+$].

7-mercaptoheptyl (2-(2-(2-methoxyethoxy)ethoxy)ethyl)carbamate (11). **C14** (37.5 mg, 0.0988 mmol) was dissolved in ethanol (2.0 mL). A 6 M HCl solution in water (2.0 mL) was added and the mixture was stirred at 78 °C for 2 hours. The reaction mixture was allowed to cool and the solvent was evaporated to obtain 33.3 mg (quantitative) of **11**.

^{1}H-NMR (500 MHz, MeOD) δ 4.07-4.01 (t, 2H, CH$_2$O), 3.69 – 3.59 (m, 6H, CH$_2$O), 3.59 – 3.50 (m, 4H, CH$_2$O), 3.38 (s,3H, CH$_3$O), 3.32-3.25 (t, 2H, CH$_2$S), 2.56-2.46 (t, 2H, CH$_2$N), 1.68-1.55 (m, 4H, CH$_2$), 1.48-1.28 (m, 6H, CH$_2$).

^{13}C-NMR (126 MHz, CDCl$_3$) δ 157.78 (1C, CON), 71.53 (1C, CH$_2$O), 70.44 (1C, CH$_2$O), 69.96 (1C, CH$_2$O), 69.85 (1C, CH$_2$O), 69.60 (1C, CH$_2$O), 64.54 (1C, CH$_2$O), 57.76 (1C, CH$_3$O), 40.35 (1C, CH$_2$N), 33.71 (1C, CH$_2$S), 28.75 (1C, CH$_2$), 28.45 (1C, CH$_2$), 27.91 (1C, CH$_2$), 25.51 (1C, CH$_2$), 23.59 (1C, CH$_2$).

ESI-MS (m/z): 338.2 [M+H$^+$], 360.2 [M+Na$^+$].

4.6.3 Synthesis of 2-(2-(2-methoxyethoxy)ethoxy)ethyl (7-mercaptoheptyl)carbamate (thiol 12)

Thiol 12 was prepared according to the following procedure:
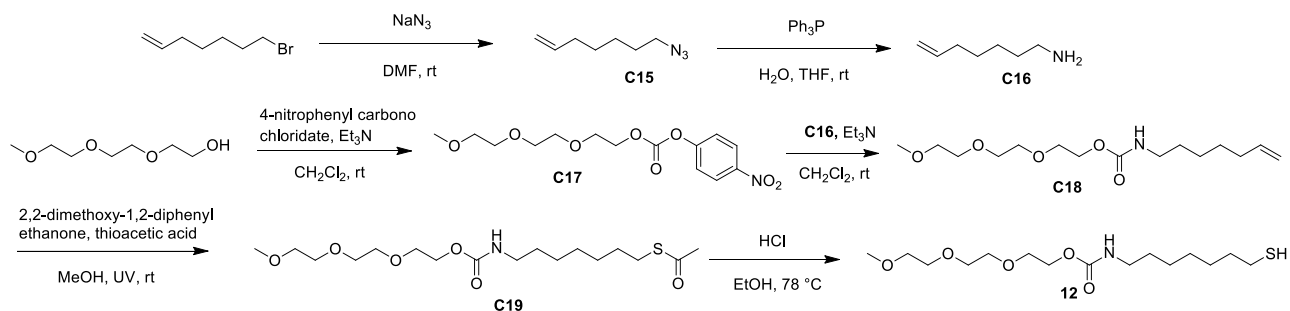
Scheme 2. Synthesis of thiol 12.

Synthesis of 7-azidohept-1-ene (C15). 7-bromohept-1-ene (0.516 g, 3.14 mmol) and sodium azide (0.220 g, 9.16 mmol) were dissolved in aqueous DMF (10 mL). After 10 hour stirring, the mixture was washed with H$_2$O and extracted with DCM. The combined organic layer was concentrated in vacuo and used in the next step without any purification.

Synthesis of hept-6-en-1-amine hydrochloride (C16). C15 (1.18 g, 8.47 mmol) was dissolved in H$_2$O (5 mL) and THF (13 mL). Triphenylphosphine (4.40 g, 33.9 mmol) was then added to the mixture. The solution was stirred for 12 hours at room temperature. After the completion of the reaction, the mixture was washed with DCM and extracted with HCl solution (1 M). the combined aqueous solution was evaporated to dryness in vacuo. 785 mg (82%) of **C16** were obtained as white solid.

^{1}**H-NMR** (500 MHz, D$_2$O) δ 5.89 – 5.73 (m, 1H, CH), 5.02–4.86 (dd, 2H, CH$_2$), 2.94-2.87 (t, 2H, CH$_2$N), 2.05–1.94 (q, 2H, CH$_2$), 1.63 – 1.50 (q, 2H, CH$_2$), 1.40–1.24 (m, 4H, CH$_2$).

^{13}**C-NMR** (126 MHz, D$_2$O) δ 139.67 (1C, CH), 114.32 (1C, CH$_2$), 39.42 (1C, CH$_2$N), 32.69 (1C, CH$_2$), 27.41 (1C, CH$_2$), 26.47 (1C, CH$_2$), 25.00 (1C, CH$_2$).

ESI-MS (m/z): 114.1 [M+H$^+$].

2-(2-(2-methoxyethoxy)ethoxy)ethyl (4-nitrophenyl) carbonate (C17). 2-(2-(2-methoxyethoxy)-ethoxy)ethanol (1.00 g, 6.09 mmol, 1.0 equiv) and 4-nitrophenyl carbonochloridate (1.84 g, 9.14 mmol, 1.5 equiv) were dissolved in anhydrous CH$_2$Cl$_2$ (5 mL), then triethylamine (0.924 g, 9.14 mmol, 1.5 equiv) were added to the above solution. The mixture was stirred for 12 hours at room temperature. After solvent evaporation, the crude product was purified by flash chromatography

(silica gel, eluent: PE/ EtOAc 4:6). 1.20 g (60%) of 2-(2-(2-methoxyethoxy)ethoxy)ethyl (4-nitrophenyl) carbonate (**C17**) were obtained.

^{1}H-NMR (500 MHz, CDCl$_3$) δ 8.38-8.22 (d, 2H, CH), 7.48 − 7.34 (dd, 2H, CH), 4.54 − 4.38 (t, 2H, CH$_2$O), 3.88-3.79 (t, 2H, CH$_2$O), 3.77 − 3.64 (m, 6H, CH$_2$O), 3.63 − 3.53 (s, 2H, CH$_2$O), 3.39 (s, 3H, CH$_3$O).

^{13}C-NMR (126 MHz, CDCl$_3$) δ 155.51 (1C, C), 152.46 (1C, COO), 145.36 (1C, CN), 125.28 (2C, CH), 121.78(2C, CH), 71.90 (1C, CH$_2$O), 70.69 (1C, CH$_2$O), 70.63 (1C, CH$_2$O), 70.58 (1C, CH$_2$O), 68.61 (1C, CH$_2$O), 68.30 (1C, CH$_2$O), 59.02 (1C, CH$_3$O).

ESI-MS (m/z): 330.2 [M+H$^+$], 352.2 [M+Na$^+$].

2-(2-(2-methoxyethoxy)ethoxy)ethyl hept-6-en-1-ylcarbamate (C18). C16 (250 mg, 1.67 mmol, 1.0 equiv) and **C17** (0.660 g, 2.00 mmol, 1.2 equiv) were dissolved in anhydrous CH$_2$Cl$_2$ (3 mL), then triethylamine (0.676 g, 6.68 mmol, 4.0 equiv) were added to the above solution. The mixture was stirred for 12 hours at room temperature. After solvent evaporation, the crude product was purified by flash chromatography (silica gel, eluent: toluene/ EtOAc 5:5). 331 mg (65%) of 2-(2-(2-methoxyethoxy)ethoxy)ethyl hept-6-en-1-ylcarbamate (**C18**) were obtained.

^{1}H-NMR (500 MHz, CDCl$_3$) δ 5.84-5.68 (m, 1H, CH), 5.03 − 4.88 (dd, 2H, CH$_2$), 4.26 − 4.14 (t, 2H, CH$_2$O), 3.72-3.58 (m, 8H, CH$_2$O), 3.58 − 3.48 (t, 2H, CH$_2$O), 3.36 (s, 3H, CH$_3$O), 3.22-3.09 (t, 2H, CH$_2$N), 2.10-1.98 (q, 2H, CH$_2$), 1.52-1.44 (qn, 2H, CH$_2$), 1.43-1.35 (qn, 2H, CH$_2$), 1.35-1.27 (qn, 2H, CH$_2$).

^{13}C-NMR (126 MHz, CDCl$_3$) δ 156.38 (1C, COO), 138.70 (1C, CH), 114.45 (1C, CH$_2$), 71.91 (1C, CH$_2$O), 70.52 (1C, CH$_2$O), 70.50 (1C, CH$_2$O), 69.64 (1C, CH$_2$O), 63.77 (1C, CH$_2$O), 59.00 (1C, CH$_3$O), 40.94 (1C, CH$_2$N), 33.59 (1C, CH$_2$), 29.77 (1C, CH$_2$), 28.47 (1C, CH$_2$), 26.16 (1C, CH$_2$).

ESI-MS (m/z): 304.2 [M+H$^+$], 326.2 [M+Na$^+$].

S-(12-oxo-2,5,8,11-tetraoxa-13-azaicosan-20-yl) ethanethioate (C19). C18 (250 mg, 0.824 mmol, 1.0 equiv) was dissolved in methanol (3 mL). Nitrogen was injected into the solution for 20 min to remove oxygen. Afterwards, 2, 2-Dimethoxy-2-phenylacetophenone (10.7 mg, 0.0412 mmol, 0.05 equiv) and thioacetic acid (251 mg, 3.30 mmol, 4.0 equiv) were added. The mixture was left under irradiation (UV, 365 nm) for 2 hours. After solvent evaporation, the crude product was purified by flash chromatography (silica gel, eluent: DCM/ MeOH 9.9:0.1). 200 mg (64%) of S-(12-oxo-2,5,8,11-tetraoxa-13-azaicosan-20-yl) ethanethioate (**C19**) were obtained.

¹H-NMR (500 MHz, MeOD) δ 4.20-4.13 (t, 2H, CH$_2$O), 3.71 – 3.67 (t, 2H, CH$_2$O), 3.67 – 3.62 (m, 6H, CH$_2$O), 3.58-3.54 (t, 2H, CH$_2$O), 3.38 (s, 3H, CH$_3$O), 3.13 – 3.07 (q, 2H, CH$_2$N), 2.91-2.85 (t, 2H, CH$_2$S), 2.32 (s, 3H, CH$_3$CO), 1.62-1.54 (qn, 2H, CH$_2$), 1.54-1.45 (qn, 2H, CH$_2$), 1.43-1.30 (m, 6H, CH$_2$).

¹³C-NMR (126 MHz, MeOD) δ 196.12 (1C, COS), 152.52 (1C, CON), 71.57 (1C, CH$_2$O), 70.15 (1C, CH$_2$O), 70.00 (1C, CH$_2$O), 69.21 (1C, CH$_2$O), 63.55 (1C, CH$_2$O), 57.71 (1C, CH$_3$O), 40.30 (1C, CH$_2$N), 29.42 (1C, CH$_3$), 29.30 (1C, CH$_2$S), 29.13 (1C, CH$_2$), 28.46 (1C, CH$_2$), 28.41 (1C, CH$_2$), 28.32 (1C, CH2), 26.26 (1C, CH$_2$).

ESI-MS (m/z): 380.3 [M+H$^+$], 402.2 [M+Na$^+$].

2-(2-(2-methoxyethoxy)ethoxy)ethyl (7-mercaptoheptyl)carbamate (12). C19 (37.5 mg, 0.0988 mmol) was dissolved in ethanol (2.0 mL). A 6 M HCl solution in water (2.0 mL) was added and the mixture was stirred at 78 °C for 2 hours. The reaction mixture was allowed to cool and the solvent was evaporated to obtain 33.3 mg (quantitative) of 2-(2-(2-methoxyethoxy)ethoxy)ethyl (7-mercaptoheptyl)carbamate (**12**).

¹H-NMR (500 MHz, MeOD) δ 4.20-4.14 (t, 2H, CH$_2$O), 3.71 – 3.67 (t, 2H, CH$_2$O), 3.67 – 3.62 (m, 6H, CH$_2$O), 3.58-3.54 (t, 2H, CH$_2$O), 3.38 (s, 3H, CH$_3$O), 3.13 – 3.07 (t, 2H, CH$_2$N), 2.54-2.48 (t, 2H, CH$_2$S), 1.66-1.57 (qn, 2H, CH$_2$), 1.54-1.47 (qn, 2H, CH$_2$), 1.47-1.39 (m, 2H, CH$_2$), 1.38-1.32 (m, 4H, CH$_2$).

¹³C-NMR (126 MHz, MeOD) δ 157.53 (1C, CON), 71.56 (1C, CH$_2$O), 70.16 (1C, CH$_2$O), 70.14 (1C, CH$_2$O), 69.97 (1C, CH$_2$O), 69.19 (1C, CH$_2$O), 63.62 (1C, CH$_2$O), 57.74 (1C, CH$_3$O), 40.41 (1C, CH$_2$N), 33.73 (1C, CH$_2$), 29.48 (1C, CH$_2$S), 28.47 (1C, CH$_2$), 27.93 (1C, CH$_2$), 26.33 (1C, CH$_2$), 23.58 (1C, CH$_2$).

ESI-MS (m/z): 338.2 [M+H$^+$], 360.2 [M+Na$^+$].

4.6.4 Synthesis of 1-(7-mercaptoheptyl)-3-(2-(2-(2-methoxyethoxy)ethoxy)ethyl)-urea (thiol 13)

Thiol 13 was prepared according to the following procedure:
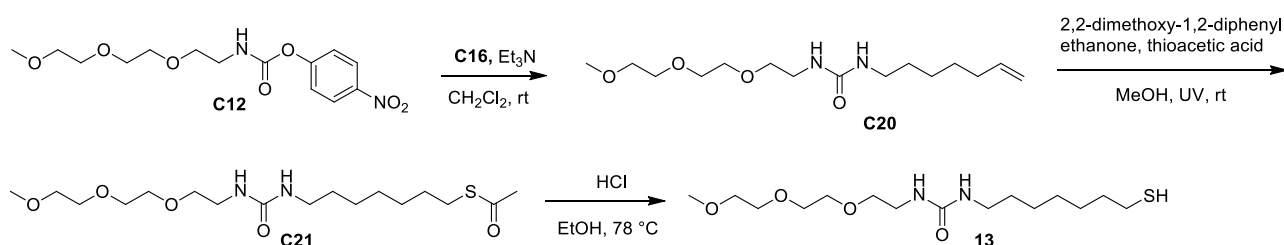
Scheme 3. Synthesis of thiol 13.

1-(hept-6-en-1-yl)-3-(2-(2-(2-methoxyethoxy)ethoxy)ethyl)urea (C20). C12 (500 mg, 1.52 mmol, 1.0 equiv) was dissolved in anhydrous CH$_2$Cl$_2$ (3 mL), then **C16** (274 mg, 1.83 mmol, 1.2 equiv) and

triethylamine (0.925 g, 9.14 mmol, 6.0 equiv) were added to the above solution. The mixture was stirred for 12 hours at room temperature. After solvent evaporation, the crude product was purified by flash chromatography (silica gel, eluent: DCM/ MeOH 9.5:0.5). 324 mg (70%) of (**C20**) were obtained.

^{1}H-NMR (500 MHz, MeOD) δ 3.68-3.60 (m, 6H, CH$_2$O), 3.59 – 3.55 (t, 2H, CH$_2$O), 3.55 – 3.51 (t, 2H, CH$_2$O), 3.38 (s, 3H, CH$_3$O), 3.33-3.28 (t, 2H, CH$_2$N), 3.15-3.09 (t, 2H, CH$_2$S), 2.91-2.85 (t, 2H, CH$_2$N), 2.31 (s, 3H, CH$_3$), 1.62-1.54 (m, 2H, CH$_2$), 1.52-1.45 (m, 2H, CH$_2$), 1.45-1.30 (m, 6H, CH$_2$).

^{13}C-NMR (126 MHz, MeOD) δ 196.09 (1C, COS), 159.80 (1C, CON), 71.56 (1C, CH$_2$O), 70.15 (1C, CH$_2$O), 69.93 (1C, CH$_2$O), 69.86 (1C, CH$_2$O), 57.69 (1C, CH$_2$O), 39.58 (1C, CH$_2$O), 29.85 (1C, CH$_3$O), 29.31 (1C, CH$_2$N), 29.14 (1C, CH$_2$N), 29.52 (1C, CH$_2$N), 28.42 (1C, CH$_2$N), 28.35 (1C, CH$_2$), 26.37 (1C, CH$_2$).

ESI-MS (m/z): 303.3 [M+H$^+$], 325.3 [M+Na$^+$].

S-(12-oxo-2,5,8-trioxa-11,13-diazaicosan-20-yl) ethanethioate (C21). C20 (300 mg, 0.992 mmol, 1.0 equiv) was dissolved in methanol (3 mL). Nitrogen was injected into the solution for 20 min to remove oxygen. Afterwards, 2, 2-Dimethoxy-2-phenylacetophenone (12.9 mg, 0.0496 mmol, 0.05 equiv) and thioacetic acid (302 mg, 3.97 mmol, 4.0 equiv) were added. The mixture was left under irradiation (UV, 365 nm) for 2 hours. After solvent evaporation, the crude product was purified by flash chromatography (silica gel, eluent: DCM/ MeOH 9.5:0.5). 221 mg (59%) of S-(12-oxo-2,5,8,11-tetraoxa-13-azaicosan-20-yl) ethanethioate (**C21**) were obtained.

^{1}H-NMR (500 MHz, MeOD) δ 3.67-3.61 (m, 6H, CH$_2$O), 3.58 – 3.55 (t, 2H, CH$_2$O), 3.55 – 3.51 (t, 2H, CH$_2$O), 3.38(s,3H, CH$_3$O), 3.32-3.28 (t, 2H, CH$_2$N), 3.15-3.09 (t, 2H, CH2N), 2.91-2.85 (t, 2H, CH$_2$), 2.32 (s, 3H, CH$_3$S), 1.62-1.53 (m, 2H, CH$_2$), 1.53-1.44 (m, 2H, CH$_2$), 1.44-1.31 (m, 6H, CH$_2$).

^{13}C-NMR (126 MHz, MeOD) δ 196.09 (1C, COS), 159.80 (1C, CON), 71.56 (1C, CH$_2$O), 70.15 (2C, CH$_2$O), 69.93 (1C, CH$_2$O), 69.86 (1C, CH$_2$O), 57.69 (1C, CH$_3$O), 39.58 (1C, CH$_2$N), 29.85 (1C, CH$_2$N), 29.31 (1C, CH$_3$S), 29.14 (1C, CH$_2$), 28.52 (1C, CH$_2$), 28.42 (1C, CH$_2$), 28.35 (1C, CH$_2$), 26.37 (1C, CH$_2$).

ESI-MS (m/z): 379.3 [M+H$^+$], 401.3 [M+Na$^+$].

1-(7-mercaptoheptyl)-3-(2-(2-(2-methoxyethoxy)ethoxy)ethyl)urea (13). **C21** (37.4 mg, 0.0988 mmol) was dissolved in ethanol (2.0 mL). A 6 M HCl solution in water (2.0 mL) was added and the mixture was stirred at 78 °C for 2 hours. The reaction mixture was allowed to cool and the solvent was evaporated to obtain 33.2 mg (quantitative) of **13**.

¹H-NMR (500 MHz, MeOD) δ 3.69-3.61 (m, 8H, CH₂O), 3.58 – 3.54 (t, 2H, CH₂O), 3.48 – 3.42 (t, 2H, CH₂N), 3.38(s,3H, CH₃O), 3.28-3.22 (t, 2H, CH₂N), 2.55-2.48(t, 2H, CH₂S), 1.67-1.54 (m, 4H, CH₂), 1.48-1.41 (m, 2H, CH₂), 1.41-1.34 (m, 4H, CH₂).

¹³C-NMR (126 MHz, MeOD) δ 159.47 (1C, CON), 71.54 (1C, CH₂O), 70.06 (1C, CH₂O), 70.00 (1C, CH₂O), 69.93 (1C, CH₂O), 69.23 (1C, CH₂O), 57.74 (1C, CH₃O), 41.04 (1C, CH₂N), 40.89 (1C, CH₂N), 33.68 (1C, CH₂S), 28.91 (1C, CH₂), 28.39 (1C, CH₂), 27.86 (1C, CH₂), 26.22 (1C, CH₂), 23.56 (1C, CH₂).

ESI-MS (m/z): 337.2 [M+H⁺], 359.2 [M+Na⁺].

4.6.5 Synthesis of 1-(4-(2-mercaptoethoxy)butyl)-3-(2-(2-(2-methoxyethoxy)ethoxy)-ethyl)urea (thiol 14)

Thiol 14 was prepared according to the following procedure:
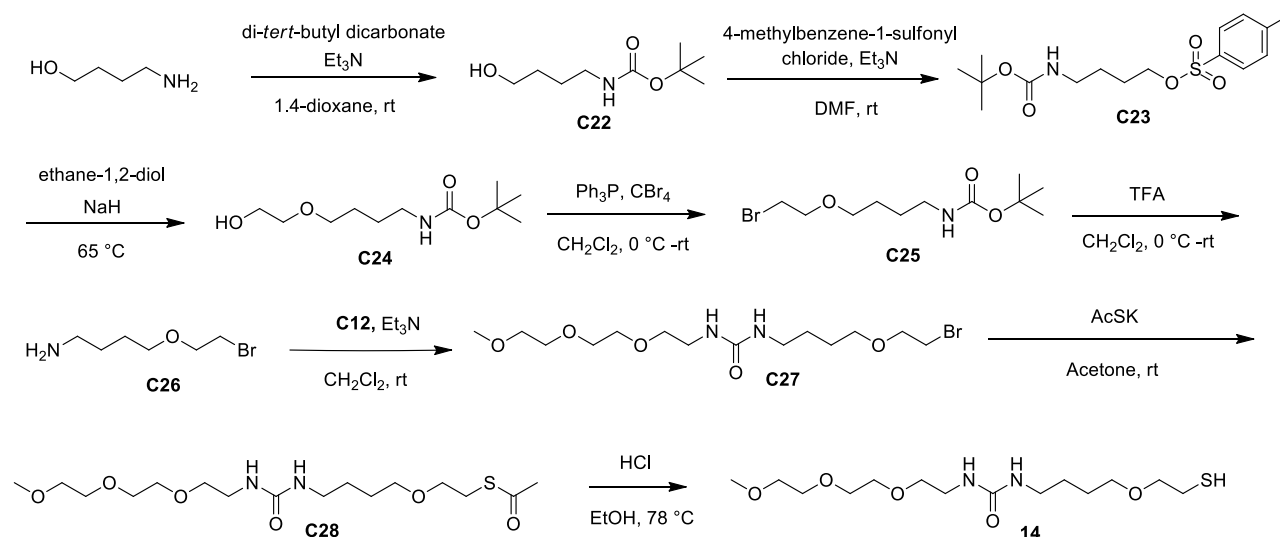
Scheme 4-4. Synthesis of thiol 14.

tert-butyl (4-hydroxybutyl)carbamate (C22). 4-aminobutan-1-ol (1.50 g, 16.8 mmol, 1.0 equiv) was dissolved in dioxane (2.0 mL), then di-tert-butyl dicarbonate (4.41 g, 20.2 mmol, 1.2 equiv) and trimethylamine (2.04 g, 20.2 mmol, 1.2 equiv) were added at 0 °C. The mixture was stirred at room temperature for 6 hours. After solvent evaporation, the crude product was further purified by flash chromatography (silica gel, eluent: PE/ EtOAc 3:7). 2.36 g (74%) of (**C22**) were obtained.

¹H-NMR (500 MHz, MeOD) δ 3.60-3.55 (t, 2H, CH₂O), 3.10-3.03 (t, 2H, CH₂N), 1.59-1.51 (m, 4H, CH₂), 1.45 (s, 9H, CH₃).

¹³C-NMR (126 MHz, MeOD) δ 157.14 (1C, COO), 78.41 (1C, C), 61.23 (1C, CH₂O), 39.79 (1C, CH₂N), 29.45 (1C, CH₂), 27.40 (3C, CH₃), 26.05 (1C, CH₂).

ESI-MS (m/z): 212.0 [M+Na⁺].

4-((tert-butoxycarbonyl)amino)butyl 4-methylbenzenesulfonate (C23). C22 (600 mg, 3.17 mmol, 1.0 equiv) was dissolved in CH_2Cl_2 (3.0 mL), then 4-methylbenzene-1-sulfonyl chloride (1.21 g, 6.34 mmol, 2.0 equiv) and trimethylamine (642 mg, 6.34 mmol, 2.0 equiv) were added. The mixture were stirred at room temperature for 10 hours. After solvent evaporation, the crude product was further purified by flash chromatography (silica gel, eluent: PE/ EtOAc 7:3). 820 mg (75%) of (**C23**) were obtained.

^{1}H-NMR (500 MHz, CDCl$_3$) δ 7.81-7.76 (d, 2H, CH), 7.39–7.32 (d, 2H, CH), 4.06 – 4.01 (t, 2H, CH$_2$O), 3.14-3.02 (t, 2H, CH$_2$N), 2.46 (s, 3H, CH$_3$), 1.73-1.62 (m, 2H, CH$_2$), 1.58-1.45 (m, 2H, CH$_2$), 1.43 (s, 9H, CH$_3$).

^{13}C-NMR (126 MHz, CDCl$_3$) δ 155.94 (1C, COO), 144.78 (1C, C), 133.02 (1C, C), 129.86 (1C, CH), 127.86 (1C, CH), 70.12 (1C, C), 60.39 (1C, CH$_2$O), 39.78 (1C, CH$_2$N), 28.38 (1C, CH$_3$), 26.19 (1C, CH$_2$), 21.64 (1C, CH$_2$).

ESI-MS (m/z): 366.1 [M+Na$^+$], 382.0 [M+K$^+$].

tert-butyl (4-(2-hydroxyethoxy)butyl)carbamate (C24). NaH (443 mg, 11.1 mmol, 4.0 equiv) was washed with petroleum ether for three times. Then ethane-1,2-diol (5.0 mL) was added. The mixture was stirred under N$_2$ for 30 mins. Subsequently, **C23** (950 mg, 2.77 mmol, 1.0 equiv) was added to the above solution. The mixture was stirred for 10 hours at 65 °C. After solvent evaporation, the crude product was further purified by flash chromatography (silica gel, eluent: PE/ EtOAc 3:7). 420 mg (65%) of (**C24**) were obtained.

^{1}H-NMR (500 MHz, CDCl$_3$) δ 3.76-3.72 (t, 2H, CH$_2$O), 3.56-3.52 (t, 2H, CH$_2$O), 3.52-3.48 (t, 2H, CH$_2$O), 3.18-3.11 (t, 2H, CH$_2$N), 1.67-1.54 (m, 4H, CH$_2$), 1.44 (s, 9H, CH$_3$).

^{13}C-NMR (126 MHz, CDCl$_3$) δ 156.10 (1C, COO), 79.22 (1C, C), 72.04 (1C, CH$_2$O), 70.87 (1C, CH$_2$O), 61.75 (1C, CH$_2$O), 40.46 (1C, CH$_2$N), 28.42 (3C, CH$_3$), 26.92 (2C, CH$_2$).

ESI-MS (m/z): 256.0 [M+Na$^+$].

tert-butyl (4-(2-bromoethoxy)butyl)carbamate (C25). **C24** (400 mg, 1.72 mmol, 1.0 equiv) was dissolved in CH_2Cl_2 (3.0 mL), then 4- tetrabromomethane (1.14 g, 3.43 mmol, 2.0 equiv) and triphenylphosphine (899 mg, 3.43 mmol, 2.0 equiv) were added at 0 °C. The mixture were stirred at room temperature for 12 hours. After solvent evaporation, the crude product was further purified by flash chromatography (silica gel, eluent: PE/ EtOAc 9:1). 220 mg (43%) of (**C25**) were obtained.

^{1}H-NMR (500 MHz, CDCl$_3$) δ 3.77-3.73 (t, 2H, CH$_2$O), 3.54–3.50 (t, 2H, CH$_2$Br), 3.49 – 3.45 (t, 2H, CH$_2$O), 3.19-3.11 (q, 2H, CH$_2$N), 1.67-1.54 (m, 4H, CH$_2$), 1.45 (s, 9H, CH$_3$).

^{13}**C-NMR** (126 MHz, CDCl$_3$) δ 155.99 (1C, COO), 79.03 (1C, C), 70.74 (1C, CH$_2$O), 70.64 (1C, CH$_2$O), 40.28 (1C, CH$_2$N), 30.49 (1C, CH$_2$Br), 28.43 (3C, CH$_3$), 26.88 (1C, CH$_2$), 26.80 (1C, CH$_2$).

ESI-MS (m/z): 318.0 [M+Na$^+$].

4-(2-bromoethoxy)butan-1-amine (C26). **C25** (220 mg, 0.743 mmol, 1.0 equiv) was dissolved in anhydrous CH$_2$Cl$_2$ (1.5 mL). Then trifluoride acetic acid (1.5 mL) was added slowly to the solution at 0 °C. The mixture was stirred for 3 hours at room temperature. After solvent evaporation, the obtained product (146 mg, quantitative) is pure enough to be used for the next step.

^{1}**H-NMR** (500 MHz, CDCl$_3$) δ 3.82-3.75 (t, 2H, CH$_2$O), 3.60–3.53 (t, 2H, CH$_2$Br), 3.52 − 3.46 (t, 2H, CH$_2$O), 3.09-2.99 (b, 2H, CH$_2$N), 1.87-1.78 (m, 2H, CH$_2$), 1.77-1.68 (m, 2H, CH$_2$).

^{13}**C-NMR** (126 MHz, CDCl$_3$) δ 70.79 (1C, CH$_2$O), 70.41 (1C, CH$_2$O), 39.86 (1C, CH$_2$N), 30.48 (1C, CH$_2$Br), 26.52 (1C, CH$_2$), 24.82 (1C, CH$_2$).

ESI-MS (m/z): 195.9 [M+H$^+$].

1-(4-(2-bromoethoxy)butyl)-3-(2-(2-(2-methoxyethoxy)ethoxy)ethyl)urea (C27). **C26** (146 mg, 0.740 mmol, 1.0 equiv) was dissolved in CH$_2$Cl$_2$ (3.0 mL), then **C12** (292 mg, 1.12 mmol, 1.2 equiv) and triethylamine (301 mg, 2.97 mmol, 4.0 equiv) were added. The mixture was stirred at room temperature for 10 hours. After solvent evaporation, the crude product was further purified by flash chromatography (silica gel, eluent: DCM/ MeOH 10:0.5). 230 mg (81%) of (**C27**) were obtained.

^{1}**H-NMR** (500 MHz, CDCl$_3$) δ 3.77-3.73 (t, 2H, CH$_2$O), 3.68–3.59 (m, 8H, CH$_2$O), 3.59 − 3.56 (t, 2H, CH$_2$O), 3.54-3.50 (t, 2H, CH$_2$O), 3.50-3.45 (t, 2H, CH$_2$O), 3.41 (s, 3H, CH$_3$), 3.40-3.37 (t, 2H, CH$_2$N), 3.24-3.19 (t, 2H, CH$_2$N), 1.68-1.54 (m, 4H, CH$_2$).

^{13}**C-NMR** (126 MHz, CDCl$_3$) δ 158.73 (1C, CO), 71.92 (1C, CH$_2$O), 70.81 (1C, CH$_2$O), 70.61 (1C, CH$_2$O), 70.32 (1C, CH$_2$O), 70.15 (1C, CH$_2$O), 70.00 (1C, CH$_2$O), 58.84 (1C, CH$_3$), 40.26 (1C, CH$_2$N), 40.02 (1C, CH$_2$N), 30.68 (1C, CH$_2$Br), 27.05 (1C, CH$_2$), 26.92 (1C, CH$_2$).

ESI-MS (m/z): 385.0 [M+H$^+$].

S-(12-oxo-2,5,8,18-tetraoxa-11,13-diazaicosan-20-yl) ethanethioate (C28). **C27** (230 mg, 0.597 mmol, 1.0 equiv) was dissolved in acetone (3.0 mL) and potassium thioacetate (136 mg, 1.19 mmol, 2.0 equiv) was added. The mixture was stirred for 10 hours at room temperature. After solvent evaporation, the crude product was purified by flash chromatography (silica gel, eluent: DCM/ MeOH 10:0.5). 201 mg (88%) of **C28** were obtained.

^{1}H-NMR (500 MHz, CDCl$_3$) δ 3.67-3.52 (m, 12H, CH$_2$O), 3.48–3.44 (t, 2H, CH$_2$O), 3.40 (s, 3H, CH$_3$O), 3.39-3.35 (t, 2H, CH$_2$N), 3.22-3.17 (t, 2H, CH$_2$N), 3.10-3.06 (t, 2H, CH$_2$S), 2.35 (s, 3H, CH$_3$), 1.64-1.50 (m, 4H, CH$_2$).

^{13}C-NMR (126 MHz, CDCl$_3$) δ 195.64 (1C, CO), 158.70 (1C, CO), 70.91 (1C, CH$_2$O), 70.68 (1C, CH$_2$O), 70.62 (1C, CH$_2$O), 70.33 (1C, CH$_2$O), 70.16 (1C, CH$_2$O), 69.99 (1C, CH$_2$O), 69.22 (1C, CH$_2$O), 58.84 (1C, CH$_3$O), 40.21 (1C, CH$_2$N), 40.00 (1C, CH$_2$N), 30.58 (1C, CH$_2$S), 28.99 (1C, CH$_3$), 27.06 (1C, CH$_2$), 26.91 (1C, CH$_2$).

ESI-MS (m/z): 381.2 [M+H$^+$].

1-(4-(2-mercaptoethoxy)butyl)-3-(2-(2-(2-methoxyethoxy)ethoxy)ethyl)urea (14). **C28** (37.6 mg, 0.0988 mmol) was dissolved in ethanol (2.0 mL). A 6 M HCl solution in water (2.0 mL) was added and the mixture was stirred at 78 °C for 2 hours. The reaction mixture was allowed to cool and the solvent was evaporated to obtain 33.4 mg (quantitative) of **14**.

^{1}H-NMR (500 MHz, MeOD) δ 3.68-3.58 (m, 10H, CH$_2$O), 3.58–3.56 (t, 2H, CH$_2$O), 3.54-3.49 (t, 2H, CH$_2$O), 3.46-3.41 (t, 2H, CH$_2$N), 3.38 (s, 3H, CH$_3$O), 3.30-3.25 (t, 2H, CH$_2$N), 2.70-2.64 (t, 2H, CH$_2$S), 1.70-1.60 (m, 4H, CH$_2$).

^{13}C-NMR (126 MHz, CDCl$_3$) δ 159.56 (1C, CO), 72.30 (1C, CH$_2$O), 71.52 (1C, CH$_2$O), 70.04 (1C, CH$_2$O), 69.98 (1C, CH$_2$O), 69.95 (1C, CH$_2$O), 69.91 (1C, CH$_2$O), 69.29 (1C, CH$_2$O), 57.77 (1C, CH$_3$O), 40.91 (1C, CH$_2$N), 40.61 (1C, CH$_2$N), 26.41 (1C, CH$_2$S), 26.00 (1C, CH$_2$), 23.41 (1C, CH$_2$).

ESI-MS (m/z): 339.2 [M+H$^+$], 361.2 [M+Na$^+$]

4.6.6 Synthesis and characterization of AuNPs (**1, 11, 12, 13** and **14-**AuNP)

Monolayer protected gold nanoparticles (**1, 11, 12, 13, 14**- AuNP) were prepared according to a previously reported two-step procedure.[18] A solution of HAuCl$_4$·3H$_2$O (50.0 mg, 0.127 mmol, 1.0 equiv) in water (2.0 mL) was extracted with a solution of tetraoctylammonium bromide (0.175 g, 0.318 mmol, 2.5 equiv) in N$_2$ purged toluene (125 mL). To the resulting reddish-orange organic solution dioctylamine (0.613 g, 2.54 mmol, 20.0 equiv) was added (the amount of dioctylamine was calculated in order to obtain 2 nm nanoparticles). The mixture is vigorously stirred under N$_2$ for 1.5 hours. During this period of time the color of the mixture fades. Then the solution is cooled at 0°C and a NaBH$_4$ solution (48.0 mg, 1.27 mmol, 10.0 equiv) in H$_2$O (1.0 mL) is then rapidly added. The color of the solution turns rapidly to black and after 1.5 hours of stirring at 0°C, the aqueous layer is removed. To the obtained nanoparticle solution, the desired thiol (0.254 mmol, 2.0 equiv) dissolved in 3 mL of ethyl acetate was rapidly added. The reaction mixture was stirred for 3 hours

at 0°C. Then the solvent was evaporated and the resulting crude was purified by centrifuging with water, ethyl acetate and methanol for 8 times.

Characterization of 1, 11, 12, 13, 14-AuNP. The characterization of **1**-AuNP was reported in the previous literature. TEM analysis (Figures 4-10, 4-11, 4-12, 4-13) of the different samples of nanoparticles yields an average diameter for 11-AuNP of 1.5 ± 0.2 nm, for 12-AuNPof 1.6 ± 0.2 nm, for 13-AuNP and 14-AuNP of 1.6 ± 0.2 nm and 1.5± 0.2 nm. This data, together with the loss of organic weight obtained by TGA analysis (Figures 4-14, 4-15, 4-16, 4-17), indicate that the formula for AuNP is $Au_{104}SR_{54}$ for AuNP-11, $Au_{127}SR_{65}$ for AuNP-12, $Au_{127}SR_{58}$ for AuNP-13, $Au_{111}SR_{50}$ for AuNP-14. NMR analysis (Figure 4-18, 4-19, 4-20, 4-21) indicates monolayer formation (broadening of all signals and missing of the SCH_2CH_2 protons' signals). UV-vis spectra (Figure 4-22, 4-23, 4-24, 4-25) recorded also showed no or small plasmonic band at 520 nm, which suggests the size of the AuNPs is smaller than 3 nm.
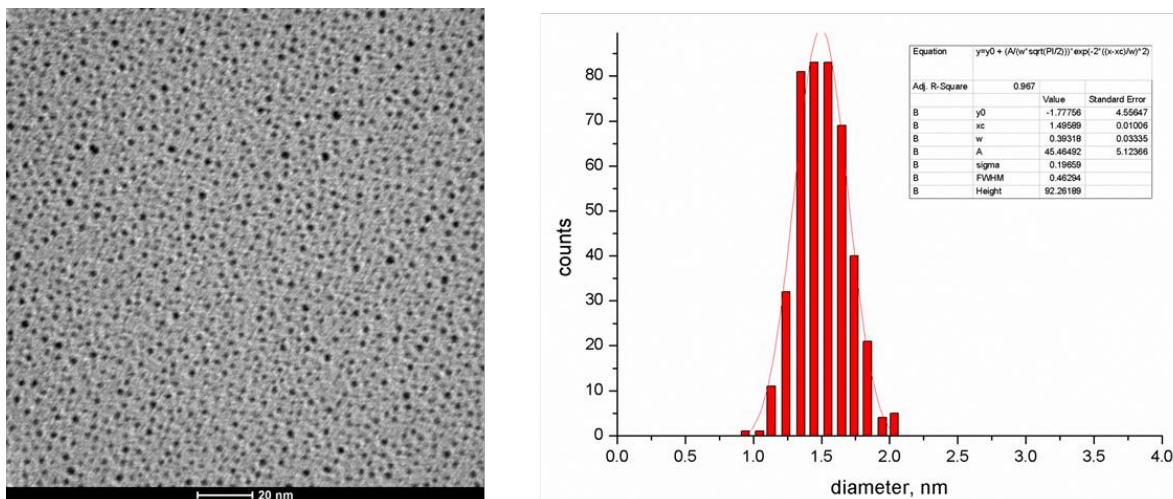
Figure 4-10: TEM image of **11**-AuNP and size distribution: average diameter = 1.5 ±0.2 nm.
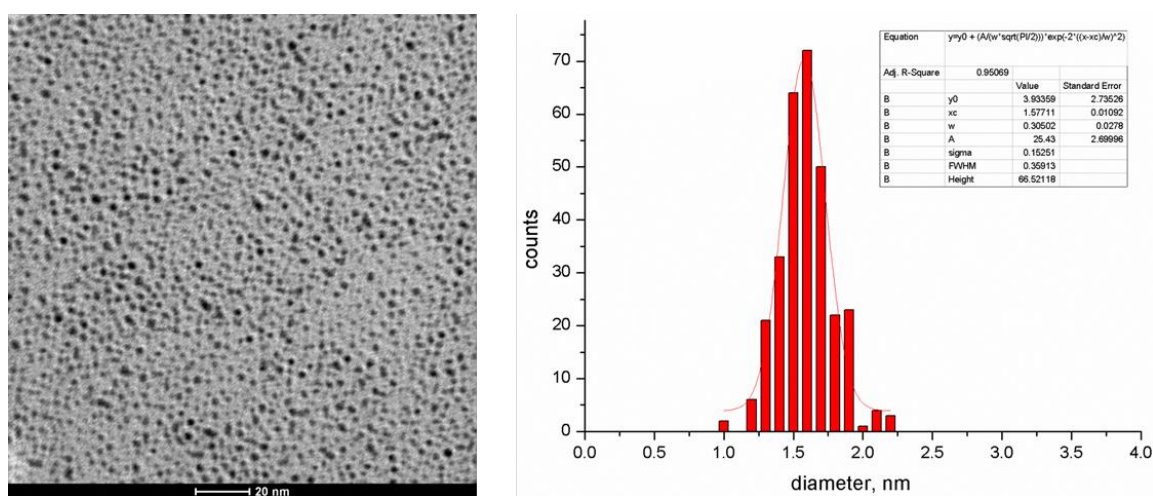
Figure 4-11: TEM image of **12**-AuNP and size distribution: average diameter = 1.6 ±0.2 nm.
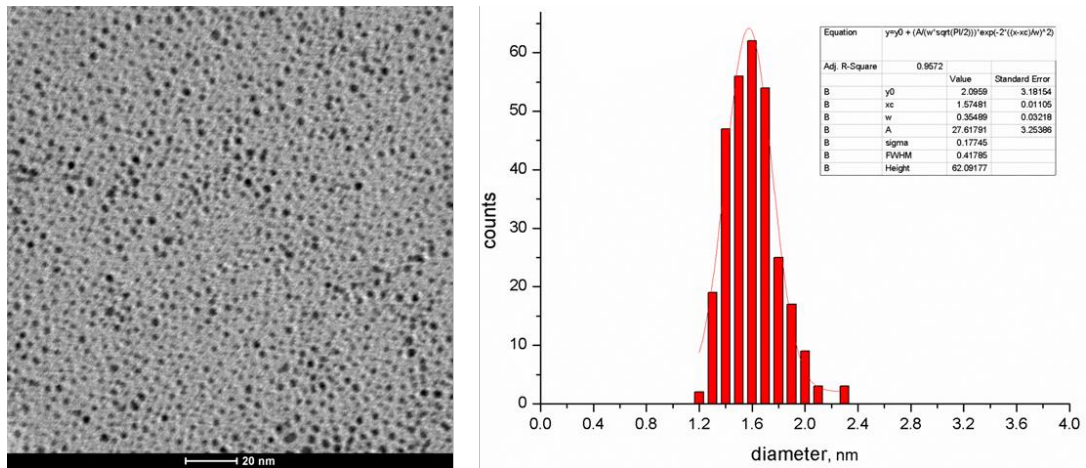
Figure 4-12: TEM image of **13**-AuNP and size distribution: average diameter = 1.6 ±0.2 nm.
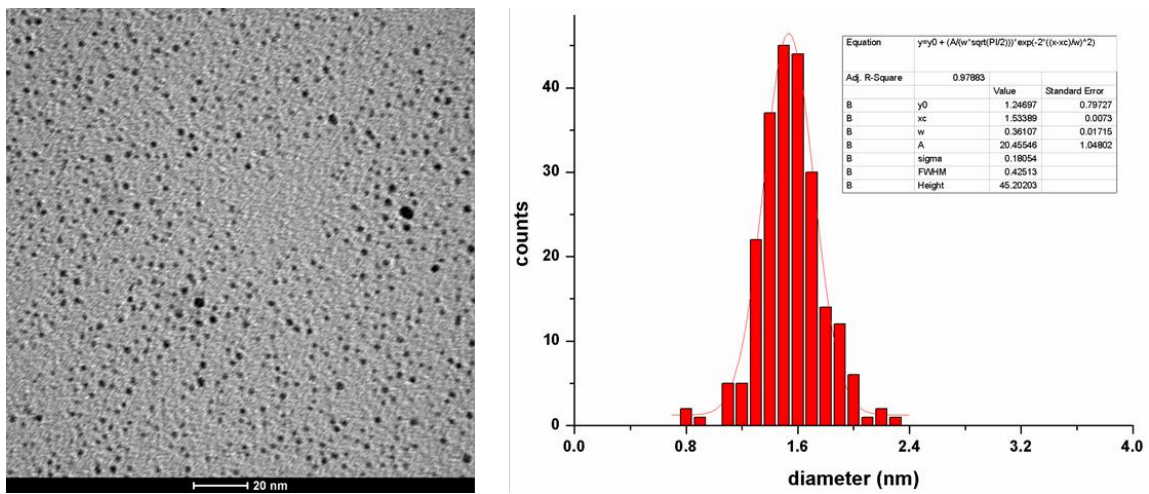
Figure 4-13: TEM image of **14**-AuNP and size distribution: average diameter = 1.5 ±0.2 nm.
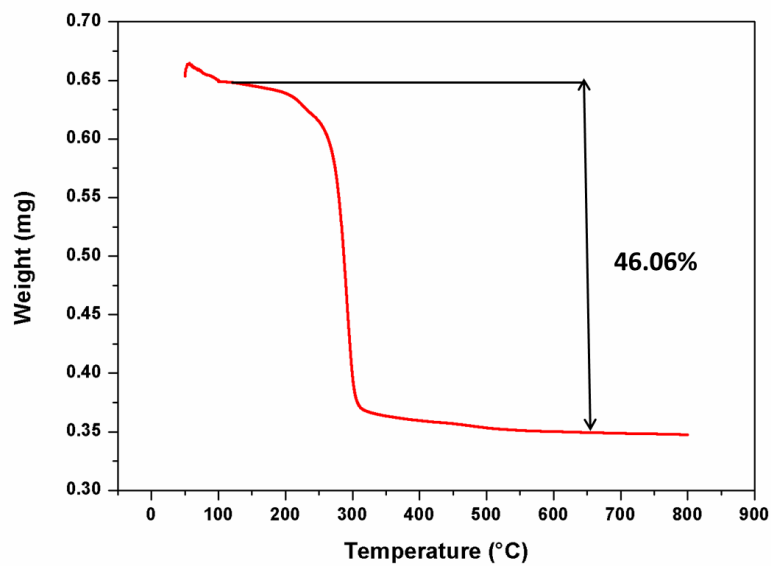
Figure 4-14: TGA analysis of **11**-AuNP under air atmosphere.
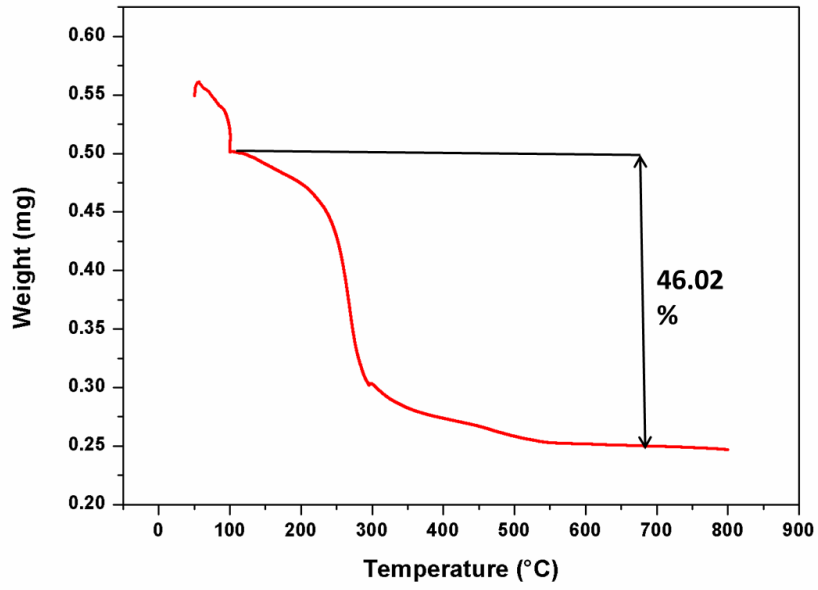
Figure 4-15: TGA analysis of **12**-AuNP under air atmosphere.
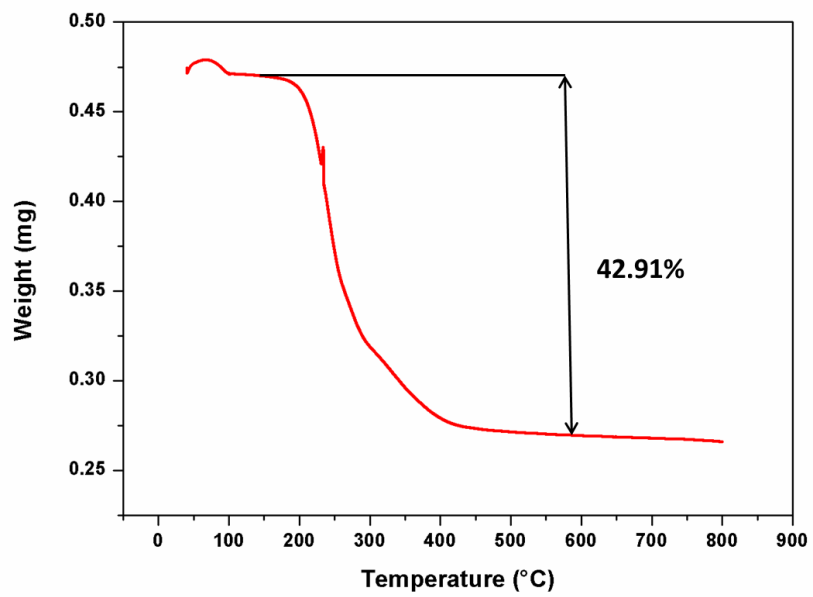
Figure 4-16: TGA analysis of **13**-AuNP under air atmosphere.
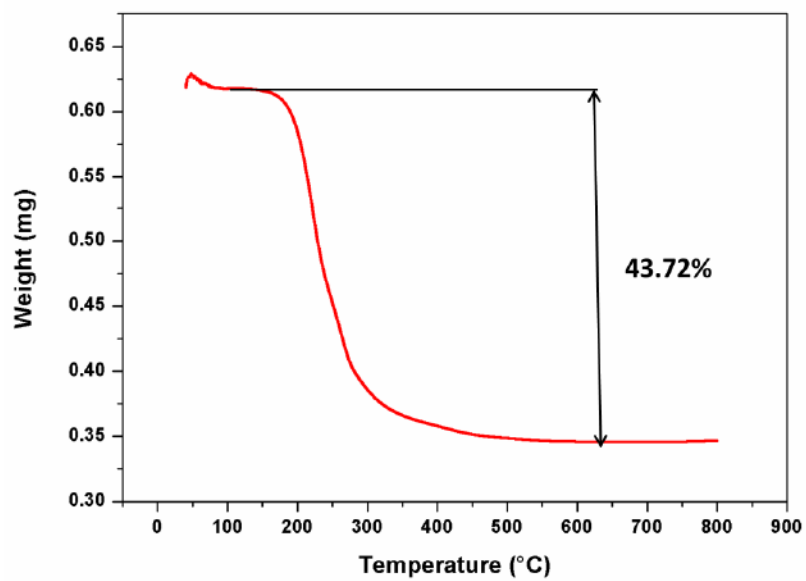
Figure 4-17: TGA analysis of **14**-AuNP under air atmosphere.
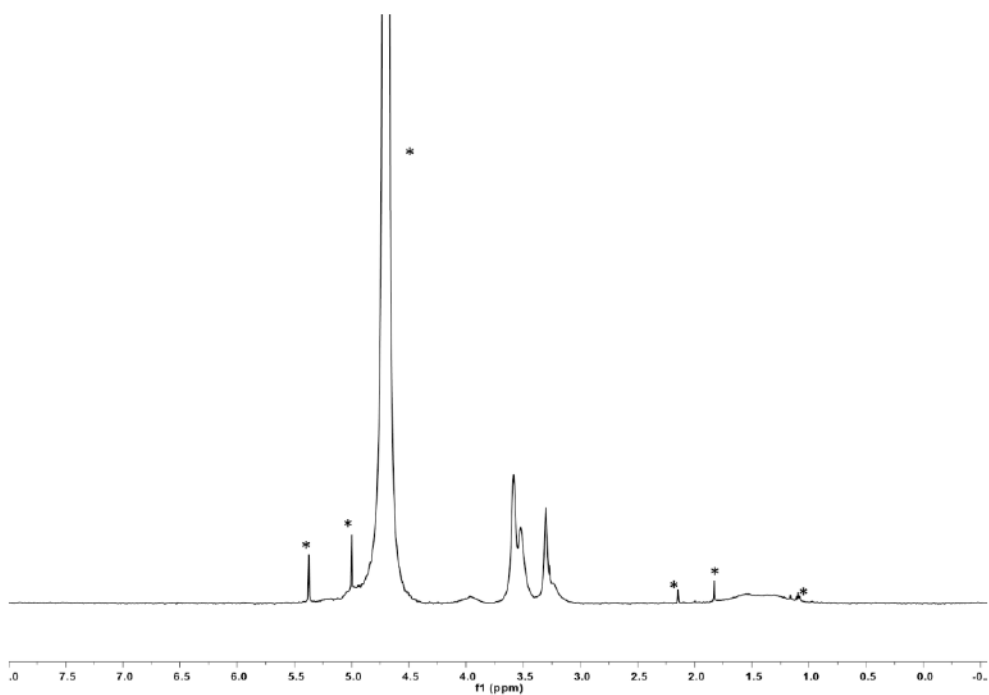
Figure 4-18: ^{1}HNMR spectrum of **11**-AuNP in D_2O (* indicates the residual solvents and impurities).
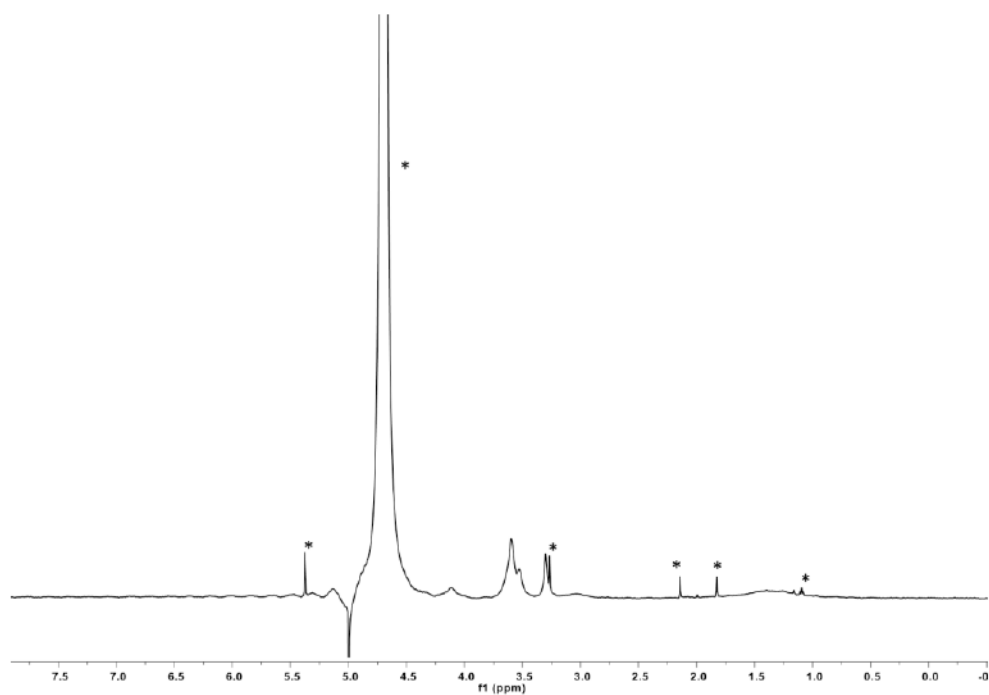
Figure 4-19: ^{1}HNMR spectrum of **12**-AuNP in D_2O (* indicates the residual solvents and impurities).
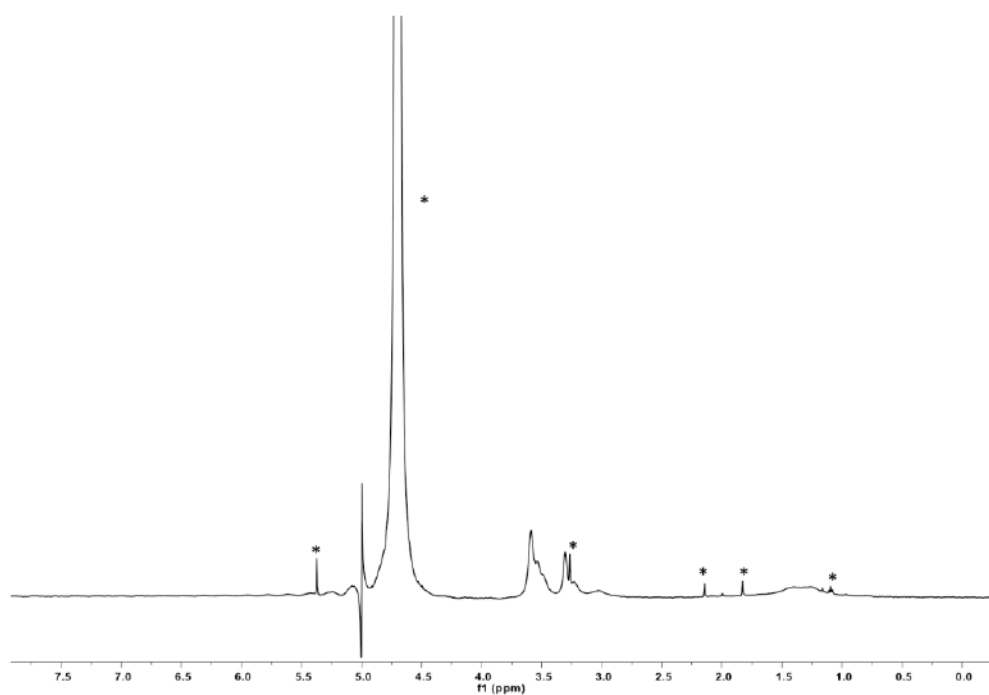
Figure 4-20: ^{1}HNMR spectrum of **13**-AuNP in D_2O (* indicates the residual solvents and impurities).
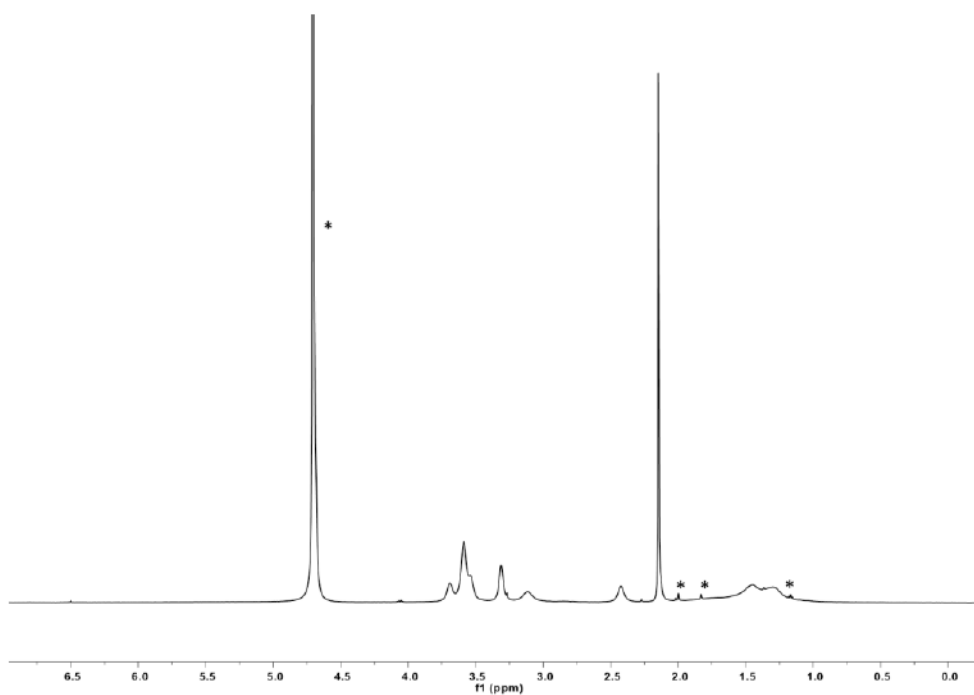
Figure 4-21: ^{1}HNMR spectrum of **14**-AuNP in D_2O (* indicates the residual solvents and impurities).
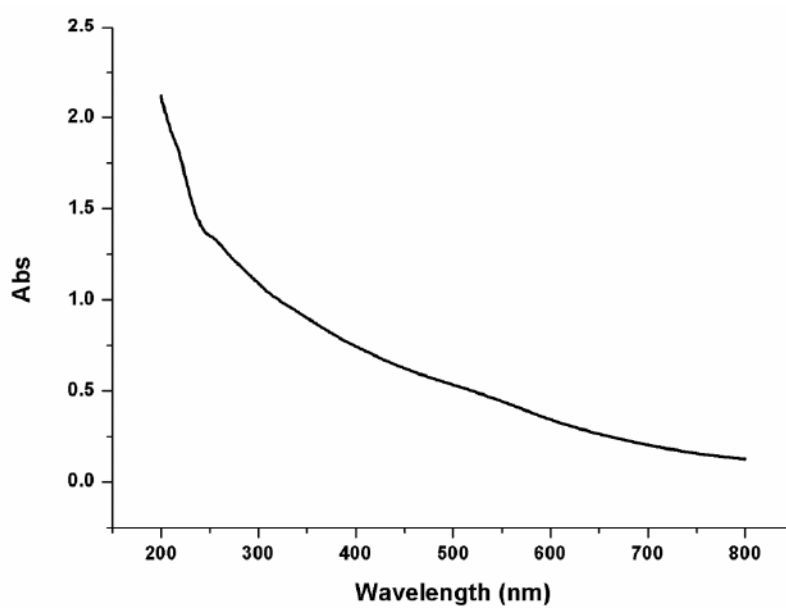
Figure 4-22: UV-Vis spectrum of **11**-AuNP (0.1 mg/mL) at 25°C in water.
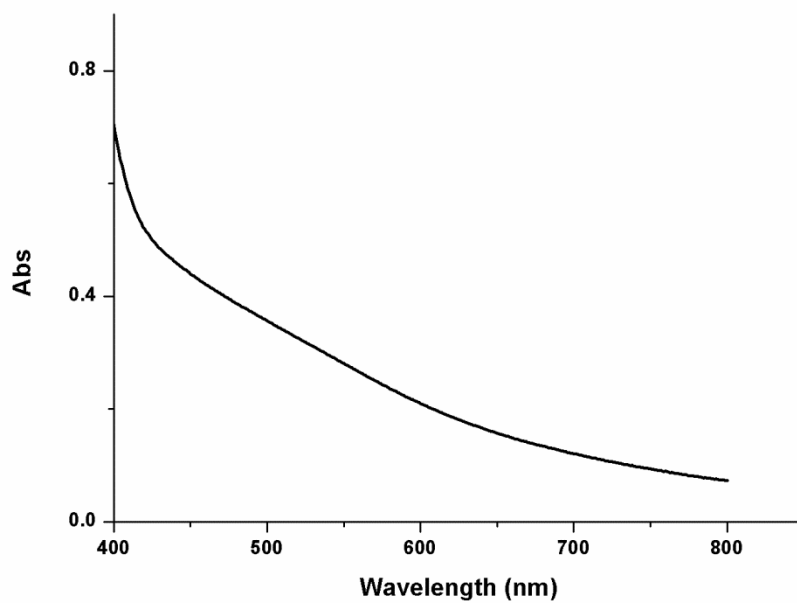
Figure 4-23: UV-Vis spectrum of **12**-AuNP (0.1 mg/mL) at 25°C in water.
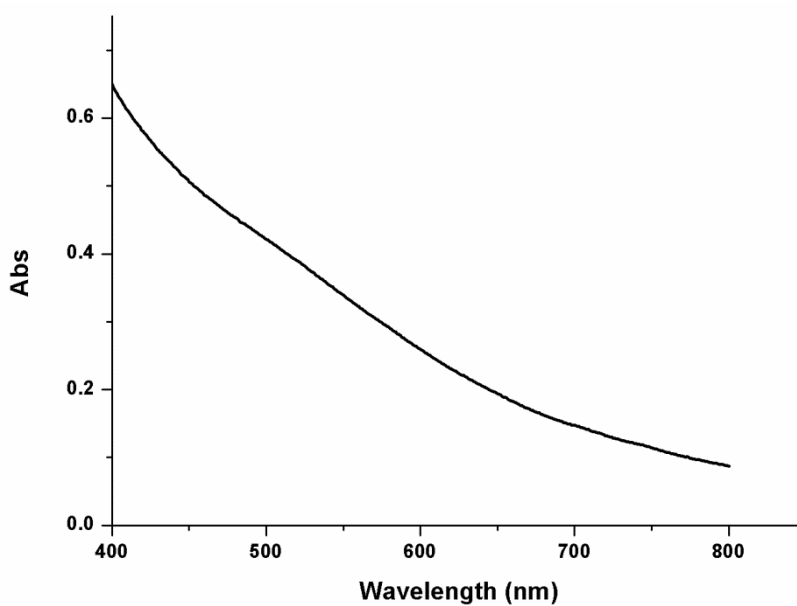
Figure 4-24: UV-Vis spectrum of **13**-AuNP (0.1 mg/mL) at 25°C in water.
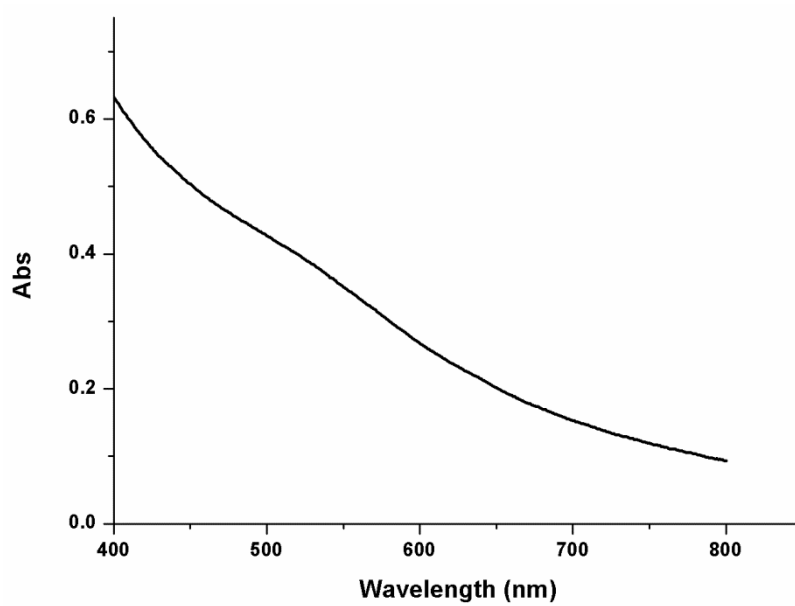
Figure 4-25: UV-Vis spectrum of **14**-AuNP (0.1 mg/mL) at 25°C in water.

Chapter 5. Sensor arrays made by self-organized nanoreceptors for detection and discrimination of carboxylate drugs

5.1 Introduction

Having individuated the urea group as the best potential recognition moiety for the recognition of salicylate in water, the logical follow-up was the realization of nanoparticles bearing thiourea and gunidinium groups, since they are known to be the better H-bond donors for carboxylate recognition. In these perspective, thiols **15**, **18** (Figure 5-1), and corresponding nanoparticles **15**- and **18**-AuNPs were prepared following standard procedures. The nanoparticles resulted to be well soluble and well disperse in water. However, when used in the NOE-pumping experiments, they both proved to be less effective than **13**-AuNP in salicylate NOE pumping detection. Subsequent investigations revealed that the reason of this result is exactly the higher affinity these nanoreceptors have for salicylate. As discussed in Chapter 1, strong binding resulted into a poor fraction of free ligand and a high probability of small turnover, which eventually produce weak signals in the NOE-pumping spectra.
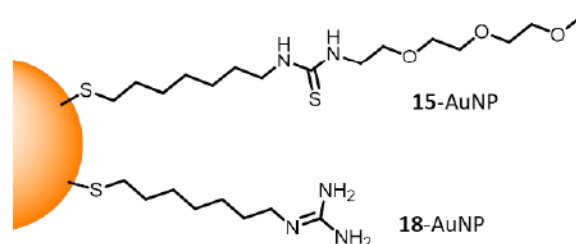
Figure 5-1. The structure of the thiol **15** and thiol **18**.

When considering these results, we reasoned that high affinity nanoreceptors, while not suitable for NMR chemosensing applications, might still find application in sensing by the use of different protocols.

Several examples[58-60] have already demonstrated that AuNPs are excellent candidates to create sensor arrays able to recognize a number of analytes with high classification accuracy. However, most of the AuNPs-based sensor arrays reported were focused on the detection of biological macromolecules or poly-charged species. In these systems, a strong polyionic interaction dominates the target recognition and affinity modulation is obtained by small modifications of the charged headgroups. In this chapter, we show that nanoparticle arrays built using the nanoreceptors optimized in this thesis can be applied also to detection of singly charged small molecules, and that a larger chemical space can be explored to achieve fine tuning and modulation of the interactions at play within the nanoparticle-coating monolayer.

5.2 AuNPs design

In this chapter, we focus our attention on four carboxylate derivatives which are currently used as nonsteroidal anti-inflammatory drugs (NSAIDs), namely sodium diclofenac, naproxen, sodium salicylate and ketoprofen (Figure 5-2c).[116] Even if having quite different chemical structures, most of NSAIDs share an amphiphilic nature due to the presence of the anionic carboxylate headgroup and a hydrophobic moiety featuring one or more phenyl rings. This feature likely reflects the structure of the active pocket of the cyclooxygenase enzymes that are inhibited NSAIDs. Due to their relevance, several detection methods, with excellent limits of detection, have been developed for the detection of NSAIDs and in particular of diclofenac. However, most of such methods rely on chromatography,[117-119] requiring quite intensive sample preparation and time-consuming operations, or on antibody-based immunoassays.[120-122] The need for time and cost-effective detection methods, which can be easily adapted to different NSAIDs, induced the development of array-based differential sensing systems based on series of ligand-fluorophore conjugates.[116] This array showed an excellent performance in NSAIDs detection included the possibility to work in biological media as human urine. Still, the realization of arrays based on complex chemosensors is synthetically demanding.
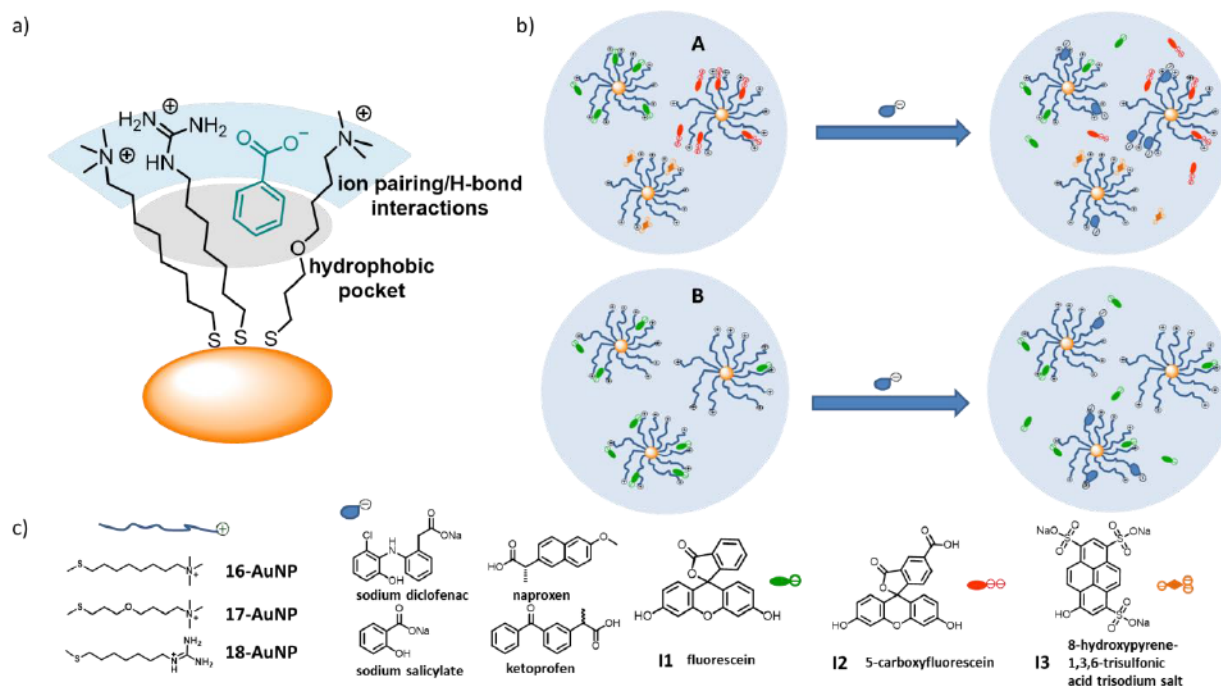
Figure 5-2. a) Organic anion recognition by nanoparticle coating monolayers; b) Schematic representation of the construction of the indicator based sensor array A and B. c) the molecular structure of nanoparticle-coating thiols, analytes and indicators used in this study.

Taking this into consideration, we decided to explore the use of non-covalent AuNP-dye conjugates to realize a sensor array for NSAID. We selected three cationic AuNPs (Figure 5-2a,c) capable of recognizing NSAIDs by multipoint interactions. The rationale behind the choice of cationic thiols **16-18** was to expand the range of interactions that the nanoparticle coating monolayer can establish with the target molecules (Figure 5-2a). Thiol **16** can be considered as the "standard" cationic thiol used for organic anions recognition, with the trimethylammonium headgroup providing ion pairing interaction and the alkyl moiety creating an hydrophobic pseudo-phase within the monolayer. Thiols **17** and **18** were designed on the basis of the results obtained in the previous chapter. Thiol **17** was prepared in the attempt to reduce the hydrophobicity of the inner region of the monolayer, as found in the case of thiol **14**, by the insertion of a polar ether oxygen in the alkyl chain. Thiol **18**, featuring a guanidinium headgroup, was selected as it likely provides additional hydrogen bonding to the ion pairing interaction, as in the case of thiol **13**.

AuNPs **16-18** were first tested for their ability to interact with anionic carboxylates via NMR spectroscopy. As mentioned at the begninnig of the chapter, relevant broadening of the NMR signals of sodium diclofenac, naproxen, sodium salicylate and ketoprofen was observed in the presence of the AuNPs (Figure 5-3). Such a behavior is likely the result of a strong interaction of the analytes with the monolayer, which results in an increase of their correlation time and a decrease of the conformational mobility. DOSY experiments (Figure 5-4) revealed that the apparent diffusion coefficients of the organic anions in the samples are identical to that of the AuNPs confirming the strong binding of the analyte to the AuNPs.[43, 47, 123]
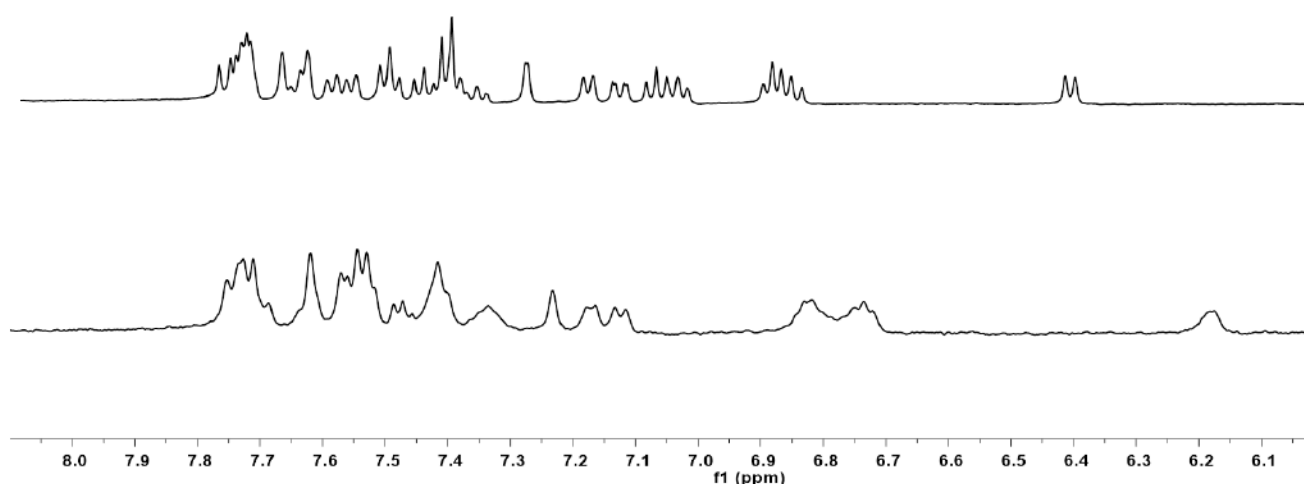
Figure 5-3. ^{1}H NMR spectrum of a mixture of sodium diclofenac, naproxen, sodium salicylate and ketoprofen in D_2O (250 μM each). Upper): in the presence of HEPES buffer (10 mM). Lower): in the presence of **16**-AuNP (2 mM in thiol) and HEPES buffer (10 mM).
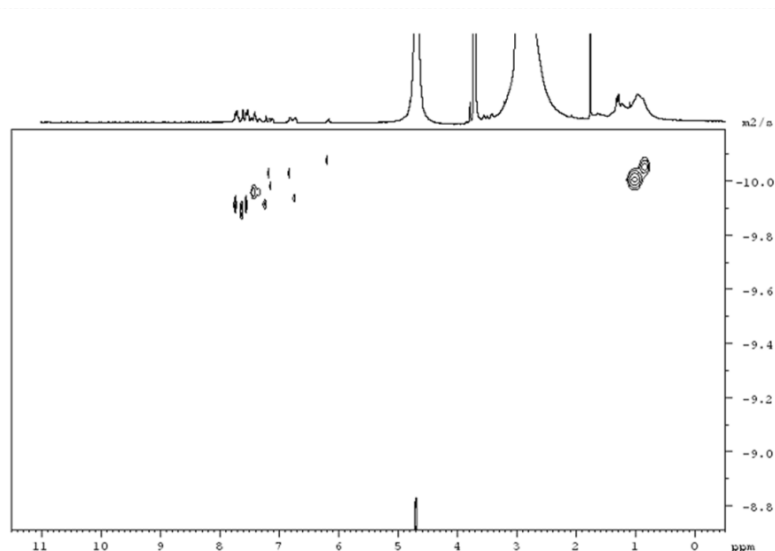
Figure 5-4. The DOSY spectrum of **16**-AuNP in the presence of sodium diclofenac, naproxen, sodium salicylate and ketoprofen. Experimental conditions: Solvent, D_2O. **16**-AuNP, 2 mM in thiols. Analytes, 250 µM each.

5.3 Set up of IDA-based sensor array A

Comforted by these results, which indeed confirmed that AuNPs **16**-**18** are good receptors for organic monoanions, we set-up an indicator displacement assay (IDA) to monitor the different response of AuNPs to various analytes (Figure 5-2b). As mentioned, in this strategy the sensing performance of the system is based on the displacement of the fluorescent indicator from the AuNPs-indicator complex. The AuNPs prepared are expected to feature different electrostatic, hydrophobic and hydrogen bonding functionalities, which tune the AuNPs-indicator and AuNPs-analytes interaction. Among them, ion pairing is expected to be the most relevant interaction controlling the affinity of organic ions to polyionic nanoparticles.[47] In order to generate specific response patterns, we selected three fluorescent indicators on the basis of two specific criteria: 1) ability to bind with the AuNPs at low micromolar concentration in aqueous solution, 2) different binding affinity (modulated by the number and the nature of negatively charged groups). We hence selected fluorescein (**I1**, charge -1 at pH 7.0), 5-carboxyfluorescein (**I2**, charge -2 at pH 7.0) and 8-hydroxypyrene-1,3,6-trisulfonic acid trisodium salt (**I3**, charge -3 at pH 7.0). Affinity of the probes for AuNP **16**-**18** was investigated by fluorescence titrations ([thiols] = 100 µM, [HEPES buffer, pH 7.0] = 10 mM). The fluorescence titrations were performed by adding consecutive amount of indicator to a solution of the AuNPs (100 µM in thiols) in buffered H_2O (HEPES 10 mM, pH=7.0). The fluorescence spectra were recorded for several times to make sure the system has reached to equilibrium. The maximum fluorescence intensity were then collected and plotted

against the concentration of the fluorescent indicators added. The titrations were fitted according to 1:1 (thiol: analyte) binding model using DynaFit for Windows.
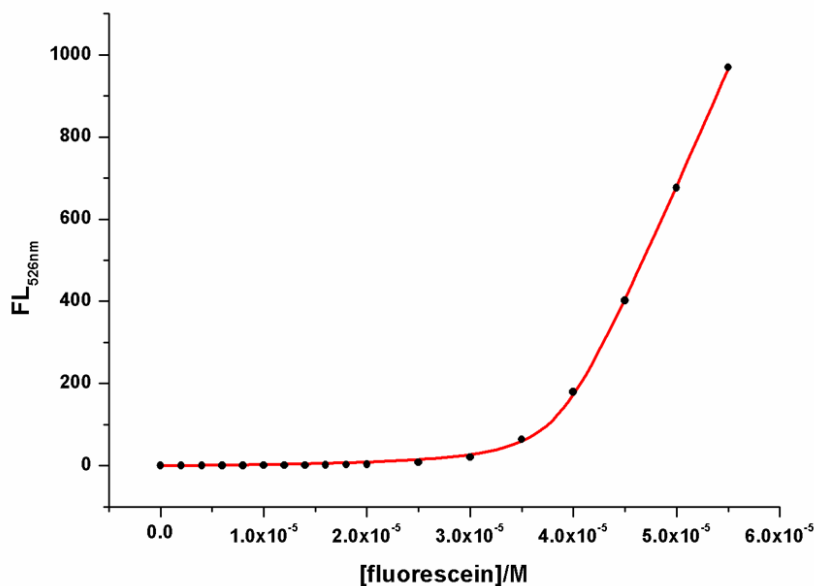
Figure 5-5. The fluorescence emission of the solution of **16**-AuNP as a function of the concentration of added fluorescein (black sphere). The fitting curve obtained from Dynafit (red line). Experimental conditions: AuNP-1, 100 μM in thiol. HEPES, pH=7, 10 mM.

The values of binding constants and the concentration of binding sites between the indicators and AuNPs, obtained by fitting the titration data, are reported in Table 5-1. Inspection of the data reveals that a large diversity of binding affinities and stoichiometries was observed, as expected, when different indicators were employed. In general, larger affinities are obtained for dyes featuring a larger charge, as **I2** and **I3**, and for **18**-AuNP featuring the guanidinium headgroup. Such observation confirms once again the ion pairing interaction as the most relevant and indicates that hydrogen bonding can effectively complement it. On the other hand, the presence of the oxygen atom in the inner chain of the thiol coating **17**-AuNP does not reduce the affinity for the three dyes with respect to **16**-AuNP. However, peculiar combinations of specific interactions are different of each nanoparticle/dye pair yielding relevant deviations from these general trends. Saturation concentrations reported, which depend on the number of binding sites per particles (i.e. the maximum number of indicators that bind to a single nanoparticles), are also quite variable depending on the indicator/nanoparticle pair investigated.

AuNPs	Binding constant			Binding sites		
	I1	I2	I3	I1	I2	I3
16-AuNP	6.85E+06	3.28E+07	1.04E+07	38.88	49.99	29.80
17-AuNP	6.06E+06	4.17E+07	5.26E+07	18.81	27.79	13.66
18-AuNP	2.27E+08	2.42E+07	5.56E+07	28.43	45.11	47.70

Table 5-1. Binding constants and binding sites between AuNPs and indicators. Experimental conditions: AuNPs (100 µM in thiol), HEPES buffer (10 mM, pH=7.0).
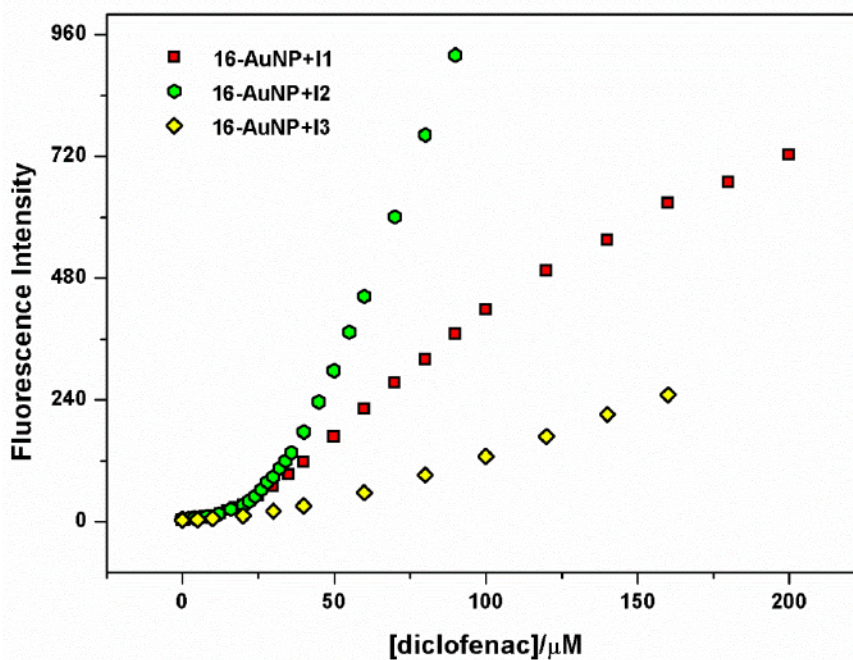
Figure 5-6. Fluorescence emission intensity of I1, I2 and I3 as a function of the concentration of diclofenac in the presence of **16**-AuNP (H_2O, HEPES buffer 10 mM, pH 7.0, 25 °C).

Having characterized the affinity of the nanoparticles for the indicators, we investigated the ability of diclofenac and salicylate to displace them from the nanoparticles. The fluorescent indicators, at a sub-saturation concentration, and AuNPs (100 µM) were mixed in buffered H_2O (HEPES, 10 mM, pH=7.0) before adding different concentration of analytes. The concentration of I1, I2 and I3 were 32 µM, 20 µM and 40 µM, respectively, when associated with **16-AuNP**. The concentration of I1, I2 and I3 were 16 µM, 12 µM and 20 µM, respectively, when associated with **17-AuNP**. The concentration of I1, I2 and I3 were 24 µM, 40 µM and 36 µM, respectively, when associated with **18-AuNP**. In these conditions, stable but extremely weak fluorescence, less than 5% of the respective maximum fluorescence intensity observed with the free indicators, was detected for each of the sensing platforms. This efficient quenching of the fluorescence confirmed that the indicators were strongly associated with the surface of the AuNPs. Furthermore, such a low background emission was expected to improve the performance of the sensing system with respect to sensitivity. The displacement experiments, performed by adding increasing amounts of

drugs (Figure 5-6), revealed that the indicators are effectively released from the nanoparticles when the analyte concentration is above a threshold value. Different responses of the different sensing platforms were obtained upon addition of diclofenac and salicylate. Apparently, diclofenac has a stronger binding affinity since it produces a steady increase of fluorescence emission with a relatively low threshold concentration (Figure 5-6). In the case of salicylate, the displacement is much less effective and only a weak emission increase is observed in the same concentration interval. Such a result is in agreement with expectations. Being the ion pairing similar with the two substrates, hydrophobic interaction is likely the second most relevant interaction between AuNPs and the analytes, and diclofenac is undoubtedly more hydrophobic than salicylate.

SI	S2	S3	S4	S5	S6	S7	S8	S9
16-AuNP+I1	16-AuNP+I2	16-AuNP+I3	17-AuNP+I1	17-AuNP+I2	17-AuNP+I3	18-AuNP+I1	18-AuNP+I2	18-AuNP+I3

Table 5-2. The sensor construction of sensor array A.

Having confirmed the feasibility of the IDA approach, we generated a multi-indicator sensor array A (Table 5-2) by loading the different probes onto the AuNPs at sub-saturation concentration and monitored the response of the sensor array to four kinds of NSAIDs, namely, diclofenac, salicylate, naproxen and ketoprofen. As mentioned, these representative drugs were chosen as targets because of their threat to the environment but also because their subtle chemical differences make detection and differentiation challenging. The studies were conducted on a multimode microwell plate reader for rapid data acquisition in an array format and each analysis was replicated 8 times on independent arrays. Different batches of the same nanoparticles gave similar results. To obtain rich signals, the information from both fluorescence (8 channels) and UV-Vis absorption (4 channels) at different wavelength were recorded. For S1, S4 and S7, the fluorescence was excited using both 460 nm and 480 nm respectively. The fluorescence intensity was recorded at the wavelength of 530, 550, 570 and 590 nm for both cases. The absorption intensity was recorded at the wavelength of 450, 470, 490 and 510 nm. For S2, S5 and S8, the fluorescence was excited using both 492 nm and 512 nm respectively. The fluorescence intensity was recorded at the wavelength of 530, 550, 570 and 590 nm for both cases. The absorption intensity was recorded at the wavelength of 450, 470, 490 and 510 nm. For S3, S6 and S9, the fluorescence was excited using both 452 nm and 472 nm respectively. The fluorescence intensity was recorded at the wavelength of 510, 530, 550 and 570 nm for both cases. The absorption

intensity was recorded at the wavelength of 440, 456, 470 and 486 nm. Since the raw values from different channels have different ranges, the fluorescence emission and the absorption recorded from the same fluorescent indicator were rescaled (0 to 1) by dividing them for the maximum intensity value obtained and the rescaled values are reported as the color gradient map. Figure 5-7 reports in a false color scale the response of each channel of the nine sensor components to the different analytes. Its inspection immediately reveals that each analyte induce a specific pattern response of the sensors array, demonstrating the discriminative capability of the system. However, differences between analytes with lower affinity, namely salicylate and ketoprofen, appear quite subtle.
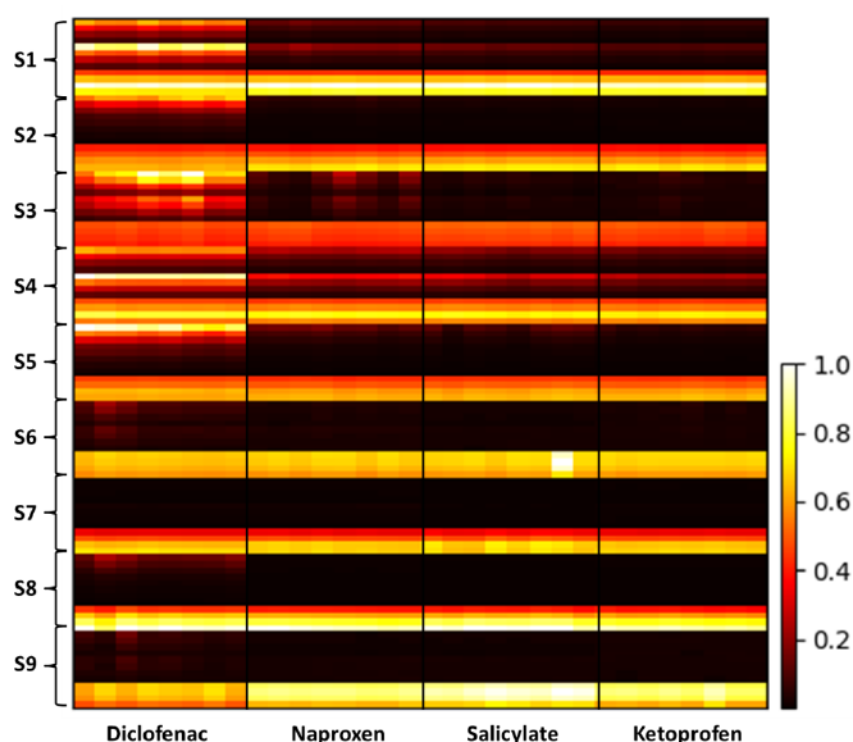
Figure 5-7. A visual map of the response of the sensor array A in the presence of the four kinds of analytes at the concentration of 50 μM.

This complex information was evaluated using statistical methods for data reduction and classification commonly used with sensor arrays, namely principal component analysis (PCA)[124] and linear discriminant analysis (LDA).[124, 125] PCA is an unsupervised method for the analysis and clustering of the response data which operated without additional information as the sample identity and allows the identification of response patterns. PCA of the datasets acquired from the 108 dimensions showed that well separated clusters (79% total variance) could be obtained by using only the first two principal components at two different analytes concentrations (Figure 5-8). However 8 dimensions are required to reach 95% of discrimination, indicating a good degree of

dispersion of the array responses. The clear boundaries between the clusters in the PCA score plot confirm the excellent discriminatory capacity of the sensing system for the four analytes tested even in the case of salicylate and ketoprofen.

The datasets acquired were further analyzed using LDA (Figure 5-9), a supervised dimensionality reductions statistical method whose purpose is to provide the tightest clustering, separated by the largest possible intercluster distance. Indeed, better clustering and higher degree of dispersion with respect to PCA analysis was obtained with 99% of discrimination obtained using only the first tree components. Furthermore, the leave-one-out (jackknife) cross-validation routine indicates 100% accuracy for the classification of all the analytes under study.
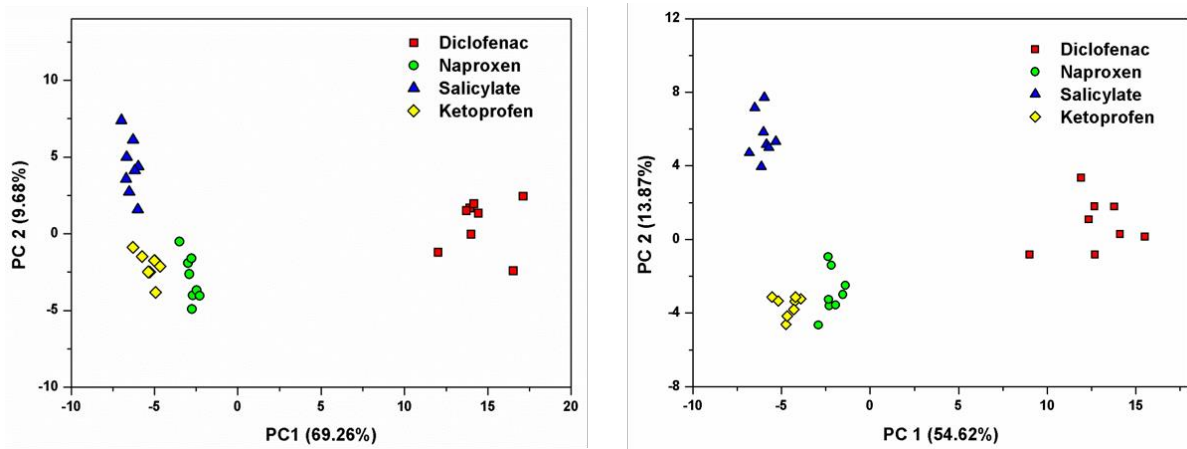
Figure 5-8. Left) The PCA score plot for the analysis of the four kinds of carboxylate anions at the concentration of 50 μM using sensor array A. Right) The PCA score plot for the analysis of the four kinds of carboxylate anions at the concentration of 30 μM using sensor array A.
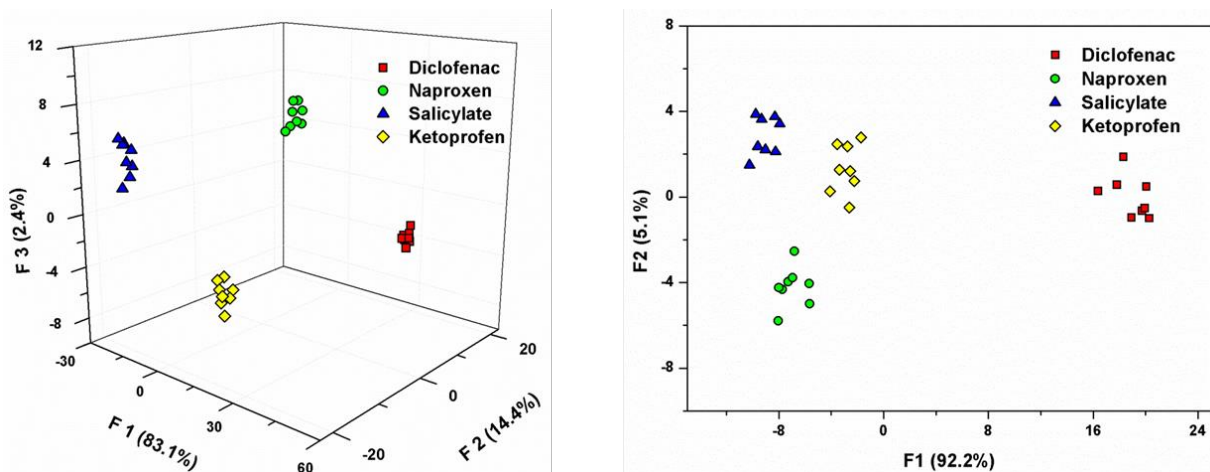
Figure 5-9. Left) The LDA score plot for the analysis of the four kinds of carboxylate anions at the concentration of 50 μM using sensor array A. Right) The LDA score plot for the analysis of the four kinds of carboxylate anions at the concentration of 30 μM using sensor array A.

We further analyzed the discriminatory performance of the system by analyzing commercial drug formulations. Diclofenac, naproxen and ketoprofen samples (salicylate is not available in commercial formulations) were prepared by dissolving a commercial tablets in water and analyzed with the sensor array. LDA analysis (Figure 5-10) revealed that the samples prepared from both the pure compounds and the drug tablets stayed in the same clusters which, albeit the larger dispersion, were well separated from the other analytes (only two components were required to reach 99% discrimination). We also tested the behavior of the array in synthetic urine (Figure 5-10), also in this case very good clustering and separation of the different analytes was obtained.
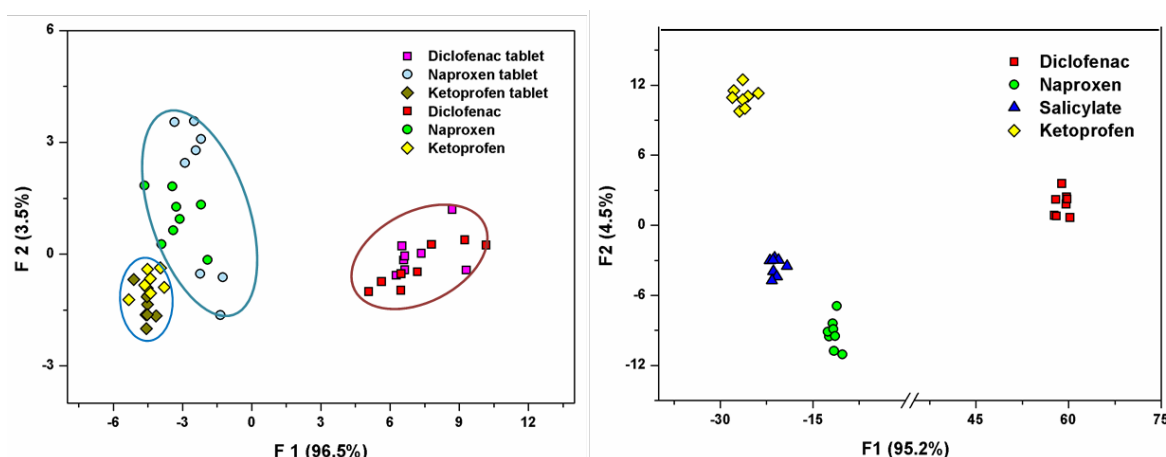
Figure 5-10. Left) LDA score plot for the analysis of the diclofenac, naproxen and ketoprofen as pure compounds and commercial tablets at the concentration of 50 μM using sensor array A. Right) LDA score plot for the analysis of the diclofenac, naproxen, ketoprofen and salycilate at the concentration of 50 μM in artificial urine using sensor array A.
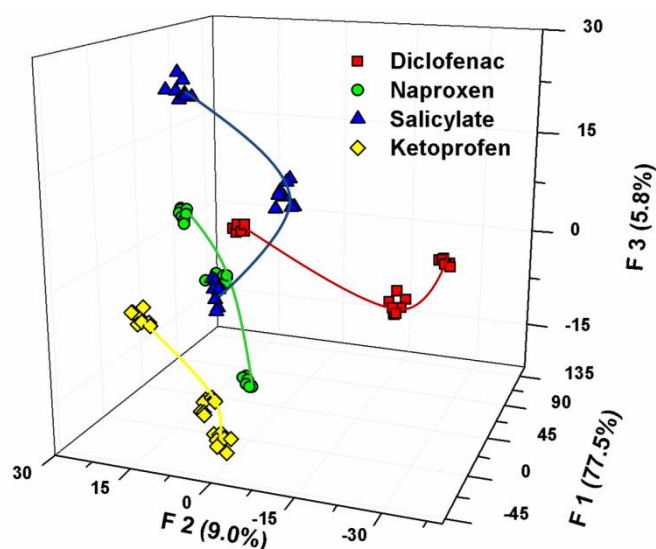
Figure 5-11. The LDA score plot for the analysis of the four carboxylate anions at the concentration of 30, 50 and 70 μM using sensor array **A**.

Finally we turned our attention to the ability of the sensor to discriminate the four NSAIDs independently from their concentration. This is quite a difficult task for an IDA-based sensor array,

since different analytes may produce similar displacement extents at different concentrations. Still, the four analytes were tested at three concentrations (30, 50 and 70 μM) with sensor array **A**. The resulting data were analyzed with LDA (Figure 5-11). In this case, 92% of discrimination was obtained using the first three components. Inspection of the LDA score plot reveals all analytes produce well grouped clusters at each concentration. Separation is large enough to allow the individuation of well-defined trajectories for each compound, enabling concentration independent analyte identification.

Besides the sensing performance, the large amount of data produced by the sensor array can also provide relevant information on the correlation between the structural features of the sensors and the discriminatory capability of the sensor array. With this perspective, we tried to individuate the smallest subset of sensors still keeping the discriminatory ability using as series of PCA analysis followed by final LDA validation as proposed by Anzenbacher and co-workers.[116, 124] In this approach, the contribution of each individual sensor to the construction of the principal component can be evaluated by the analysis of the factor loadings, which corresponds to the cosine of the angle between a principal component axis and the original variable.[126] The array components providing the most relevant contributions to the firsts PCs are individuated and their combined responses are reanalyzed via PCA to obtain the new contributions of the components and start a new reduction stage. Eventually the discriminatory ability of the reduced array is tested with LDA and cross validation.

The process of sensor selection is illustrated in Figure 5-12. As revealed from the PCA data of the 9-members sensor array, three PCs represents 83.49% of the total variance. In these three PCs, S7 contributes most to PC1, S4 to PC 2, and S1 to PC 3. Hence the rest of the sensors were excluded. With this reduced sensor array (S1, S4 and S7, that corresponds respectively to **16**-AuNP, **17**-AuNP and **18**-AuNP loaded with dye I1), both PCA and LDA analysis confirmed that the discrimination accuracy was maintained (Figure 5-12, 5-13). Inspection of PCA analysis data for the new sensor array showed that S4 and S7 are the main contributors, with S7 contributing most to PC 1 and S4 to PC 2. Once again, the discriminatory power of this 2-members sensor array is excellent with clearly separated clusters shown in both PCA and LDA (Figure 5-12, 5-14). In addition, the LDA cross-validation routine demonstrated that these two sensors still provide 100% classification accuracy.[124]

PCA	PC1	PC2	PC3
Eigenvalue	74.80	10.45	4.92
Proportion	69.26%	9.68%	4.55%
S1	11.37%	10.87%	16.76%
S2	11.88%	4.77%	12.77%
S3	11.16%	11.45%	1.96%
S4	8.41%	28.21%	16.20%
S5	11.04%	10.48%	13.05%
S6	11.60%	6.85%	9.25%
S7	12.72%	6.00%	13.54%
S8	12.60%	10.22%	6.90%
S9	9.22%	11.15%	9.58%

PCA	PC1	PC2	PC3
Eigenvalue	24.31	5.55	3.15
Proportion	67.53%	15.42%	8.75%
S1	33.58%	23.40%	44.25%
S2	-	-	-
S3	-	-	-
S4	27.87%	55.34%	37.60%
S5	-	-	-
S6	-	-	-
S7	38.55%	21.26%	18.15%
S8	-	-	-
S9	-	-	-

PCA	PC1	PC2	PC3
Eigenvalue	16.11	4.50	1.84
Proportion	67.15%	18.76%	7.66%
S1	-	-	-
S2	-	-	-
S3	-	-	-
S4	45.98%	57.03%	78.66%
S5	-	-	-
S6	-	-	-
S7	54.02%	42.97%	21.34%
S8	-	-	-
S9	-	-	-

S1 S2 S3 S4 S5 S6 S7 S8 S9 → Excluded S2 S3 S5 S6 S8 S9 → S1 S4 S7 → Excluded S1 → S4 S7

LDA
Jacknified Classification
Number of samples — 32
Correct number — 32
Correct Proportion — 100%

Figure 5-12. Schematic representation of the sensor selection. Left) PCA analysis using the complete dataset of S1-S9 shows that the S1, S4 and S7 are the main contributor to the cluster separation. Center) PCA analysis using the dataset of S1, S4 and S7 shows that S4 and S7 are the main contributor to the cluster separation. Right) PCA analysis using the dataset of S4 and S7. Cross-validated LDA shows 100% accurate classification for all these three arrays.
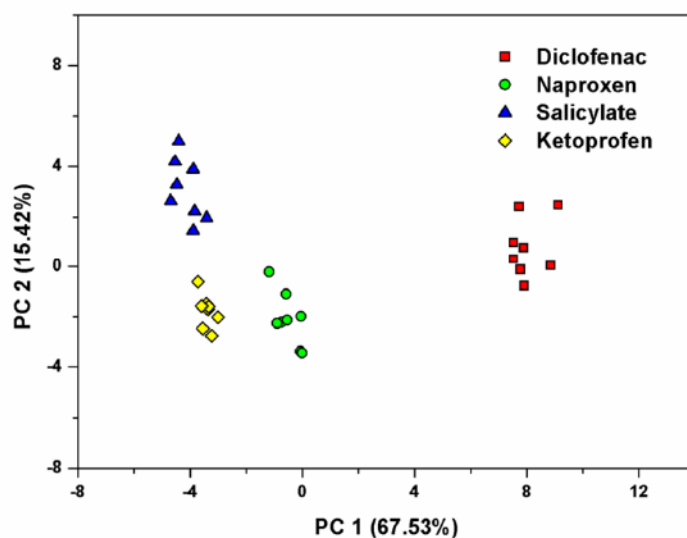
Figure 5-13. The PCA plot for the analysis of the four analytes at the concentration of 50 µM using S1, S4 and S7. Experimental conditions: AuNPs, 100 µM in thiol. HEPES, pH=7, 10 mM.
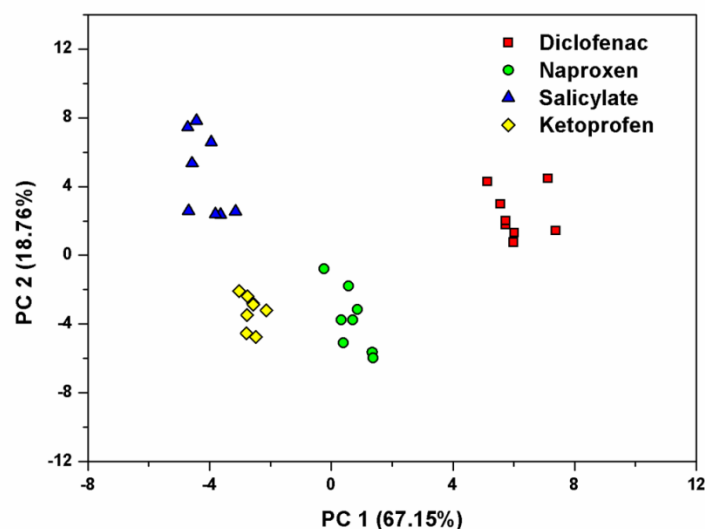
Figure 5-14. The PCA plot for the analysis of the four analytes at the concentration of 50 μM using S4 and S7. Experimental conditions: AuNPs, 100 μM in thiol. HEPES, pH=7, 10 mM.

To further analyze the sensing process, we also tried to figure out the lowest number of channels required for the 100% correct classification of the four kinds of carboxylate anions. To reach this goal, we performed a similar size reduction procedure as done for the array components. In the end, we found that with only 4 dimensions (2 sensor×2 channel), 100% correct classification can be achieved (Figure 5-15). Remarkably, the two remaining channels after reduction are emission intensity at 570 nm ($\lambda_{ex} = 480$ nm) and absorbance at 450 nm. Hence, both fluorescence and absorption of the sensing system contribute to its discriminatory ability.
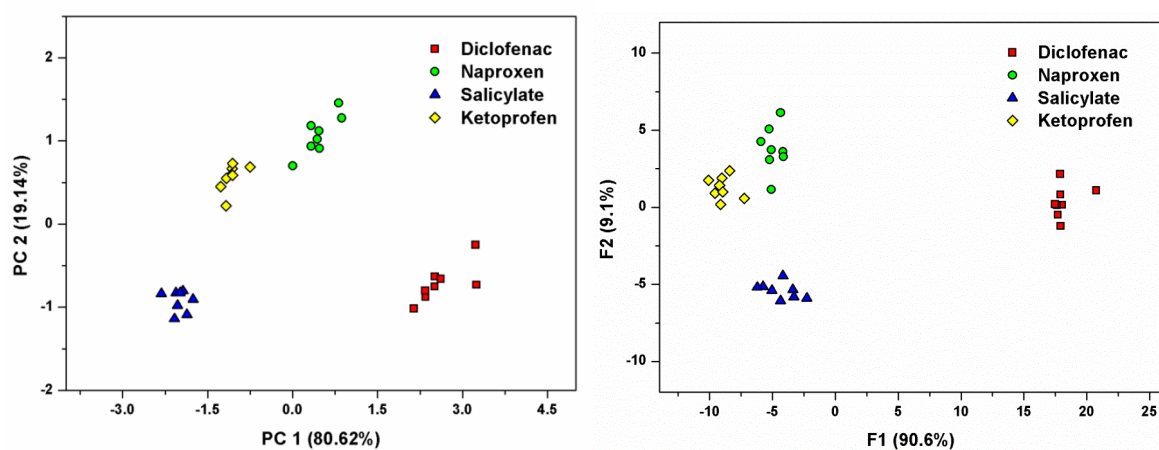
Figure 5-15. The PCA plot (Left) and LDA plot (Right) for the analysis of the four analytes at the concentration of 50 μM using S4 and S7. For each sensor, only two channels, emission at 570 nm (Ex=480 nm) and absorbance at 450 nm, were used. Experimental conditions: AuNPs, 100 μM in thiol. HEPES, pH=7, 10 mM.

The results of the sensor selection procedure provide relevant information on the recognition and detection processes. In the first reduced set a single indicator and all the nanoparticles are retained. This indicates that the discriminatory ability is more inherent to the receptors set than to

the indicators, likely because indicators and analytes have similar binding modes to the nanoparticles. Interestingly, the simplest set (2 sensors) is obtained by removing **16**-AuNP, which features the same headgroup as **17**-AuNP and the same alkyl portion as **18**-AuNP. Apparently, the highest discriminatory power is retained when a relevant chemical difference is ensured between the array components, as this allows a greater differentiation of the interactions between guests and receptors. Finally, the simplified sensor set contains only fluorescein (I1) as indicator. Fluorescein has the smallest affinity for the nanoparticles (Table 5-1). Intuitively, a sensor system featuring a low-affinity indicator is expected to provide more information on weakly interacting analytes, as here salicylate and ketoprofen.

5.4 Set up of IDA-based sensor array B
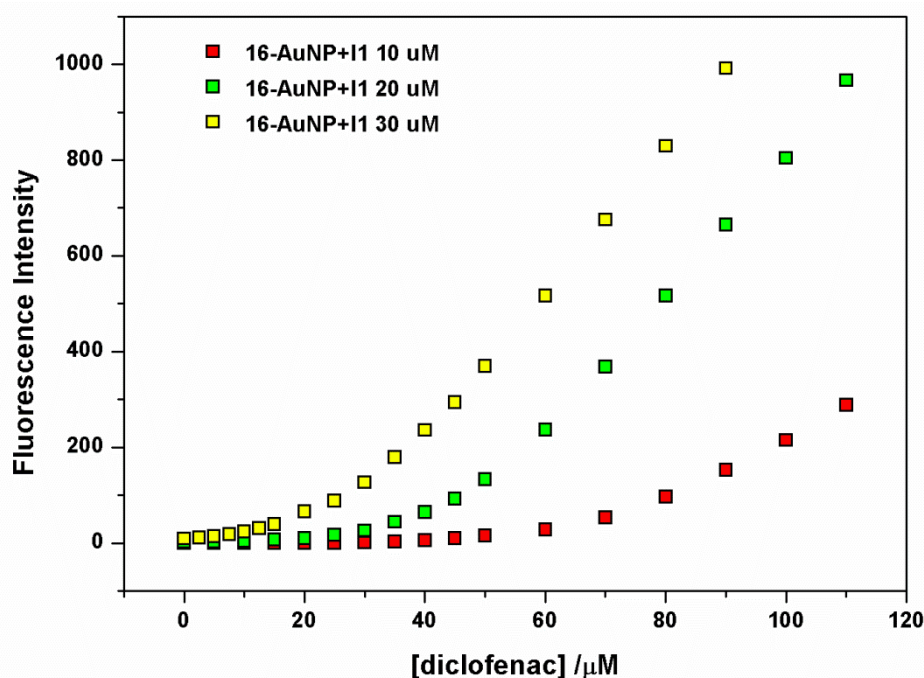
Figure 5-16. The fluorescence intensity of I1 as a function of the concentration of diclofenac in the presence of **16**-AuNP.

The concentration independent analysis reported in Figure 5-11 highlights the possibility of concentration determination using nanoparticles arrays. However, a limited concentrations range can be explored since **18**-AuNP precipitate in the presence of some analytes at concentrations greater than 70 μM. In order to explore lager concentration ranges we decided to exploit the flexibility of the AuNP-based IDA to build-up a second sensor array featuring similar discriminatory ability and a larger working range. We reasoned that sensor arrays with differential response can be in principle obtained not only using different AuNP/dye combinations but also simply changing the nanoparticle/indicator ratio.

Displacement experiments were hence conducted using **16**-AuNP (100 μM in thiol) loaded with 10, 20 and 30 μM of fluorescein (I1) respectively. As expected, when loaded with different amount of fluorescein, the sensing systems have a different sensitivity to carboxylate drugs (Figure 5-16). Such differential response was the basis for the realization of sensor array B, consisting of six sensors prepared using **16**-AuNP in the presence of 5 μM, 10 μM, 15 μM, 20 μM, 25 μM and 30 μM fluorescein (I1). Interaction information was acquired from both fluorescent (12 channels) and UV absorption (4 channels). The fluorescence of all the six sensors constructed was excited using 460 nm and 480 nm and 490 nm, respectively. The fluorescence intensity was recorded at the wavelength of 530, 550, 570 and 590 nm for all the cases. The absorption intensity was recorded at the wavelength of 450, 470, 490 and 510 nm. The sensing performance was evaluated using PCA approach. An excellent clustering and classification was observed both at analytes concentration of 50 μM and 100 μM (Figure 5-17, 5-18) with similar data dispersion (82% of discrimination with the first two components, 7 components required for 99% of discrimination). It is relevant to note that similar PCA maps are obtained with sensors arrays **A** and **B**. This suggests in line with the indications obtained by sensor size reduction, the main role of the different indicators used in sensor array A is to modulate the affinity of the indicator for the nanoparticles.
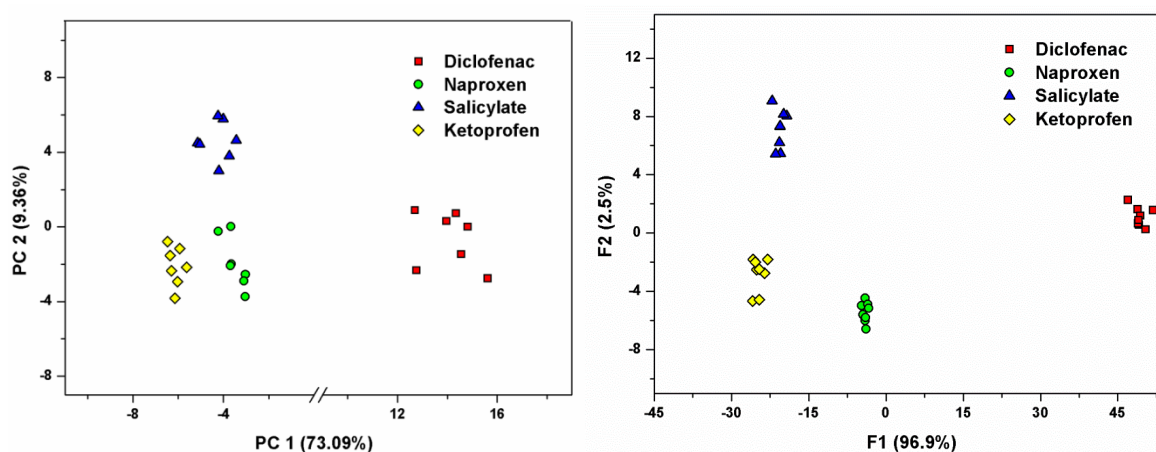
Figure 5-17. The PCA score plot (Left) and LDA score plot (Right) for the analysis of the four carboxylate anions at the concentration of 50 μM using sensor array B. Experimental conditions: AuNPs, 100 μM in thiol. HEPES, pH=7, 10 mM.
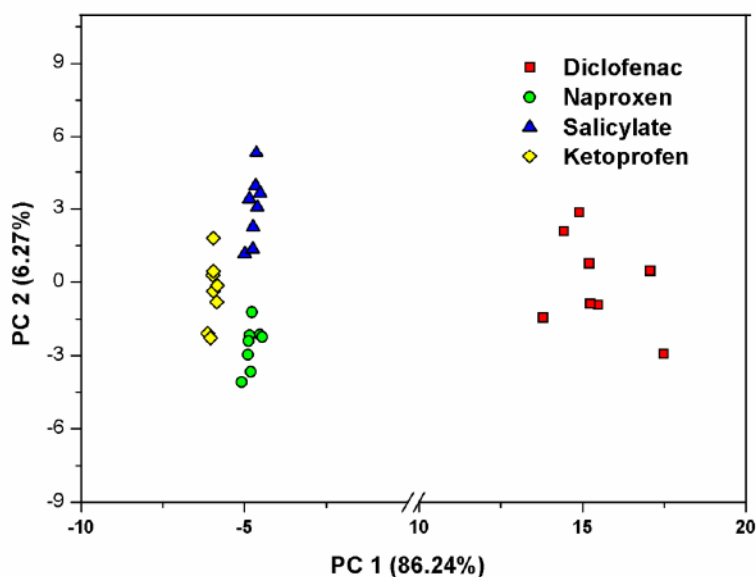
Figure 5-18. The PCA score plot for the analysis of the four carboxylate anions at the concentration of 100 μM using sensor array B. Experimental conditions: AuNPs, 100 μM in thiol. HEPES, pH=7, 10 mM.
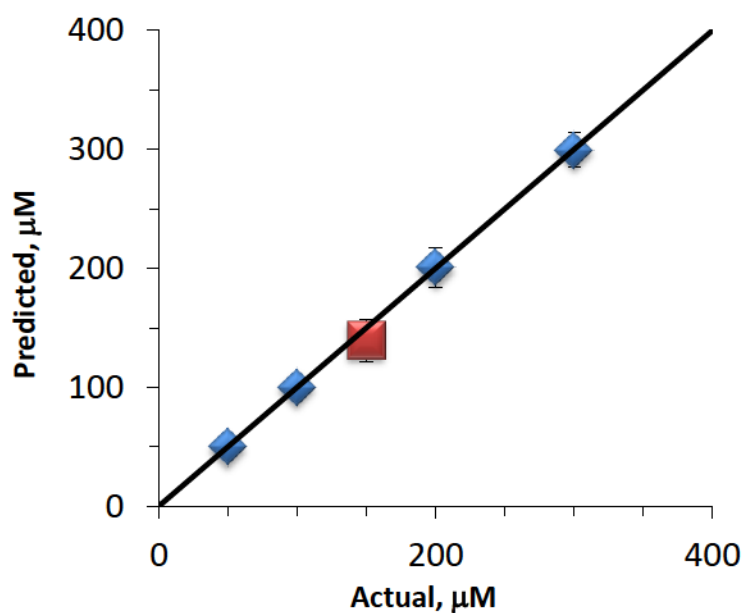
Figure 5-19. Results of linear regression for diclofenac with array B. The blue points represent the data used to train the model and the red point is the prediction of the array response at 150 mM diclofenac concetration. Error bars correspond to 3 times the standard deviation of the predicted concentrations. The RMSE (root-mean-square error) for the training of the model is 6.9204.

The excellent performance of the sensor arrays studied encouraged us to demonstrate the potential of quantitative sensing using the present method. The response of sensor array **B** was analyzed in the concentration range 50 μM-300 μM (8 repeated analysis for each concentration). Results were analyzed with linear regression analysis[127, 128] using the first three PCA components to reduce the dimensionality of the data set. Four set of data at different concentrations (50, 100,

200 and 300 μM) were used to train the model. The fifth set of data, collected at 150 μM was used as unknown to test the prediction ability of the model trained. The correlation graph between the predicted and the actual concentrations of the analyte is reported in Figure 5-19. Inspection reveals that the prediction power of the model is very good. The plot is characterized by a R^2 value of 1 for calibration and 0.998 for validation. A limit of detection of 20 μM was determined.

5.5 Conclusions

In summary, we developed AuNPs-based sensor arrays which can be used for the detection and discrimination of NSAIDs. The sensing performance was evaluated with pattern recognition method (PCA, LDA). The clear separation of response clusters was observed with 100% classification accuracy and was successfully applied to commercial drug tablets and complexed media, urine. Furthermore, the quantitative analysis was successfully performed at low micromolar concentrations.

We hence confirmed that by increasing the number of interactions between the targets and the monolayer also molecules with single charge, and likely even no charge, can be recognized by the spontaneous binding sites formed in the monolayer.

The sensing system is highly flexible since the output signal can be altered by simply modulating the nature or the amount of the fluorescent indicator. This attractive feature comes together with the easy preparation, which relies on the self-assembly of the AuNPs and mixing with commercially available fluorescent indicators. Taken together with the literature results discussed in the introduction, our data demonstrated that AuNPs could really provide a universal receptor platform for the development of IDA protocols.

5.6 Experimental section

5.6.1 Synthesis of 8-mercapto-N,N,N-trimethyloctan-1-aminium (thiol 16)

Synthesis of thiol 16.

Thiol 16 were prepared according to the literature.[44]

5.6.2 Synthesis of 4-(3-mercaptopropoxy)-N,N,N-trimethylbutan-1-aminium (thiol 17)

Thiol **17** was prepared according to the following scheme:
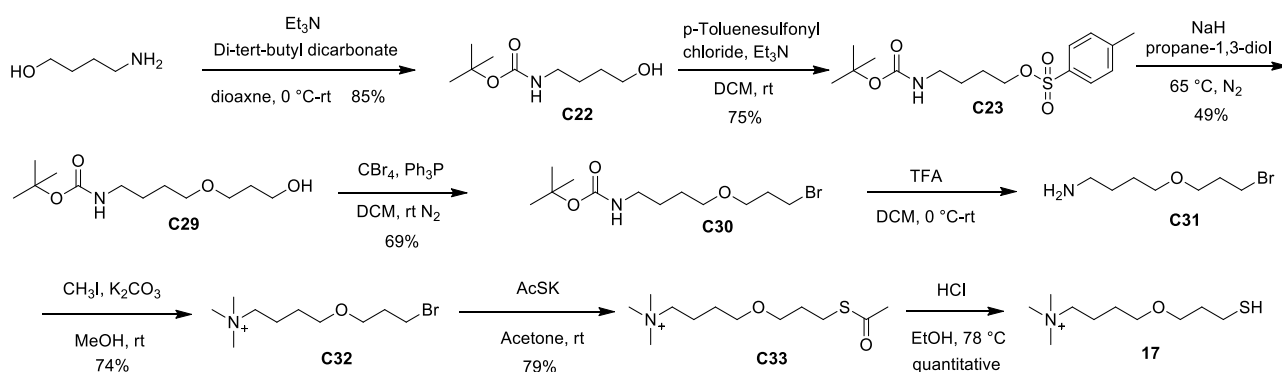
Scheme 5-1. Synthesis of thiol 17.

Synthesis of tert-butyl (4-hydroxybutyl)carbamate (C22). C22 was synthesized according to the previous procedure (Chapter 3, Experimental section).

Synthesis of 4-((tert-butoxycarbonyl)amino)butyl 4-methylbenzenesulfonate (C23). C23 was synthesized according to the previous procedure (Chapter 3, Experimental section).

Synthesis of tert-butyl (4-(3-hydroxypropoxy)butyl)carbamate (C29). Sodium hydride (605 mg, 15.4 mmol) was added to propane-1,3-diol (8.0 mL). The solution was stirred for 30 minutes and then **C23** (1.30 g, 3.79 mmol) was added. The mixture was refluxed at 65 °C for 14 hours. After the completion of the reaction, the mixture was washed with H_2O and extracted with DCM. The combined organic layer was dried with $MgSO_4$ and filtered. After solvent evaporation, the crude product was purified by flash chromatography (silica gel, eluent: PE/EtOAc 3:7). 461 mg (49%) of **C29** were obtained.

^{1}H-NMR (500 MHz, MeOD) δ 3.68-3.62 (t, 2H, CH_2O), 3.56-3.51 (t, 2H, CH_2O), 3.49-3.44 (t, 2H, CH_2O), 3.09-3.04 (t, 2H, CH_2N), 1.83-1.76 (qn, 2H, CH_2), 1.64 – 1.50 (m, 4H, CH_2), 1.45 (s, 9H, CH_3).

^{13}C-NMR (126 MHz, MeOD) δ 157.14 (1C, CO), 78.44 (1C, C), 70.17 (1C, CH_2O), 67.28 (1C, CH_2O), 58.61 (1C, CH_2OH), 39.78 (1C, CH_2N), 32.27 (1C, CH_2), 27.35 (3C, CH_3), 26.60 (1C, CH_2), 26.34 (1C, CH_2).

TOF ES+ HRMS: [M+Na+] calcd. for $C_{12}H_{25}NNaO_4$ = 270.1681. Found = 270.1700.

Synthesis of tert-butyl (4-(3-bromopropoxy)butyl)carbamate (C30). C29 (435 mg, 1.76 mmol), tetrabromomethane (1.17 g, 3.52 mmol) and triphenylphosphine (923 mg, 3.52 mmol) were dissolved in DCM. The mixture was stirred for 12 hours at room temperature. Then the solvent was evaporated and the crude product was purified by flash chromatography (silica gel, eluent: PE/EtOAc 1:9). 375 mg (69%) of **C30** were obtained.

^{1}H-NMR (500 MHz, MeOD) δ 3.57-3.49 (m, 4H, CH_2), 3.48-3.44 (t, 2H, CH_2O), 3.18-3.11 (t, 2H, CH_2N), 2.16 – 2.07 (q, 2H, CH_2), 1.67 – 1.52 (m, 4H, CH_2), 1.46 (s, 9H, CH_3).

^{13}C-NMR (126 MHz, MeOD) δ 157.15 (1C, CO), 78.33 (1C, C), 70.18 (1C, CH$_2$O), 67.76 (1C, CH$_2$O), 39.72 (1C, CH$_2$N), 32.65 (1C, CH$_2$Br), 29.65 (1C, CH$_2$), 27.38 (3C, CH$_3$), 26.60 (1C, CH$_2$), 26.34 (1C, CH$_2$).

TOF ES+ HRMS: [M+Na$^+$] calcd. for C$_{12}$H$_{24}$BrNNaO$_3$ = 332.0837. Found = 332.0847.

Synthesis of 4-(3-bromopropoxy)butan-1-amine (C31). C30 (375 mg, 1.21 mmol) was dissolved in DCM and trifluoroacetic acid (2.0 mL) was added at 0 °C. The mixture was stirred for 4 hours at room temperature. Then the solvent was evaporated and the product (250 mg, quantitative) was obtained.

^{1}H-NMR (500 MHz, CDCl$_3$) δ 3.66-3.61 (t, 2H, CH$_2$Br), 3.56-3.52 (t, 2H, CH$_2$O), 3.50-3.46 (t, 2H, CH$_2$O), 3.11-3.03 (m, 2H, CH$_2$N), 2.15-2.08 (q, 2H, CH$_2$), 1.89-1.82 (q, 2H, CH$_2$), 1.79-1.72 (q, 2H, CH$_2$).

^{13}C-NMR (126 MHz, CDCl$_3$) δ 70.43 (1C, CH$_2$O), 68.79 (1C, CH$_2$O), 40.22 (1C, CH$_2$N), 32.09 (1C, CH$_2$Br), 30.05 (1C, CH$_2$), 26.93 (1C, CH$_2$), 25.19 (1C, CH$_2$).

TOF ES+ HRMS: [M+H$^+$] calcd. for C$_7$H$_{17}$BrNO = 210.0494. Found = 210.0502.

Synthesis of 4-(3-bromopropoxy)-N,N,N-trimethylbutan-1-aminium (C32). C31 (123 mg, 0.585 mmol) and iodomethane (332 mg, 2.34 mmol) was dissolved in methanol and potassium carbonate (324 mg, 2.34 mmol) was added. The flask used for this reaction was covered with aluminum paper. The mixture was stirred for 12 hours at room temperature. Then the solvent was evaporated and the crude product was purified by flash chromatography (silica gel, eluent: DCM/MeOH 8.5:1.5). 110 mg (74%) of **C32** were obtained.

^{1}H-NMR (500 MHz, CDCl$_3$) δ 3.58-3.52 (t, 4H, CH$_2$), 3.49-3.43 (t, 2H, CH$_2$O), 3.37--3.32 (t, 2H, CH$_2$NH), 2.08-2.01 (m, 2H, CH$_2$), 1.97-1.87 (q, 2H, CH$_2$), 1.73-1.64 (q, 2H, CH$_2$).

^{13}C-NMR (126 MHz, CDCl$_3$) δ 69.44 (1C, CH$_2$O), 67.82 (1C, CH$_2$O), 66.23 (1C, CH$_2$N), 52.42 (3C, CH$_3$), 33.17 (1C, CH$_2$Br), 29.97 (1C, CH$_2$), 25.89 (1C, CH$_2$), 19.7 (1C, CH$_2$).

ESI-MS (m/z): 253.2 [M+H$^+$].

Synthesis of 4-(3-(acetylthio)propoxy)-N,N,N-trimethylbutan-1-aminium (C33). C32 (0.263 g, 0.716 mmol, 1.0 equiv) was dissolved in acetone (4.0 mL) and potassium thioacetate (0.0981 g, 0.859 mmol, 1.2 equiv) was added. The mixture was stirred for 12 hours at room temperature. After solvent evaporation, the crude product was purified by flash chromatography (silica gel, eluent: DCM/ MeOH 8.5:1.5). 81.0 mg (79%) of **C33** were obtained.

^{1}H-NMR (500 MHz, MeOD) δ 3.56-3.44 (m, 6H, CH$_2$), 3.24-3.17 (s, 9H, CH$_3$), 3.02-2.96 (t, 2H, CH$_2$N), 2.34 (s, 3H), 1.98–1.90 (q, 2H, CH$_2$), 1.87-1.80 (q, 2H, CH$_2$), 1.73-1.65 (q, 2H, CH$_2$).

^{13}**C-NMR** (126 MHz, MeOD) δ 196.28 (1C, COS), 69.32 (1C, CH$_2$O), 68.68 (1C, CH$_2$O), 66.29 (1C, CH$_2$N), 52.32 (3C, CH$_3$), 33.45 (1C, CH$_2$S), 29.38 (1C, CH$_2$), 25.77 (1C, CH$_2$), 19.52 (1C, CH$_2$).

ESI-MS (m/z): 248.2 [M+H$^+$].

Synthesis of 4-(3-mercaptopropoxy)-N,N,N-trimethylbutan-1-aminium (17). C33 (24.6 mg, 0.0987 mmol) was dissolved in ethanol (2.0 mL). A 6 M HCl solution in water (2.0 mL) was added and the mixture was stirred at 78 °C for 2 hours. The reaction mixture was allowed to cool and the solvent was evaporated to obtain 20.4 mg (quantitative) of **17**.

^{1}**H-NMR** (500 MHz, MeOD) δ 3.59-3.56 (t, 2H, CH$_2$O), 3.55-3.52 (t, 2H, CH$_2$O), 3.46–3.40 (t, 2H, CH$_2$N), 3.18 (S, 9H, CH$_3$), 2.63-2.58 (t, 2H, CH$_2$S), 1.96–1.82 (m, 4H, CH$_2$), 1.71-1.64 (q, 2H, CH$_2$).

^{13}**C-NMR** (126 MHz, MeOD) δ 69.32 (1C, CH$_2$O), 68.39 (1C, CH$_2$O), 66.25 (1C, CH$_2$N), 52.18 (1C, CH$_3$), 33.46 (1C, CH$_2$S), 25.92 (1C, CH$_2$), 20.32 (1C, CH$_2$), 19.67 (1C, CH$_2$).

TOF ES+ HRMS: [M+H$^+$] calcd. for C$_{10}$H$_{25}$NOS = 207.1651. Found = 207.1599.

5.6.3 Synthesis of N-(diaminomethylene)-7-mercaptoheptan-1-aminium (thiol 18)

Thiol **18** was prepared according to the following scheme:
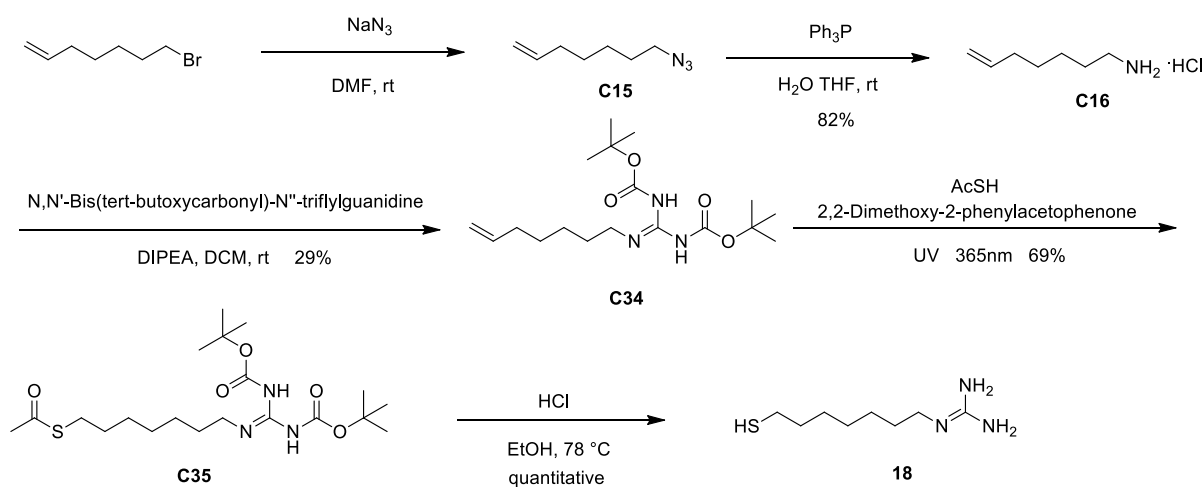
Scheme 5-2. Synthesis of thiol 18.

Synthesis of 7-azidohept-1-ene (C15). C15 was synthesized according to the previous procedure (Chapter 3, Experimental section).

Synthesis of hept-6-en-1-amine hydrochloride (C16). C16 was synthesized according to the previous procedure (Chapter 3, Experimental section).

Synthesis of C34. C16 (216 mg, 1.44 mmol) and N,N'-Bis(tert-butoxycarbonyl)-N''-triflylguanidine (470 mg, 1.20 mmol) were dissolved in DCM. Then N,N-Diisopropylethylamine (466 mg, 3.60 mmol) was added to the solution. The mixture was stirred for 25 hours at room temperature. After

the solvent evaporation, the crude product was purified by flash chromatography (silica gel, eluent: PE/ EtOAc 9.5:0.5). 150 mg (29%) of **C34** were obtained.

^{1}H-NMR (500 MHz, CDCl$_3$) δ 5.86-8-5.75 (m, 1H, CH), 5.06-4.91 (m, 2H, CH$_2$), 3.46-3.39 (q, 2H, CH$_2$), 2.11-2.04 (q, 2H, CH$_2$N), 1.63-1.56 (m, 2H, CH$_2$), 1.55-1.49 (d, 18H, CH$_3$), 1.48-1.35 (m, 4H, CH$_2$).

^{13}C-NMR (126 MHz, CDCl$_3$) δ 156.09 (1C, C), 153.33 (2C, CH$_2$O), 138.71 (1C, CH), 114.39 (1C, CH$_2$), 83.04 (1C, C), 79.23 (1C, C), 40.93 (1C, CH$_2$N), 33.54 (1C, CH$_2$), 28.83 (1C, CH$_2$), 28.47 (1C, CH$_2$), 28.32 (3C, CH$_3$), 28.08 (3C, CH$_3$), 26.30 (1C, CH$_2$).

TOF ES+ HRMS: [M+H$^+$] calcd. for C$_{18}$H$_{34}$N$_3$O$_4$ = 356.2549. Found = 356.2561.

Synthesis of C35. C34 (130 mg, 0.366 mmol) was dissolved in methanol (3.0 mL). Nitrogen was injected into the solution for 20 min to remove oxygen. Afterwards, 2, 2-Dimethoxy-2-phenylacetophenone (4.74 mg, 0.0183 mmol) and ethanethioic S-acid (111 mg, 1.46 mmol) were added. The mixture was left under irradiation (UV, 365 nm) for 2 hours. After solvent evaporation, the crude product was purified by flash chromatography (silica gel, eluent: PE/ EtOAc 9.5:0.5). 108 mg (69%) of **C35** were obtained.

^{1}H-NMR (500 MHz, MeOD) δ 3.39-3.34 (t, 2H, CH$_2$S), 2.91-2.86 (t, 2H, CH$_2$), 2.32-2.30 (s, 3H, CH$_3$), 1.63-1.56 (m, 4H, CH$_2$), 1.55 (s, 9H, CH$_3$), 1.49 (s, 9H, CH$_3$), 1.44-1.35 (m, 6H, CH$_2$).

^{13}C-NMR (126 MHz, MeOD) δ 196.15 (1C, COS), 163.17 (1C, CN), 156.17 (1C, CO), 152.85 (1C, CO), 83.04 (1C, C), 78.93 (1C, C), 40.31 (1C, CH$_2$N), 29.24 (1C, CH$_3$), 29.09 (1C, CH$_2$), 28.55 (1C, CH$_2$), 28.39 (1C, CH$_2$), 28.31 (1C, CH$_2$), 28.22 (1C, CH$_2$), 27.17 (1C, CH$_3$), 26.82 (1C, CH$_3$), 26.23 (1C, CH$_2$).

Synthesis of 2-(7-mercaptoheptyl)guanidine (18). C35 (42.6 mg, 0.0987 mmol) was dissolved in ethanol (2.0 mL). A 6 M HCl solution in water (2.0 mL) was added and the mixture was stirred at 78 °C for 2 hours. The reaction mixture was allowed to cool and the solvent was evaporated to obtain 18.7 mg (quantitative) of **18**.

^{1}H-NMR (500 MHz, MeOD) δ 3.23-3.17 (t, 2H, CH$_2$N), 2.54-2.48 (t, 2H, CH$_2$S), 1.65-1.56 (m, 4H, CH$_2$), 1.48 – 1.33 (m, 6H, CH$_2$).

^{13}C-NMR (126 MHz, MeOD) δ 157.23 (1C, CN), 41.12 (1C, CH$_2$N), 33.68 (1C, CH$_2$S), 30.05 (1C, CH$_2$), 28.42 (1C, CH$_2$), 28.36 (1C, CH$_2$), 27.84 (1C, CH$_2$), 26.2 (1C, CH$_2$).

TOF ES+ HRMS: [M+H$^+$] calcd. for C$_8$H$_{19}$NS = 190.1378. Found = 190.1398.

5.6.4 Preparation and characterization of **16**, **17** and **18**-AuNP

Preparation of 16, **17** and **18**-AuNP. Monolayer protected gold nanoparticles (**16**, **17** and **18**-AuNP) were prepared following a previously reported two-step procedure.[18] A solution of

HAuCl$_4$×3H$_2$O (50.0 mg, 0.127 mmol, 1.0 equiv) in water (0.5 mL) was extracted with a solution of tetraoctylammonium bromide (0.175 g, 0.318 mmol, 2.5 equiv) in N$_2$ purged toluene (125 mL). To the resulting reddish-orange organic solution dioctylamine (0.613 g, 2.54 mmol, 20.0 equiv) was added (the amount of dioctylamine was calculated in order to obtain 2 nm nanoparticles). The mixture is vigorously stirred under N$_2$ for 1.5 hours. During this period of time the color of the mixture fades. Then the solution is cooled at 0°C and a NaBH$_4$ solution (48.0 mg, 1.27 mmol, 10.0 equiv) in H$_2$O (1 mL) is then rapidly added. The color of the solution turns rapidly to black and after 1.5 hours of stirring at 0 °C, the aqueous layer is removed. To the obtained nanoparticle solution, the desired thiol 16-18 (0.0988 mmol, 2.0 equiv) dissolved in 3 mL of MeOH was rapidly added. The reaction mixture was stirred for 3 hours at 0°C. All the formed AuNPs were unsoluble in toluene, hence the mixtures were centrifuged and the collected AuNPs were washed with EtOAc and MeOH for 8 times.

Characterization of 16, 17 and 18-AuNP. TEM analysis (Figures 5-20, 5-21 and 5-22) of the different samples of nanoparticles yields an average diameter for **16**-AuNPof 1.6 ± 0.3nm, for **17**-AuNP and **18**-AuNP of 1.6 ± 0.3 nm and 1.4± 0.2 nm. This data, together with the loss of organic weight obtained by TGA analysis (Figures 5-23, 5-24 and 5-25), indicate that the formula for AuNP is Au$_{120}$SR$_{60}$ for AuNP-1, Au$_{131}$SR$_{46}$ for AuNP-2, Au$_{90}$SR$_{47}$ for AuNP-3. Thiols concentrations in the nanoparticles solutions for all the fluorescence experiments were determined by the weight of nanoparticles dissolved and the average formula determined for the nanoparticles as shown above. NMR analysis (Figure 5-26, 5-27, 5-28) indicates monolayer formation (broadening of all signals and missing of the SCH$_2$CH$_2$ protons' signals). UV-vis spectra (Figure 5-29, 5-30, 5-31) recorded also showed no or small plasmonic band at 520 nm, which suggests the size of the AuNPs is smaller than 3 nm.
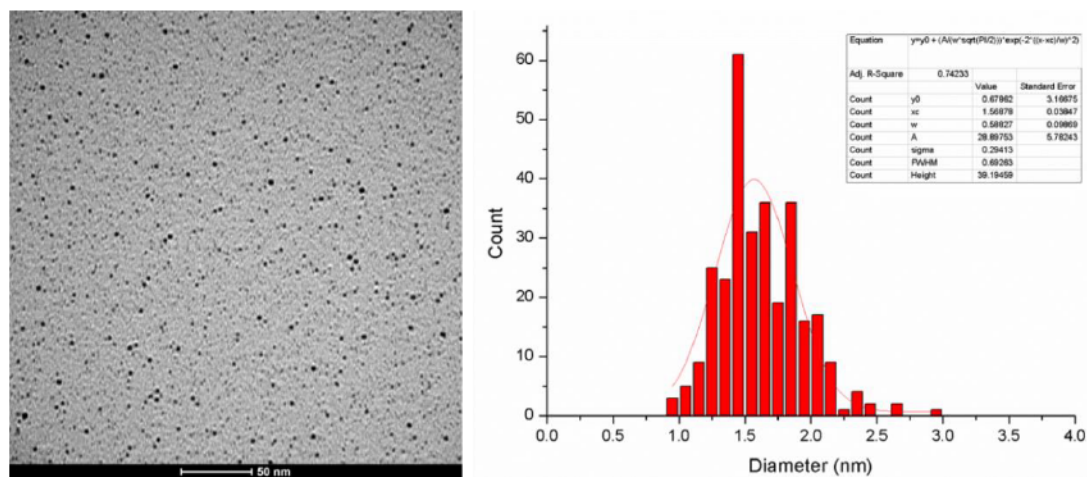
Figure 5-20. TEM image of **16**-AuNP and its size distribution: average diameter=1.6 nm (σ= 0.3 nm).
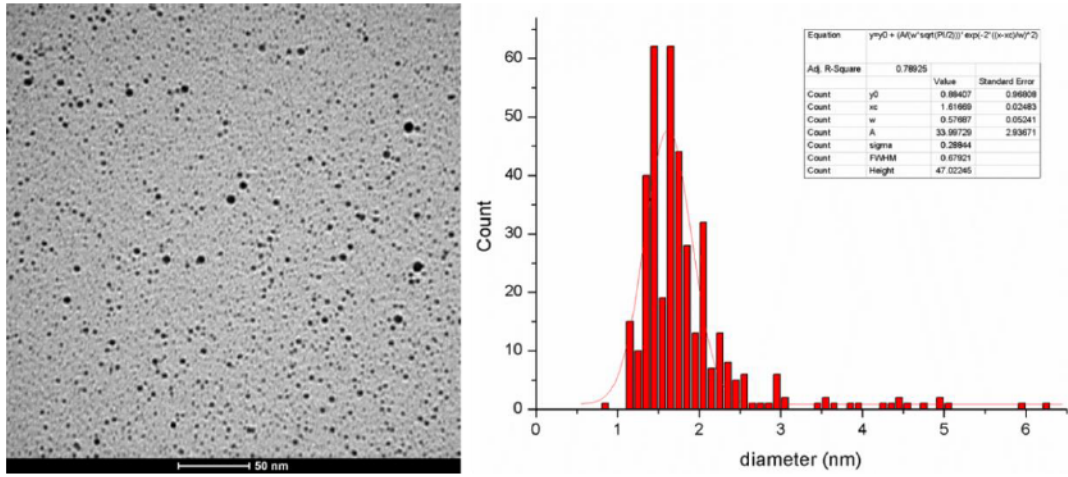
Figure 5-21. TEM image of **17**-AuNP and its size distribution: average diameter=1.6 nm (σ= 0.3 nm).
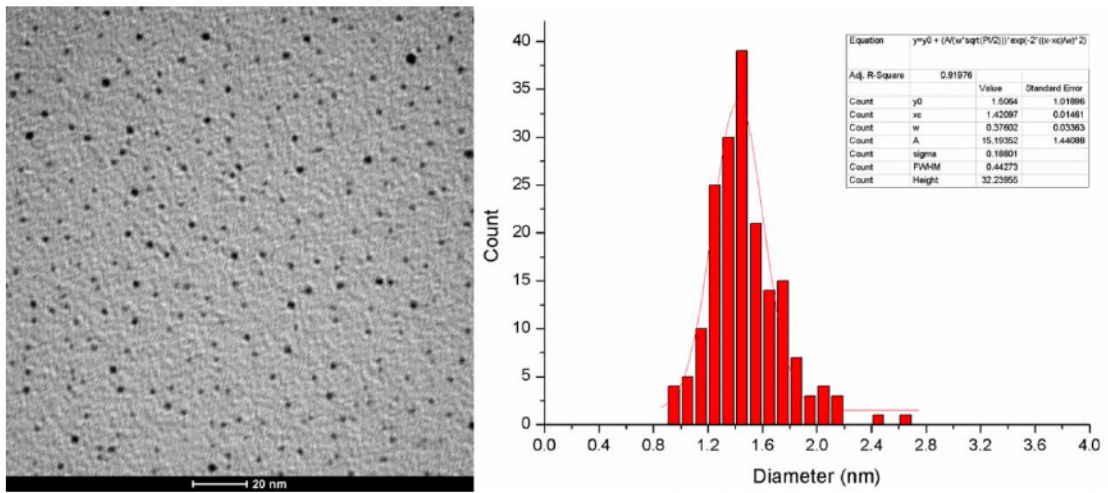
Figure 5-22. TEM image of **18**-AuNP and its size distribution: average diameter=1.4 nm (σ= 0.2 nm).
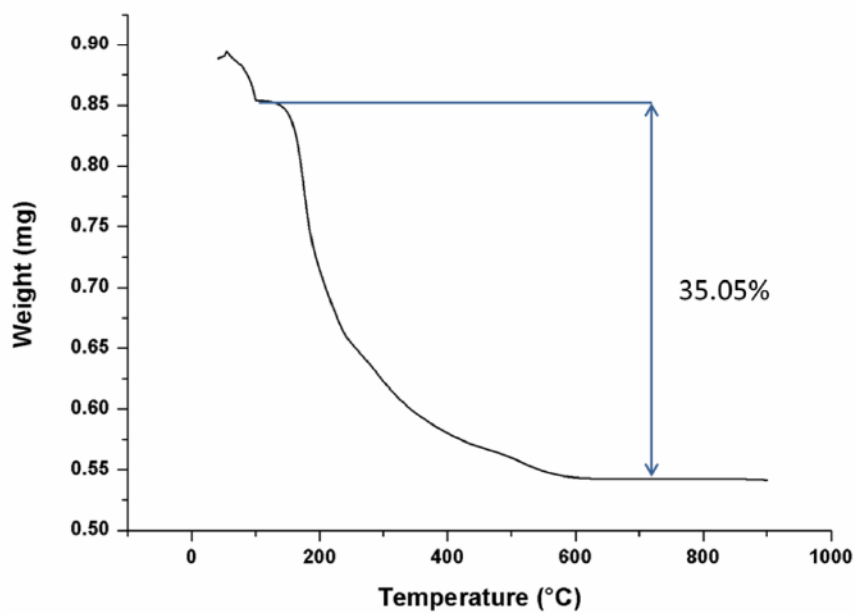
Figure 5-23. TGA analysis of **16**-AuNP under air atmosphere.
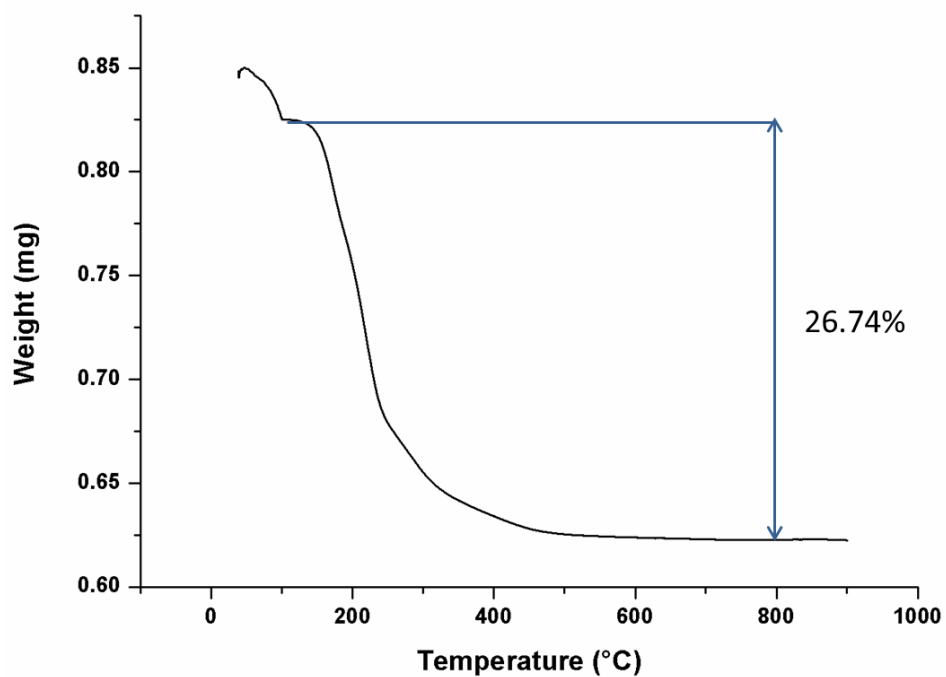
Figure 5-24. TGA analysis of **17**-AuNP under air atmosphere.
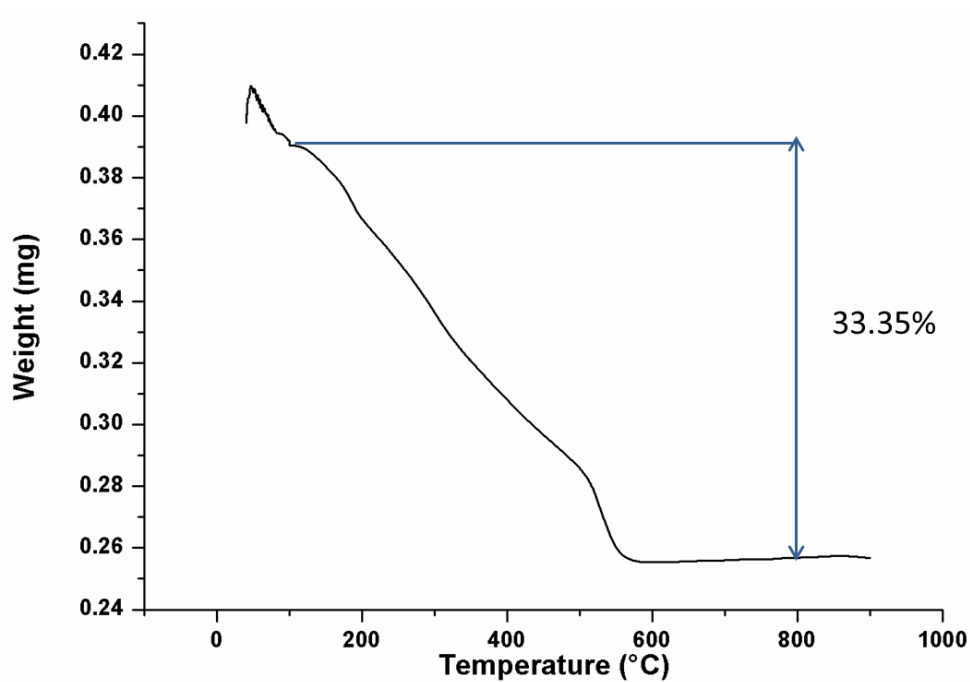
Figure 5-25. TGA analysis of **18**-AuNP under air atmosphere.
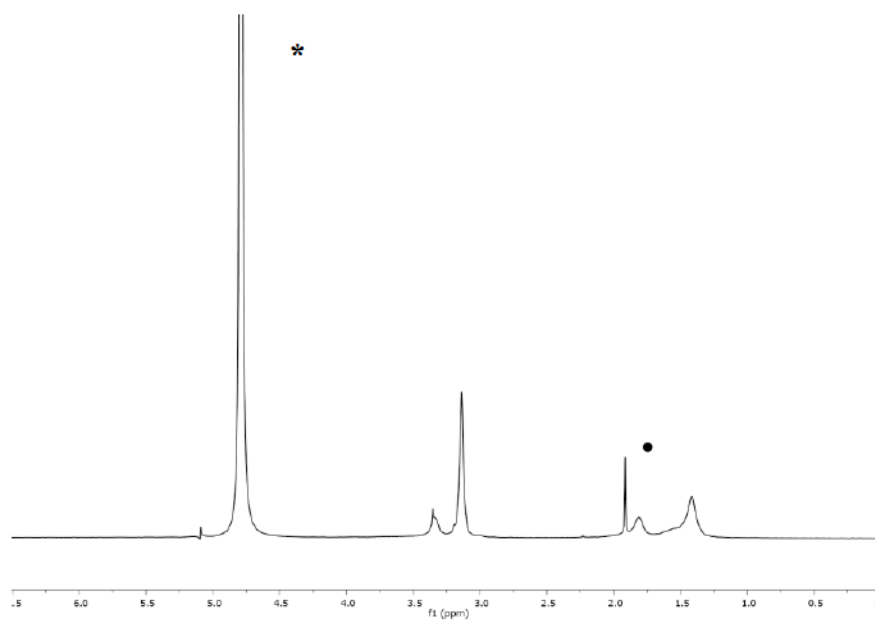
Figure 5-26. ^{1}H NMR spectrum of **16**-AuNP in D_2O (* indicates the residual solvents, • indicates CH_3COO^-).
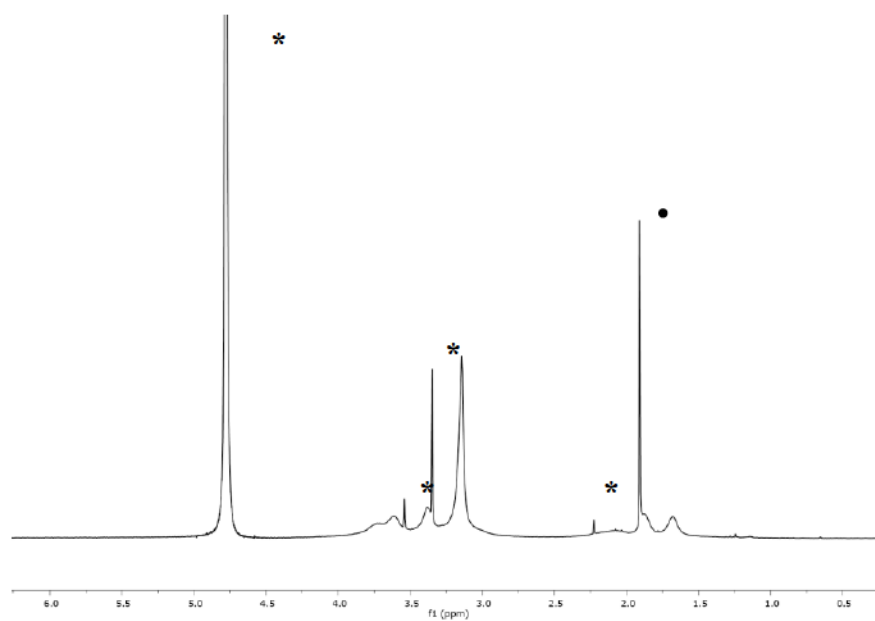
Figure 5-27. ^{1}H NMR spectrum of **17**-AuNP in D_2O (* indicates the residual solvents , • indicates CH_3COO^-).
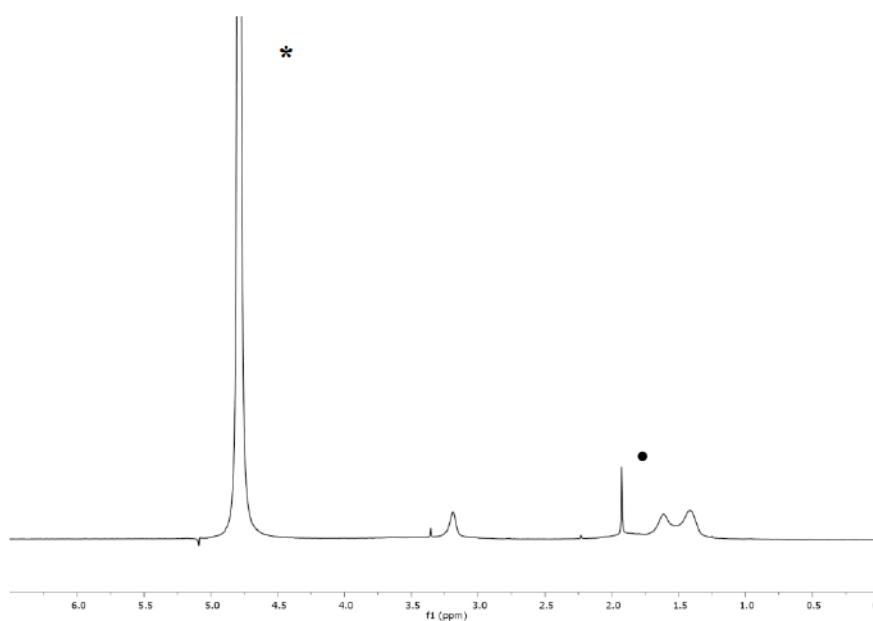
Figure 5-28. ^{1}H NMR spectrum of **18**-AuNP in D$_2$O (* indicates the residual solvents, • indicates CH$_3$COO$^-$).
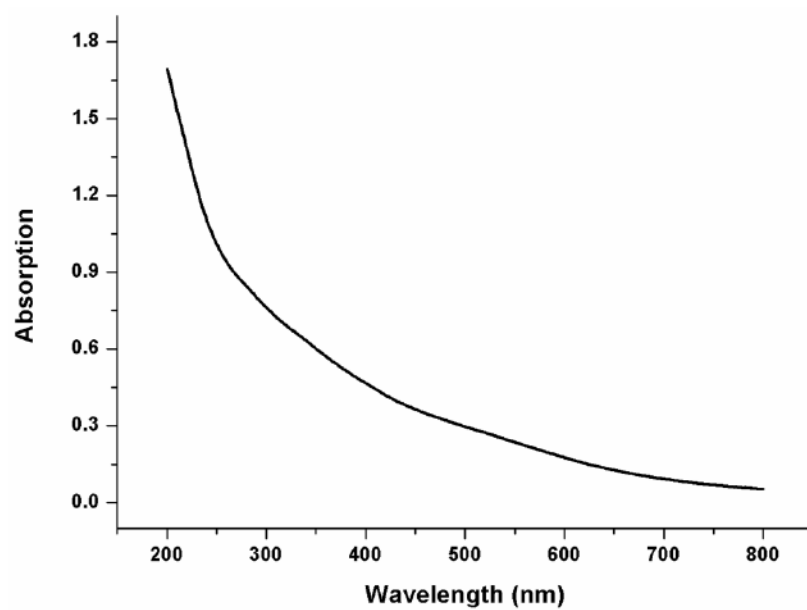
Figure 5-29. UV-Vis spectrum of **16**-AuNP (0.1 mg/mL) at 25 °C in H$_2$O.
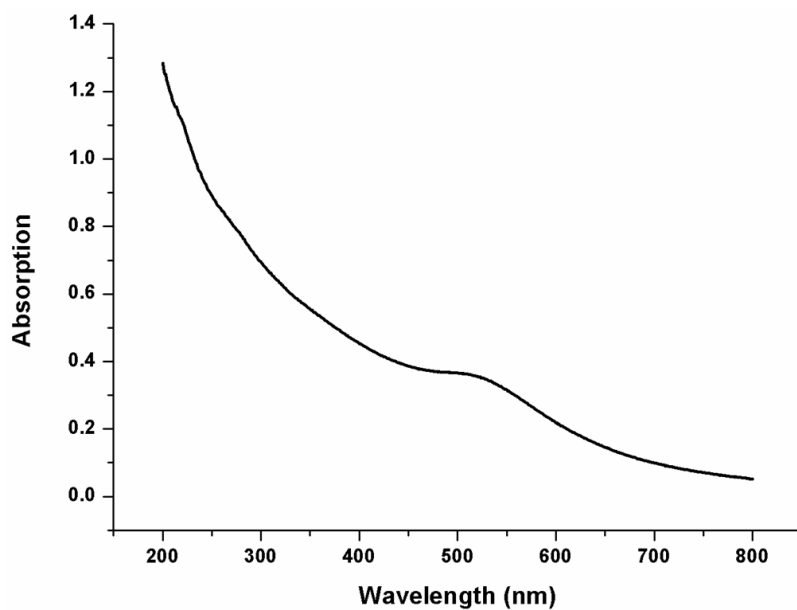
Figure 5-30. UV-Vis spectrum of **17-**AuNP (0.1 mg/mL) at 25 °C in H_2O.
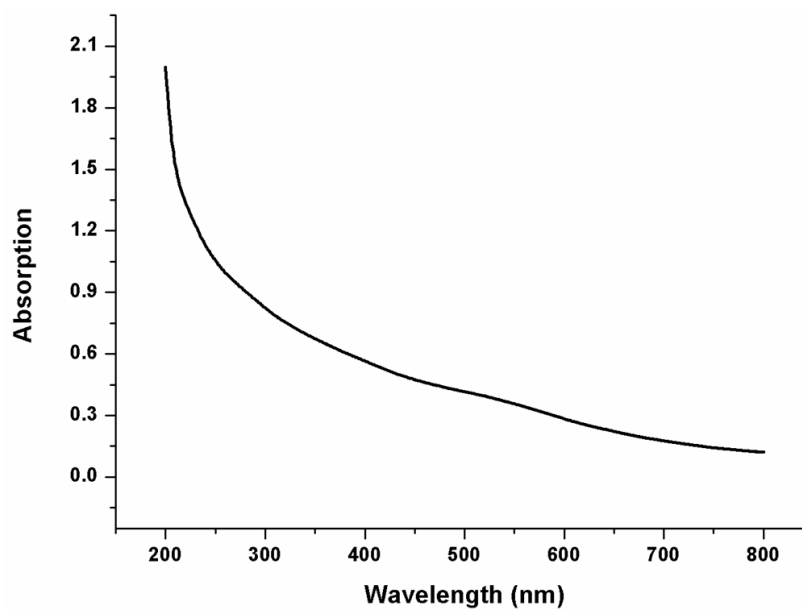
Figure 5-31. UV-Vis spectrum of **18-**AuNP (0.1 mg/mL) at 25 °C in H_2O.

Chapter 6. Morphology investigation of mixed-monolayer-protected nanoparticles

6.1 Introduction

It is accepted that the morphology of mixed monolayer gold nanoparticles can be partly responsible for their properties.[129] Defined motifs formed by monolayers, such as Janus, stripes or patches, have been observed. It is quite evident that such morphologies could also influence the receptor properties of the nanoparticles, defining the structure of the possible binding sites.

Until now, the methods proposed for the investigation of the monolayer distribution are based on microscopy techniques, ^{1}H and NOESY NMR, MALDI, SANS, FTIR and so on.[77] However, all the methods developed suffer from several limitations, such as, the need of expensive instruments, the harsh requirements of sample preparation, providing indirect information or the necessity to synthesize a series of AuNPs with various compositions. Therefore it is still challenging to develop new methods to investigate the monolayer distribution of mixed AuNPs, in particularly the combination of different techniques.

In this chapter, NMR (Paramagnetic Relaxation Enhancement) and EPR (Pulsed Electron-Electron Double Resonance) techniques were combined to study the morphology of mixed AuNPs.

6.2 Paramagnetic relaxation enhancement study
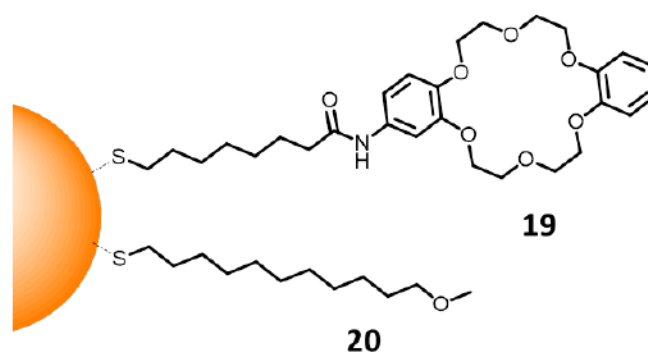
Figure 6-1. The molecular structure of the coating thiols used in this chapter.

Paramagnetic relaxation enhancement (PRE) has been exploited to determine the structure of proteins a long time ago. Recently, a large number of study also confirmed the potential of PRE-based application in structure determination. This effect is induced, among the others, by lanthanide ions because of their large and varied paramagnetism arising from unpaired electrons in the f orbitals. Among all the lanthanide ions, Gd^{3+} is the only paramagnetic lanthanide with an

isotropic environment of the unpaired electrons, resulting in a long electronic relaxation time that gives rise to strong relaxation enhancements in the NMR spectrum without significant changes in chemical shifts. Due to its outstanding relaxation enhancement properties, Gd^{3+} are the mostly used ions in this field. When Gd^{3+} is bound to a macromolecule the signals of the resonant spins surrounding (within a defined distance) the metal ion will broaden and eventually disappear from the NMR spectrum. The different broadening patterns observed for the mixed coating monolayers would provide the direct information on the morphology of the AuNPs.
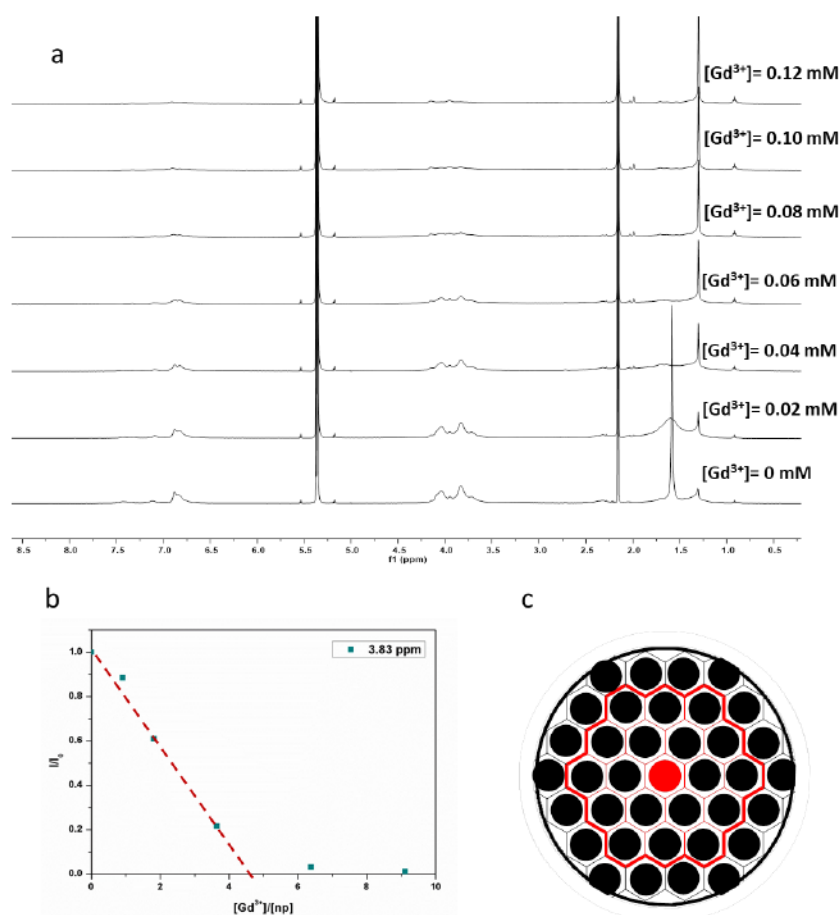
Figure 6-2. a) The ^1H NMR spectra of **19**-AuNP in CD_2Cl_2 recorded upon addition of increase amount of Gd^{3+}, b) the relative intensity of signals at 3.83 ppm as a function of the Gd^{3+}/np ratio, c) Schematic interpretation of the experiment. The black circle represents thiol 19 in the monolayer. The red circle represents Gd^{3+}. The red profile indicates the quenching area.

In this chapter we prepared homoligand AuNPs with thiol 19 (**19**-AuNP) and thiol 20 (**20**-AuNP), respectively (Figure 6-1). In addition, mixed AuNPs coated with thiol 19 and thiol 20 in different ratio (**21**-AuNP: thiol 19/thiol 20=50%/50%, **22**-AuNP: thiol 19/thiol 20=25%/75%) were synthesized using the thiol exchange method. We chose thiol 19 and thiol 20 as coating ligands

based on the following reasons: 1) they provide separated ^{1}H NMR signals. 2) they have different binding affinity to Gd^{3+}. Indeed, the benzocrown moiety enables thiol 19 with the binding sites for Gd^{3+}, while thiol 20 is not able to interact with it.
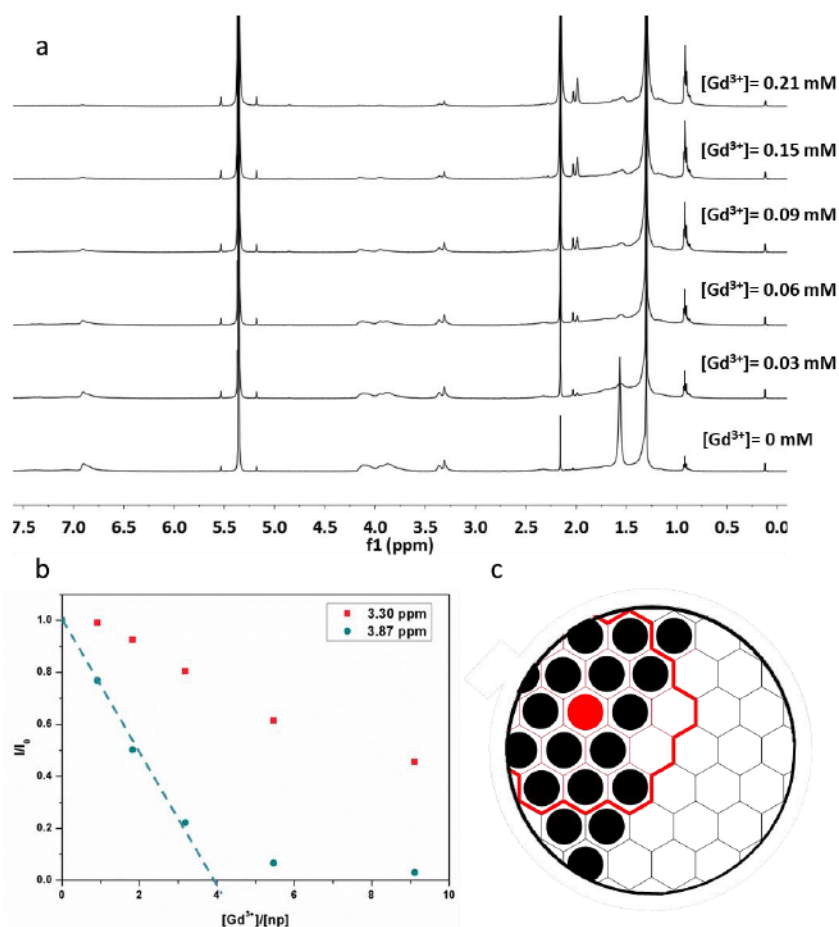
Figure 6-3. a) The 1H NMR spectra of **21**-AuNP in CD_2Cl_2 recorded upon addition of increase amount of Gd^{3+}, b) the relative intensity of signals at 3.83 ppm and 3.87 nm as a function of the Gd^{3+}/np ratio, c) Schematic interpretation of the experiment. The black circle represents thiol 19 in the monolayer. The red circle represents Gd^{3+}. The red profile indicates the quenching area.

When Gd^{3+} was added to the solution of **19**-AuNP (100% crown ether, [thiol]=1.6 mM), the signals of thiol 19 broadened from the first addition of Gd^{3+} and eventually disappeared when the concentration of Gd^{3+} reached 0.12 mM. It is easy to observe from Figure 6-2 that not only the signals of the protons close to the binding sites are cancelled from the spectrum but also the ones of the protons of the inner alkyl chain and even those of the thiols that do not bind Gd^{3+}. In fact, when complete broadening occurs, the concentration of Gd^{3+} is less than one tenth of the concentration of thiol **19**. This indicates that when Gd^{3+} was bounded with thiol **19**, its PRE effect was exerted on a large number of the surrounding molecules. Further analysis of the signal intensity as a function of the Gd^{3+}/np ratio suggested that about five Gd^{3+} ions can completely

quench the signals of a whole nanoparticle. Considering the radius of the nanoparticles, including the monolayer, is 2 nm, it is easy to calculate that the quenching radius of one Gd^{3+} is around 1.8 nm. It is very important to note that the signals of impurities and residual solvents remain unaffected over the whole titration. This confirm that the PRE effects observed are due to an intramolecular process (Gd^{3+} ions bound to the particles) and not to the more efficient and unspecifit intermolecular process that take plase when Gd^{3+} is free in solution.
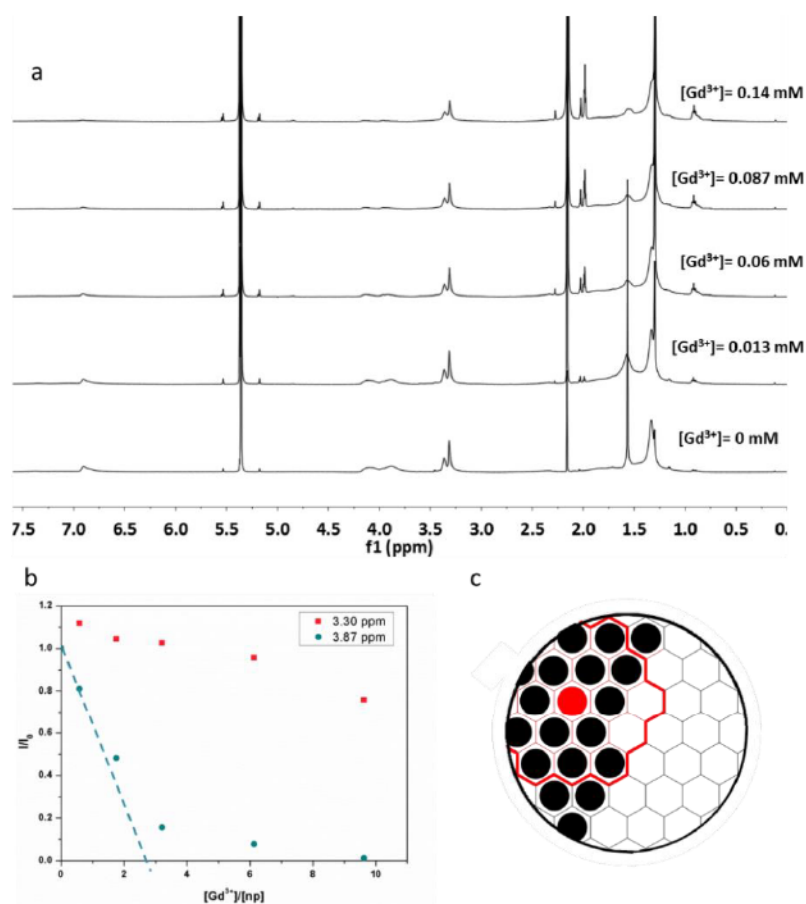
Figure 6-4. a) The 1H NMR spectra of **22**-AuNP in CD_2Cl_2 recorded upon addition of increase amount of Gd^{3+}, b) the relative intensity of signals at 3.83 ppm and 3.87 nm as a function of the Gd^{3+}/np ratio, c) Schematic interpretation of the experiment. The black circle represents thiol 18 in the monolayer. The red circle represents Gd^{3+}. The red profile indicates the quenching area.

When Gd^{3+} is added to the solution of **21**-AuNP (50% crown ether, [thiol]=1.6 mM), as revealed from Figure 6-3, the signals arising from thiol **19** broadened at first and eventually disappeared when the concentration of Gd^{3+} was 0.1 mM. On the other hand, the signals of thiol **20**, while also broadening as the concentration of Gd^{3+} increased, still 40% of them (with respect to the initial intensity) survived at the highest concentration of Gd^{3+}. A similar behavior was observed when Gd^{3+} was added to the solution of **22**-AuNP (25% crown ether, [thiol]=1.6 mM, Figure 6-4). The signals of thiol **19** were quenched very quickly after the first additions of Gd^{3+}. When they were

completely disappeared, 80% of the signals from thiol **20** still remained unaffected. In both the cases, the partial broadening of the signals arising from thiol **20** suggests that part of thiol **20** molecules were located around thiol **19** but another part of thiol **20** molecules were relatively far from thiol **19**, remaining outside of the "quenching" area created by the bounded Gd^{3+} ions. Based on the results above, it is safe to conclude that in the mixed monolayers the two thiols can't be either randomly or stripe distributed. Indeed in such cases, all the signal of thiol **20** would be quenched when the Gd^{3+} concentration is high enough, since any thiol **20** would be closer than 1.8 nm to a thiol **19** molecule. Geometrical calculation proved that also patches distribution isn't possible, again because all the signals will be cancelled eventually. So the only possible arrangement for **21**-AuNP and **22**-AuNP are Janus or very large domains (not more than two) distribution, which grant that a part, large or small depending on the monolayer composition and distribution, of thiols **20** is distant enough from any thiol **19** to not undergo PRE effect after saturation with Gd^{3+} ions.

6.3 Electron paramagnetic resonance study

The EPR technique we used to investigate the morphology of mixed AuNPs is pulsed electron-electron double resonance (PELDOR). PELDOR is a technique that can measure the distance between two paramagnetic centers. It is widely used in the characterization of protein conformation distribution at a nm level. Considering the structure similarity of AuNPs and proteins, we assume that the PELDOR technique can also be employed in the morphology study of mixed AuNPs.
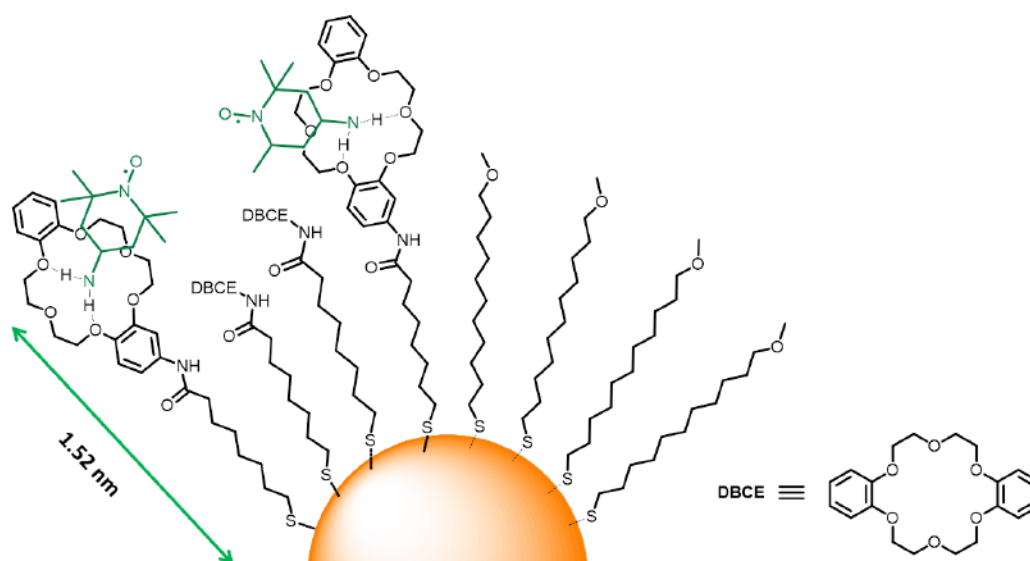
Figure 6-5. Schematic representation of the interaction between 4-amino-TEMPO and thiol 19.

It is well known that crown ether moiety is able to bind with primary amines in non-protic solvents due to the formation of two NH··O hydrogen bonds (Figure 6-5). Taking this into consideration, 4-amino-TEMPO was chosen as the EPR probe to study the monolayer distribution of **21**-AuNP and **22**-AuNP. When 4-amino-TEMPO was added to the mixed AuNPs, it can interact only with the thiol 19. Therefore we supposed that, by analyzing the distribution of the radical, we can obtain the direct information of the distribution of thiol **19**, and consequently on the morphology of the mixed AuNPs.
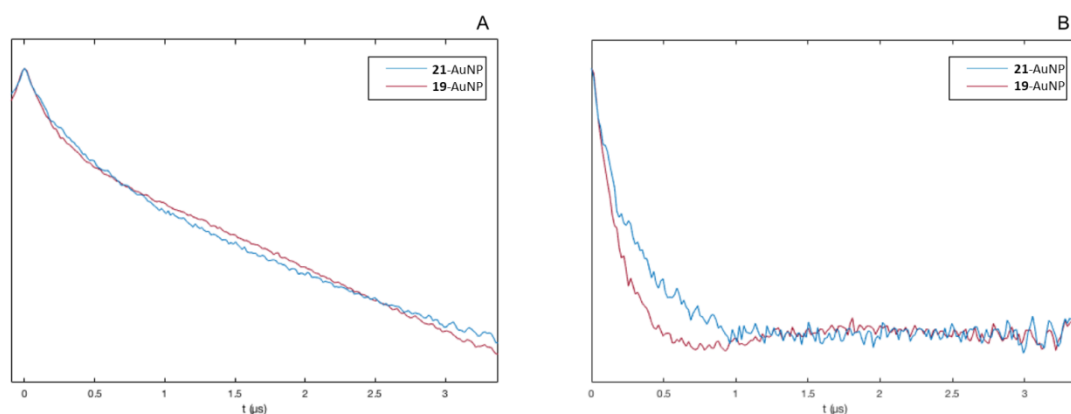
Figure 6-6. PELDOR time traces of 4-amino-TEMPO in the presence of **21**-AuNP and **19**-AuNP A) before background subtraction, B) after background subtraction.

The PELDOR experiments (cooperated with Prof. Di Valentin, University of Padova) were conducted using the samples containing AuNPs (200 µM) and 4-amino-TEMPO (300 µM) in a mixed solvents (CD_2Cl_2:$CDCl_3$=2:1). The reason to use 1.5 equiv of 4-amino-TEMPO with respect to the concentration of AuNPs is to guarantee that there will not be more than two spin labels bound with one AuNP, which is a prerequisite of the PELDOR experiments. The PELDOR time traces for the spin labeled **19**-AuNP and **21**-AuNP are shown in Figure 6-6. As revealed from Figure 6-6, both the traces before and after the background subtraction were different for **19**-AuNP and **21**-AuNP. This by no doubt indicated that the mixed monolayer of **21**-AuNP distributed differently with **19**-AuNP.
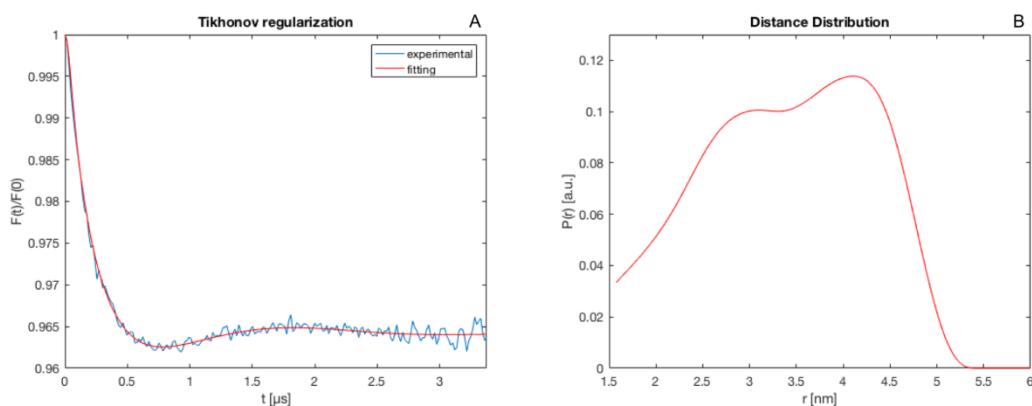
Figure 6-7. A) PELDOR time trace of 4-amino-TEMPO in the presence of 19-AuNP and its fitting result using the Tikhonov regularization. B) the distance distribution obtained from the Tikhonov regularization. Average distance=3.36 nm (σ=0.92 nm).

The PELDOR time trace of **19**-AuNP was first analyzed taking advantage of the Tikhonov regularization. As revealed from Figure 6-7, the fitting line based on this method perfectly matched with the experimental time traces. In addition the distance distribution showed that the average distance of the spin labels is 3.36 nm (σ=0.92 nm). Considering the geometric structure of the AuNPs, a sphere model was then employed in order to obtain an accurate analysis of the system. As revealed from Figure 6-8, a good fitting of the experimental result was obtained also with this model and the distance distribution obtained indicates that the spin labels are distributed over a sphere with a diameter of 4.58 nm (σ=0.57 nm). These results fit very well with the size distribution of the nanoparticles obtained from TEM result (average diameter of gold core is 1.6±0.3 nm) and the length of the thiol 19 (1.52 nm in fully extended configuration).
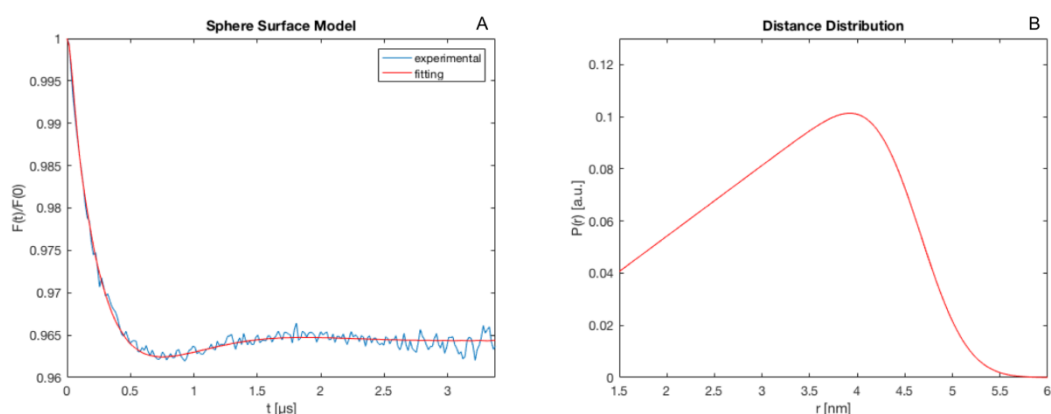
Figure 6-8. A) PELDOR time trace of 4-amino-TEMPO in the presence of 19-AuNP and its fitting result using the sphere model. B) the distance distribution obtained from the sphere model. Average distance=4.58 nm (σ=0.57 nm).
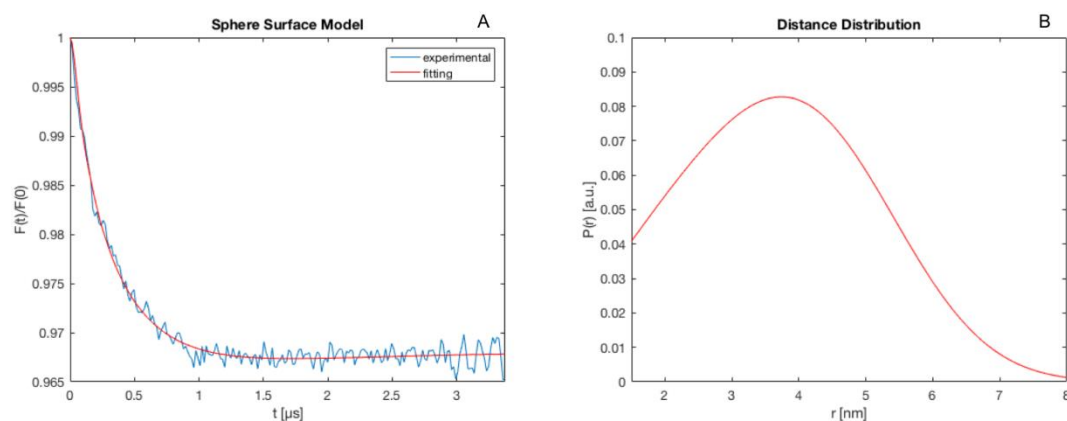
Figure 6-9. A) PELDOR time trace of 4-amino-TEMPO in the presence of 21-AuNP and its fitting result using the sphere model. B) the distance distribution obtained from the sphere model. Average distance=4.82 nm (σ=1.77 nm).

Then we used the sphere model to analyze the PELDOR time traces of **21**-AuNP. The results (Figure 6-9) showed that the fitting is good. However, the fitting indicates that the spins are distributed over a sphere with an average diameter of 4.82 nm and standard deviation of 1.77 nm. This data, in particular the size distribution largely deviates from the experimental size of the nanoparticles and confirm that there is no possibility that **21**-AuNP is random distributed, in agreement with the NMR experiments.

The development of other models (Janus, large patches) that can be used to analyze the PELDOR time traces of **21**-AuNP and **22**-AuNP is still in progress.

6.4 Experimental section

6.4.1 Synthesis of 11-methoxyundecane-1-thiol (19)

Thiol **19** was prepared according to the following scheme:
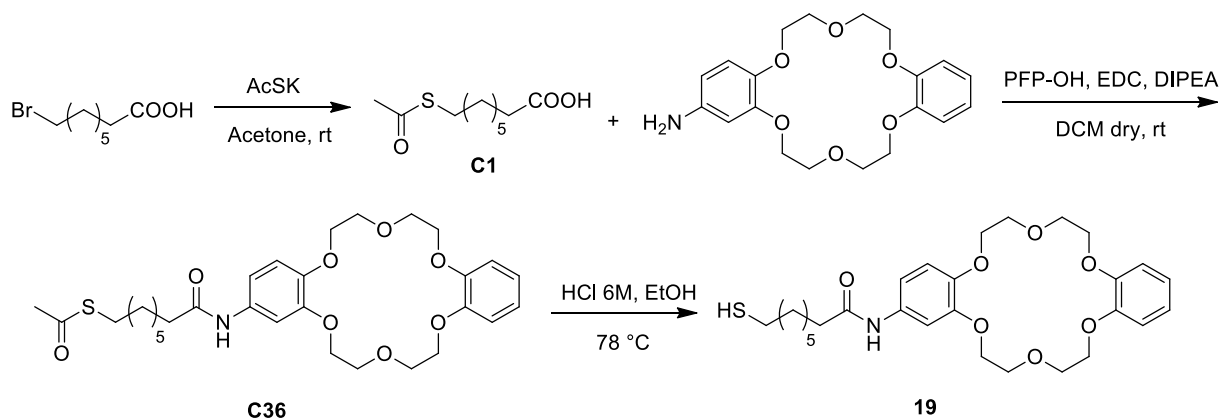
Scheme 6-1. Synthesis of thiol **19**.

Synthesis of C1. C1 was synthesized according to the previous procedure (Experimental section, chapter 3).

Synthesis of C36. C1 (174 mg, 0.799 mmol, 2.0 equiv) and pentafluorophenol (191 mg, 1.04 mmol, 2.6 equiv) were dissolved in aanhydrous CH_2Cl_2 (4.0 mL) and N-(3-Dimethylaminopropyl)-N-ethyl-carbodiimide hydrochloride (EDC, 199 mg, 1.04 mmol, 2.6 equiv) was added. The mixture was stirred for 12 hours under nitrogen. Then N,N-diisopropylethylamine (DIPEA, 51.7 mg, 0.399 mmol, 1.0 equiv) and 4-aminodibenzo-18-crown-6 (150 mg, 0.399 mmol, 1.0 equiv) were added. The mixture was stirred at 40 °C for another 12 hours. After solvent evaporation, the crude product was purified by flash chromatography (silica gel, eluent: toluene/CH_3OH 9:1). 162 mg (70%) of **C36** were obtained.

^{1}H NMR (500 MHz, $CDCl_3$) δ 7.75 (s, 1H, NH), 7.40 (s, 1H, CH), 6.97 – 6.81 (m, 5H, CH), 6.75 (d, 1H, CH), 4.21 – 4.06 (m, 8H, CH_2O), 4.05-3.93 (m, 8H, CH_2O), 2.90-2.81 (t, 2H, CH_2CO), 2.36–2.29 (m, 5H, CH_3CO, CH_2), 1.74-1.64 (m, 2H, CH_2), 1.61 – 1.49 (m, 2H, CH_2), 1.42 – 1.28 (m, 6H, CH_2).

^{13}C NMR (126 MHz, $CDCl_3$) δ 196.22 (1C, CONH), 171.46 (1C, COS), 148.56 (1C, CH), 144.89 (1C, CH), 132.35 (1C, CH), 121.30 (1C, CH), 113.52 (1C, CH), 113.28 (1C, CH), 112.02 (1C, CH), 106.18 (1C, CH), 69.83 (1C, CH_2O), 69.74 (1C, CH_2O), 69.62 (1C, CH_2O), 68.89 (1C, CH_2O), 68.60 (1C, CH_2O), 68.40 (1C, CH_2O), 37.45 (1C, CH_2NH), 30.66 (1C, CH_2S), 29.42 (1C, CH_2), 29.04 (1C, CH_2), 28.79 (1C, CH_2), 28.53 (1C, CH_2), 25.49 (1C, CH_2).

ESI-MS (m/z): 576.4 [M+H$^+$], 598.4 [M+Na$^+$].

Synthesis of thiol 19. C36 (51.0 mg, 0.0886 mmol, 1.0 equiv) was dissolved in methanol (2.0 mL). Sodium methoxide (14.4 mg, 0.266 mmol, 3.0 equiv) was added and the mixture was stirred at room temperature for 2 hours. The reaction mixture was allowed to cool and the solvent was evaporated to obtain thiol 19 (quantitative).

^{1}H NMR (500 MHz, $CDCl_3$) δ 7.54 (s, 1H, NH), 7.38 (s, 1H, CH), 6.95-6.83 (m, 5H, CH), 6.81-6.74 (d, 1H, CH), 4.21-4.07 (m, 8H, CH_2O), 4.05-3.90 (m, 8H, CH_2O), 2.57-2.47 (q, 2H, CH_2CO), 2.36-2.29 (t, 2H, CH_2S), 1.75-1.65 (m, 2H, CH_2), 1.65-1.56 (m, 2H, CH_2), 1.44-1.29 (m, 6H, CH_2).

^{13}C NMR (126 MHz, $CDCl_3$) δ 171.20 (1C, CONH), 148.87 (1C, CH), 148.74 (1C, CH), 145.22 (1C, CH), 132.17 (1C, CH), 121.38 (1C, CH), 114.08 (1C, CH), 113.70 (1C, CH), 112.04 (1C, CH), 106.51 (1C, CH), 69.97 (1C, CH_2O), 69.91 (1C, CH_2O), 69.88 (1C, CH_2O), 69.75 (1C, CH_2O), 69.25 (1C, CH_2O), 68.89 (1C, CH_2O), 68.67 (1C, CH_2O), 37.59 (1C, CH2NH), 33.92 (1C, CH_2S), 29.12 (1C, CH_2), 28.82 (1C, CH_2), 28.16 (1C, CH_2), 25.50 (1C, CH_2), 24.60 (1C, CH_2).

ESI-MS (m/z): 556.1 [M+Na$^+$].

6.4.2 Synthesis of 11-methoxyundecane-1-thiol (20)
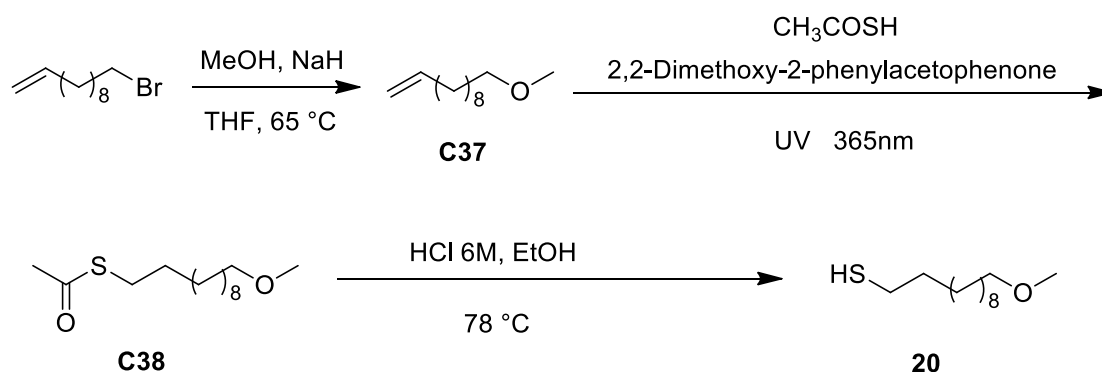
Scheme 6-2. Synthesis of thiol **20**.

Synthesis of 11-methoxyundec-1-ene (C37). 11-methoxyundec-1-ene (1.00 g, 4.29 mmol, 1.0 equiv) and methanol (1.37 g, 42.9 mmol, 10.0 equiv) was dissolved in anhydrous THF (5.0 mL) and NaH (0.600 g, 15.0 mmol, 3.5 equiv) was added. The mixture was stirred for 24 hours at 65 °C. After solvent evaporation, the crude product was purified by flash chromatography (silica gel, eluent: PE/ EtOAc 9:1). 0.735 g (93%) of 11-methoxyundec-1-ene (**C37**) were obtained.

^{1}**H NMR** (500 MHz, CDCl$_3$) δ 5.86-5.75 (m, 1H, CH), 5.08 − 4.83 (dd, 2H, CH$_2$), 3.38 − 3.34 (t, 2H, CH$_2$O), 3.32 (s, 3H, CH$_3$), 2.07 − 2.00 (q, 2H, CH$_2$), 1.60 − 1.52 (m, 2H, CH$_2$), 1.41 − 1.25 (m, 12H, CH$_2$).

^{13}**C NMR** (126 MHz, CDCl$_3$) δ 139.11 (1C, CH), 114.06 (1C, CH$_2$), 72.92 (1C, CH$_2$O), 58.46 (1C, CH$_3$O), 33.79(1C, CH$_2$), 29.65 (1C, CH$_2$), 29.52 (1C, CH$_2$), 29.47 (1C, CH$_2$), 29.42 (1C, CH$_2$), 29.11 (1C, CH$_2$), 28.92 (1C, CH$_2$), 26.13 (1C, CH$_2$).

ESI-MS (m/z): 185.1 [M+H$^+$]

Synthesis of S-(11-methoxyundecyl) ethanethioate (C38). C37 (0.500 g, 2.71 mmol, 1.0 equiv) was dissolved in methanol (3.0 mL). The solution was degassed for 20 mins. Afterwards, 2,2-Dimethoxy-2-phenylacetophenone (0.0350 g, 0.136 mmol, 0.05 equiv) and ethanethioic S-acid (0.825 g, 10.9 mmol, 4.0 equiv) were added. The mixture was left under irradiation (UV, 365 nm) for 2 hours. After solvent evaporation, the crude product was purified by flash chromatography (silica gel, eluent: PE/ EtOAc 9.5:0.5). 313 mg (44%) of **C38** were obtained.

^{1}**H NMR** (500 MHz, CDCl$_3$) δ 3.37 − 3.31 (t, 2H, CH$_2$O), 3.30(s, 3H, CH$_3$O), 2.86-2.81 (t, 2H, CH$_2$S), 2.31 − 2.28 (s, 3H, CH$_3$CO), 1.58 − 1.49 (m, 4H, CH$_2$), 1.36 − 1.20 (m, 14H, CH$_2$).

^{13}C NMR (126 MHz, CDCl$_3$) δ 195.85 (1C, CO), 72.90 (1C, CH$_3$O), 58.46 (1C, CH$_2$O), 30.56 (1C, CH$_3$), 29.62 (1C, CH$_2$), 29.51 (1C, CH$_2$), 29.47 (1C, CH$_2$), 29.45 (1C, CH$_2$), 29.41 (1C, CH$_2$), 29.09 (1C, CH$_2$), 29.07 (1C, CH$_2$), 28.77 (1C, CH$_2$), 26.10 (1C, CH$_2$).

ESI-MS (m/z): 261.2 [M+H$^+$], 283.2 [M+Na$^+$]

Synthesis of 11-methoxyundecane-1-thiol (20). C38 (0.0514 g, 0.197 mmol) was dissolved in ethanol (2.0 mL). A 6 M HCl solution in water (2.0 mL) was added and the mixture was stirred at 78 °C for 2 hours. The reaction mixture was allowed to cool and the solvent was evaporated and thiol 20 was obtained (quantitative).

^{1}H NMR (500 MHz, CDCl$_3$) δ 3.40 – 3.35 (t, 2H, CH$_2$O), 3.34 (s, 3H, CH$_3$O), 2.56-2.50 (q, 2H,CH$_2$S), 1.65-1.53 (m, 4H, CH$_2$), 1.42 – 1.24 (m, 14H, CH$_2$).

^{13}C NMR (126 MHz, CDCl3) δ 72.96 (1C, CH$_2$O), 58.53 (1C, CH$_3$), 34.05 (1C, CH$_2$S), 29.65 (1C, CH$_2$), 29.55 (1C, CH$_2$), 29.49 (1C, CH$_2$), 29.06 (1C, CH$_2$), 28.37 (1C, CH$_2$), 26.14 (1C, CH$_2$), 24.65 (1C, CH$_2$).

ESI-MS: 242.4 [M+Na$^+$]

6.4.3 Preparation and characterization of **19, 20, 21** and **22**-AuNP

Synthesis of monolayer protected gold nanoparticles (19, 20, 21 and 22-AuNP**). 19**-AuNP and **20**-AuNP were prepared following a previously reported two-step procedure.[18] A solution of HAuCl$_4$×3H$_2$O (50.0 mg, 0.127 mmol, 1.0 equiv) in water (0.5 mL) was extracted with a solution of tetraoctylammonium bromide (0.175 g, 0.318 mmol, 2.5 equiv) in N$_2$ purged toluene (125 mL). To the resulting reddish-orange organic solution dioctylamine (0.613 g, 2.54 mmol, 20.0 equiv) was added (the amount of dioctylamine was calculated in order to obtain 2 nm nanoparticles). The mixture is vigorously stirred under N$_2$ for 1.5 hours. During this period of time the color of the mixture fades. Then the solution is cooled at 0°C and a NaBH$_4$ solution (48.0 mg, 1.27 mmol, 10.0 equiv) in H$_2$O (1.0 mL) is then rapidly added. The color of the solution turns rapidly to black and after 1.5 hours of stirring at 0 °C, the aqueous layer is removed. To the obtained nanoparticle solution, the desired thiol 19 or 20 (0.0988 mmol, 2.0 equiv) dissolved in 3 mL of MeOH was rapidly added. The reaction mixture was stirred for 3 hours at 0°C. Then the solution was concentrated and washed with petroleum ether, acetonitrile and methanol using centrifuge for 8 times.
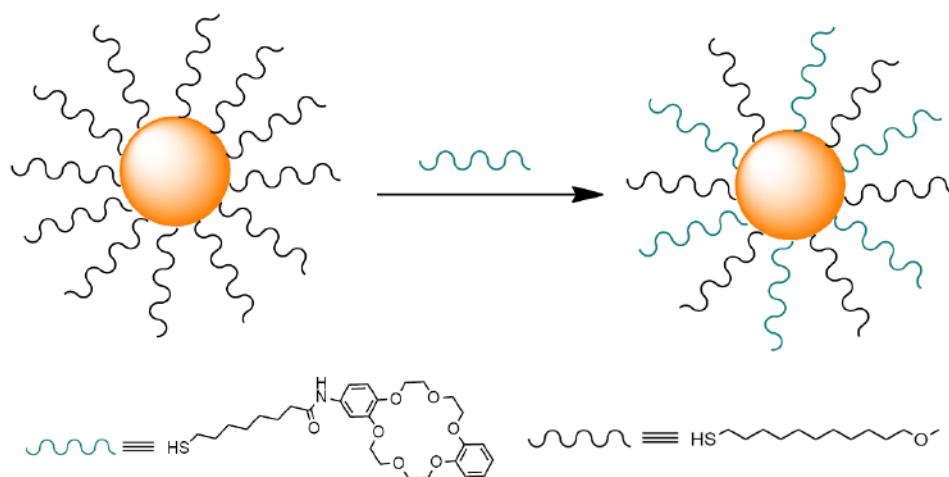
Figure 6-10. Schematic representation of the synthesis of **21**-AuNP and **22**-AuNP.

    21-AuNP and **22**-AuNP were prepared by the method of thiol exchange. To obtain **21**-AuNP and **22**-AuNP, **20**-AuNP and thiol 19 (0.65 equiv for **21**-AuNP, 0.25 equiv for **22**-AuNP) were dissolved in CH_2Cl_2. The mixture was stirred gently at room temperature for 24 h. Then the AuNPs obtained were washed with petroleum ether, ethyl acetate for 4 times. Subsequently, the resulting crude was dissolved in CH_2Cl_2 and purified with gel permeation chromatography with Sephadex S-X1.

    TEM analysis (Figures 6-11, 6-12 and 6-13) of the different samples of nanoparticles yields an average diameter for **19**-AuNP of 1.6 ± 0.2nm, for **21** and **22**-AuNP of 1.5 ± 0.3 nm and 1.5± 0.2 nm. This data, together with the loss of organic weight obtained by TGA analysis (Figures 6-14, 6-15 and 6-16), indicate that the formula for AuNP is $Au_{117}SR_{51}$ for **19**-AuNP, $Au_{104}SR_{53}$ for **21**-AuNP, $Au_{104}SR_{53}$ for **22**-AuNP. Thiols concentrations in the nanoparticles solutions for all the fluorescence experiments were determined by the weight of nanoparticles dissolved and the average formula determined for the nanoparticles as shown above. NMR analysis (Figure 6-17, 6-18, 6-19) indicates monolayer formation (broadening of all signals and missing of the SCH_2CH_2 protons' signals). In addition, the intergral of the separated signals arising from two thiols showed the monolayer composition of **21-AuNP** and **22-AuNP**. UV-vis spectra (Figure 6-20, 6-21, 6-22) recorded also showed no or small plasmonic band at 520 nm, which suggests the size of the AuNPs is smaller than 3 nm.
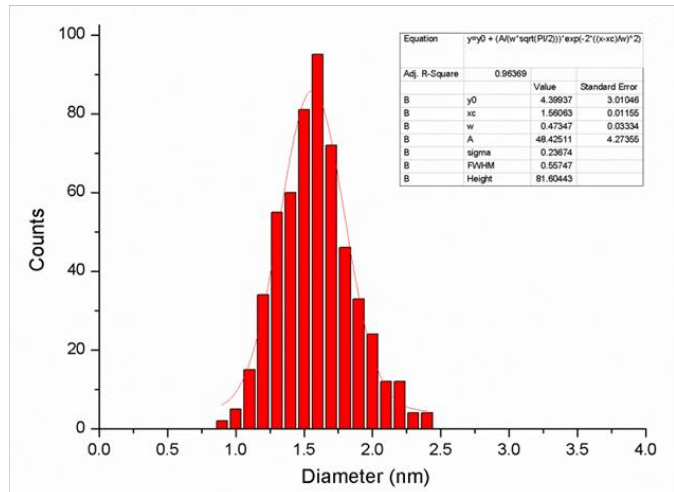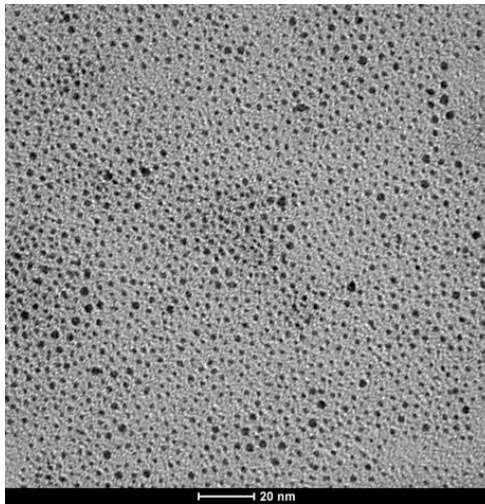
Figure 6-11. TEM image of **19**-AuNP and its size distribution: average diameter=1.56 nm (σ= 0.24 nm).
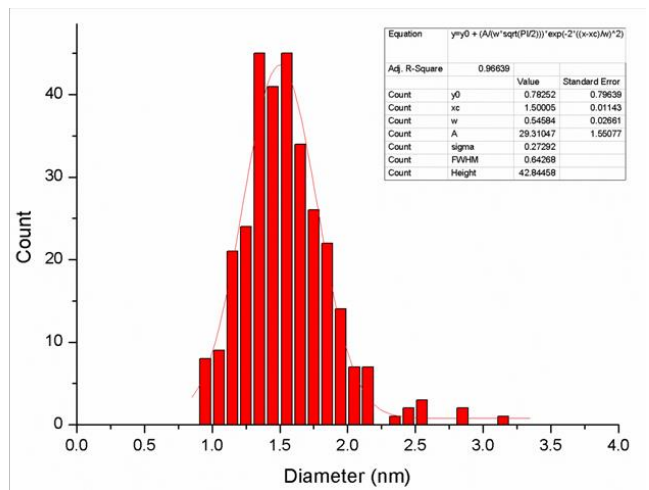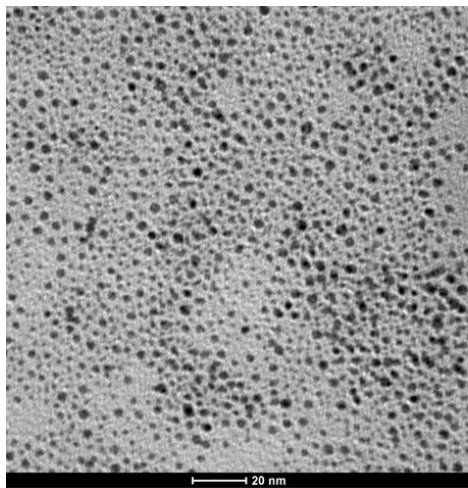
Figure 6-12. TEM image of **21**-AuNP and its size distribution: average diameter=1.50 nm (σ= 0.27 nm).
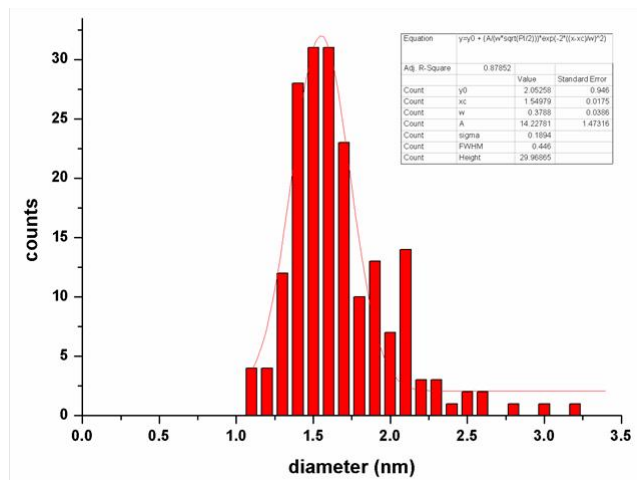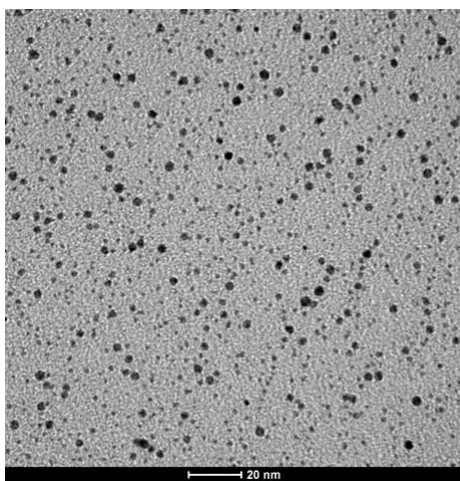
Figure 6-13. TEM image of **22**-AuNP and its size distribution: average diameter=1.55 nm (σ= 0.19 nm).
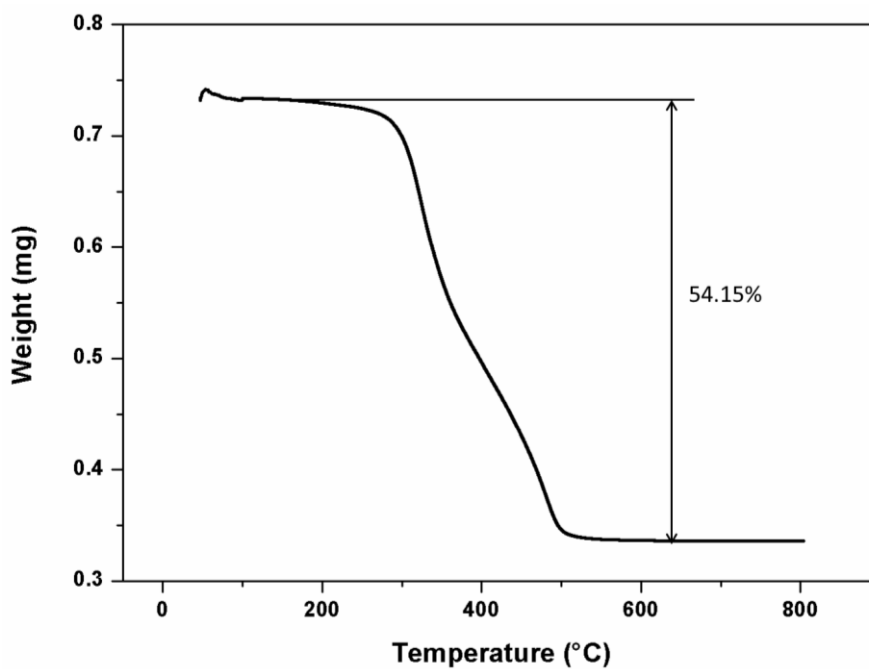
Figure 6-14. TGA analysis of **19**-AuNP under air atmosphere.
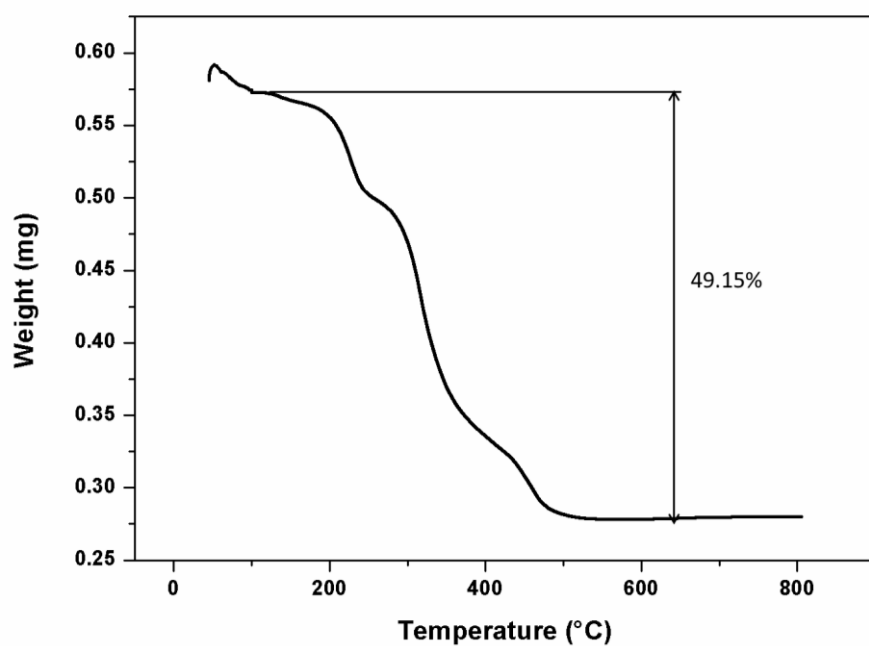
Figure 6-15. TGA analysis of **21**-AuNP under air atmosphere.
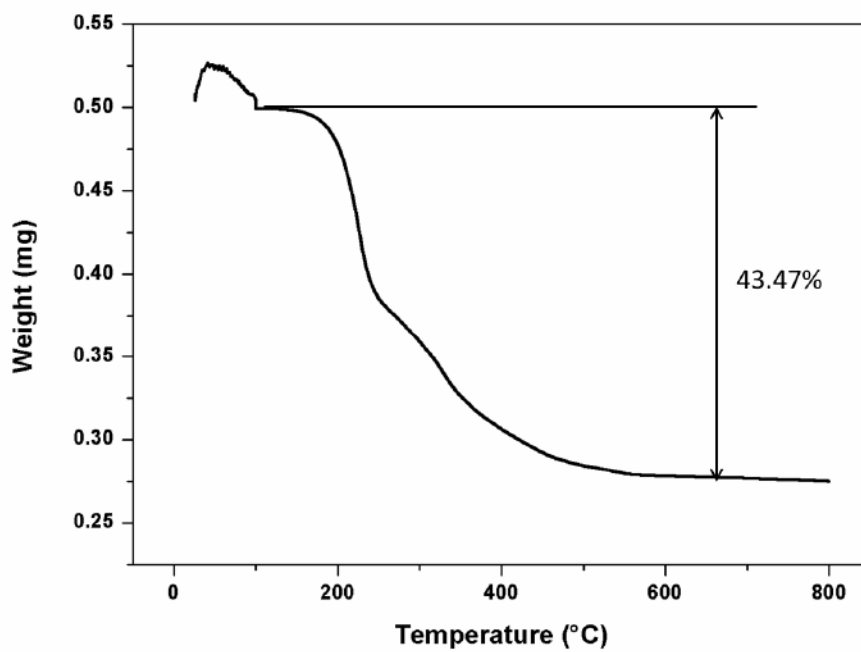
Figure 6-16. TGA analysis of **22**-AuNP under air atmosphere.
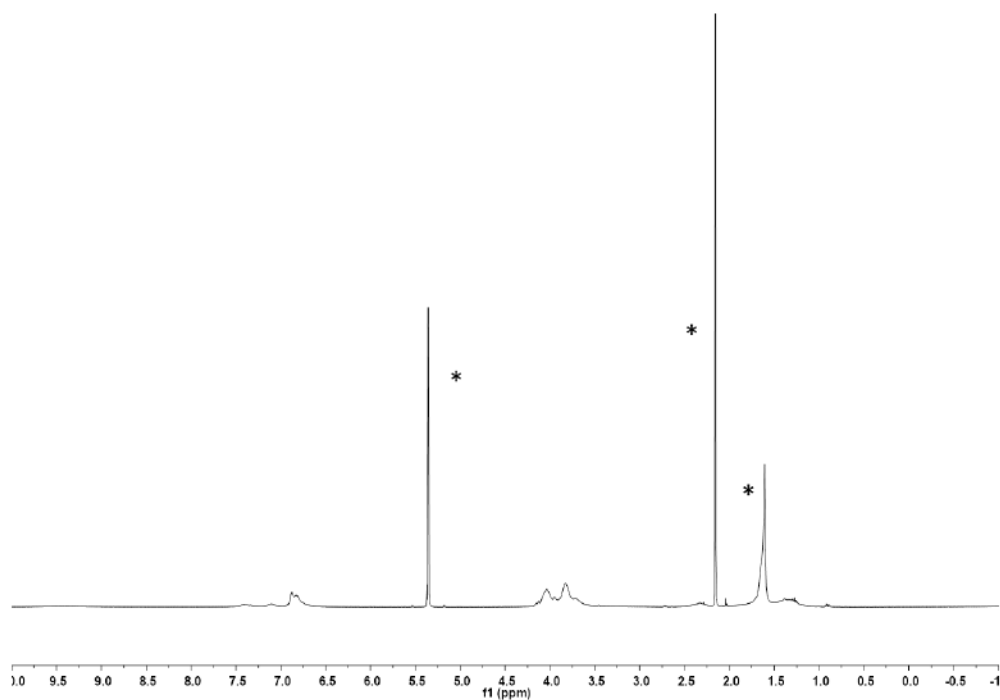
Figure 6-17. ^{1}H NMR spectrum of **19**-AuNP in CD_2Cl_2 (* indicates the residual solvents and impurities).
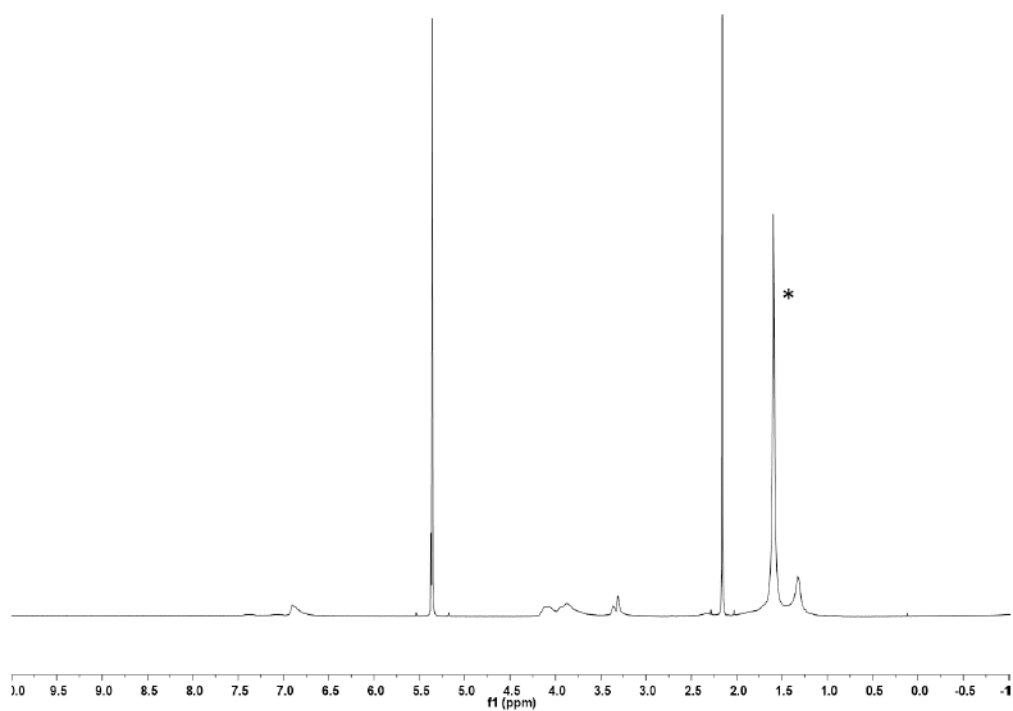
Figure 6-18. ^{1}H NMR spectrum of **21**-AuNP in CD$_2$Cl$_2$ (* indicates the residual solvents and impurities).
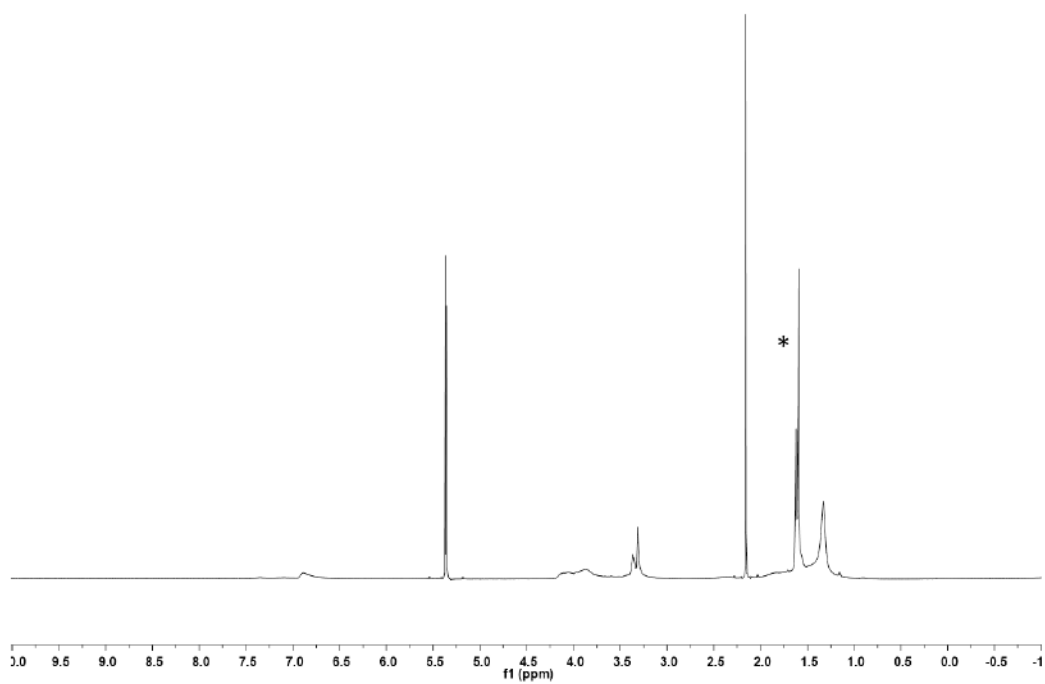
Figure 6-19. ^{1}H NMR spectrum of **22**-AuNP in CD$_2$Cl$_2$ (* indicates the residual solvents and impurities).
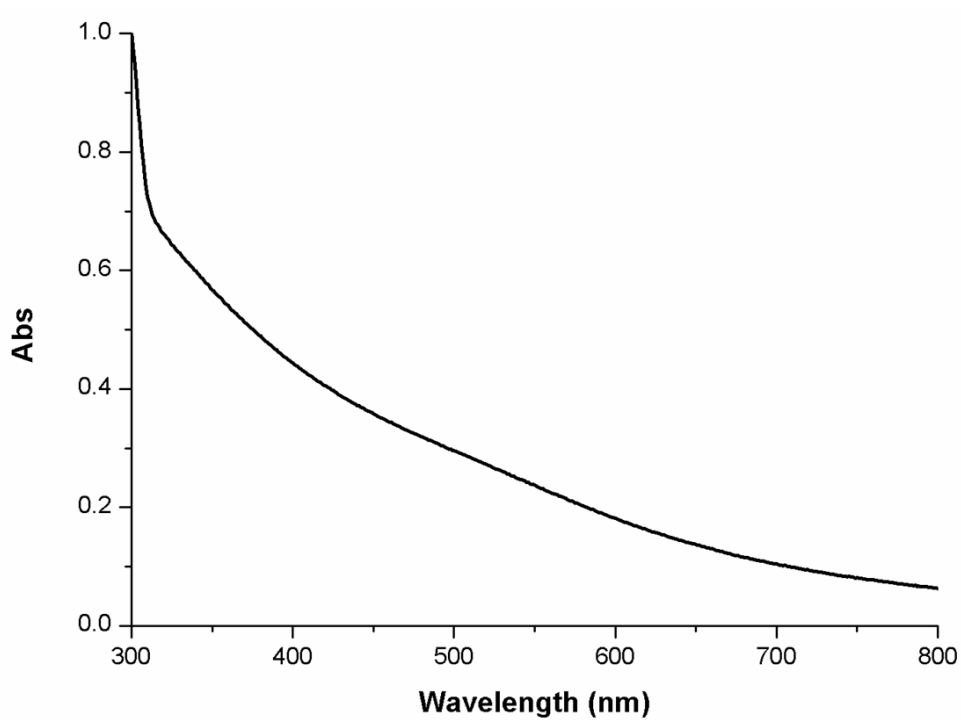
Figure 6-20. UV-Vis spectrum of **19**-AuNP (0.1 mg/mL) at 25 °C in CH_2Cl_2.
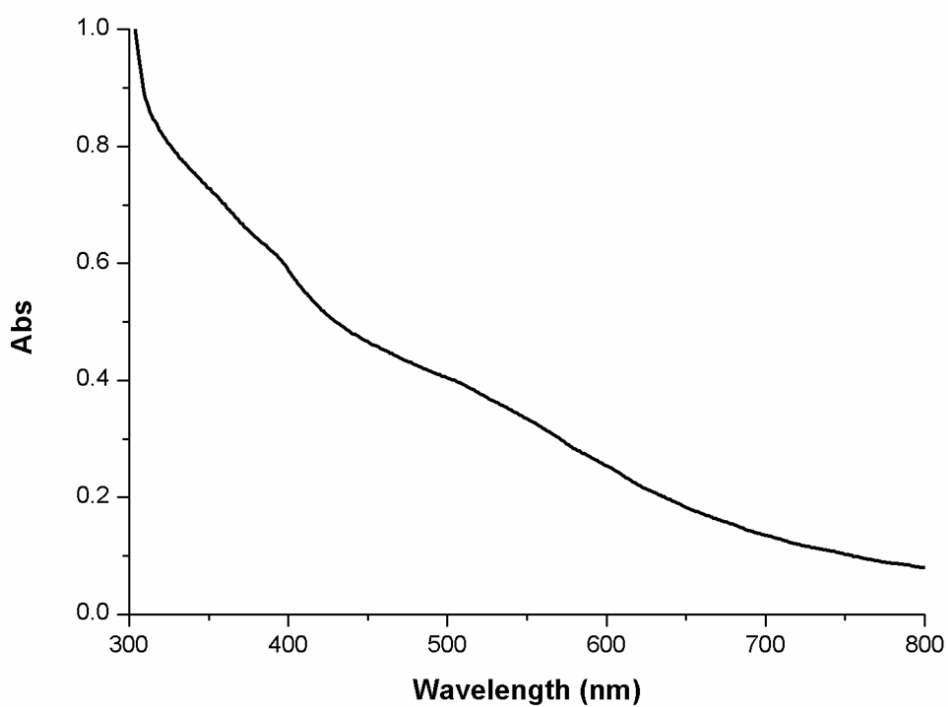
Figure 6-21. UV-Vis spectrum of **21**-AuNP (0.1 mg/mL) at 25 °C in CH_2Cl_2.
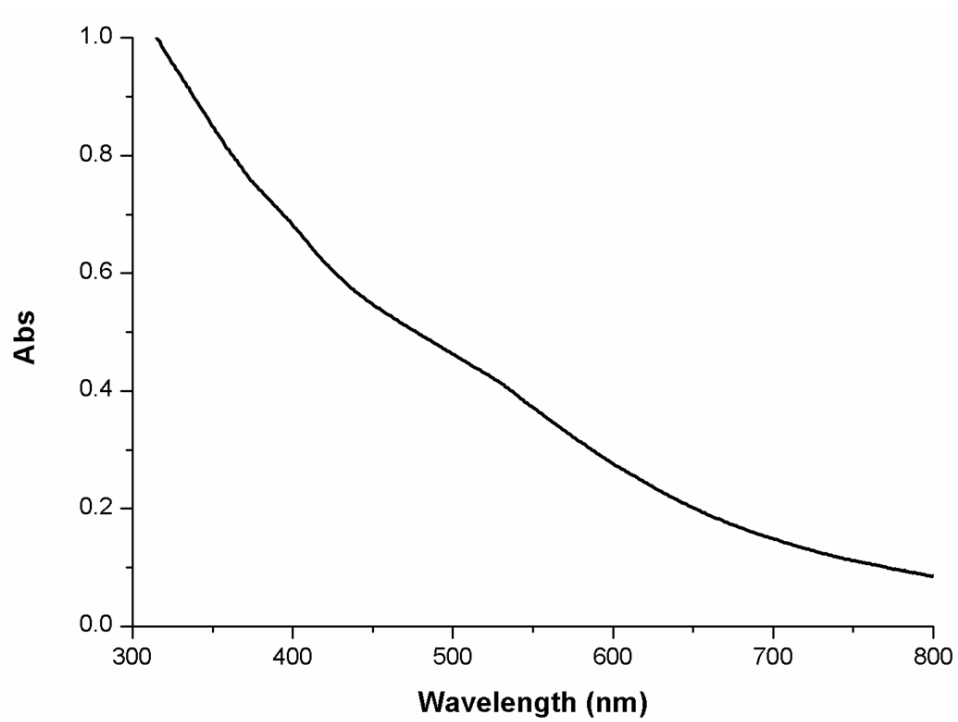
Figure 6-22. UV-Vis spectrum of **22**-AuNP (0.1 mg/mL) at 25 °C in CH_2Cl_2.

Chapter 7. Transformation of ligand-shell morphology during molecular recognition on gold nanoparticles

7.1 Introduction

The morphology of ligand-shell features a large number of properties of gold nanoparticles.[72, 130] In this chapter, we describe a well characterized randomly distributed gold nanoparticle system can be induced to cluster through the process of molecular recognition. For the first time, the morphology of the mixed monolayer is shown in the dynamic perspective.

Monolayer protected gold nanoparticles have been applied in diverse fields ranging from drug delivery,[31, 131] catalysis[132, 133] to, especially, molecular recognition.[20, 92] Emerged as a highly complex scaffolds, the AuNPs can dynamically regulate their responses to the changes in the external conditions. In particular, when a mixture of ligands is used to coat gold nanoparticles, cooperation between the mixed monolayer can be exploited.[7] Due to this benefit, mixed monolayer protected gold nanoparticle is becoming appealing to scientists. Based on the previous study, it has been shown that the morphology of the mixed monolayer of gold nanoparticles contributes significantly to their related properties. Therefore, intensive attention was paid to the investigation of the monolayer distribution of the mixed ligands.[77] Existing strategies, such as STM, AFM, NMR, EPR and so on, provided the possibility to determine the morphology of the mixed AuNPs. However, all the information acquired is based on sole the physical distribution of the monolayer. When applied to the process of molecular recognition, how the mixed monolayer would regulate in the presence of incoming analytes, which can be called chemical dynamic distribution, has never been reported.

In the previous study of our group, we have reported that gold nanoparticle coated with thiol **1** is able to detect salicylate using the NOE-pumping method[43] due to the spontaneous formation of deep hydrophobic pockets in the monolayer. **14**-AuNP, of which the hydrophobic interaction is modulated by inserting a polar oxygen atom in the alkyl chain, could not detect salicylate at the same condition. With this in mind, we assume that if these two dissimilar thiol molecules were coated on the surface of gold nanoparticles, they will respond differently in the presence of salicylate, which may in turn have an effect on the morphology of the mixed monolayer.

7.2 NMR chemosensing
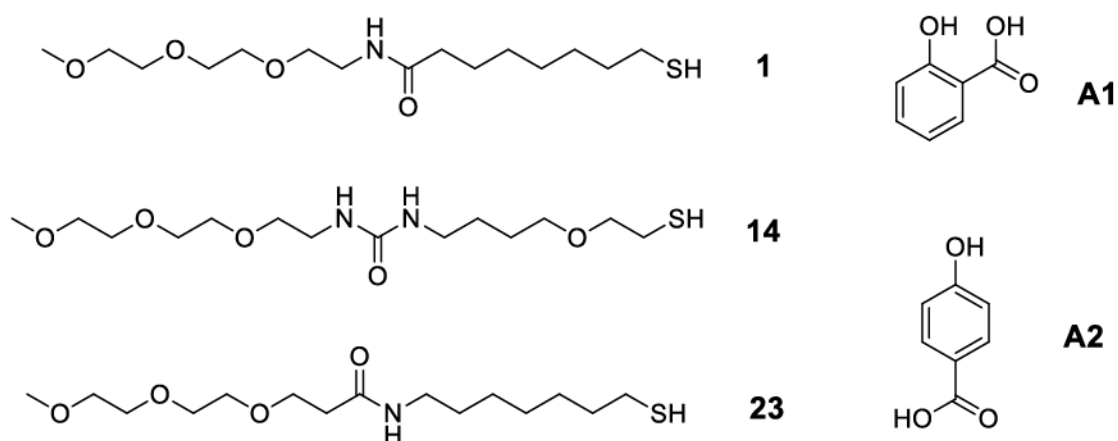
Scheme 7-1. The structure of the coating ligands and analytes used in this study.

To experimentally test our hypothesis, thiol **14** and thiol **23**, synthesized by slightly changing the chemical structure of thiol 1 to obtain separated diagnostic ^{1}H NMR signals of the two ligands, were used to prepare mixed monolayer protected gold nanoparticles. The mixed AuNPs with different surface ratio of thiol 14/thiol 23 were prepared using the method of direct synthesis. The composition of the **24**-AuNP (thiol 14/thiol 23=50%: 50%) and **25**-AuNP (thiol 14/thiol 23=25%: 75%) were determined by the integration of the diagnostic peaks arising from the two thiols of its ^{1}H NMR spectrum.
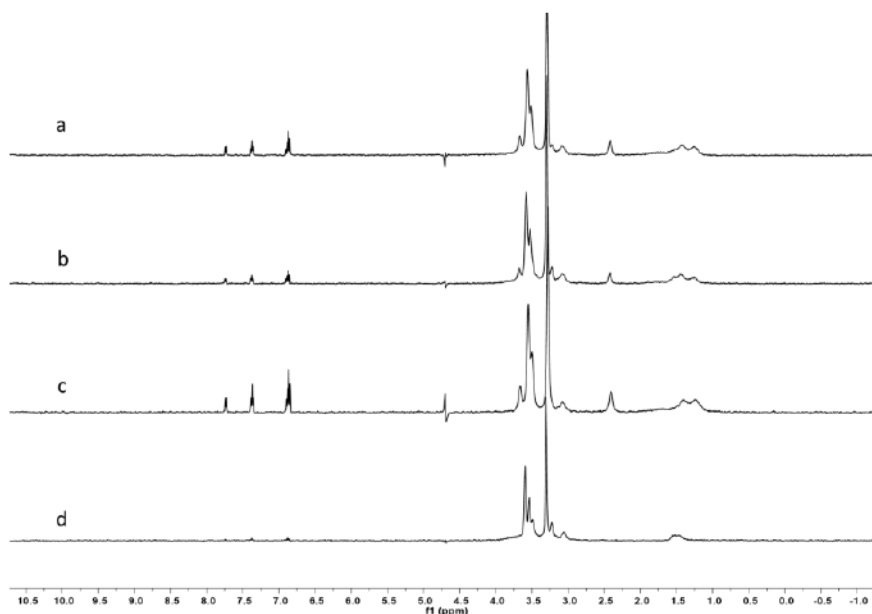
Figure 7-1. NOE-pumping spectra of salicylate in the presence of a) **25**-AuNP, b) **24**-AuNP, c) **23**-AuNP, d) **14**-AuNP. Conditions: AuNPs 2 mM in thiols, Salicylate 20 mM, carbonate buffer 20 mM pD=10.0.
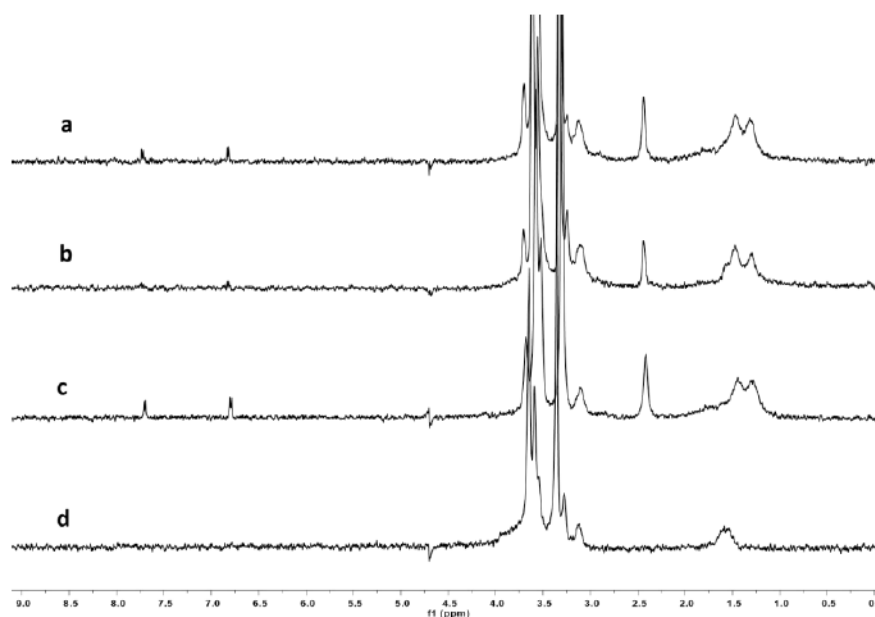
Figure 7-2. NOE-pumping spectra of 4-hydroxybenzoate in the presence of a) **25**-AuNP, b) **24**-AuNP, c) **23**-AuNP, d) **14**-AuNP. Conditions: AuNPs 2 mM in thiols, 4-hydroxybenzoate 20 mM, carbonate buffer 20 mM pD=10.0.

First, we investigated the ability of the four kinds of AuNPs (**14, 23, 24** and **25**-AuNP) to detect organic molecules with the NMR chemosensing protocol. The NOE-pumping sequence was used to anayze samples containing the nanoparticles (2 mM in thiols) and salicylate (20 mM) in buffered D_2O solution at pD=10.0. As revealed from Figure 7-1 d), **14**-AuNP could not detect salicylate at this condition since no signals of salicylate were appeared in the NOE-pumping spectrum. **23**-AuNP, as expected, is able to detect salicylate with a good sensitivity. When tested with the mixed **24,** and **25**-AuNP, though weaker compared to **23**-AuNP, clear signals arising from salicylate were observed from the NOE-pumping spectra. Further speculation suggested that **25**-AuNP has a much higher sensitivity to salicylate compared to **24**-AuNP. When 4-hydroxybenzoate was used as the substrate (Figure 7-2), a similar tendency but much lower sensitivity was observed. Considering the significant difference of these two mixed AuNPs in sensing performance and their relatively small composition difference, we assume some other factor was affecting their sensing behavior.

7.3 Morphology determination based on MALDI

Based on our previous study, it has been demonstrated that **1**-AuNP can detect salicylate thanks to the spontaneous formation of the binding pockets, which are formed by the alkyl chain. Therefore, not only the ligand-shell composition but the mixed monolayer distribution can contribute significantly to the sensing behavior of AuNPs. To further understand the different

sensing performance of the two mixed AuNPs, the monolayer distribution of the mixed AuNPs was investigated taking advantage of MALDI.[81] This approach is based on the fact that Au_4L_4 is the most abundant species within the fragments of AuNPs. Hence the distribution of $Au_4L_xL'_{4-x}$ can be exploited to investigate the ligands arrangement on the surface of the AuNPs. If the fragments of $Au_4L_xL'_{4-x}$ follow a binominal distribution, this indicates the AuNPs are randomly distributed. The larger the fragments deviate from the binominal distribution, the higher degree of phase separation occurs. When **24-AuNP** and **25-AuNP** were tested with this protocol (Figure 7-3), it turns out that the ligands distribution of both AuNPs agrees well with the binomial distribution. The residual sum of squares (r) for **24-AuNP** and **25-AuNP**, a measurement of deviation from the binomial model, is 3.18×10^{-4} and 2.58×10^{-3}, respectively. This result indicated that both of the AuNPs are well randomly distributed.
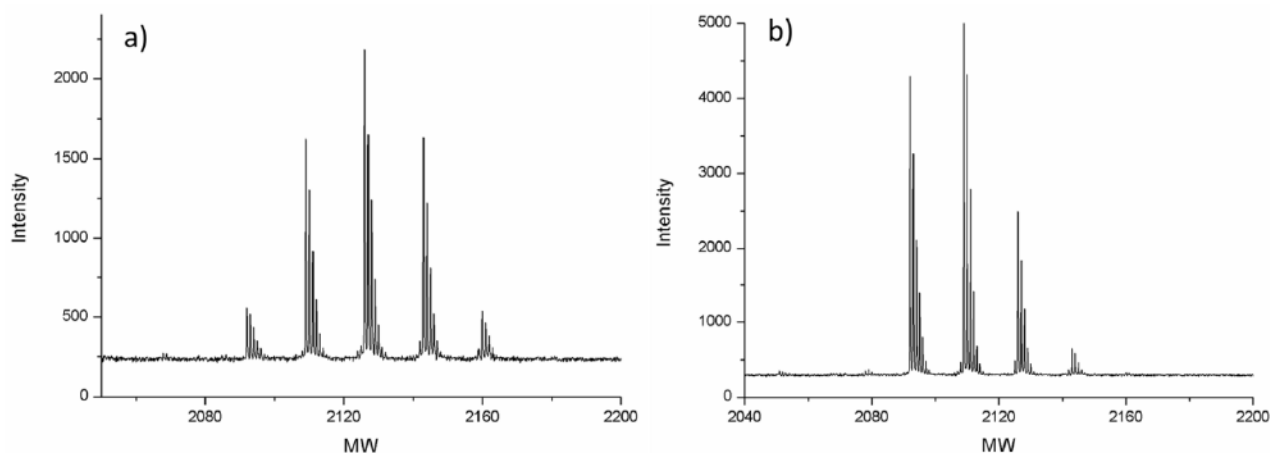
Figure 7-3. MALDI spectra of a) **24-AuNP**, b) **25-AuNP**. From left to right, the five peaks are assigned to $Au_4(23)_4$, $Au_4(23)_3(14)_1$, $Au_4(23)_2(14)_2$, $Au_4(23)_1(14)_3$, $Au_4(14)_4$.

7.4 Morphology determination during molecular recognition

To further investigate if the randomly distributed feature of the two mixed AuNPs still remained in the presence of analyte, we reversed the NOE-pumping approach by transferring magnetization from the analyte to the monolayer with a selective NOESY pulse. With this technique, the protons which are arranged in the close proximity to the analyte can receive magnetization from the substrate and their signals are present in the NOESY spectrum. From a quantitative point of view, the larger the number of close contacts between the analyte and the coating ligands, the stronger the thiol molecular' NOE signals will be obtained. The NOESY spectra in Figure 7-4 a) clearly showed that in the presence of **25-AuNP**, we can only see the NOE signal of thiol 23 because of the absence of peak at 3.23 ppm, which is diagnostic peak of thiol 14. But in the case of **24-AuNP**

(Figure 7-4 b)), both the signals arising from thiol 14 and 23 were observed, albeit weaker, in the NOESY spectrum. This result revealed that in **25-AuNP**, binding sites made only by thiol **23** are present and are effective in salicylate binding. Taking into consideration that the morphology of the mixed monolayer is confirmed to be random by MALDI, this result indicated that the addition of salicylate induced the clustering of thiol 23 to allow position optimization and conformational reorganization. On the contrary, in **24-AuNP**, the larger fraction of thiol 14 results into a higher degree of mixing of the two thiols, and no sites formed only by thiol 23 are present. Binding sites, on the other hand, were formed by both thiols 14 and 23 but their affinity for salicylate is largely reduced.
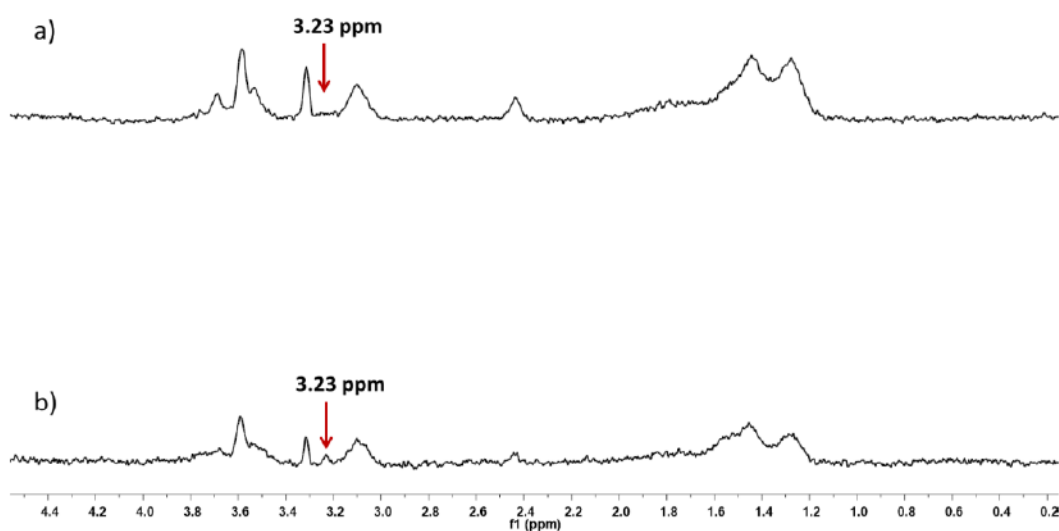
Figure 7-4. NOESY spectra of (a) **25-AuNP**, (b) **24-AuNP** in the presence of salicylate. Conditions: AuNPs 5 mM in thiols, salicylate 20 mM, carbonate buffer 20 mM pD=10.0.
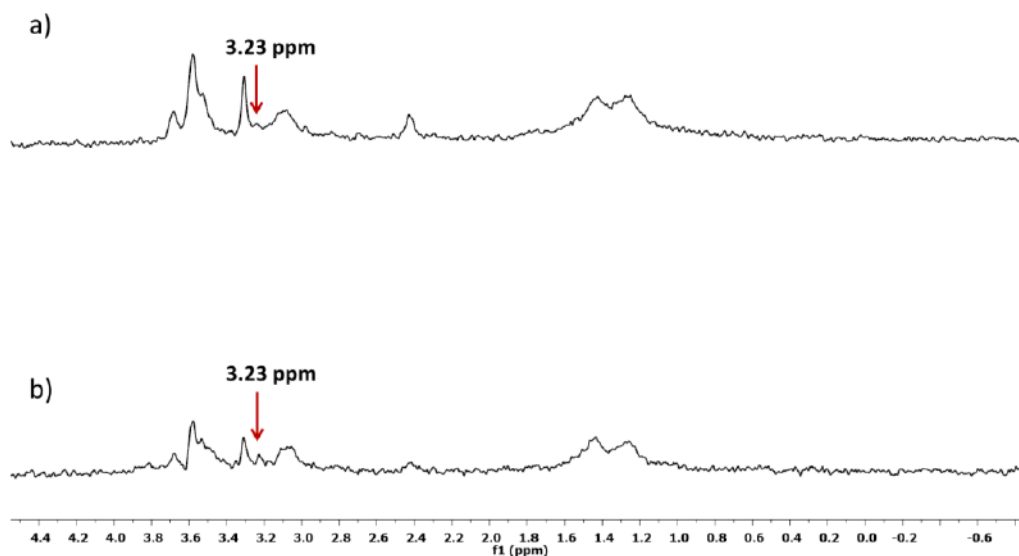
Figure 7-5. NOESY spectra of (a) **25-AuNP**, (b) **24-AuNP** in the presence of 4-hydroxybenzoate. Conditions: AuNPs 5 mM in thiols, 4-hydroxybenzoate 20 mM, carbonate buffer 20 mM pD=10.0.

The results discussed above showed that the morphology modification of the mixed AuNPs can be induced by incoming molecules. To further study this point, selective NOESY experiments were performed with samples containing AuNPs (5 mM in thiols) and 4-hydroxybenzoate (20 mM) in buffered D_2O solution. As revealed from Figure 7-5, when the magnetization was transferred from 4-hydroxybenzoate to AuNPs, both the signals of thiol 14 and 23 were observed for either **24** and **25**-AuNP. This suggested that 4-hydroxybenzoate, is not able to induce the clustering of the thiol 23, which we assume is due to its low affinity to **23**-AuNP.

7.5 Conclusions

In conclusion, here we have demonstrated that the coating ligands of the mixed AuNPs can be reorganized, from random distribution to clusters, in the presence of incoming compound. The ability to alter the morphology of the mixed AuNPs depends on both the initial mixing degree of the coating monolayer and the affinity between the analyte and the monolayer.

7.6 Experimental section

7.6.1 Synthesis of N-(7-mercaptoheptyl)-3-(2-(2-methoxyethoxy)ethoxy)propan-amide (thiol 23)

Thiol 23 was synthesized according to the following scheme:
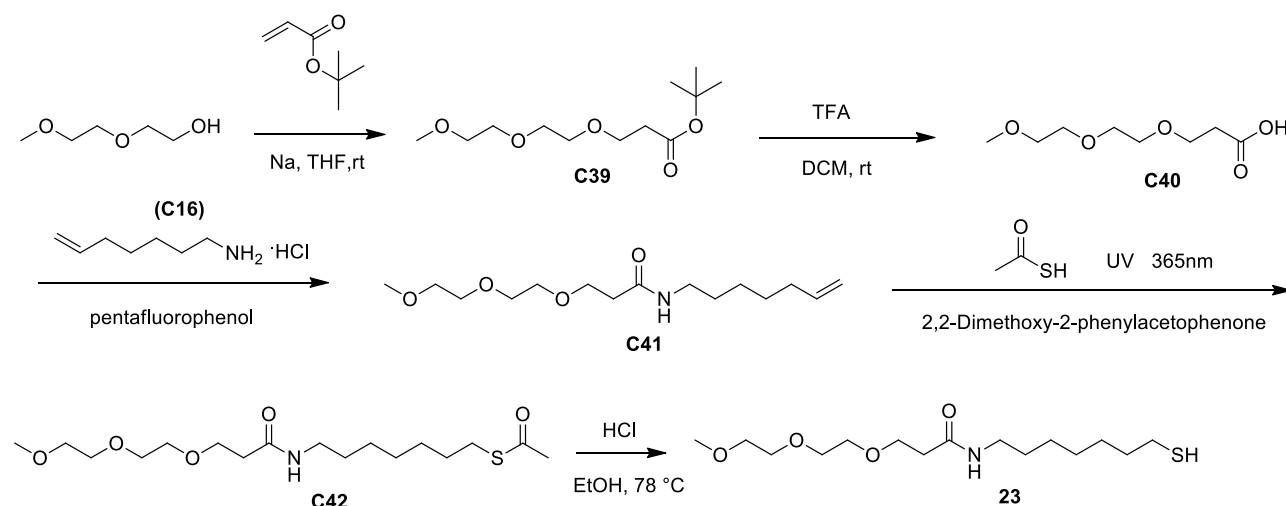
Scheme 7-2. The synthesis of thiol 23.

Synthesis of tert-butyl 3-(2-(2-methoxyethoxy)ethoxy)propanoate (C39). 2-(2-methoxyethoxy)-ethanol (2.25 g, 8.32 mmol, 3.0 equiv) was dissolved in anhydrous THF (3.0 mL), then Na (4.30 mg, 0.187 mmol, 0.03 equiv) and tert-butyl acrylate (800 mg, 6.24 mmol, 1.0 equiv) were added to the above solution. The mixture was stirred for 12 hours at room temperature. After solvent

evaporation, the crude product was purified by flash chromatography (silica gel, eluent: Hexane/ EtOAc 5:5). 930 mg (58%) of (**C39**) were obtained.

¹H NMR (500 MHz, CDCl₃) δ 3.74-3.67 (t, 2H, CH₂O), 3.66–3.59 (m, 6H, CH₂O), 3.56 – 3.51 (m, 2H, CH₂O), 3.37 (s,3H, CH₃O), 2.52-2.47 (t, 2H, CH₂), 1.44 (s, 9H, CH₃).

¹³C NMR (126 MHz, CDCl₃) δ 170.74 (1C, COO), 80.36 (1C, C), 71.85 (1C, CH₂O), 70.45 (1C, CH₂O), 70.29 (1C, CH₂O), 66.81 (1C, CH₂O), 58.91 (1C, CH₂O), 36.20 (1C, CH₂), 28.00 (1C, CH₃O).

ESI-MS (m/z): 248.7 [M+H⁺].

Synthesis of 3-(2-(2-methoxyethoxy)ethoxy)propanoic acid (C40). C39 (0.805 g, 3.24 mmol) was dissolved in anhydrous DCM (1.5 mL) and trifluoride acetic acid (1.5 mL) was added at 0 °C. The mixture was stirred for 5 hours at room temperature. After solvent evaporation, the crude product obtained was further purified by flash chromatography (silica gel, eluent: DCM/ MeOH 9:1). 580 mg (93%) of (**C40**) were obtained.

¹H NMR (500 MHz, CDCl3) δ 3.82-3.76 (t, 2H, CH₂O), 3.70 – 3.63 (m, 6H, CH₂O), 3.62 – 3.57 (t, 2H, CH₂O), 3.41 (s,3H, CH₃O), 2.70-2.63 (t, 2H, CH₂).

¹³C NMR (126 MHz, CDCl₃) δ 176.64 (1C, COO), 71.74 (1C, CH₂O), 70.31 (1C, CH₂O), 70.21 (1C, CH₂O), 70.17 (1C, CH₂O), 66.34 (1C, CH₂O), 58.88 (1C, CH₂O), 34.67 (1C, CH₂).

ESI-MS (m/z): 193.0 [M+H⁺], 215.0 [M+Na⁺].

Synthesis of N-(hept-6-en-1-yl)-3-(2-(2-methoxyethoxy)ethoxy)propanamide (C41). C40 (501 mg, 2.61 mmol, 1.3 equiv) and pentafluorophenol (960 mg, 5.21 mmol, 2.6 equiv) were dissolved in anhydrous CH₂Cl₂ (4.0 mL) and N-(3-Dimethylaminopropyl)-N-ethyl-carbodiimide hydrochloride (EDC, 999 mg, 5.21 mmol, 2.6 equiv) was added. The mixture was stirred for 12 hours under nitrogen. Then N,N-diisopropylethylamine (DIPEA, 311 mg, 2.41 mmol, 1.2 equiv) and SY83 (300 mg, 2.01 mmol, 1.0 equiv) were added. The mixture was stirred at room temperature for another 12 hours. After solvent evaporation, the crude product was purified by flash chromatography (silica gel, eluent: EtOAc/MeOH 9.5:0.5). 351 mg (61%) of **C41** were obtained.

¹H NMR (500 MHz, CDCl₃) δ 6.61-6.36 (s, 1H, NH), 5.85 – 5.68 (m, 1H, CH), 5.08 – 4.86 (dd, 2H, CH₂), 3.75-3.69 (t,2H, CH₂O), 3.67-3.61 (m, 6H, CH₂), 3.57-3.52 (t, 2H, CH₂O), 3.37 (s, 3H, CH₃O), 3.26-3.18 (q, 2H, CH₂N), 2.49-2.42 (t, 2H, CH₂), 2.08-1.99 (q, 2H, CH₂), 1.55-1.46 (qn, 2H, CH₂), 1.44-1.36 (qn, 2H, CH₂), 1.36-1.28 (qn, 2H, CH₂).

^{13}C NMR (126 MHz, CDCl$_3$) δ 171.48 (1C, CO), 138.76 (1C, CH), 114.41 (1C, CH$_2$), 71.92 (1C, CH$_2$O), 70.48 (1C, CH$_2$O), 70.36 (1C, CH$_2$O), 70.19 (1C, CH$_2$O), 67.34 (1C, CH$_2$O), 59.01 (1C, CH$_3$O), 39.32 (1C, CH$_2$N), 36.97 (1C, CH$_2$), 33.62 (1C, CH$_2$), 29.45 (1C, CH$_2$), 28.53 (1C, CH$_2$), 26.38 (1C, CH$_2$).

ESI-MS (m/z): 288.2 [M+H$^+$], 310.2 [M+Na$^+$].

Synthesis of S-(11-oxo-2,5,8-trioxa-12-azanonadecan-19-yl) ethanethioate (C42). C41 (268 mg, 0.933 mmol, 1.0 equiv) was dissolved in methanol (3.0 mL). Nitrogen was injected into the solution for 20 min to remove oxygen. Afterwards, 2, 2-Dimethoxy-2-phenylacetophenone (12.1 mg, 0.05 mmol, 0.05 equiv) and ethanethioic S-acid (284 mg, 3.73 mmol, 4.0 equiv) were added. The mixture was left under irradiation (UV, 365 nm) for 2 hours. After solvent evaporation, the crude product was purified by flash chromatography (silica gel, eluent: EtOAc/ MeOH 10:0.5). 284 mg (84%) of (**C42**) were obtained.

^{1}H NMR (500 MHz, MeOD) δ 3.76-3.71 (t, 2H, CH$_2$O), 3.66-3.59 (m, 6H, CH$_2$O), 3.57-3.53 (t, 2H, CH$_2$O), 3.38 (s, 3H, CH$_3$O), 3.22-3.16 (q, 2H, CH$_2$N), 2.91-2.84 (t, 2H, CH$_2$S), 2.47-2.41 (t, 2H, CH$_2$), 2.32 (s, 3H, CH$_3$CO), 1.63-1.55 (qn, 2H, CH$_2$), 1.55-1.46 (qn, 2H, CH$_2$), 1.45-1.31 (m, 6H, CH$_2$).

^{13}C NMR (126 MHz, CDCl$_3$) δ 196.11 (1C, COS), 172.45 (1C, CON), 71.57 (1C, CH$_2$O), 70.06 (1C, CH$_2$O), 69.98(1C, CH$_2$O), 69.93 (1C, CH$_2$O), 66.93 (1C, CH$_2$O), 57.70 (1C, CH$_3$O), 38.93 (1C, CH$_2$N), 36.32 (1C, CH$_2$), 29.30 (1C, CH$_2$S), 29.11 (1C, CH$_3$), 28.90 (1C, CH$_2$), 28.44 (1C, CH$_2$), 28.40 (1C, CH$_2$), 28.31 (1C, CH$_2$), 26.37 (1C, CH$_2$).

ESI-MS (m/z): 364.2 [M+H$^+$], 386.1 [M+Na$^+$].

Synthesis of N-(7-mercaptoheptyl)-3-(2-(2-methoxyethoxy)ethoxy)propanamide (23). C42 (35.9 mg, 0.0988 mmol) was dissolved in ethanol (2.0 mL). A 6 M HCl solution in water (2.0 mL) was added and the mixture was stirred at 78 °C for 2 hours. The reaction mixture was allowed to cool and the solvent was evaporated to obtain 31.7 mg (quantitative) of **23**.

^{1}H NMR (500 MHz, MeOD) δ 3.78-3.73 (t, 2H, CH$_2$O), 3.66–3.61 (m, 6H, CH$_2$O), 3.57 – 3.54 (t, 2H, CH$_2$O), 3.38 (s, 3H, CH$_3$O), 3.29-3.22 (t, 2H, CH$_2$N), 2.59-2.48 (m, 4H, CH$_2$S), 1.66-1.59 (qn, 2H, CH$_2$), 1.59-1.52 (m, 2H, CH$_2$), 149-1.40 (m, 2H, CH$_2$), 1.40-1.33 (m, 4H, CH$_2$).

^{13}C NMR (126 MHz, MeOD) δ 173.36 (1C, COS), 71.56 (1C, CH$_2$O), 70.06 (1C, CH$_2$O), 69.98 (1C, CH$_2$O), 69.96 (1C, CH$_2$O), 66.68 (1C, CH$_2$O), 57.73 (1C, CH$_3$O), 39.61 (1C, CH$_2$N), 35.78 (1C, CH$_2$S), 33.71 (1C, CH$_2$), 28.52 (1C, CH$_2$), 28.41 (1C, CH$_3$), 27.90 (1C, CH$_2$), 26.40 (1C, CH$_2$), 23.55 (1C, CH$_2$).

ESI-MS (m/z): 322.2 [M+H$^+$], 344.2 [M+Na$^+$].

7.6.2 Preparation and characterization of **23, 24** and **25**-AuNP.

Preparation of 23, 24 and 25-AuNP. **23, 24** and **25**-AuNP were prepared following a previously reported two-step procedure.[18] A solution of $HAuCl_4 \times 3H_2O$ (50.0 mg, 0.127 mmol, 1.0 equiv) in water (0.5 mL) was extracted with a solution of tetraoctylammonium bromide (0.175 g, 0.318 mmol, 2.5 equiv) in N_2 purged toluene (125 mL). To the resulting reddish-orange organic solution dioctylamine (0.613 g, 2.54 mmol, 20 equiv) was added (the amount of dioctylamine was calculated in order to obtain 2 nm nanoparticles). The mixture is vigorously stirred under N_2 for 1.5 hours. During this period of time the color of the mixture fades. Then the solution is cooled at 0°C and a $NaBH_4$ solution (48.0 mg, 1.27 mmol, 10 equiv) in H_2O (1.0 mL) is then rapidly added. The color of the solution turns rapidly to black and after 1.5 hours of stirring at 0 °C, the aqueous layer is removed. To the obtained nanoparticle solution, the desired thiol 23 (0.0988 mmol, 2.0 equiv) or the mixed thiols (**24**-AuNP, thiol 23/thiol 14=50%/50%. **25**-AuNP thiol 23/thiol 14=75%/25%) dissolved in 3 mL of MeOH was rapidly added. The reaction mixture was stirred for 3 hours at 0°C. Then the solution was concentrated and washed with petroleum ether, acetonitrile and methanol using centrifuge for 8 times.

Characterization of 23, 24 and 25-AuNP. TEM analysis (Figures 7-6, 7-7 and 7-8) of the different samples of nanoparticles yields an average diameter for **23**-AuNP of 1.6 ± 0.2nm, for **24**-AuNP and **25**-AuNP of 1.6 ± 0.2 nm and 1.6± 0.2 nm. This data, together with the loss of organic weight obtained by TGA analysis (Figures 7-9, 7-10 and 7-11), indicate that the formula for AuNP is $Au_{131}SR_{58}$ for **23**-AuNP, $Au_{127}SR_{59}$ for **24**-AuNP, $Au_{136}SR_{61}$ for **25**-AuNP. Thiols concentrations in the nanoparticles solutions for all the fluorescence experiments were determined by the weight of nanoparticles dissolved and the average formula determined for the nanoparticles as shown above. NMR analysis (Figure 7-12, 7-13 and 7-14) indicates monolayer formation (broadening of all signals and missing of the SCH_2CH_2 protons' signals). In addition, ^{1}H NMR of the I_2 decomposed AuNPs were performed, the integral of the separated signals arising from two thiols showed the monolayer composition of **24**-AuNP and **25**-AuNP. UV-vis spectra (Figure 7-15, 7-16 and 7-17) recorded also showed no or small plasmonic band at 520 nm, which suggests the size of the AuNPs is smaller than 3 nm.
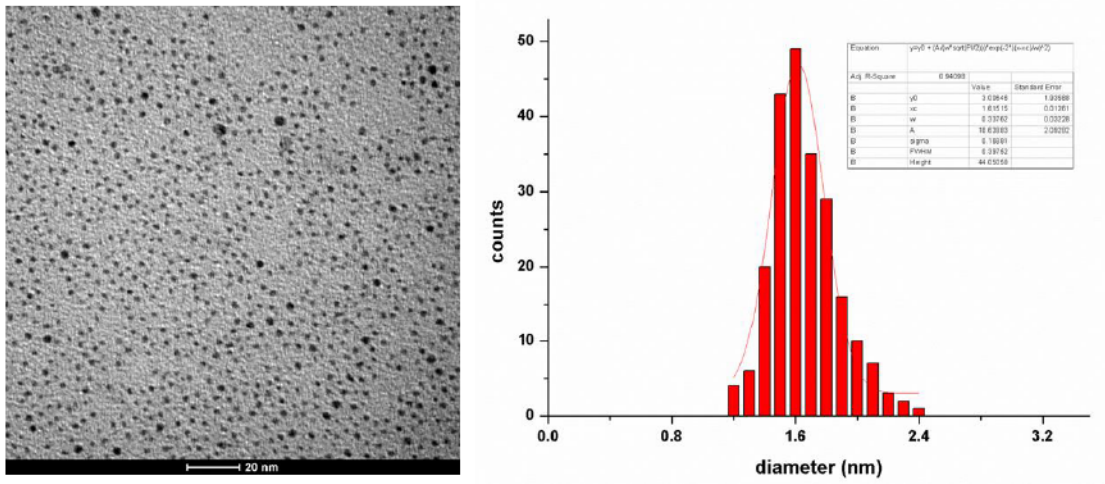
Figure 7-6. TEM analysis of **23**-AuNP. The average diameter is 1.6± 0.2nm.
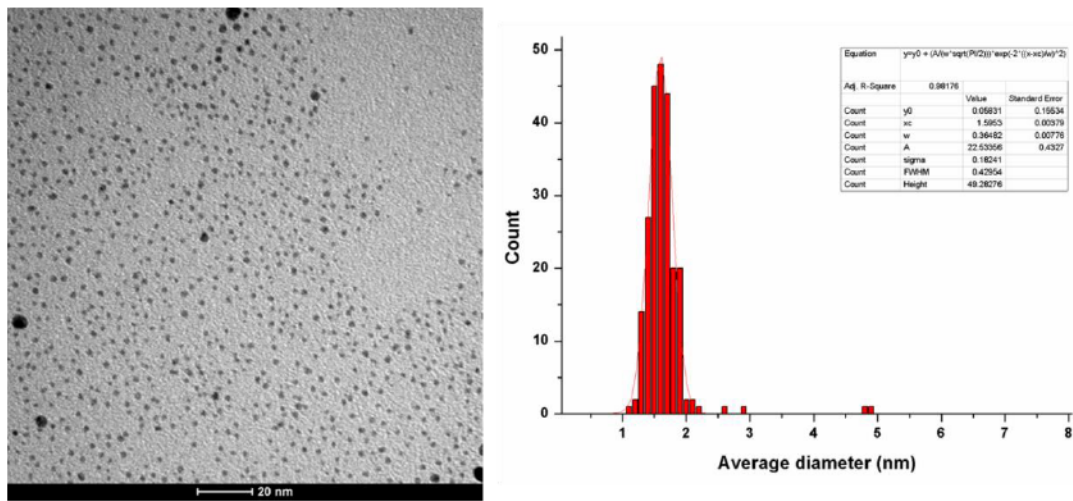
Figure 7-7. TEM analysis of **24**-AuNP. The average diameter of is 1.6± 0.2nm.
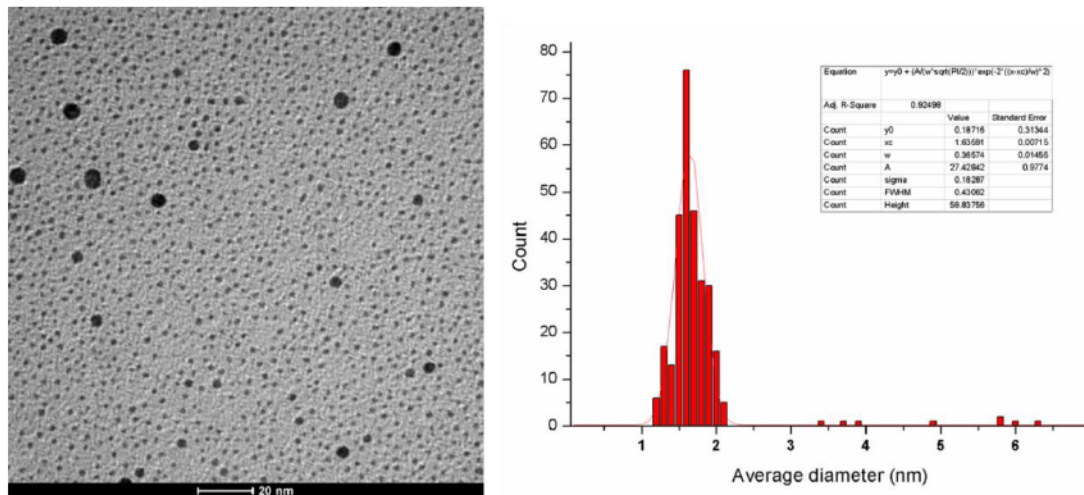
Figure 7-8. TEM analysis of **25**-AuNP. The average diameter is 1.6± 0.2nm.
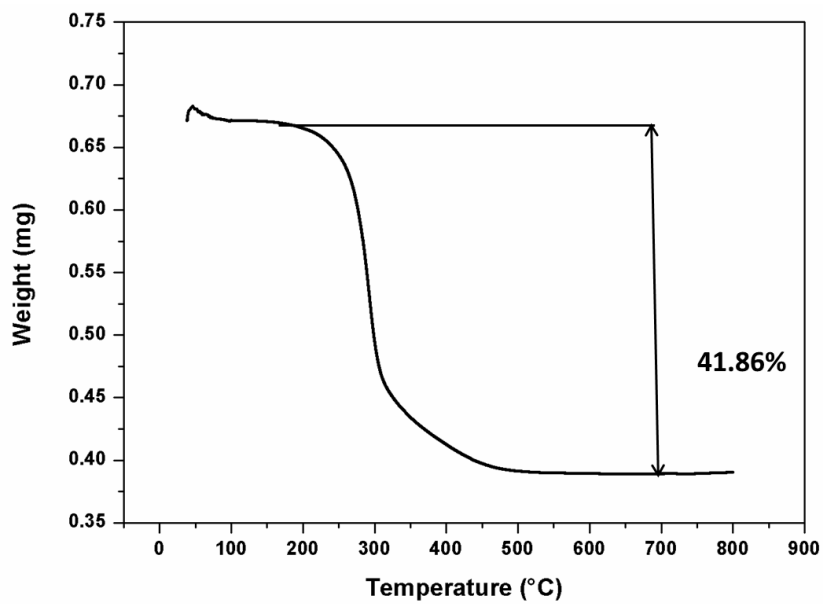
Figure 7-9. TGA analysis of **23**-AuNP under air atmosphere.
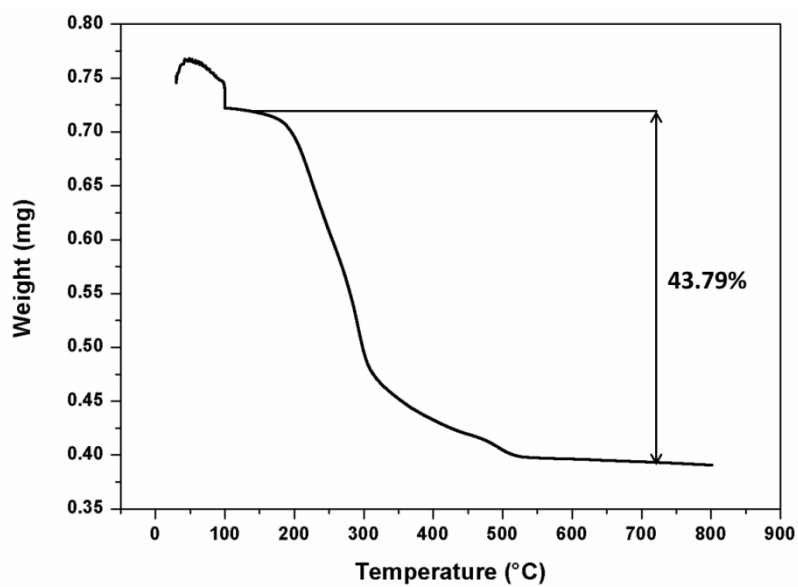
Figure 7-10. TGA analysis of **24**-AuNP under air atmosphere.
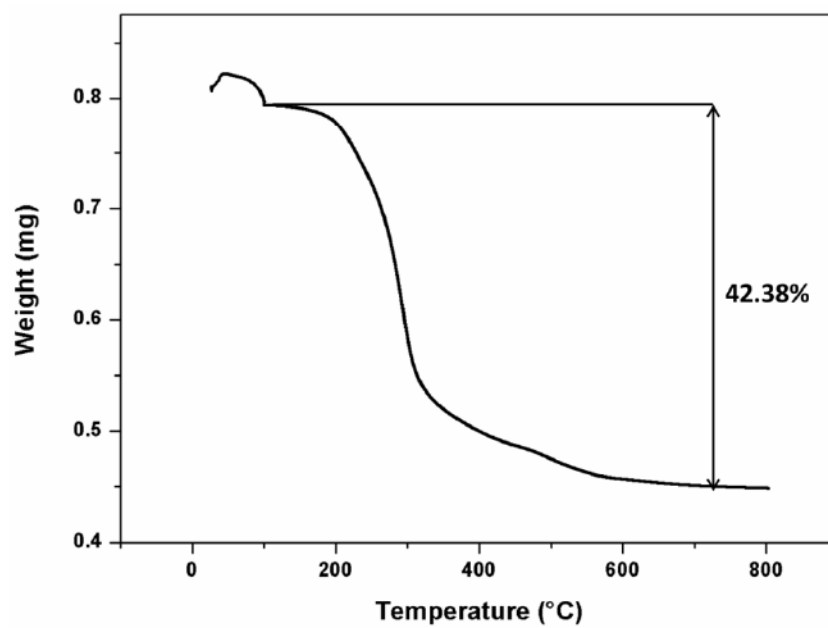
Figure 7-11. TGA analysis of **25**-AuNP under air atmosphere.
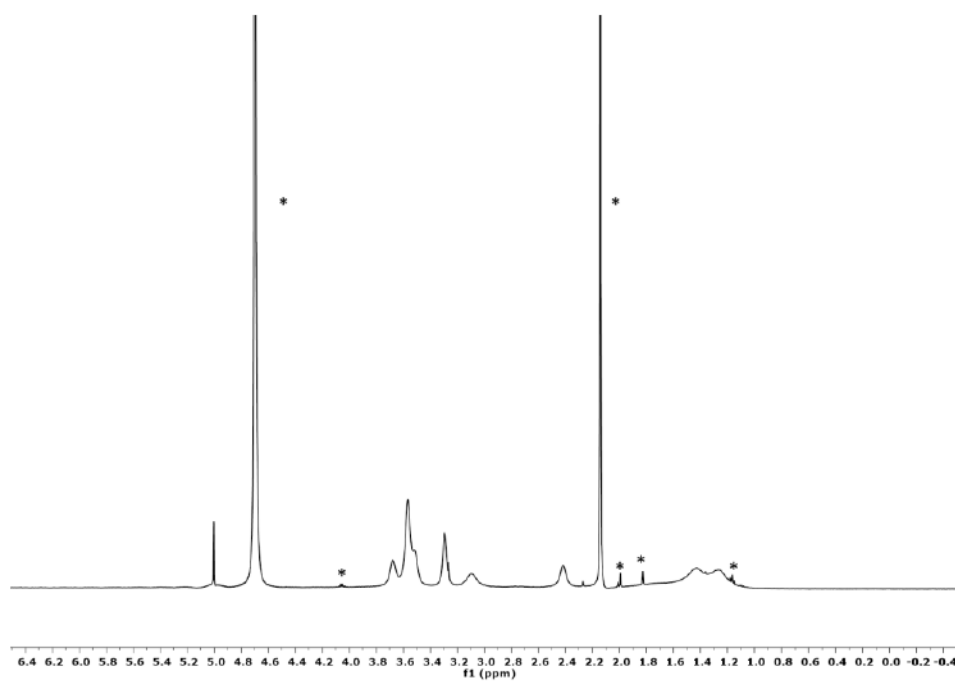
Figure 7-12. ^{1}H NMR spectrum of **23**-AuNP in D_2O. * indicates the solvents or impurities.
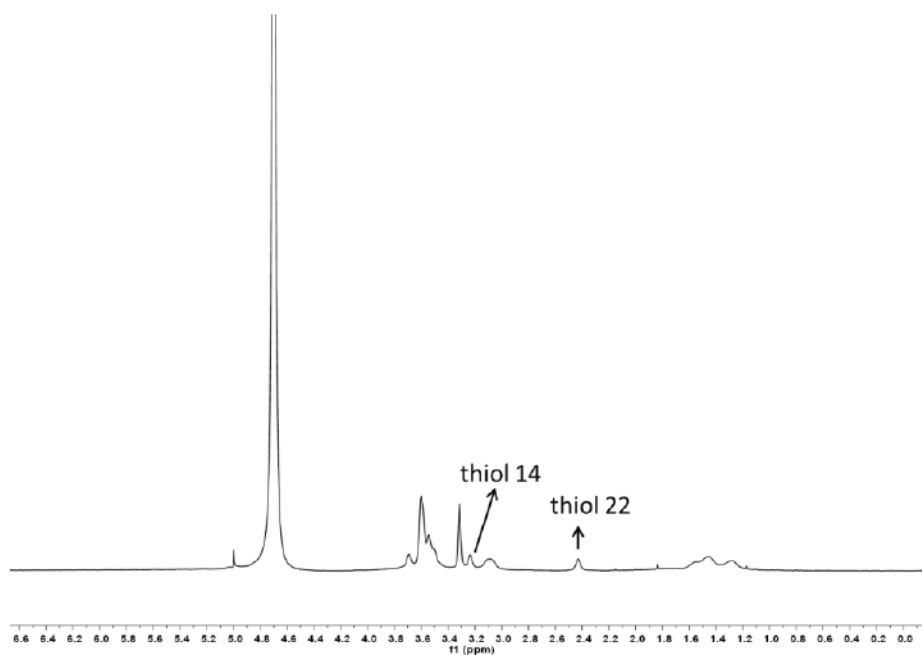
Figure 7-13. ^{1}H NMR spectrum of **24**-AuNP in D$_2$O, separated signals arising from thiol 14 and thiol 23 were labeled.
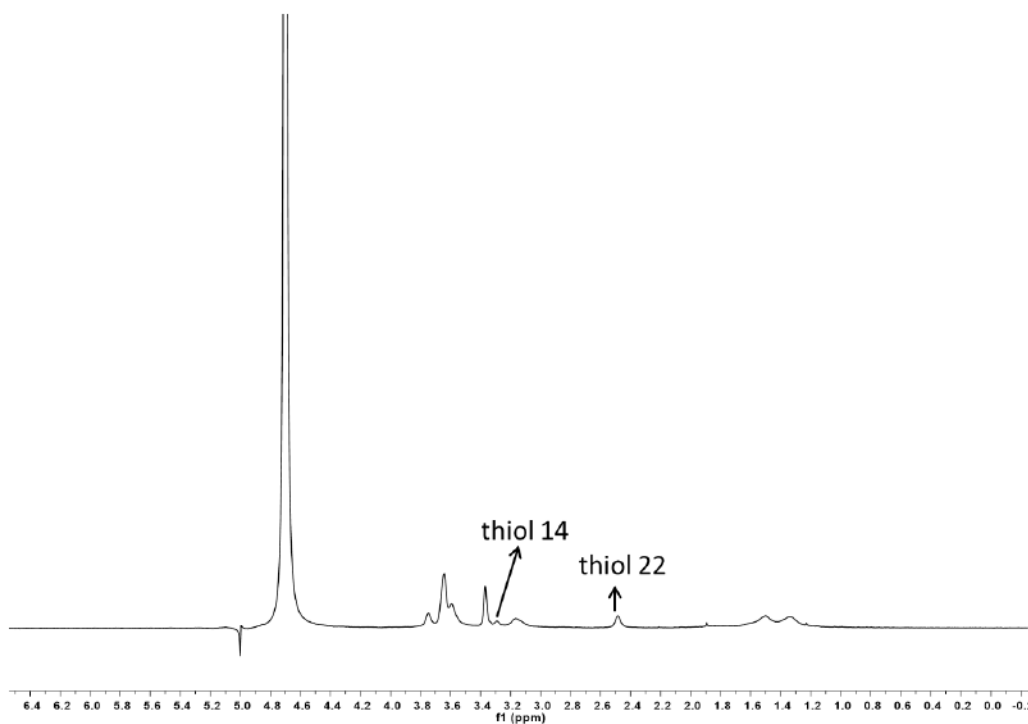
Figure 7-14. ^{1}H NMR spectrum of **25**-AuNP in D$_2$O, separated signals arising from thiol 14 and thiol 23 were labeled.
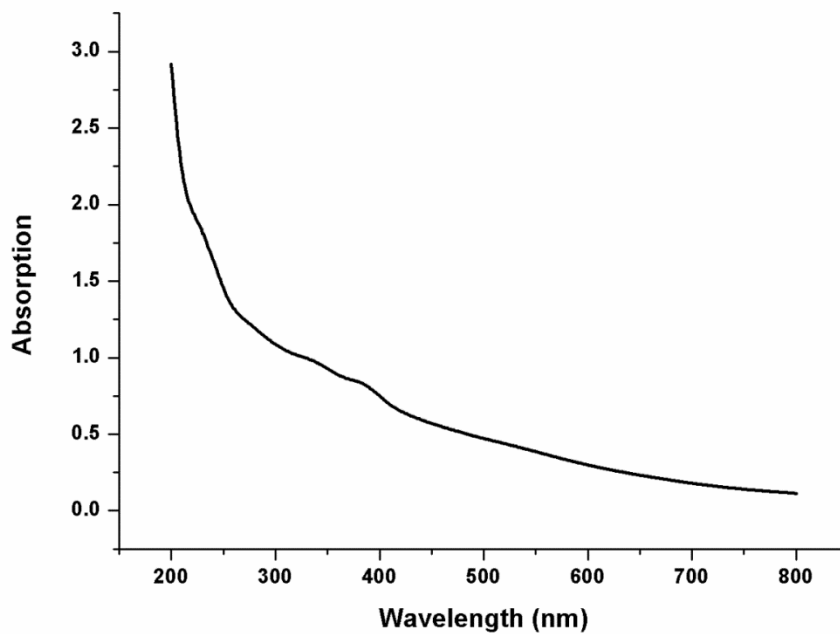
Figure 7-15. UV-Vis spectrum of **23**-AuNP (0.1 mg/mL) at 25 °C in H_2O.
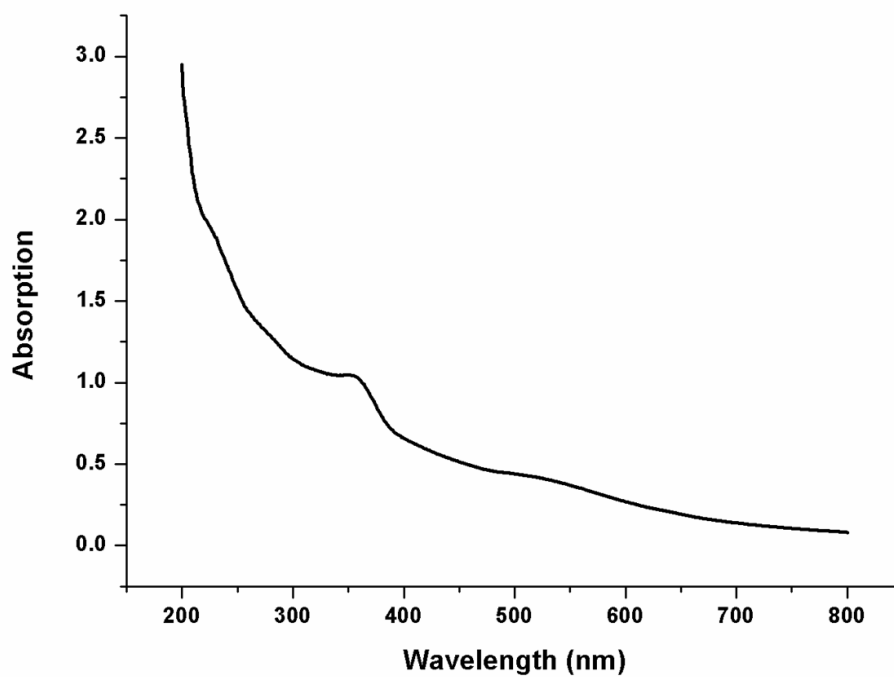
Figure 7-16. UV-Vis spectrum of **24**-AuNP (0.1 mg/mL) at 25 °C in H_2O.
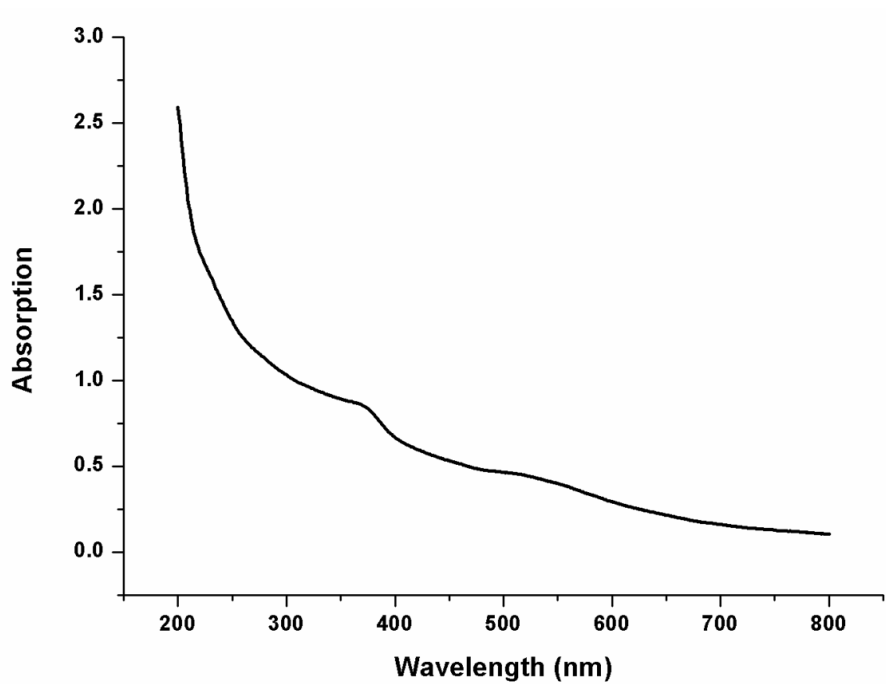
Figure 7-17. UV-Vis spectrum of **25-**AuNP (0.1 mg/mL) at 25 °C in H$_2$O.

Chapter 8. Materials and instrumentation

Materials: Solvents were purified by standard methods. All commercially available reagents and substrates were purchased from Sigma or Fluka and used as received. TLC analyses were performed using Merck 60 F_{254} precoated silica gel glass plates. Column chromatography was carried out on Macherey-Nagel silica gel 60 (70-230 mesh).

Instrumentation: NMR spectra were recorded using a Bruker AV III 500 spectrometer operating at 500 MHz for ^{1}H, 125.8 MHz for ^{13}C. Chemical shifts are reported relative to internal Me_4Si. Multiplicity is given as follow: s = singlet, d = doublet, t = triplet, q = quartet, qn = quintet, m = multiplet, br = broad peak. HRMS mass spectra were obtained with an Mariner Applied Biosystem (API-TOF) mass spectrometer (MeOH, 0.5% formic acid). TEM images were recorded on a Jeol 300 PX electron microscope. One drop of sample was placed on the sample grid and the solvent was allowed to evaporate. UV-Visible spectra and kinetic traces were recorded on Cary 50 spectrophotometer equipped with thermostatic multiple cell holders. Thermogravimetric analysis (TGA) was run on 1 mg nanoparticle samples using a Q5000 IR model TA instrument from 30 to 1000 °C under a continuous air flow. Dynamic Light Scattering (DLS) and Z-potential measurements were performed at the temperature of 25°C, with a Malvern Zetasizer Nano-S equipped with a HeNe laser (633 nm) and operating in the backscattering mode at 173°. Fluorescence spectra were recorded on Perkin Elmer LS50B fluorescence spectrometer. Fluorescence measurements for multivariate analysis were recorded on TECAN infinite M1000 PRO micro-plate reader.

Acknowledgement

There are so many people I need to thank for helping me during the last three years. Because all of you, the life of PhD became much easier than I thought.

First, I would like to show my deepest gratitude to my supervisor Prof. Fabrizio Mancin for his valuable guidance, encouragement, understanding and patience over the last three years. He showed me not only the way how to look at science but also the way how to behave as an excellent mentor. This thesis would not have been possible without his help. I really feel I am lucky to have the opportunity to study in his lab.

I owe my gratitude to Prof. Federico Rastrelli, Prof. Marco De Vivo, Prof. Marilena Di Valentin, Federico De Biasi, Laura Riccardi, Mariagiulia Dal Farra, Maria Vittoria Massagrande and all the people I have been cooperated with. I am also grateful to Prof. Fregona Dolores, Prof. Zoleo Alfonso and Prof. Realdon Nicola, who are from my PhD commission, for their discussion and suggestion on my PhD projects.

A special thanks need to be expressed to Luca Gabrielli. He taught me the basic experimental skills and the operation of the instruments. In addition, I would like to thank Sara Sprighetti, Jakub Trzcinski, Yanchao Lyu, Daniele Rosa-Gastaldo, Lucia Morillas, Joanna Czescik, Lucia Trevisan, Meng Zheng, Teresa Gatti, Rui Chen, Jiaying Yu, Chuanyu Sun and all the other people who have worked with me for their help and accompany.

I would like to express my sincere thanks to China Scholarship Council for the financial support.

Finally, many thanks are owed to my parents for their endless love. I am grateful to my sisters for their support and taking care of my parents. Appreciates also go to Wang Huan for his love, understanding, support, and being presence in my life.

Life is not always easy. Because all of you, I am sure that there are better days ahead.

Appendix

¹H NMR and ¹³C NMR spectra of the protected thiols and thiols
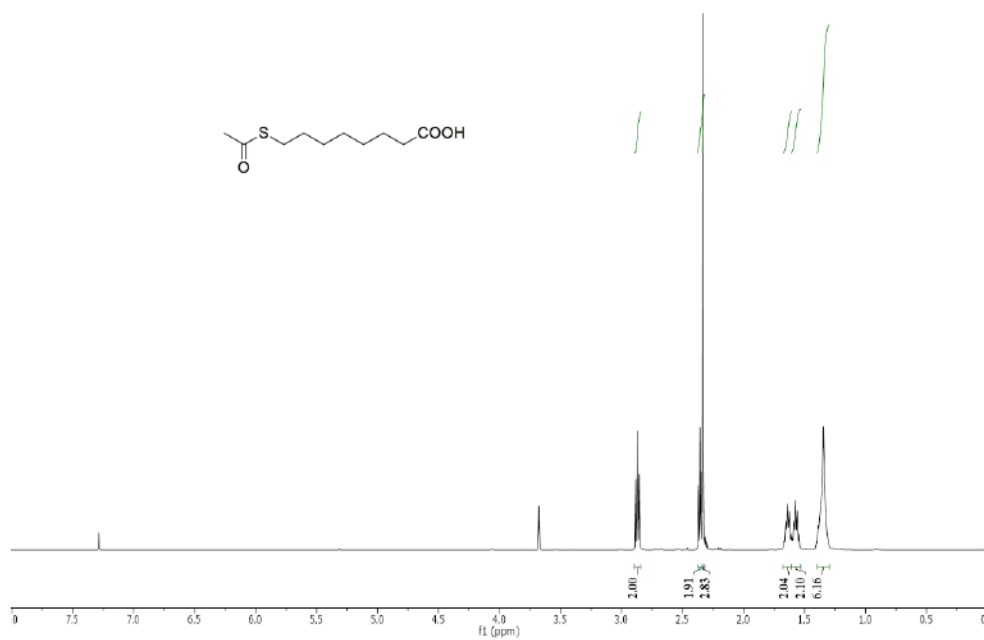
Figure A1. ¹H NMR spectrum of compound **C1**.
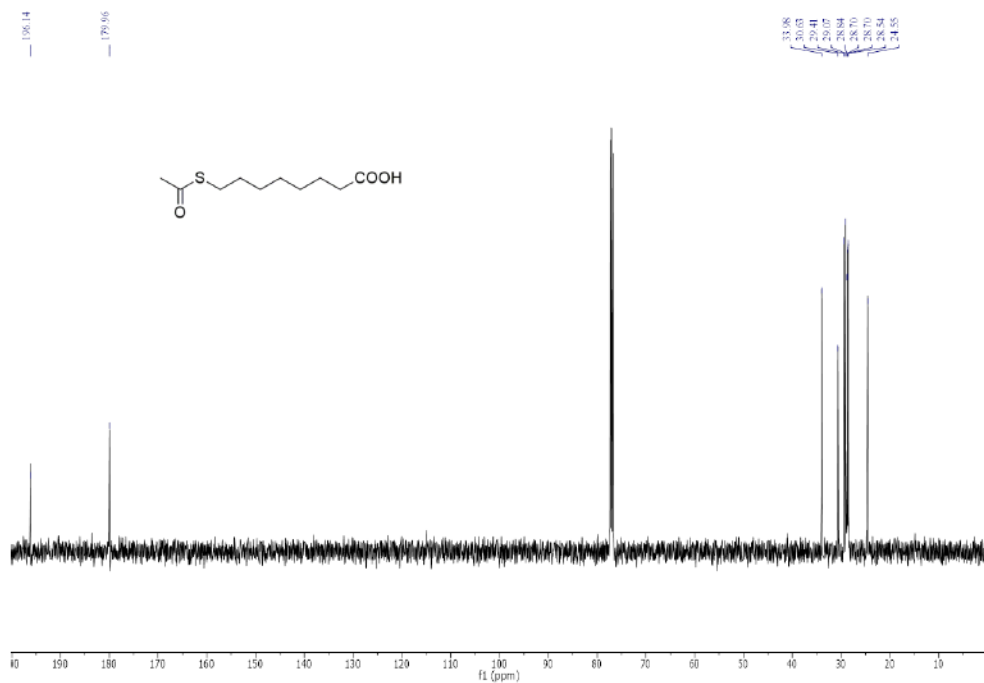
Figure A2. ¹³C NMR spectrum of compound **C1**.
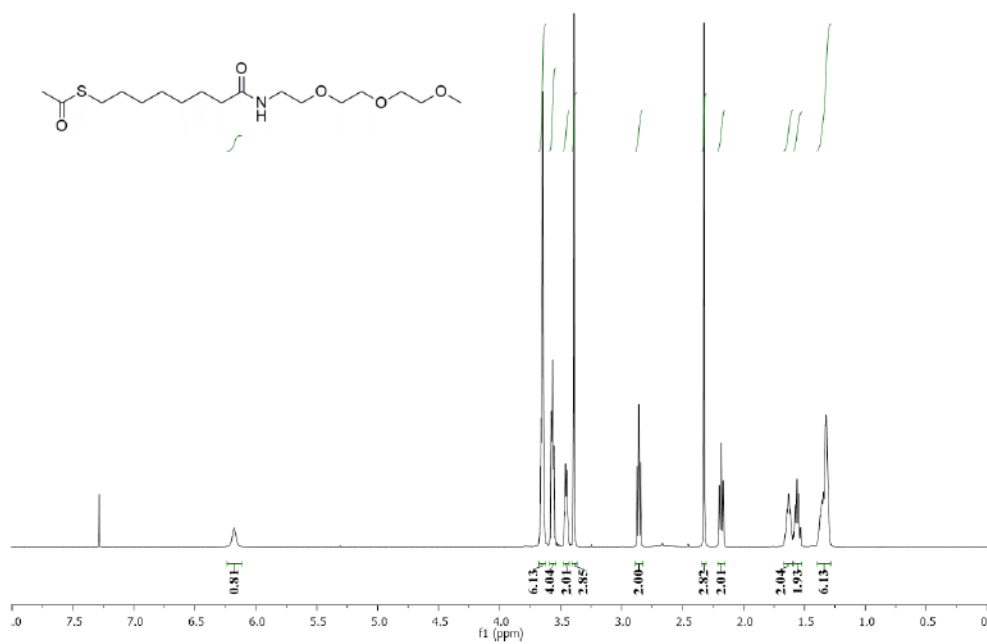
Figure A3. ^{1}H NMR spectrum of compound **C2**.
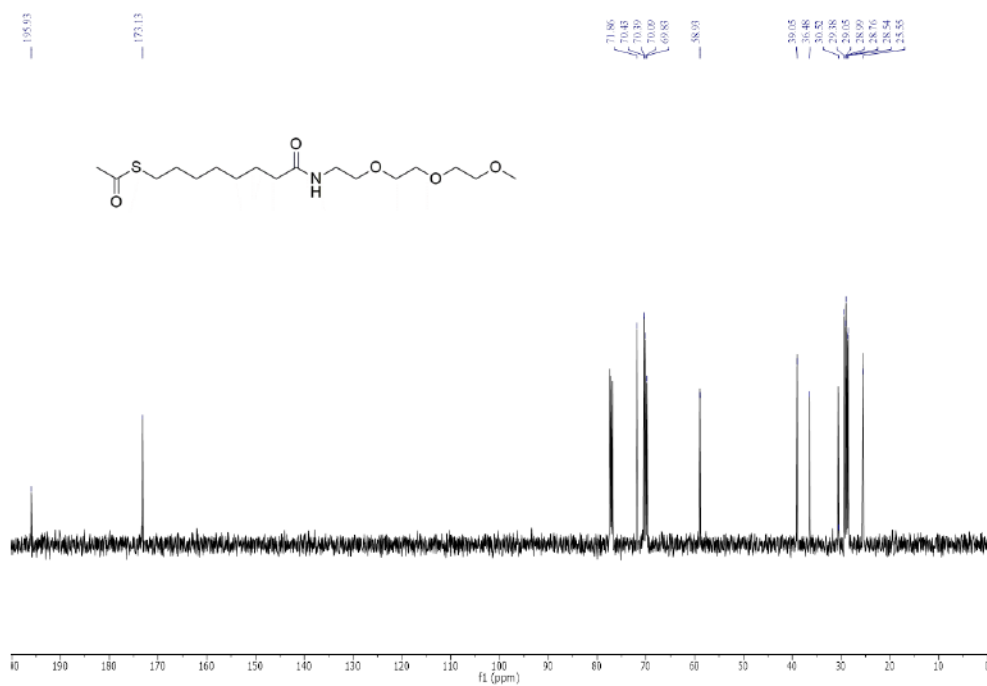
Figure A4. ^{13}C NMR spectrum of compound **C2**.

References
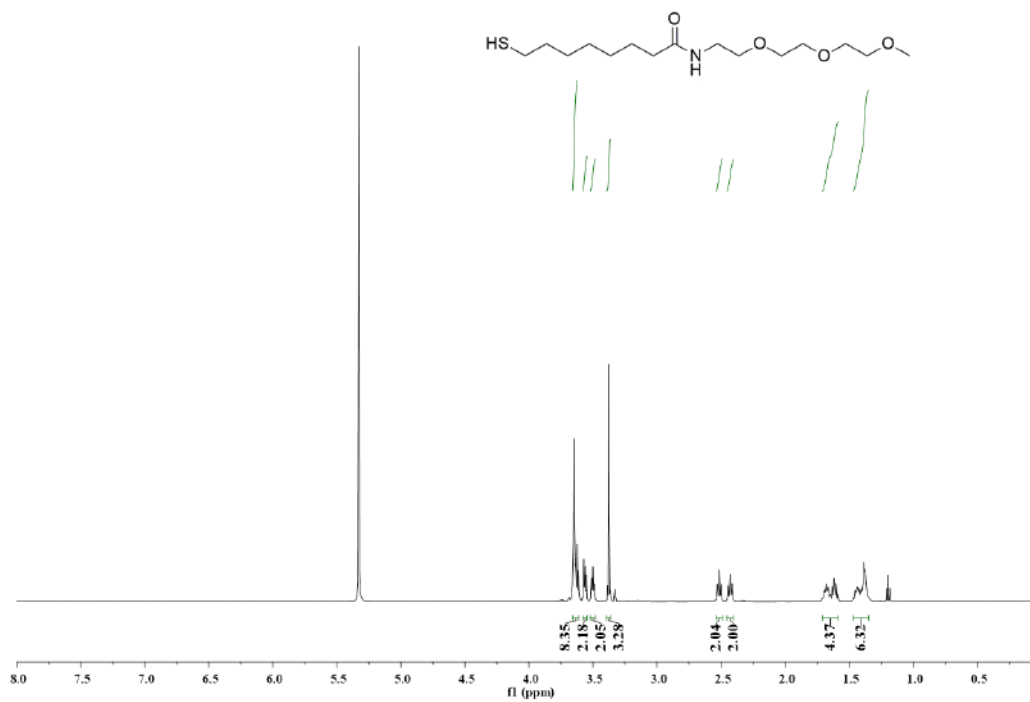
Figure A5. ^{1}H NMR spectrum of **thiol 1**.
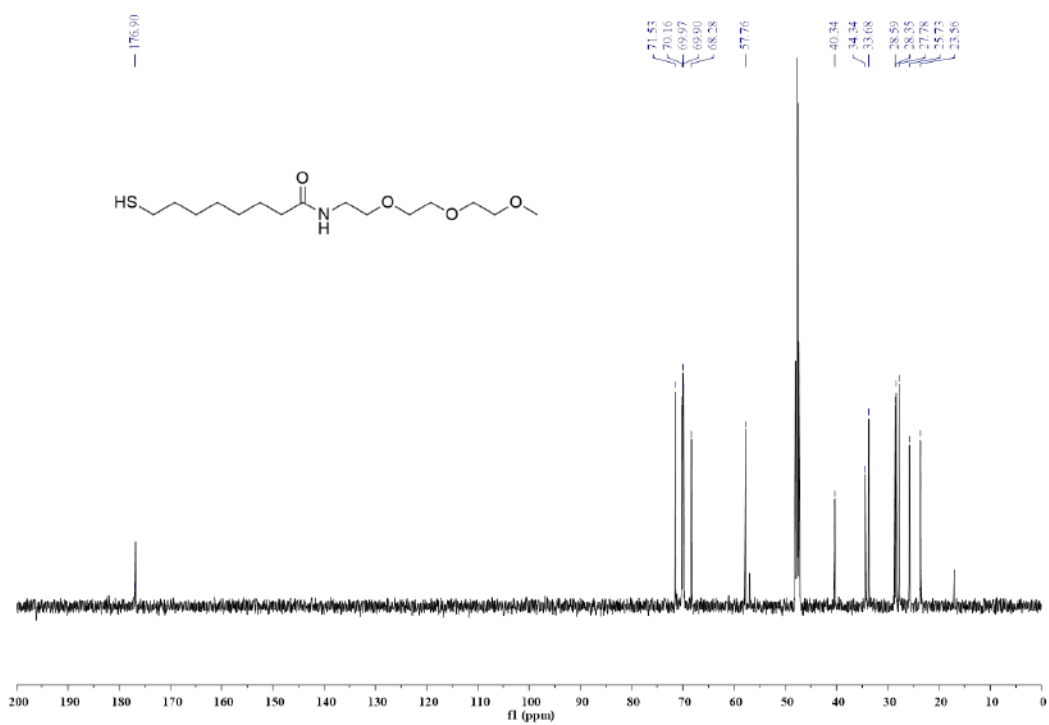
Figure A6. ^{13}C NMR spectrum of **thiol 1**.
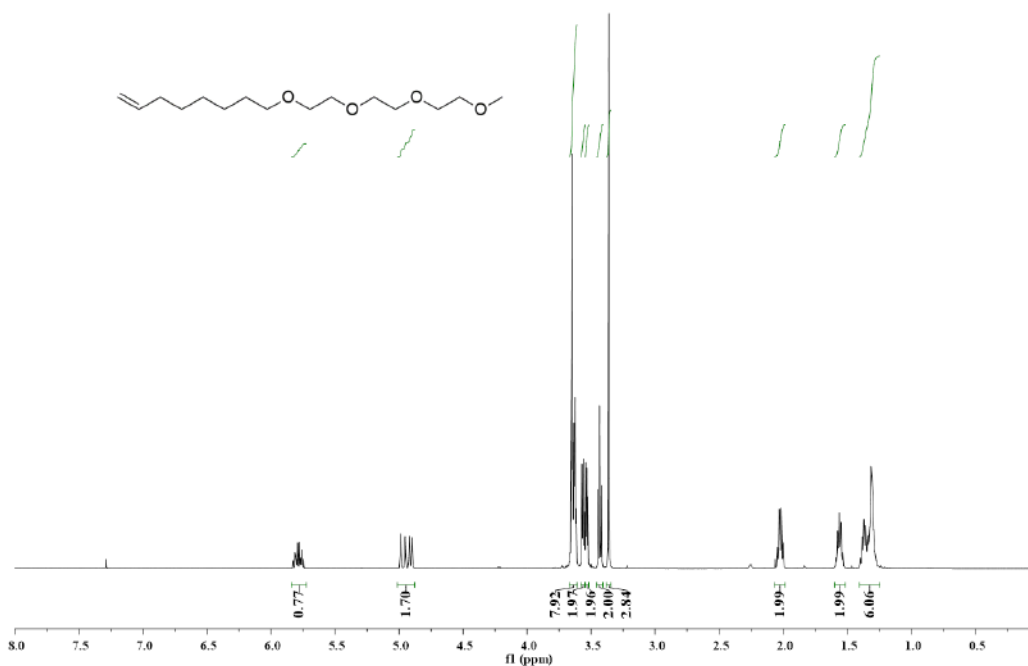
Figure A7. ^{1}H NMR spectrum of compound **C3**.
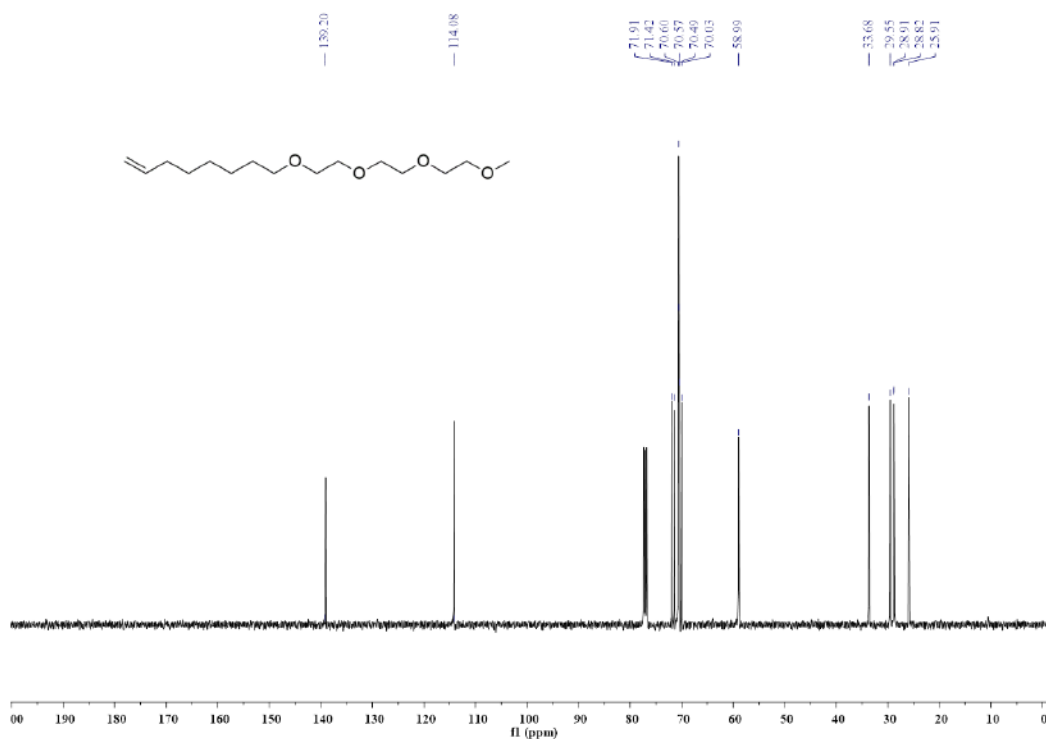
Figure A8. ^{13}C NMR spectrum of compound **C3**.

Figure A9. ^{1}H NMR spectrum of compound **C4**.

Figure A10. ^{13}C NMR spectrum of compound **C4**.
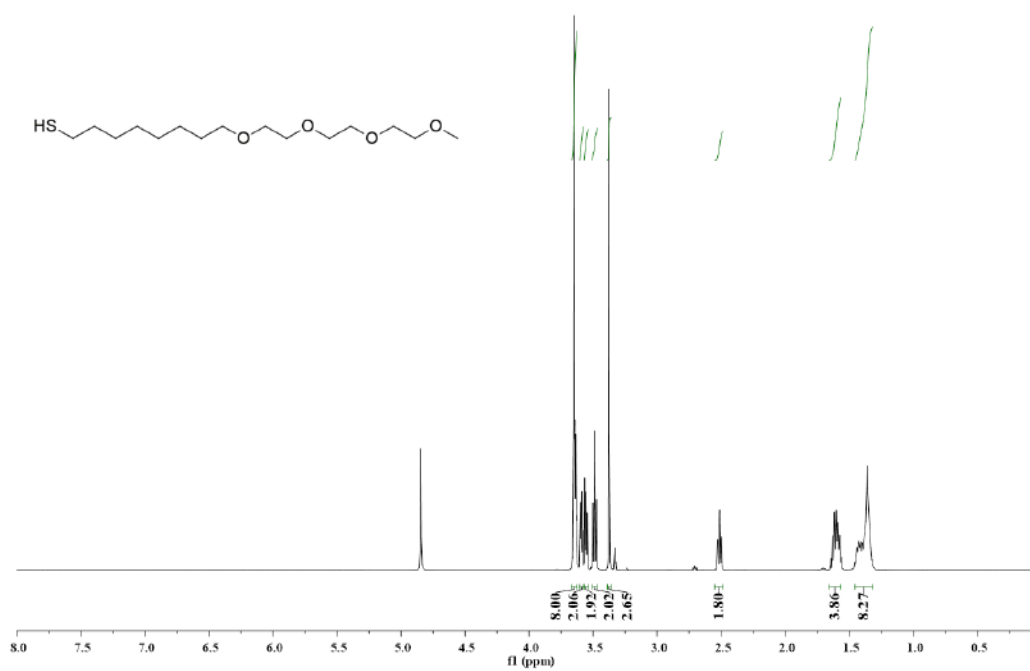
References

Figure A11. ^{1}H NMR spectrum of **thiol 7**.
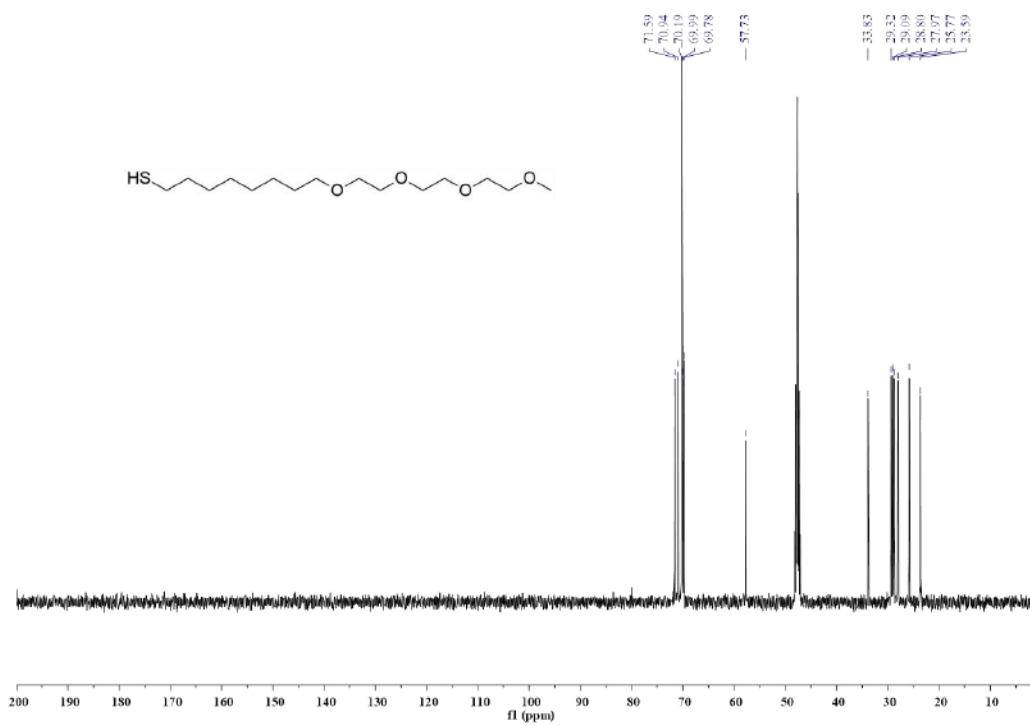
Figure A12. ^{13}C NMR spectrum of **thiol 7**.

165
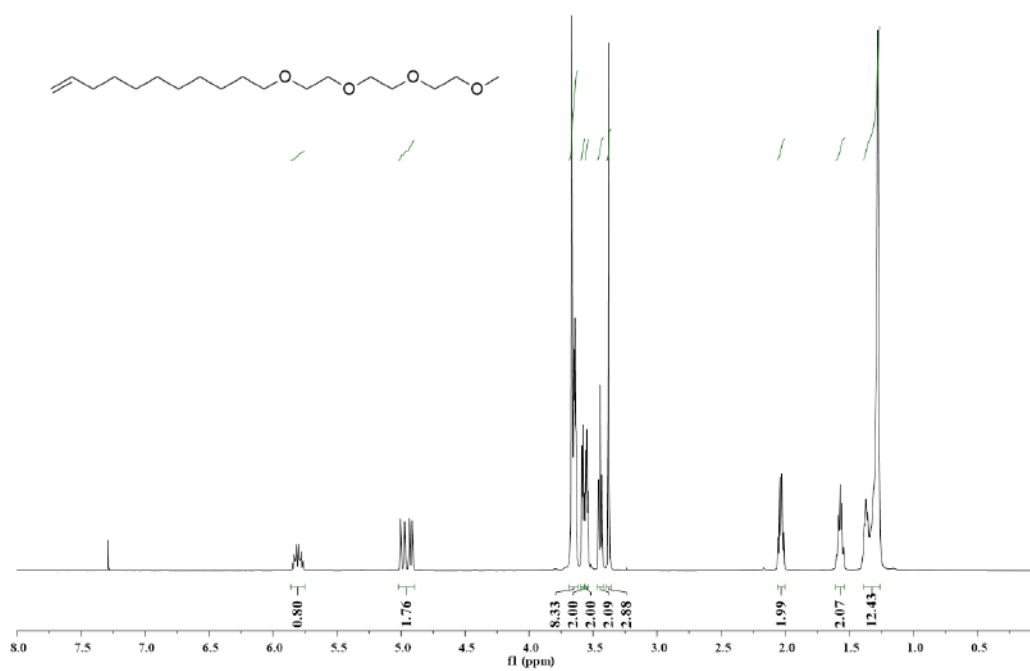
Figure A13. ^{1}H NMR spectrum of compound **C5**.
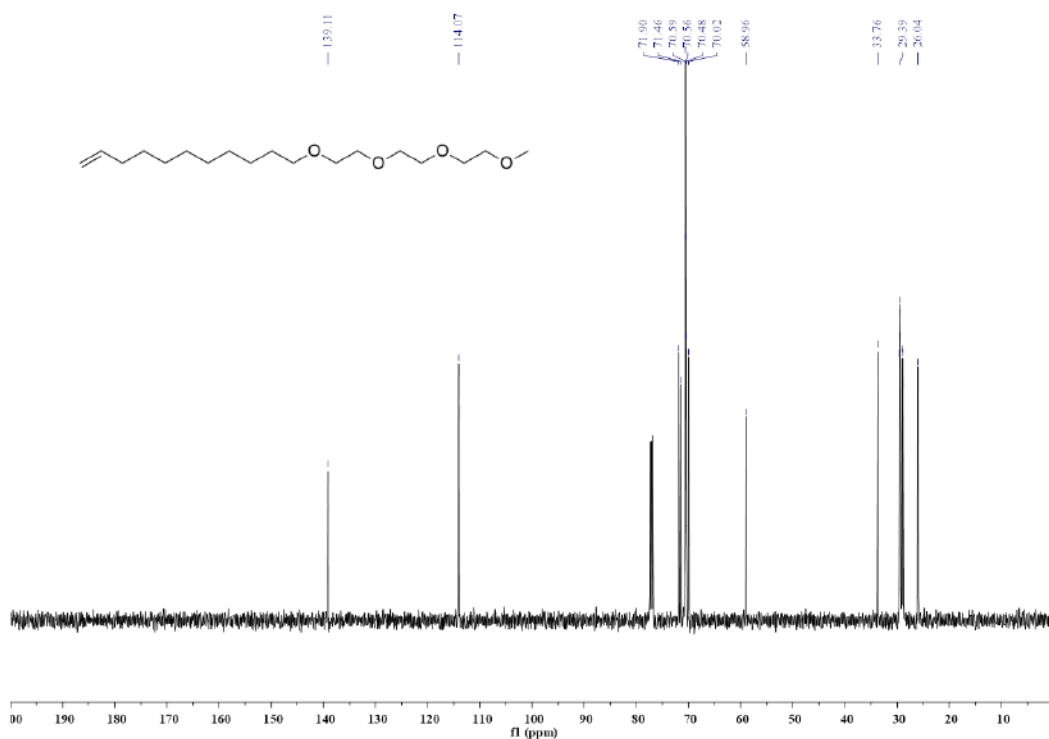
Figure A14. ^{13}C NMR spectrum of compound **C5**.

166

Figure A15. ^{1}H NMR spectrum of compound **C6**.

Figure A16. ^{13}C NMR spectrum of compound **C6**.
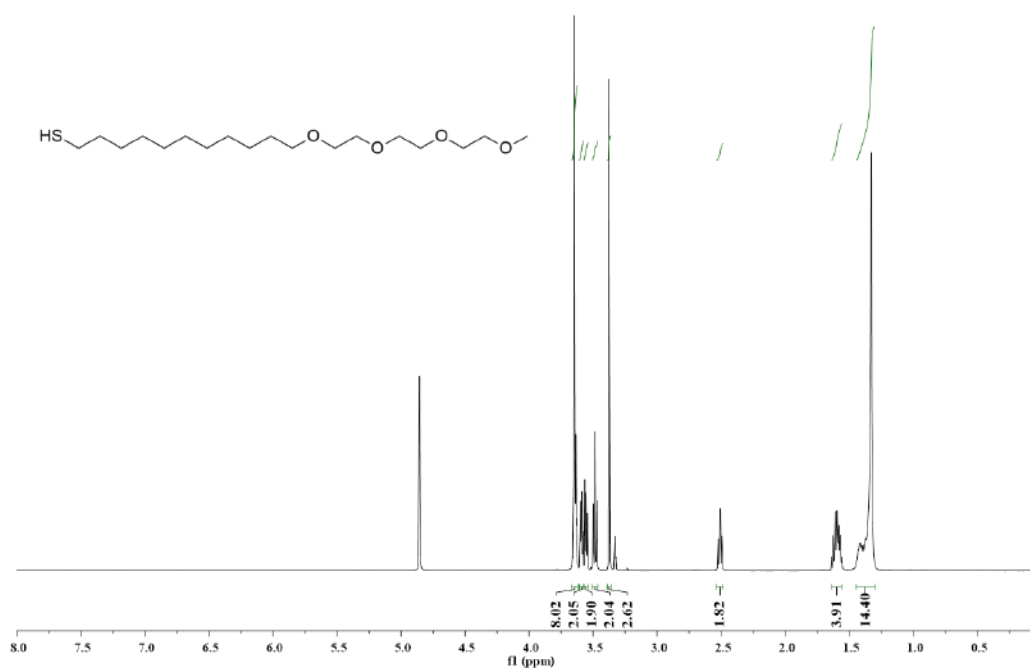
Figure A17. ^{1}H NMR spectrum of **thiol 8**.
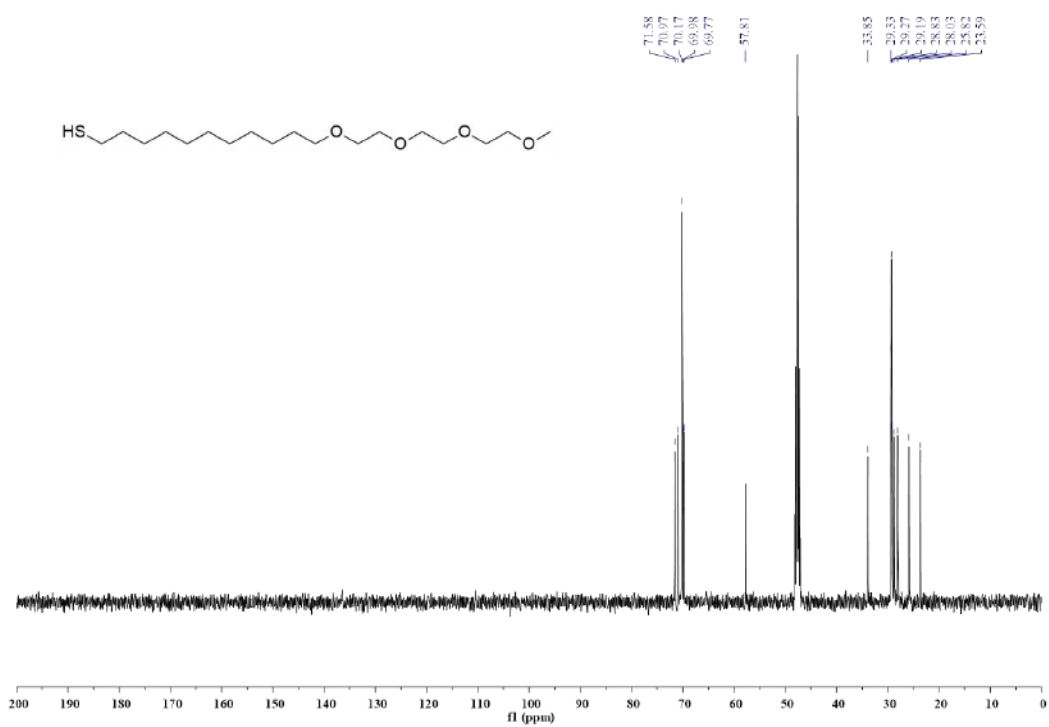
Figure A18. ^{13}C NMR spectrum of **thiol 8**.

References
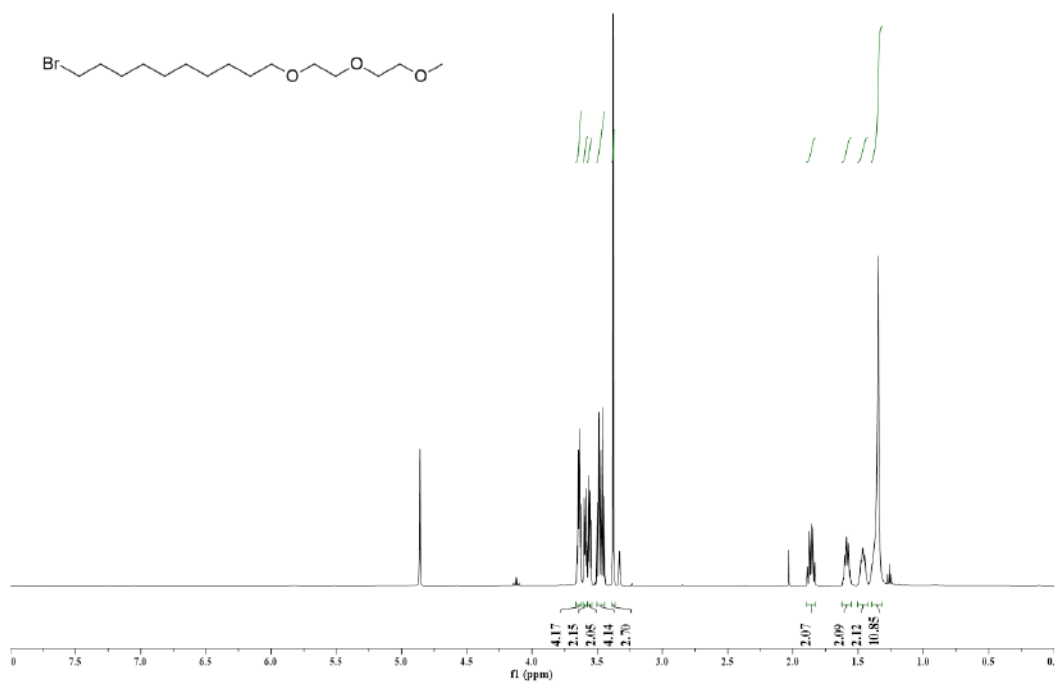
Figure A19. ^{1}H NMR spectrum of compound **C7**.
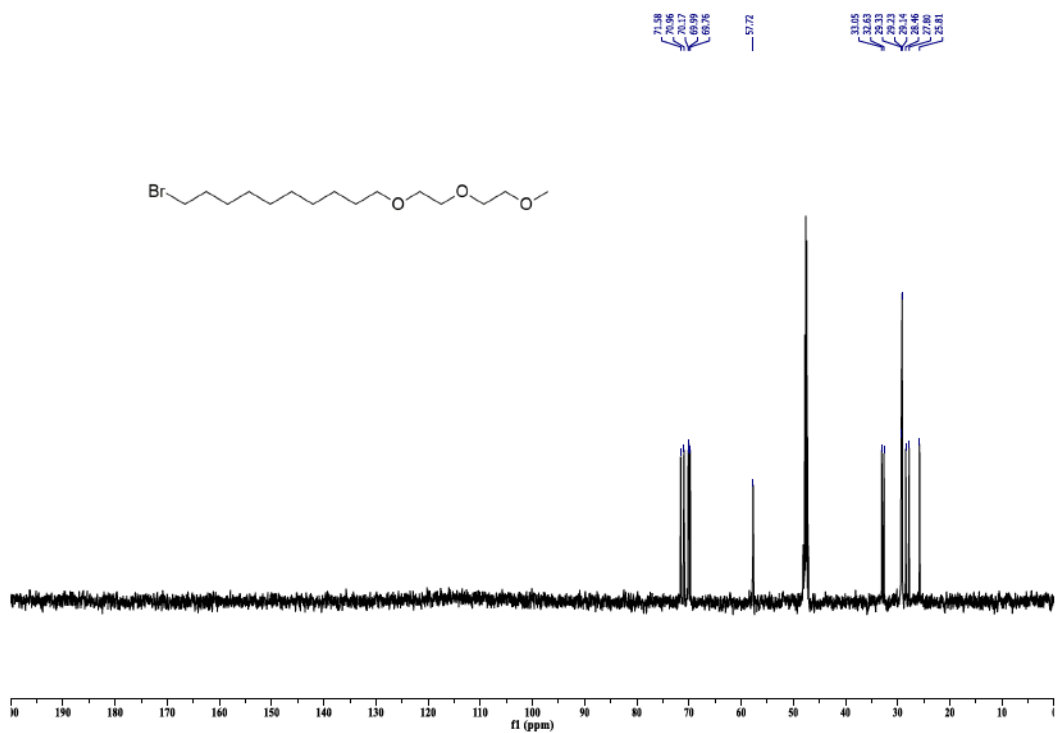
Figure A20. ^{13}C NMR spectrum of compound **C7**.

169
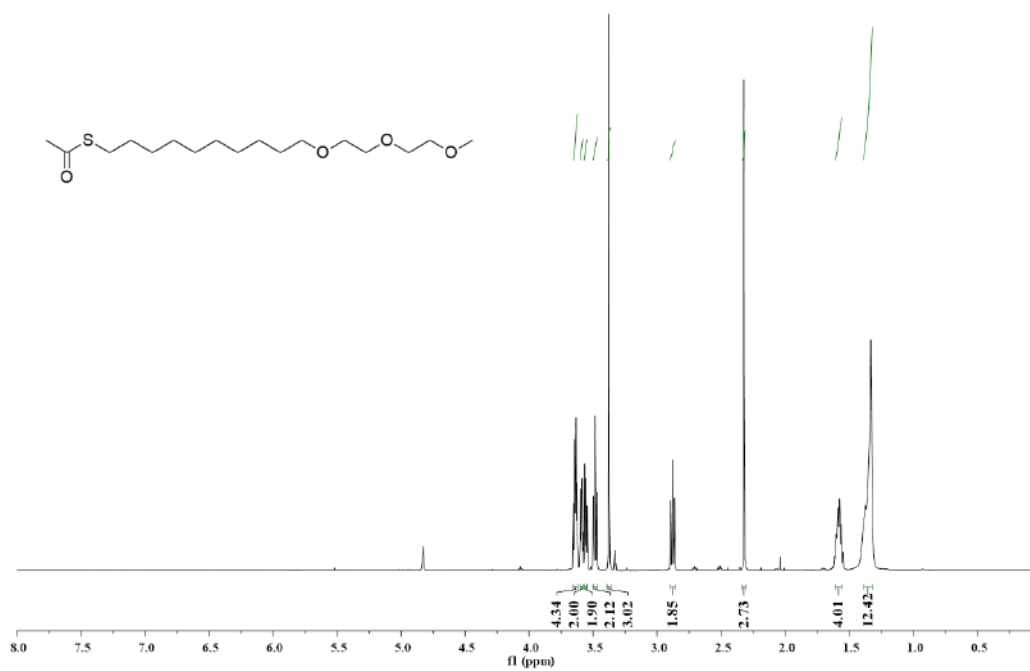
Figure A21 ^{1}H NMR spectrum of compound **C8**.
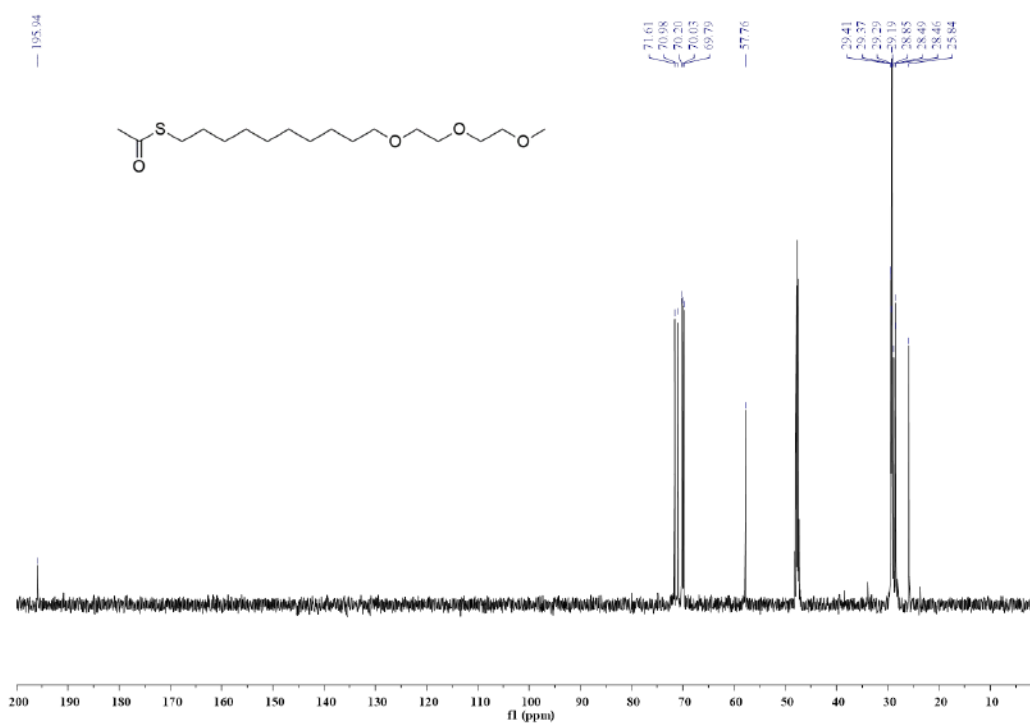
Figure A22. ^{13}C NMR spectrum of compound **C8**.
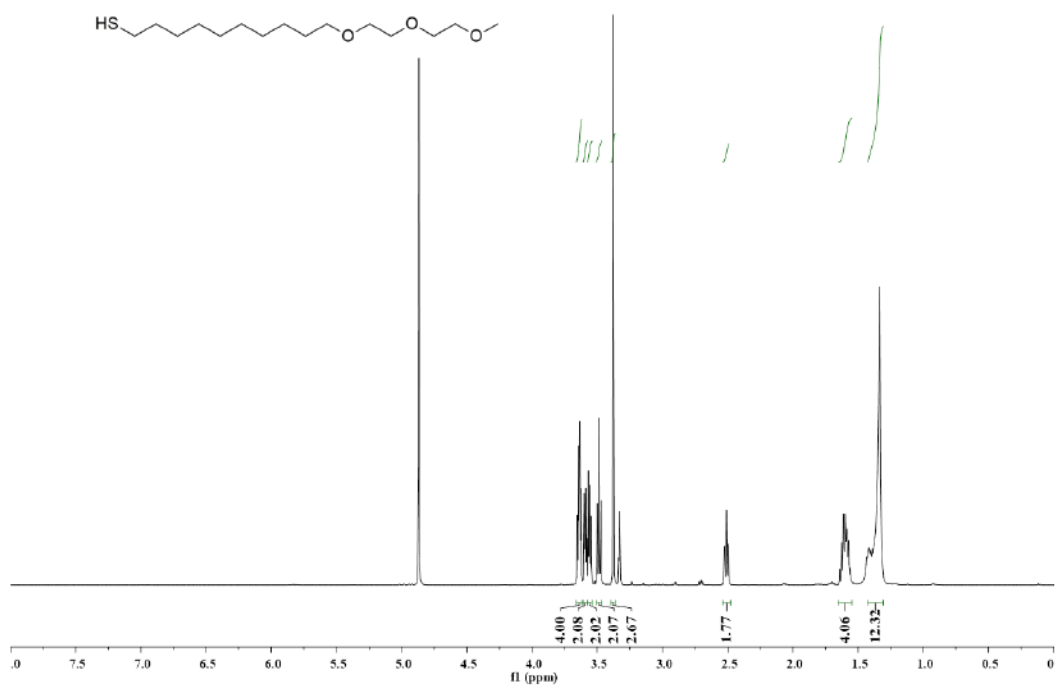
Figure A23. ^{1}H NMR spectrum of **thiol 9**.
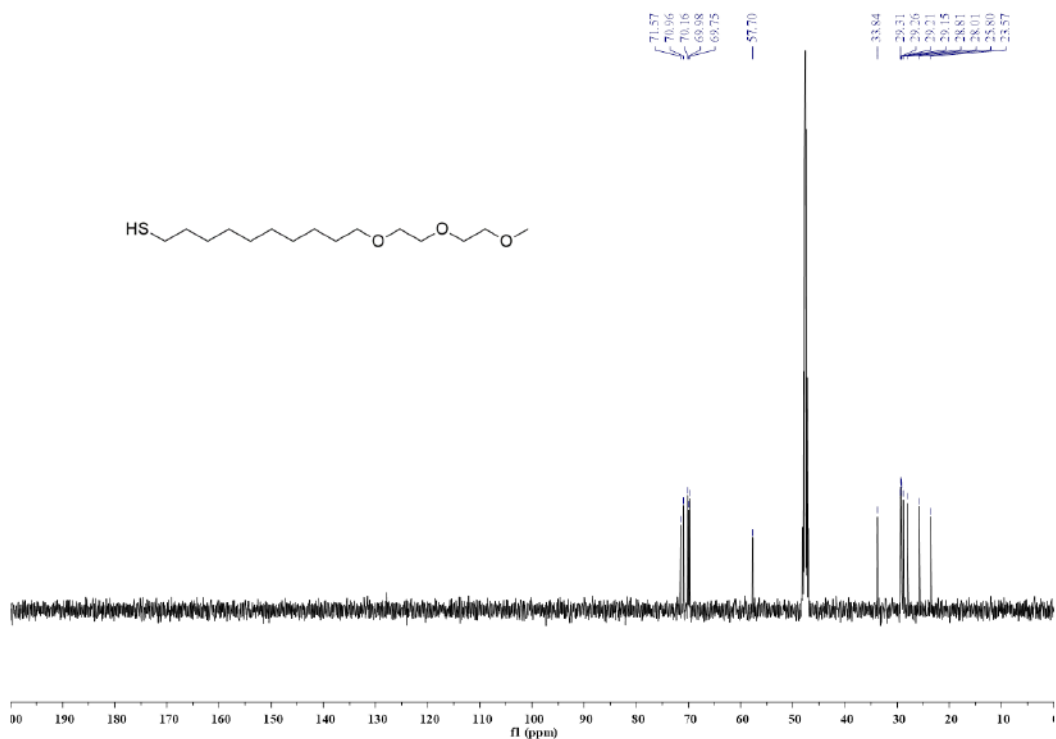
Figure A24. ^{13}C NMR spectrum of **thiol 9**.
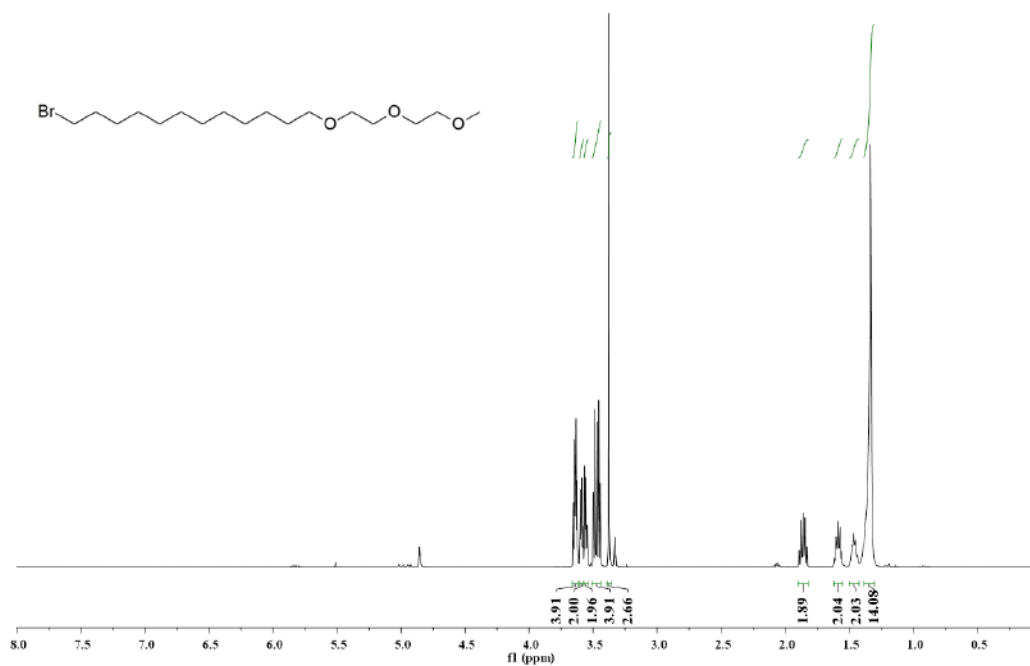
Figure A25. ^{1}H NMR spectrum of compound **C9**.
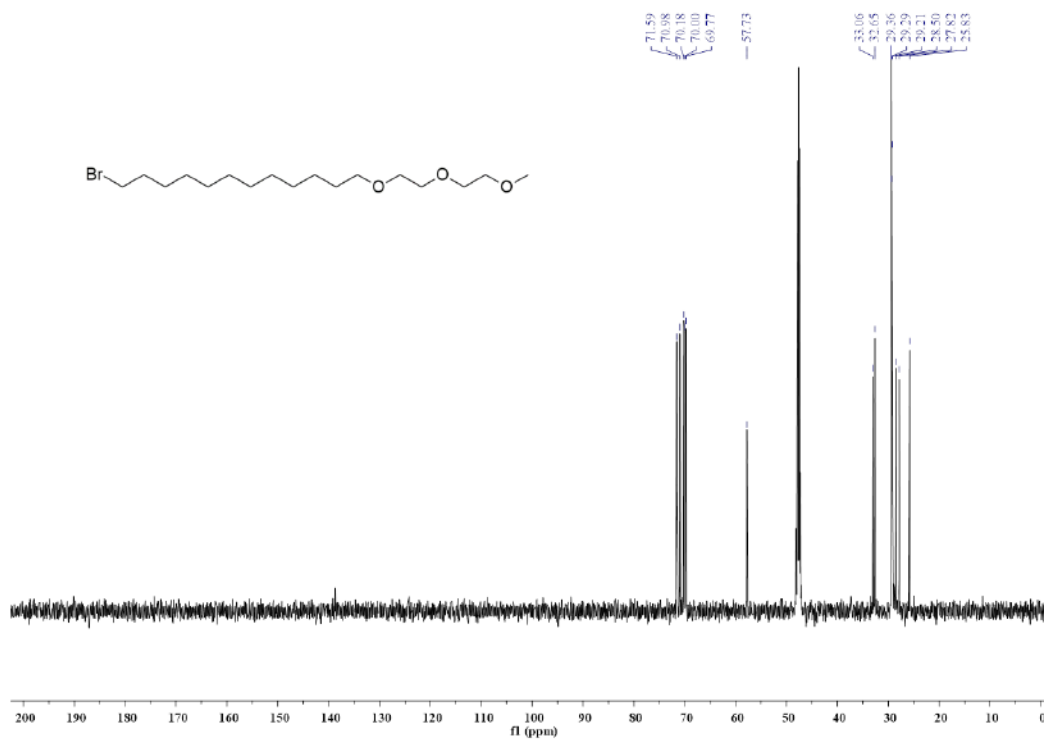
Figure A26. ^{13}C NMR spectrum of compound **C9**.
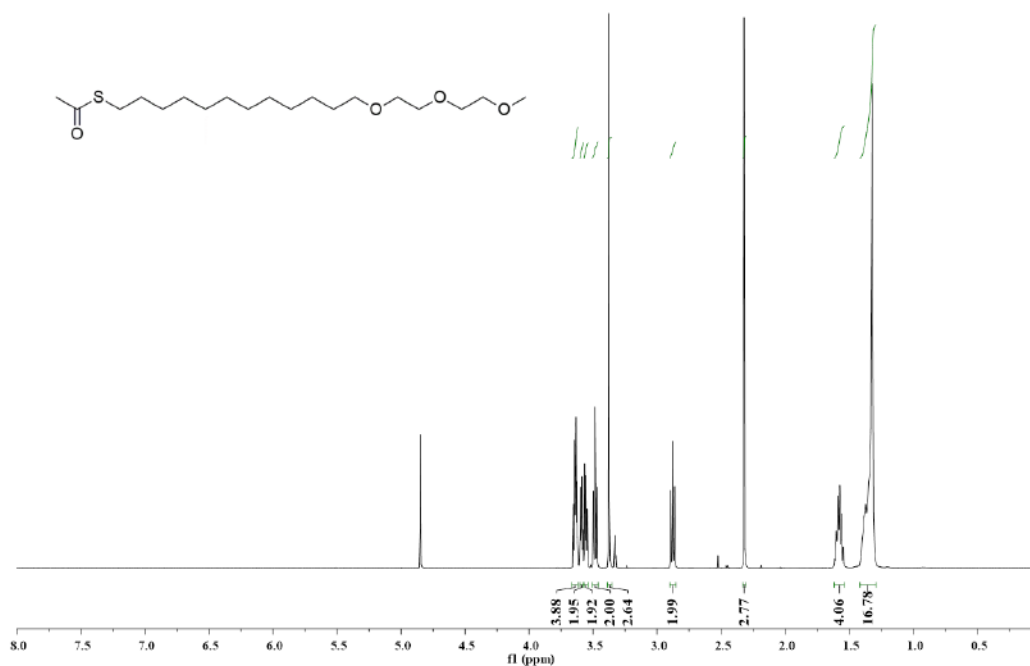
Figure A27. ^{1}H NMR spectrum of compound **C10**.
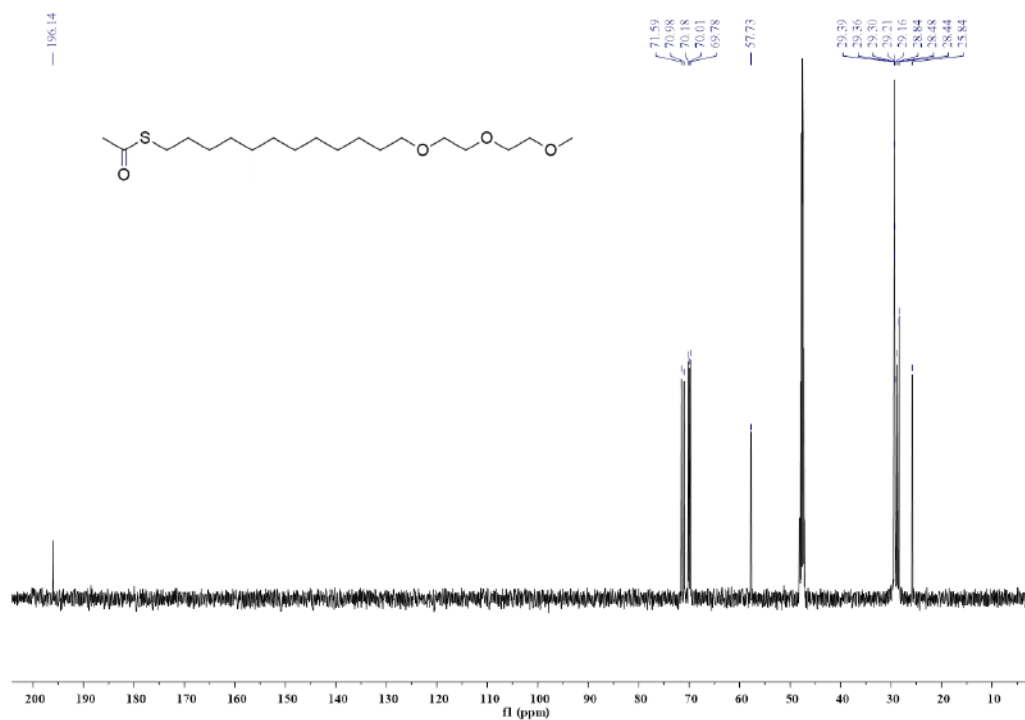
Figure A28. ^{13}C NMR spectrum of compound **C10**.
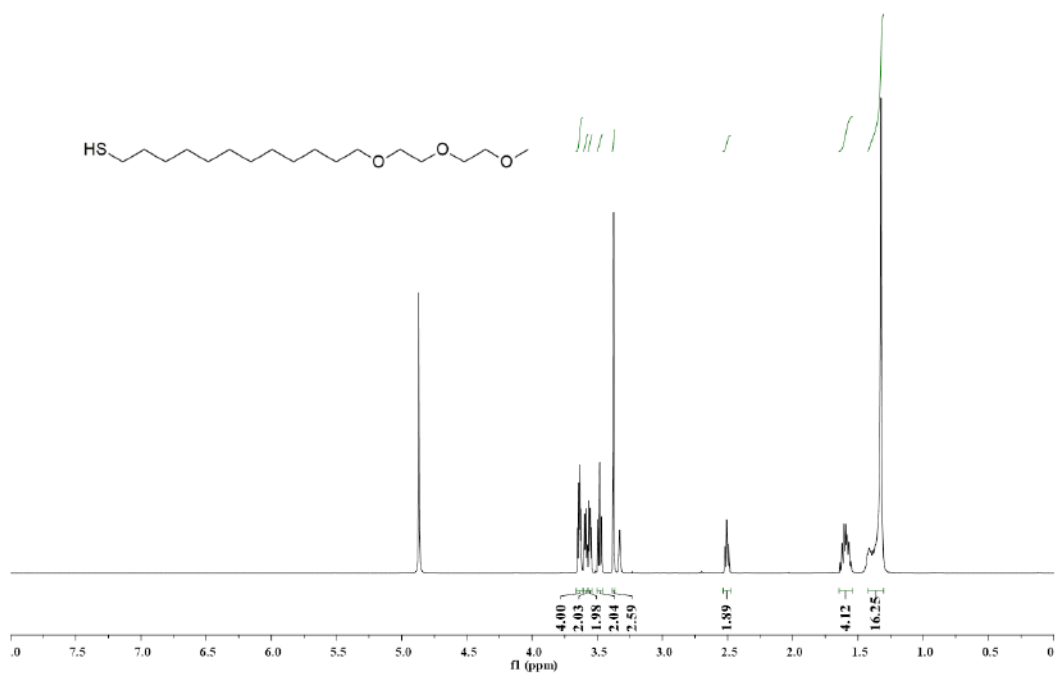
Figure A29. ^{1}H NMR spectrum of **thiol 10**.
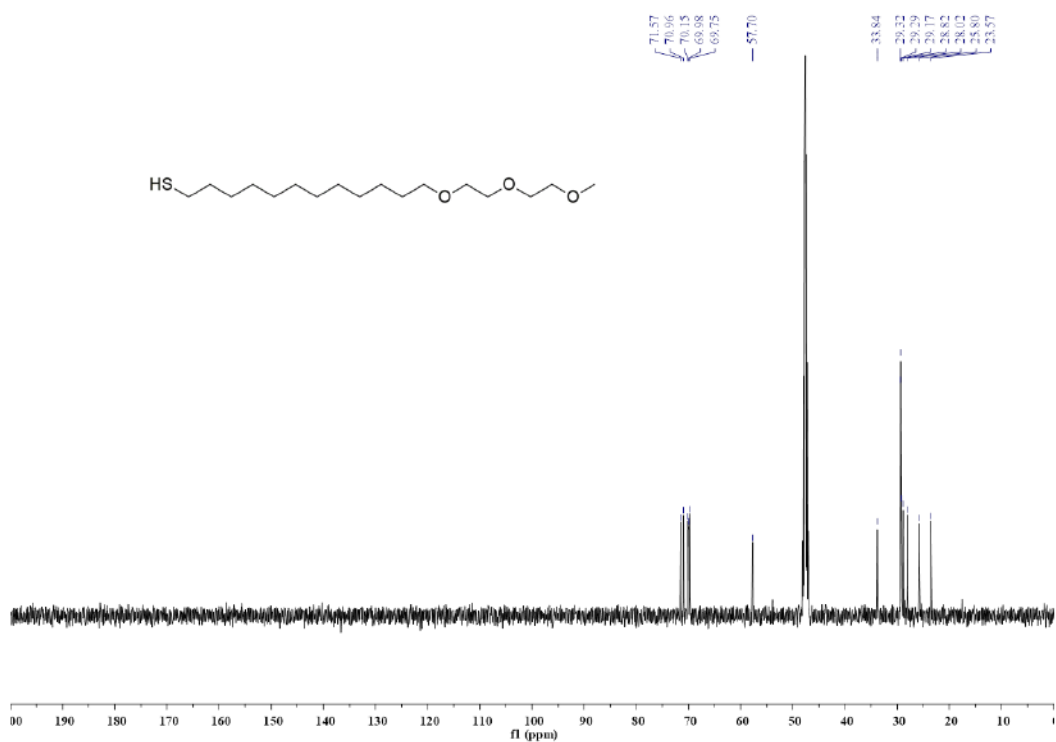
Figure A30. ^{13}C NMR spectrum of **thiol 10**.
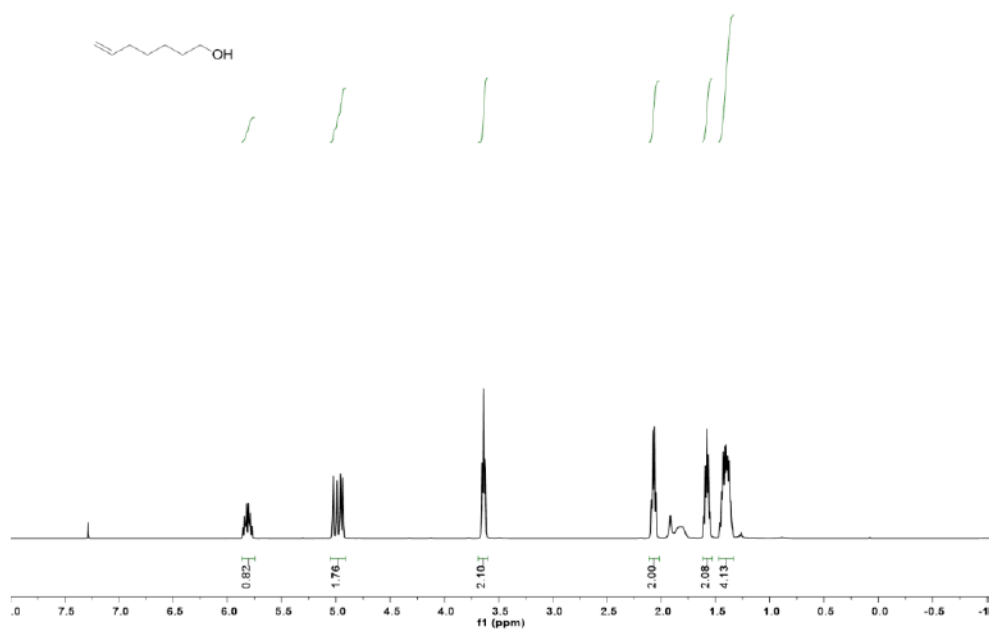
Figure A31: ^{1}H NMR spectrum of compound C11.
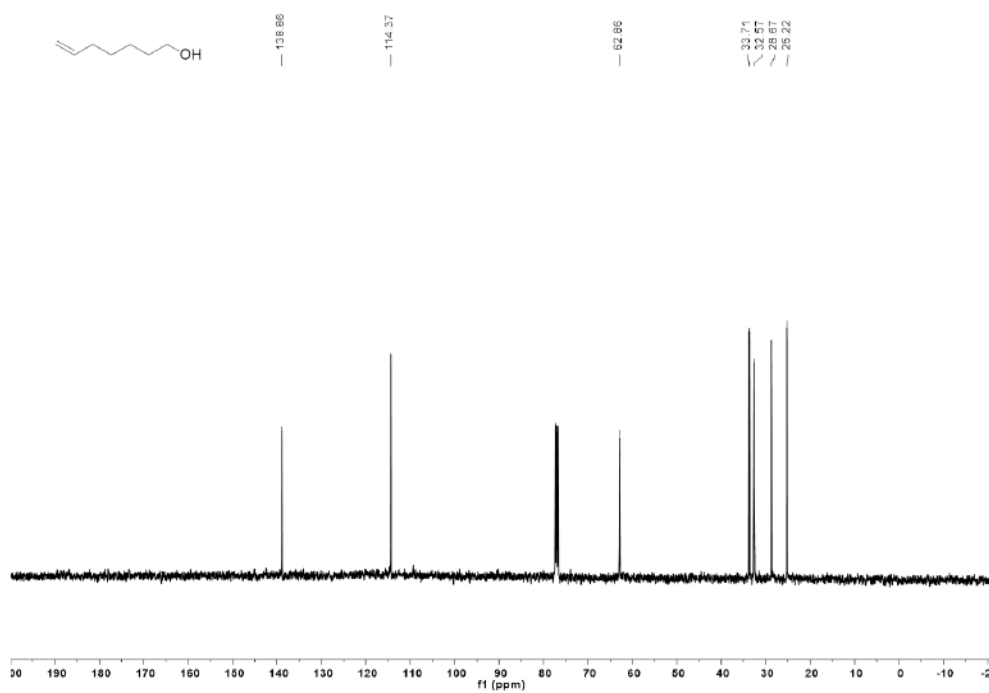
Figure A32: ^{13}C NMR spectrum of compound **C11**.
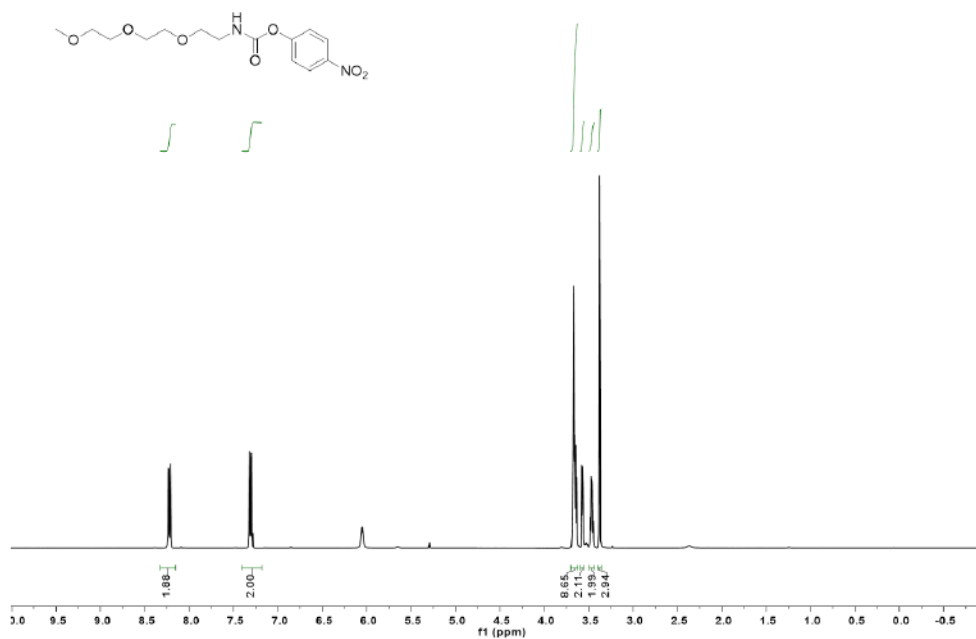
Figure A33. ^{1}H NMR spectrum of compound C12.
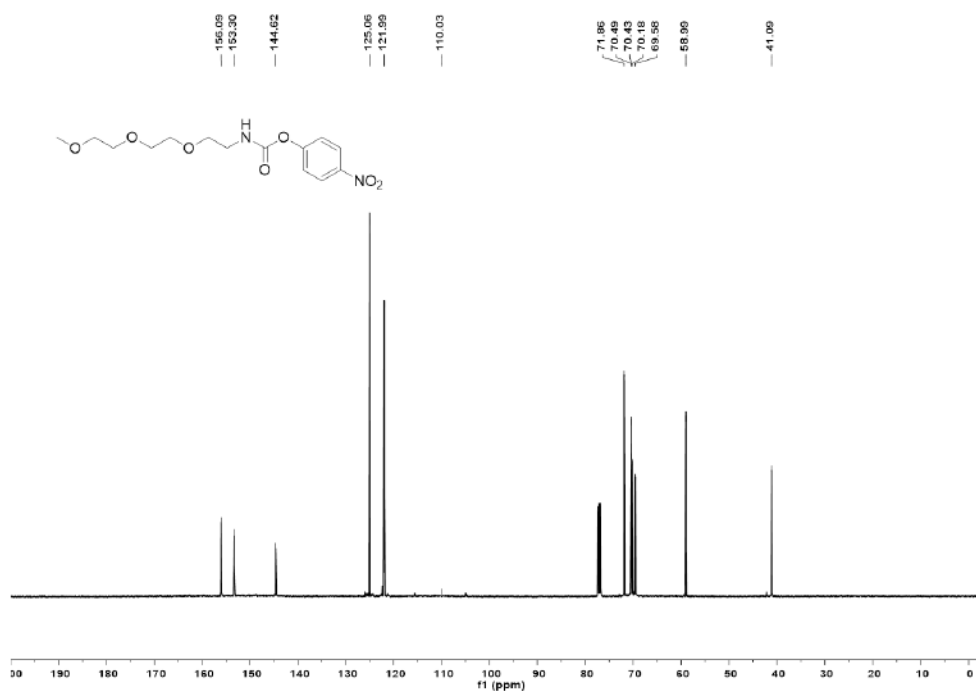
Figure A34. ^{13}C NMR spectrum of compound C12.
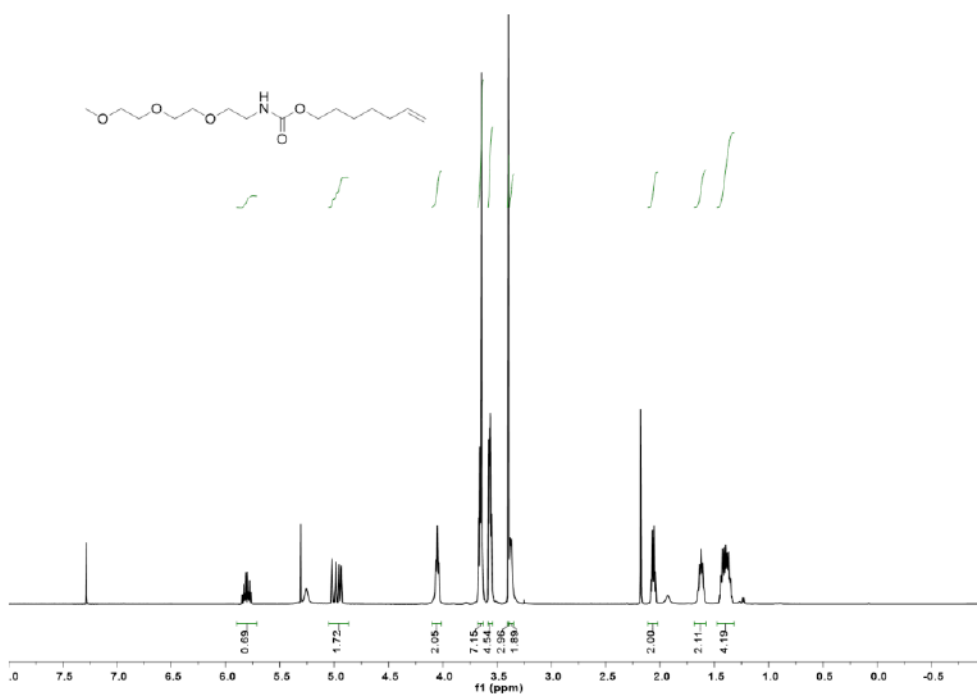
Figure A35. ^{1}H NMR spectrum of compound C13.
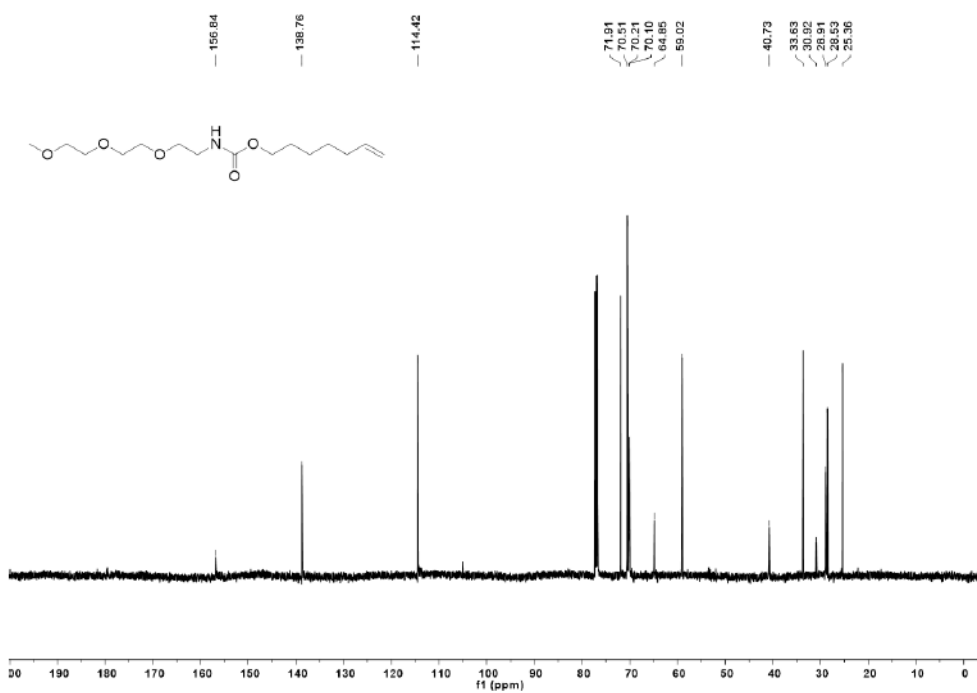
Figure A36. ^{13}C NMR spectrum of compound C13.
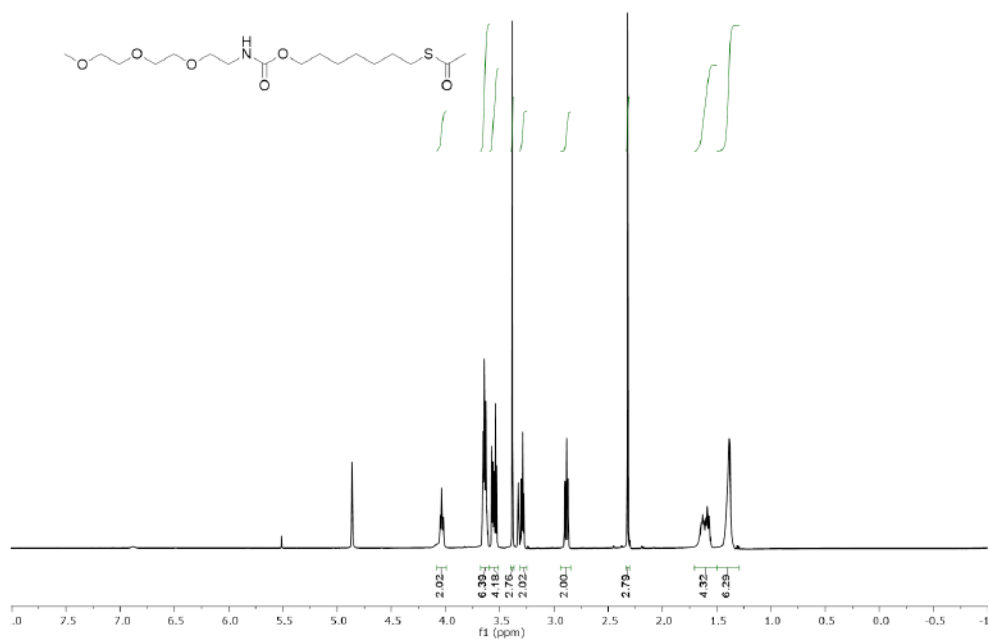
Figure A37. ^{1}H NMR spectrum of compound C14.
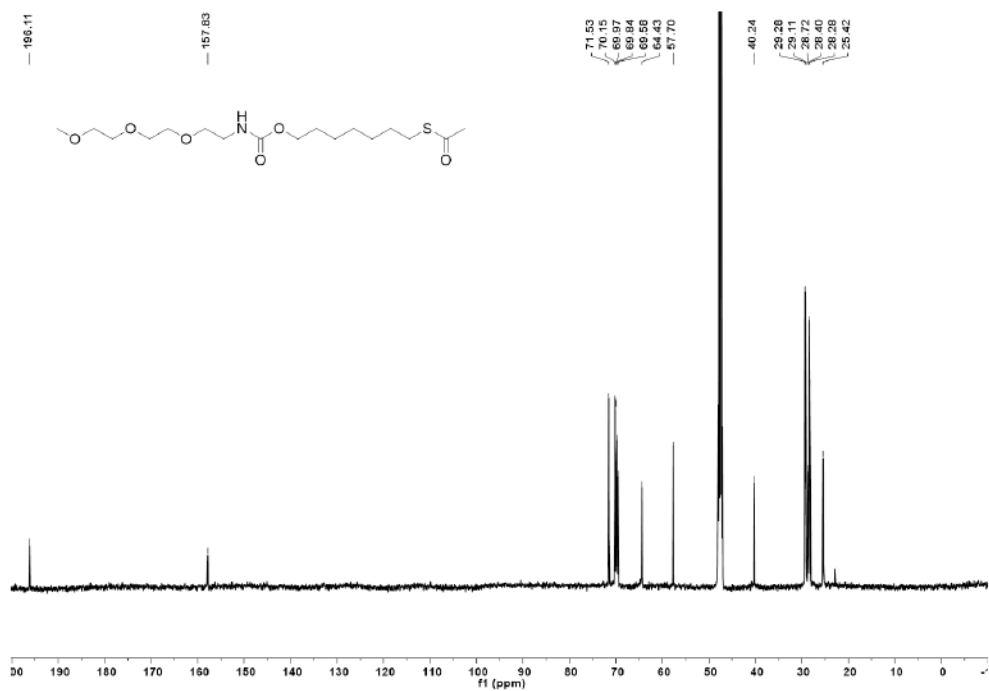
Figure A38. ^{13}C NMR spectrum of compound C14.

References
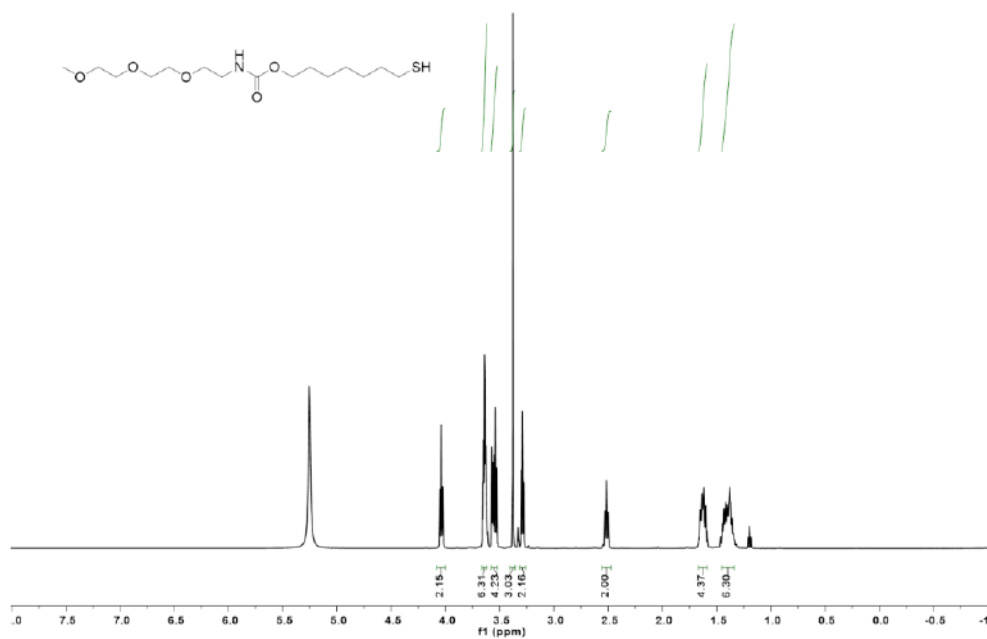
Figure A39. ^{1}H NMR spectrum of thiol 11.
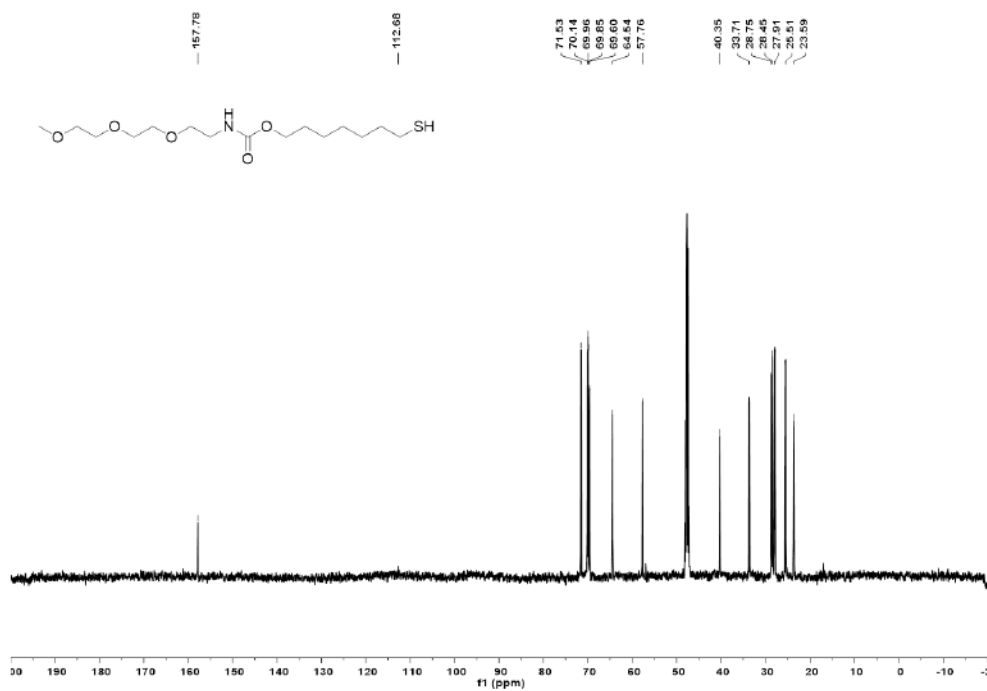
Figure A40. ^{13}C NMR spectrum of thiol 11.

179
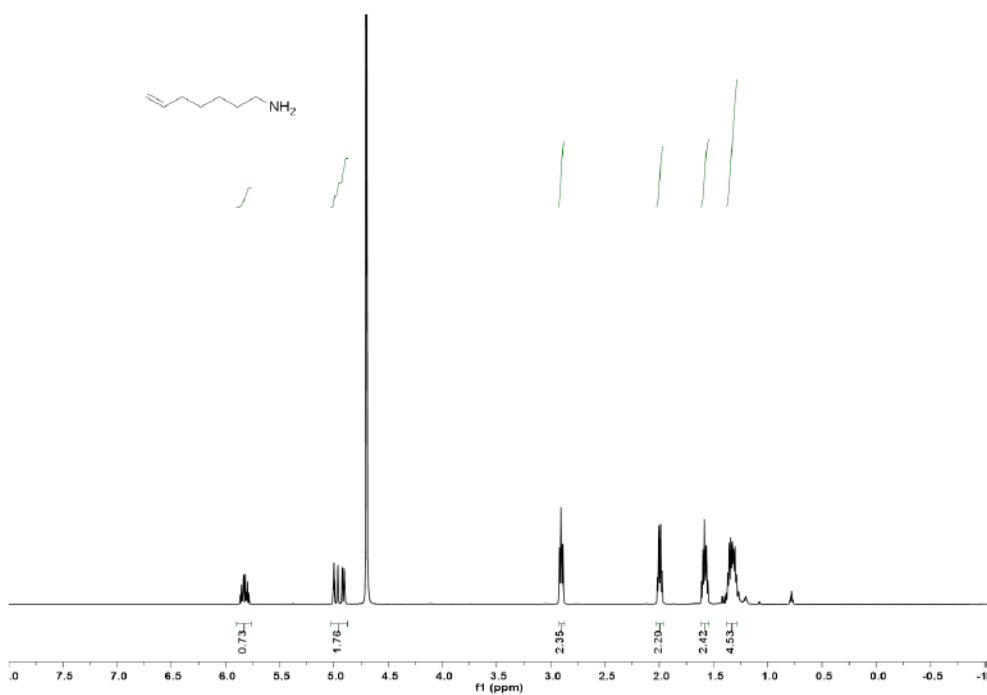
Figure A41. ^{1}H NMR spectrum of compound C16.
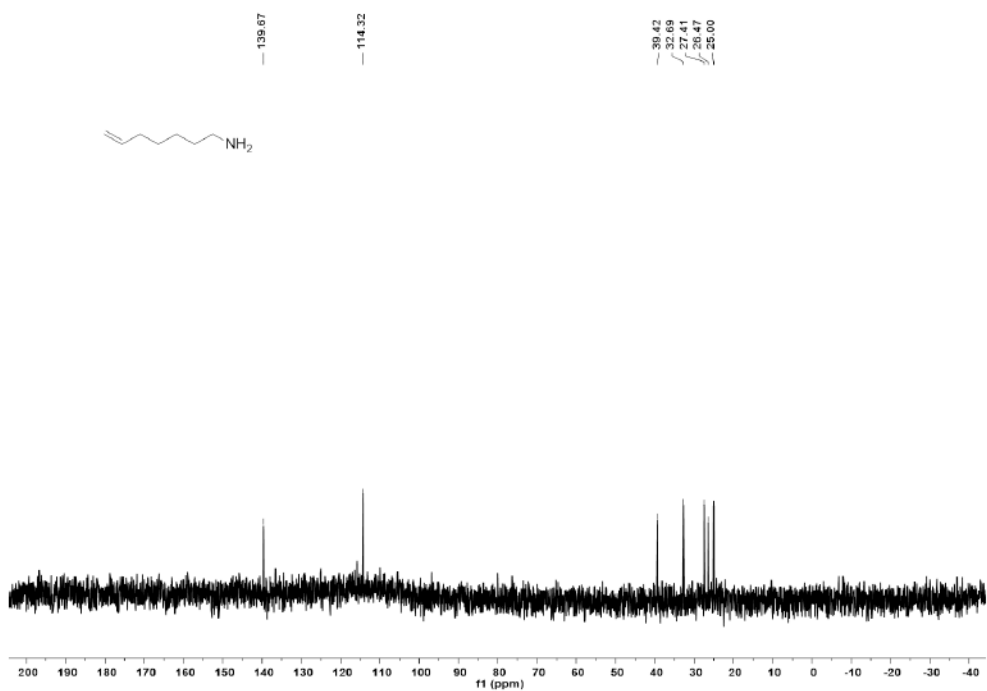
Figure A42. ^{13}C NMR spectrum of compound C16.
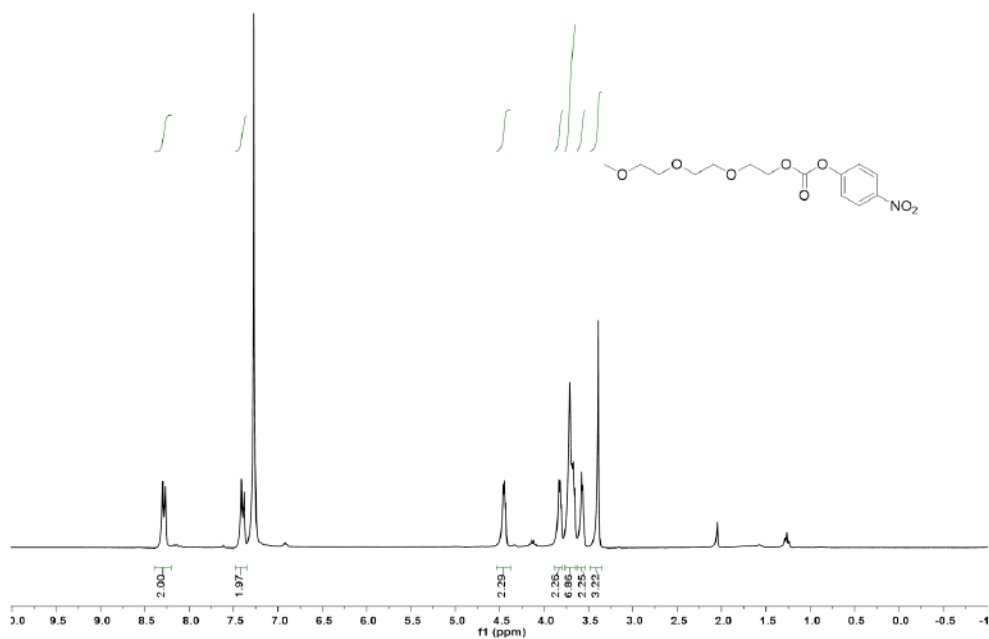
Figure A43. ^{1}H NMR spectrum of compound C17.
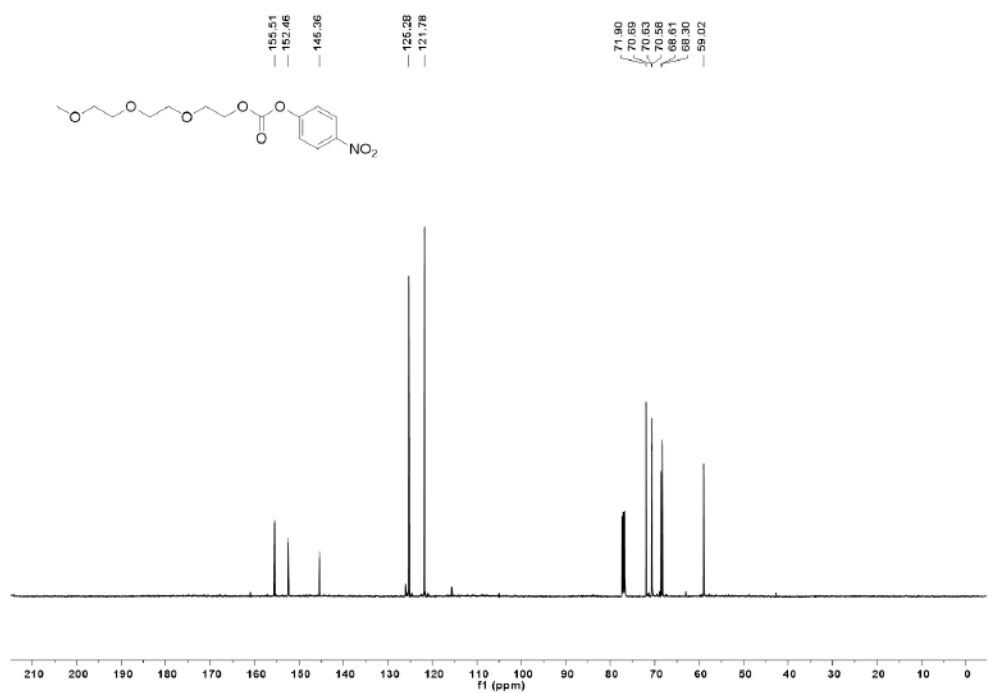
Figure A44. ^{13}C NMR spectrum of compound C17.
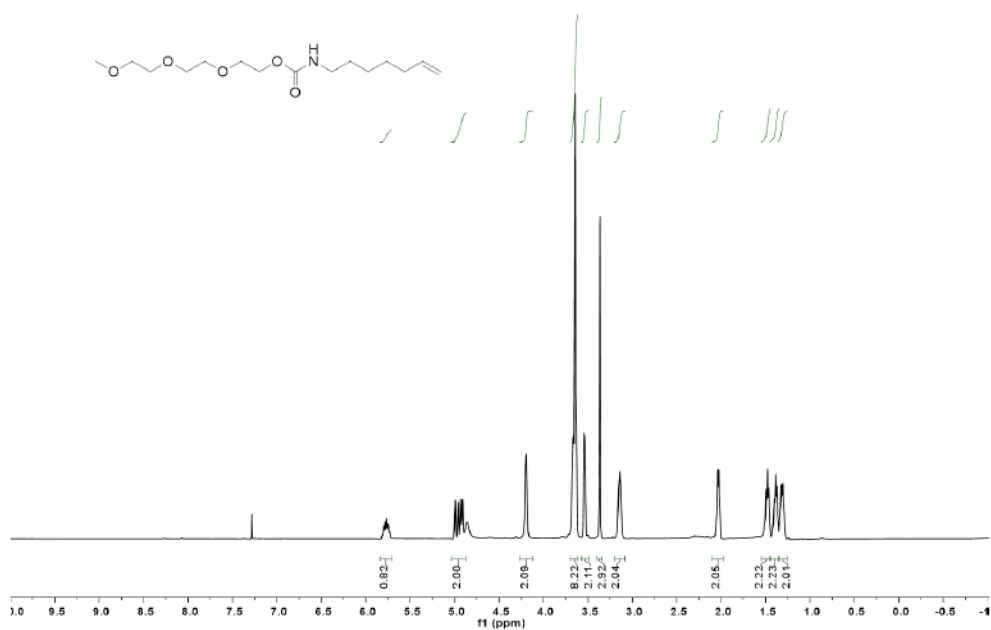
Figure A45. [^1]H NMR spectrum of compound C18.
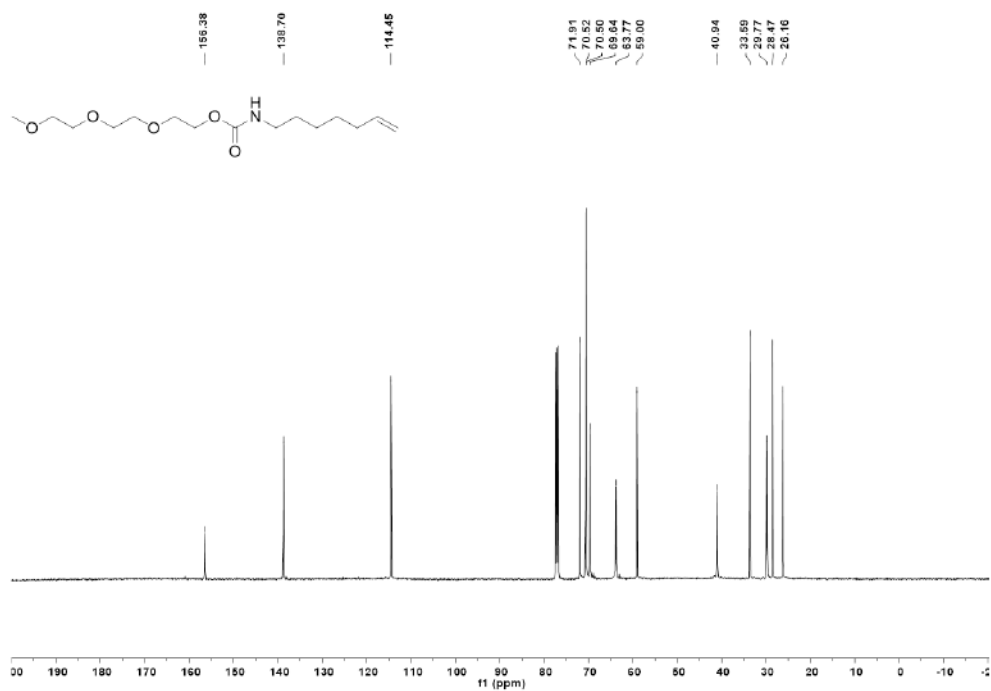
Figure A46. [^13]C NMR spectrum of compound C18.
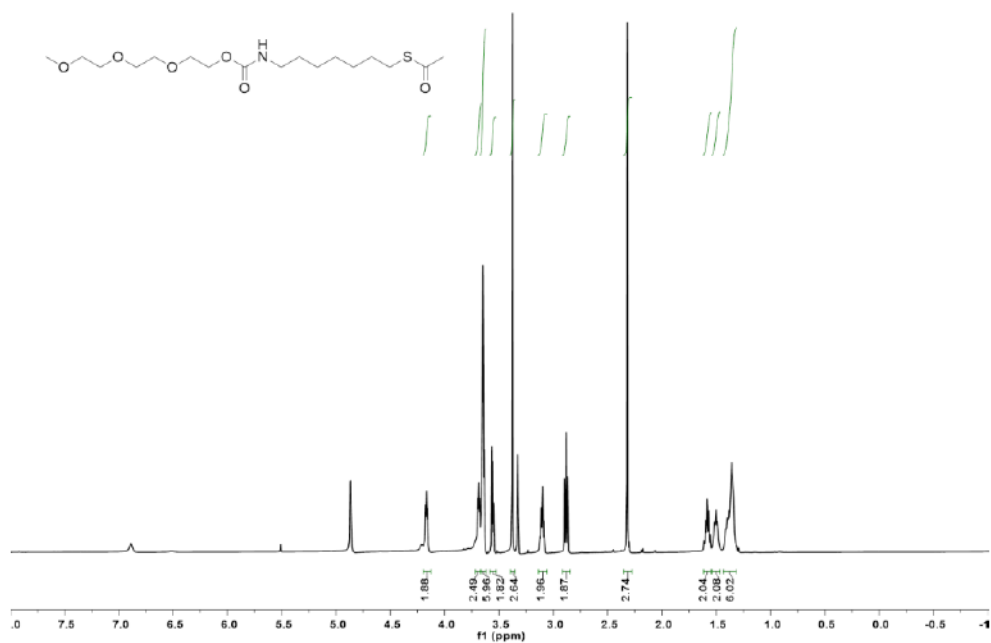
Figure A47. ^{1}H NMR spectrum of compound C19.
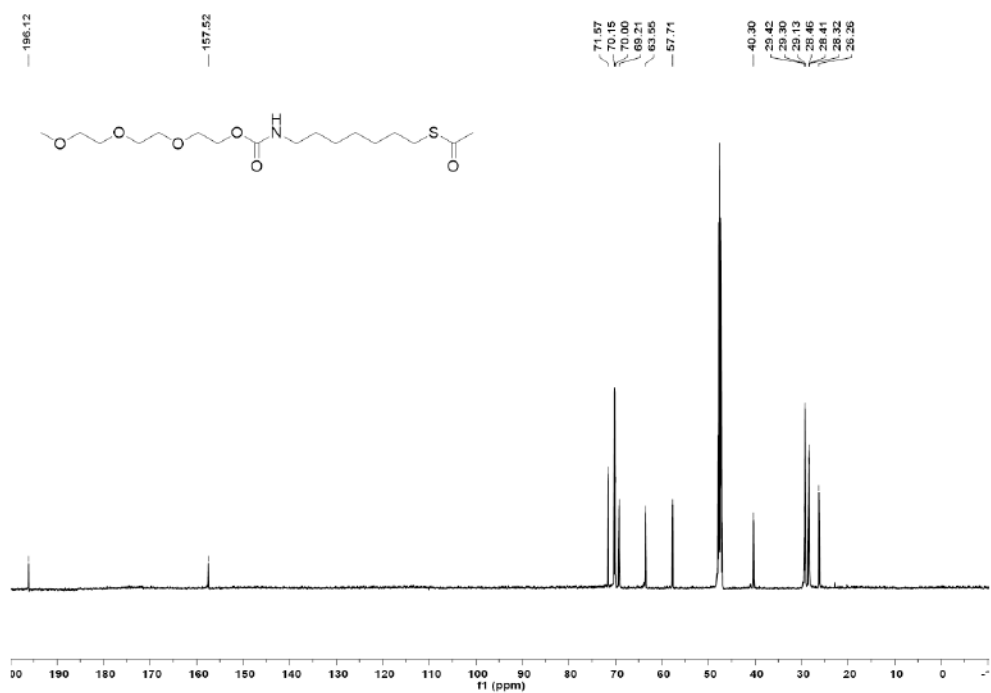
Figure A48. ^{13}C NMR spectrum of compound C19.

Figure A49. ^{1}H NMR spectrum of thiol 12.

Figure A50. ^{13}C NMR spectrum of thiol 12.
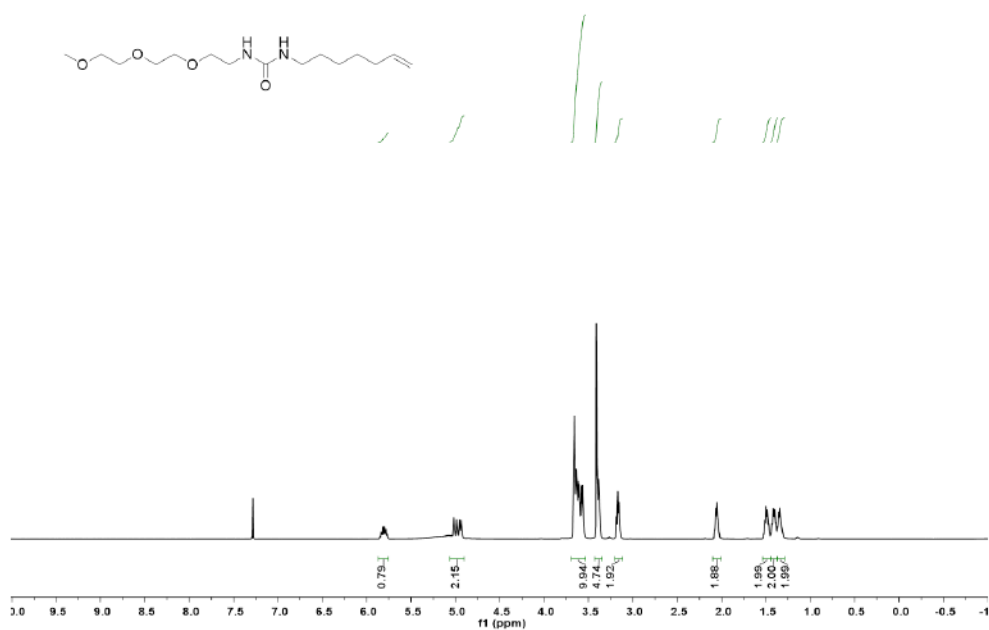
Figure A51. ^{1}H NMR spectrum of compound C20.
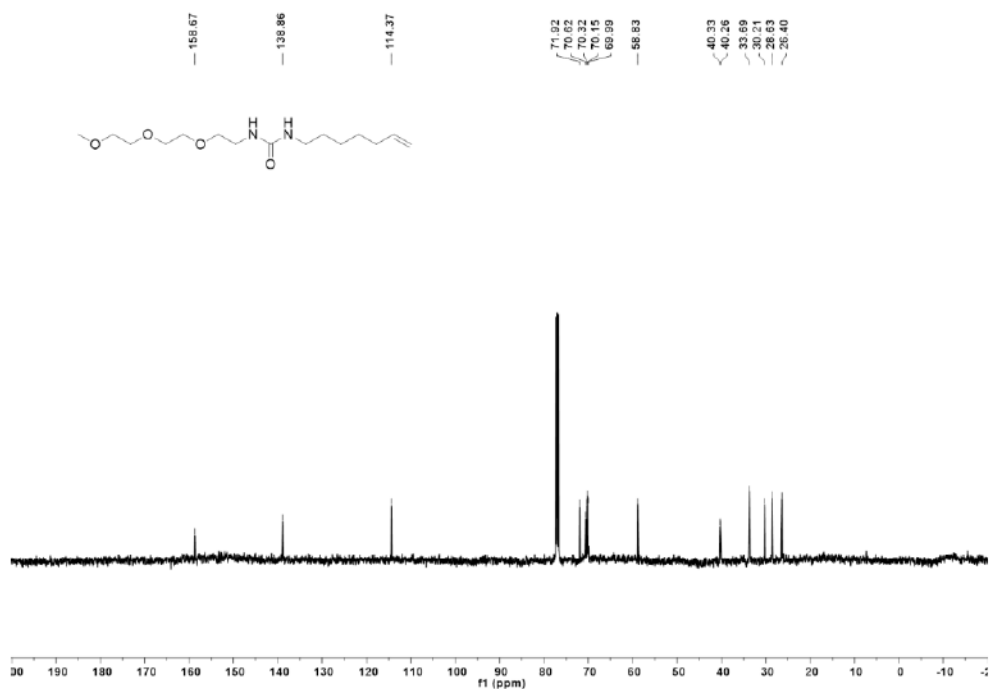
Figure A52. ^{13}C NMR spectrum of compound C20.
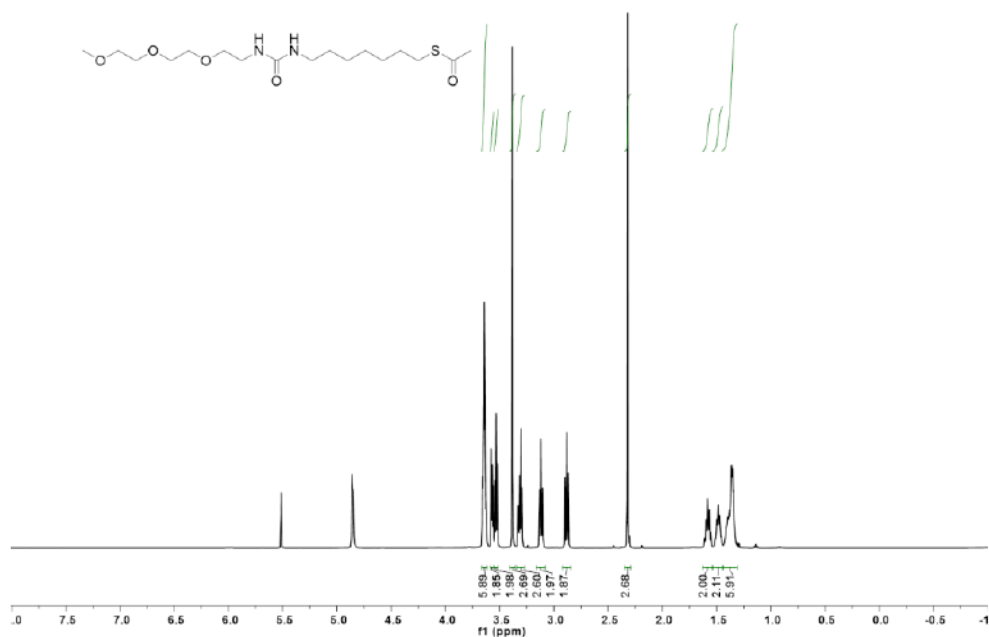
Figure A53. ^{1}H NMR spectrum of compound C21.
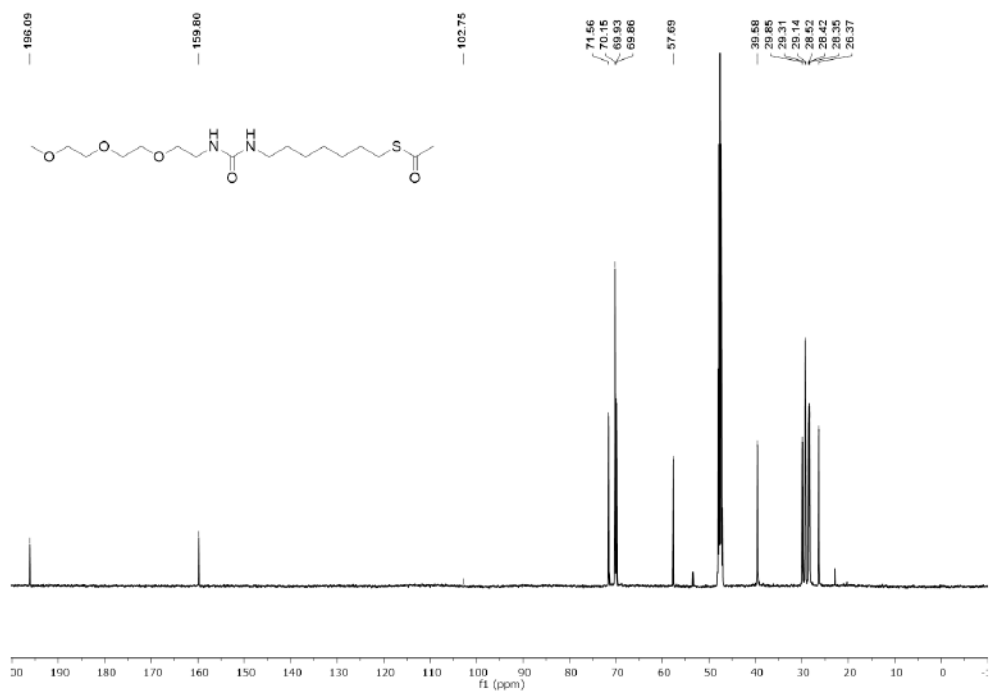
Figure A54. ^{13}C NMR spectrum of compound C21.
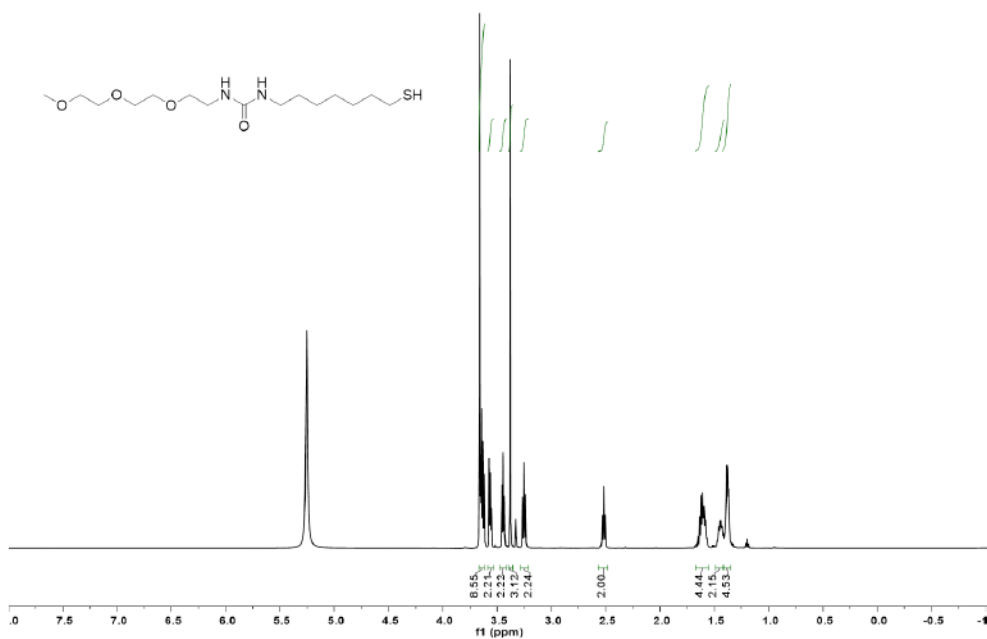
Figure A55. ^{1}H NMR spectrum of thiol 13.
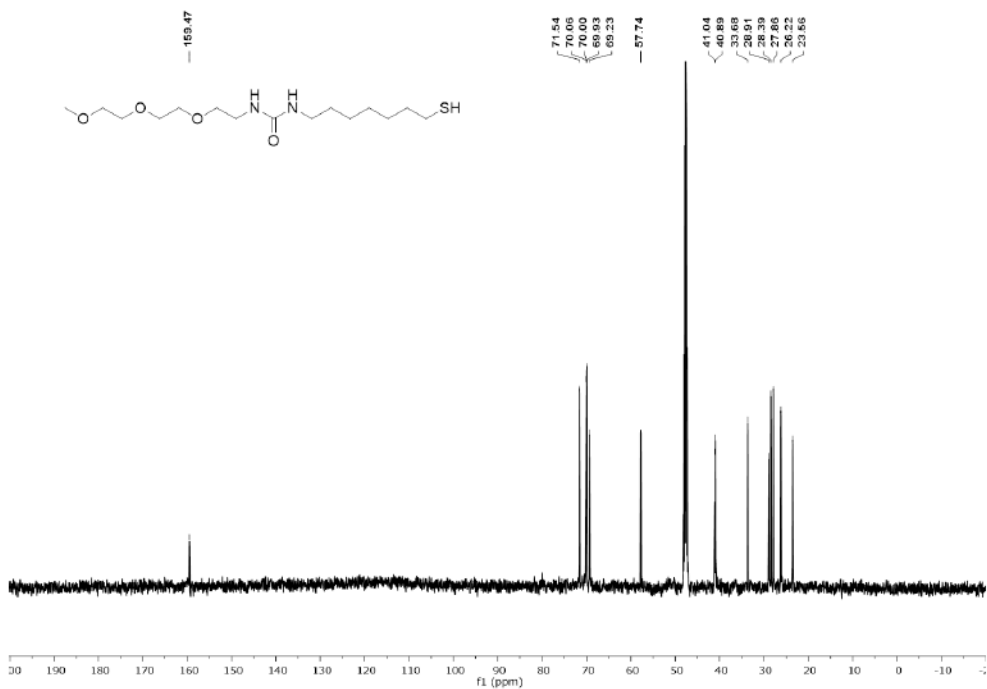
Figure A56. ^{13}C NMR spectrum of thiol 13.
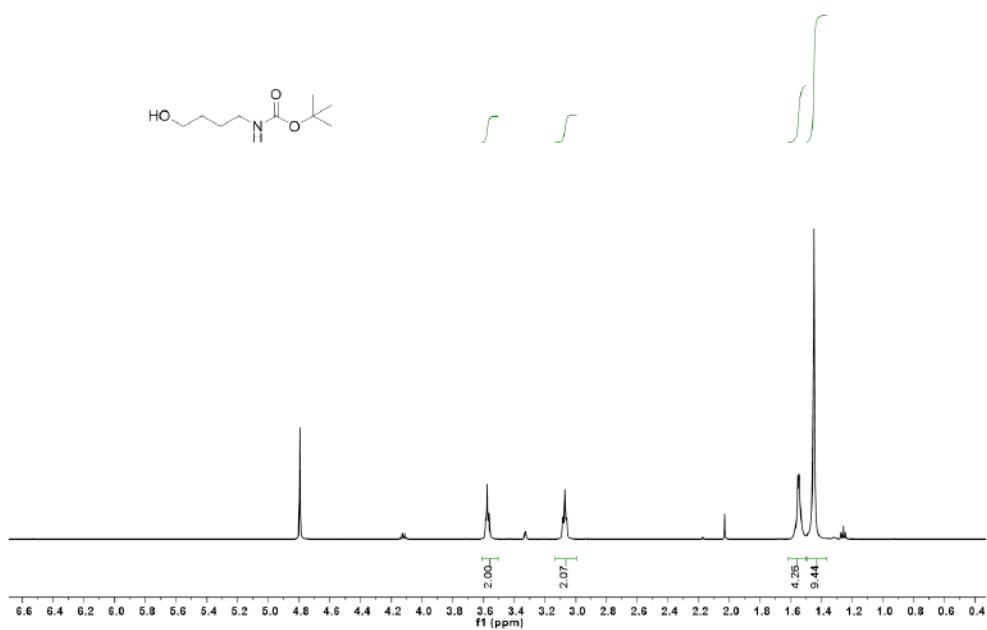
Figure A57. ^{1}H NMR spectrum of compound C22.
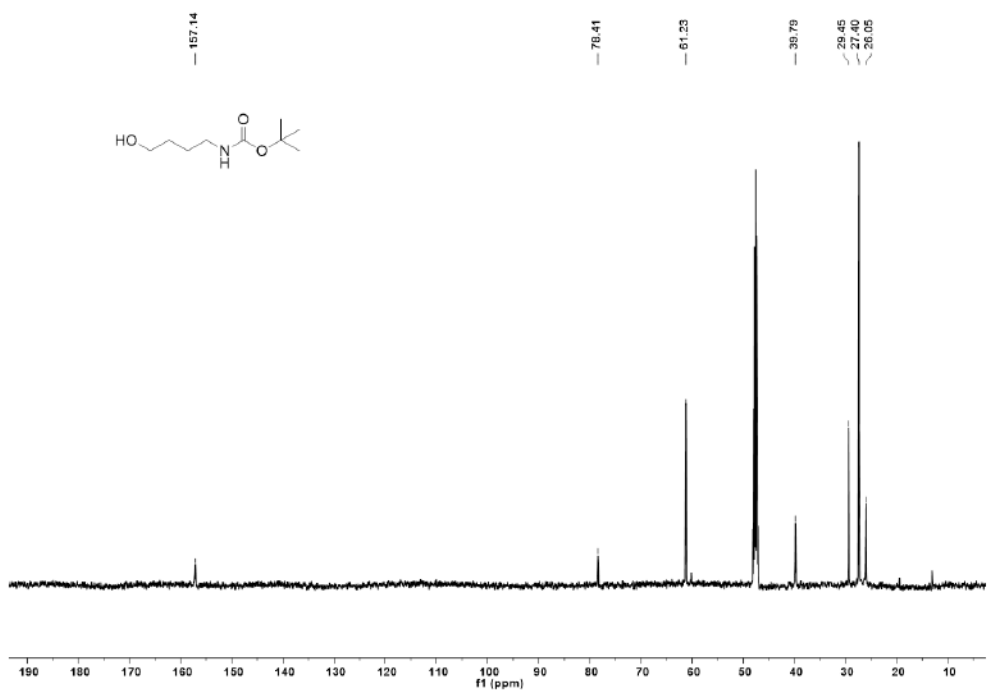
Figure A58. ^{13}C NMR spectrum of compound C22.
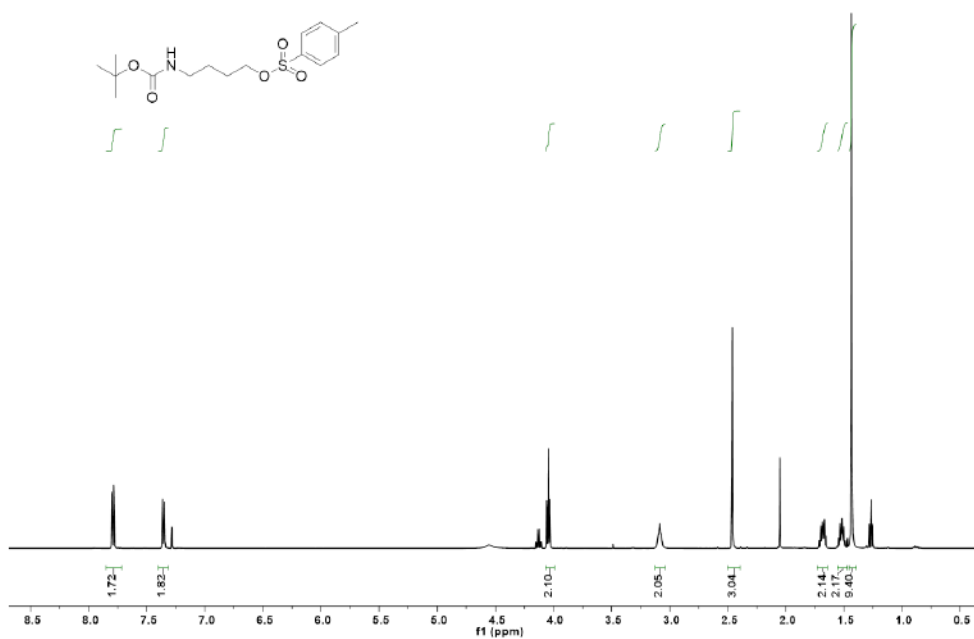
Figure A59. ^{1}H NMR spectrum of compound C23.
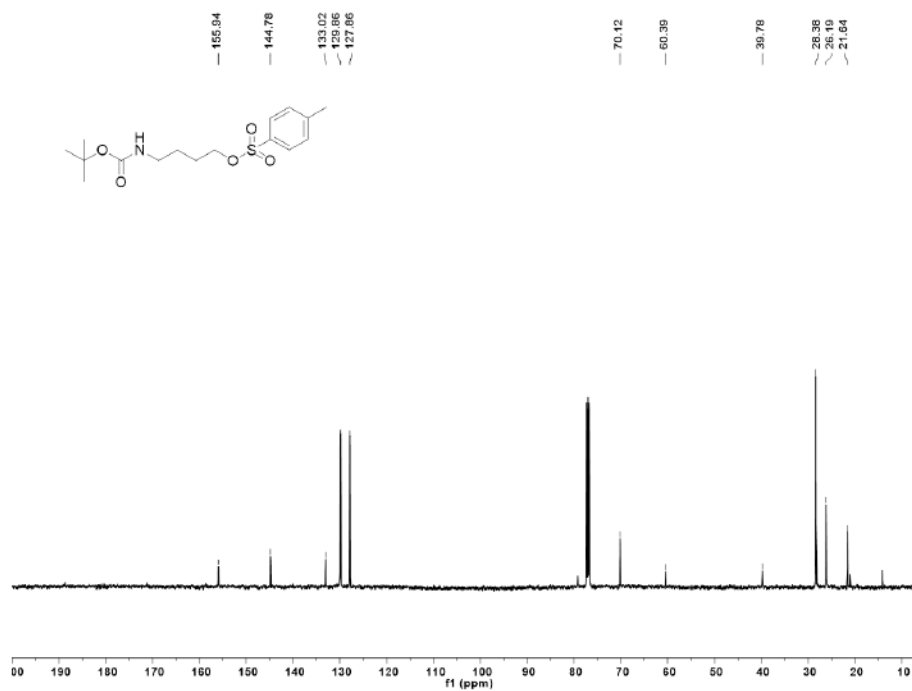
Figure A60. ^{13}C NMR spectrum of compound C23.
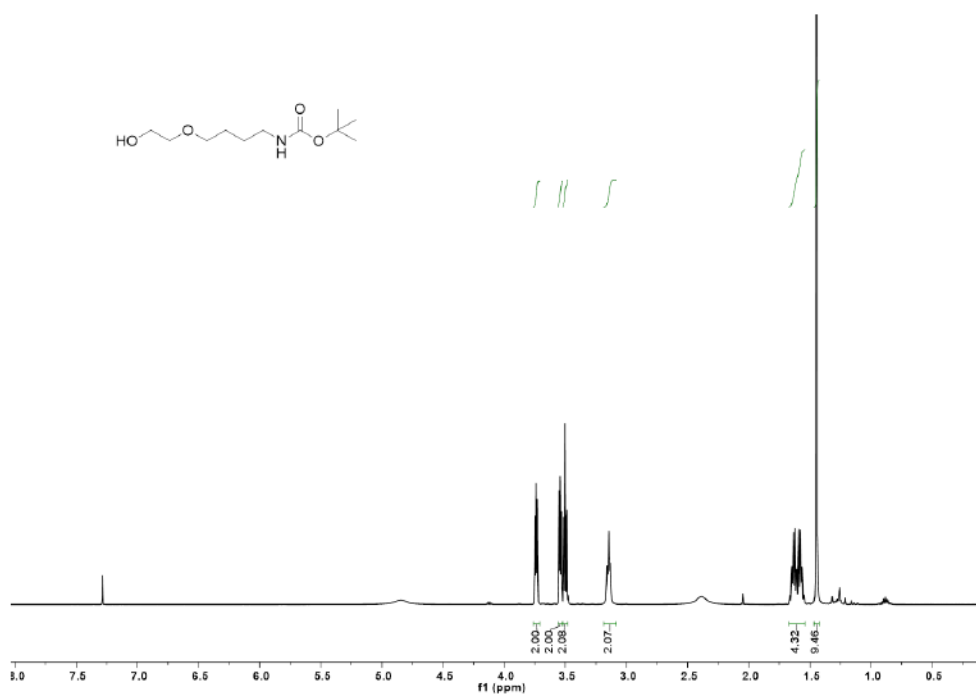
Figure A61. ^{1}H NMR spectrum of compound C24.
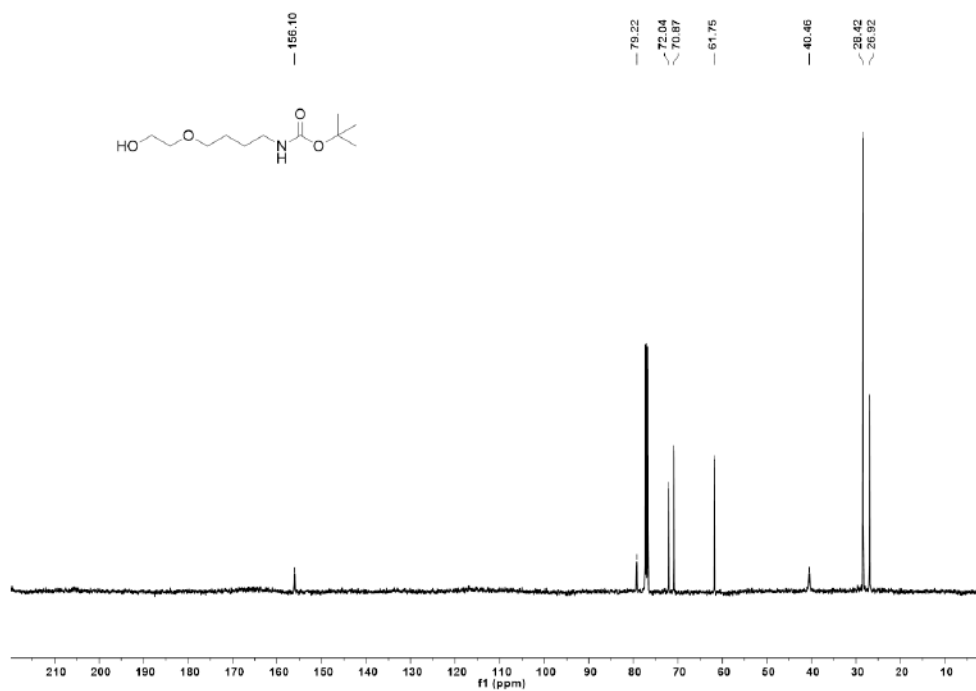
Figure A62. ^{13}C NMR spectrum of compound C24.
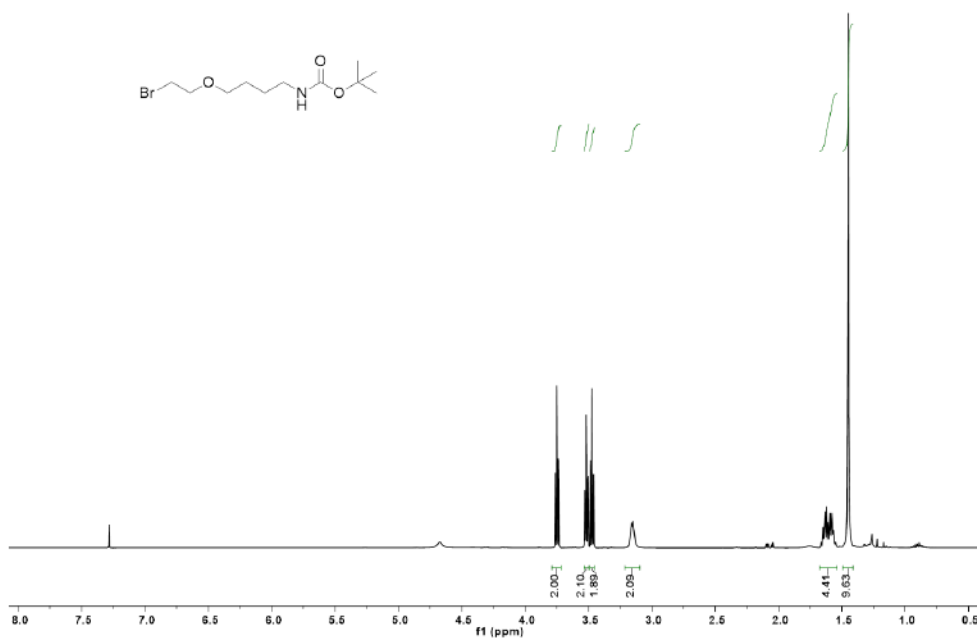
Figure A63. ^{1}H NMR spectrum of compound C25.
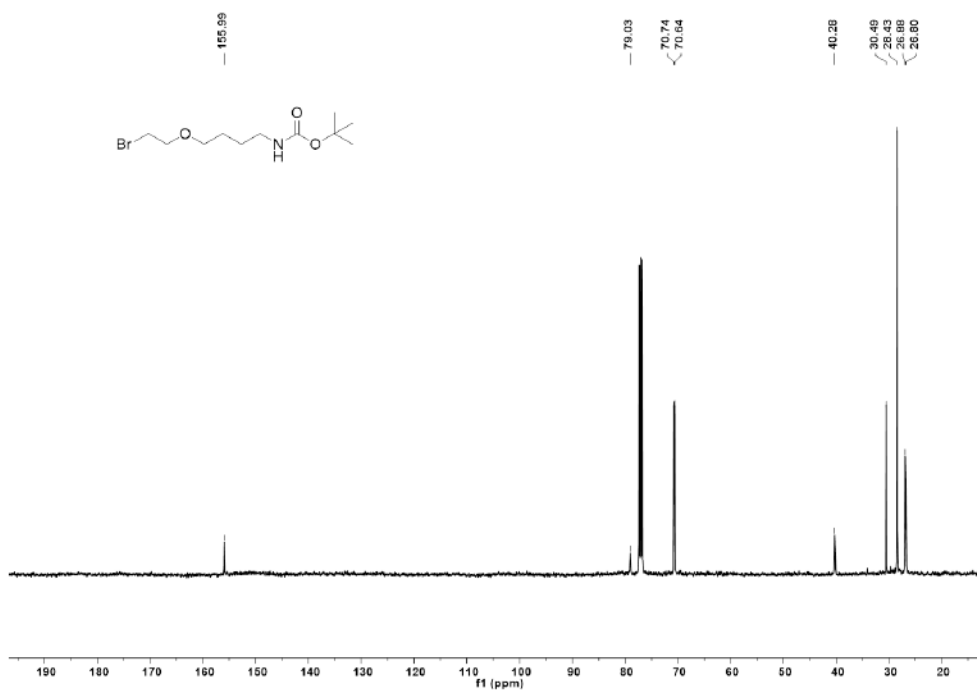
Figure A64. ^{13}C NMR spectrum of compound C25.
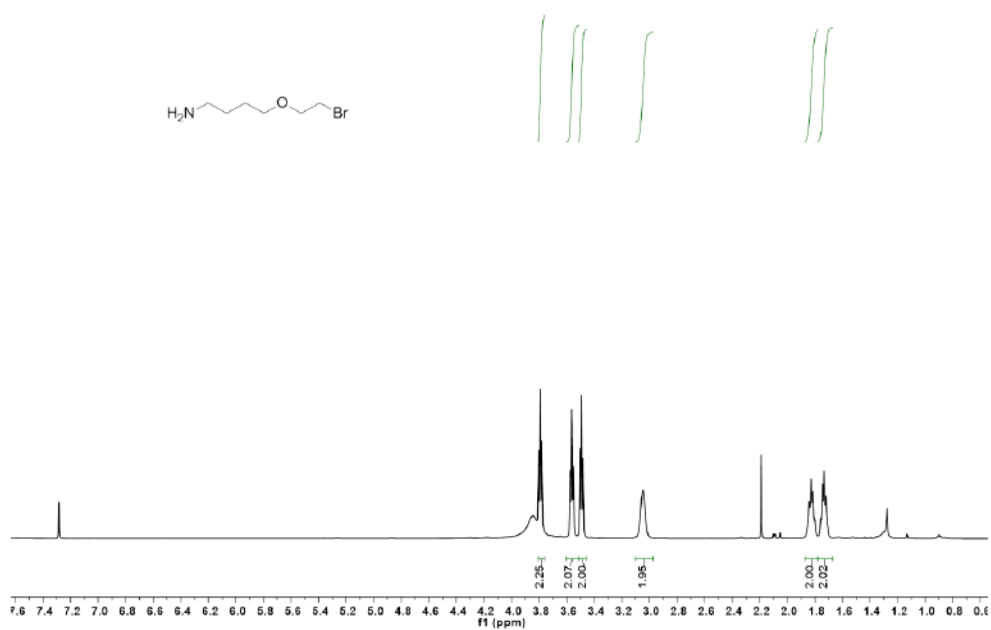
Figure A65. ^{1}H NMR spectrum of compound C26.
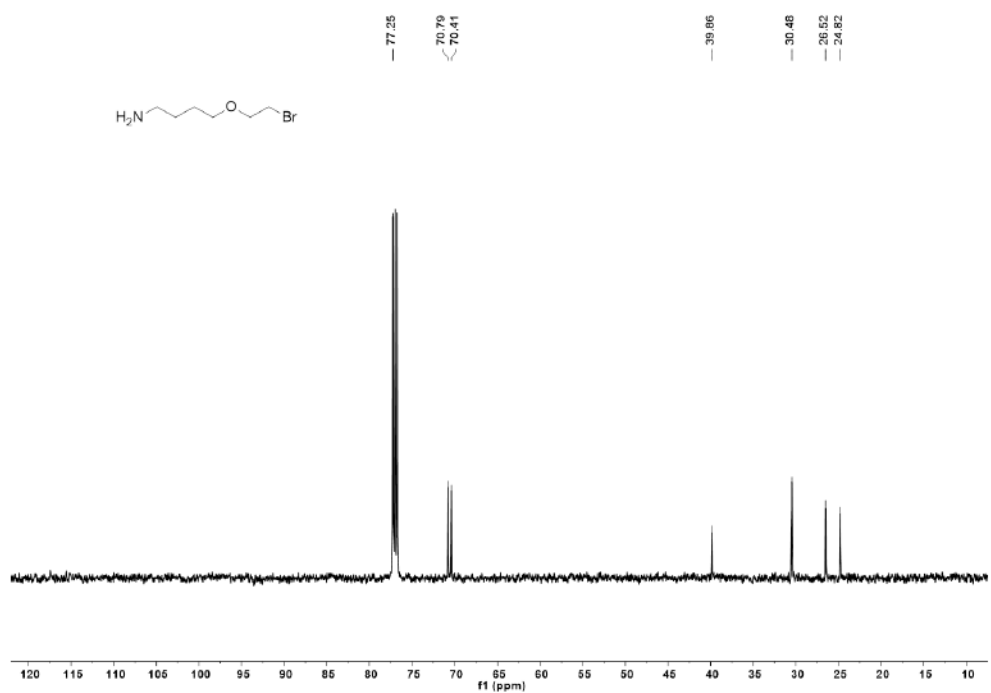
Figure A66. ^{13}C NMR spectrum of compound C26.
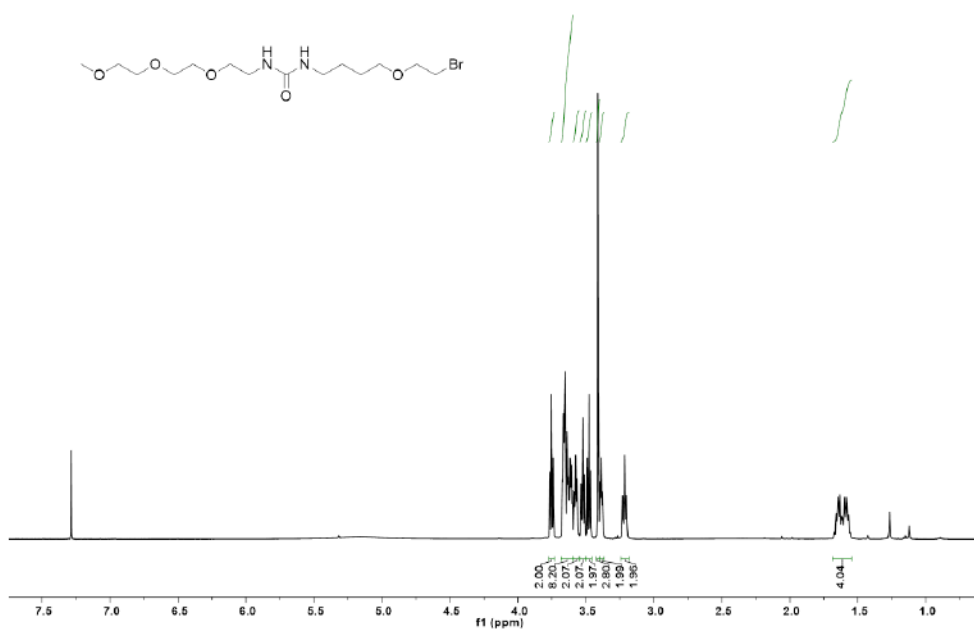
Figure A67. ^{1}H NMR spectrum of compound C27.
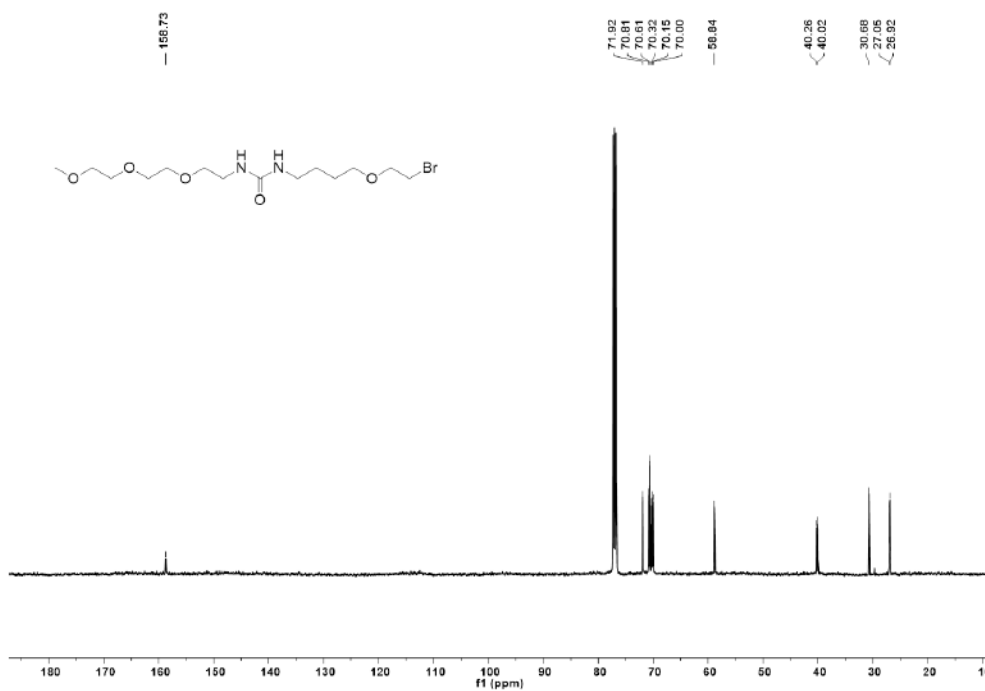
Figure A68. ^{13}C NMR spectrum of compound C27.
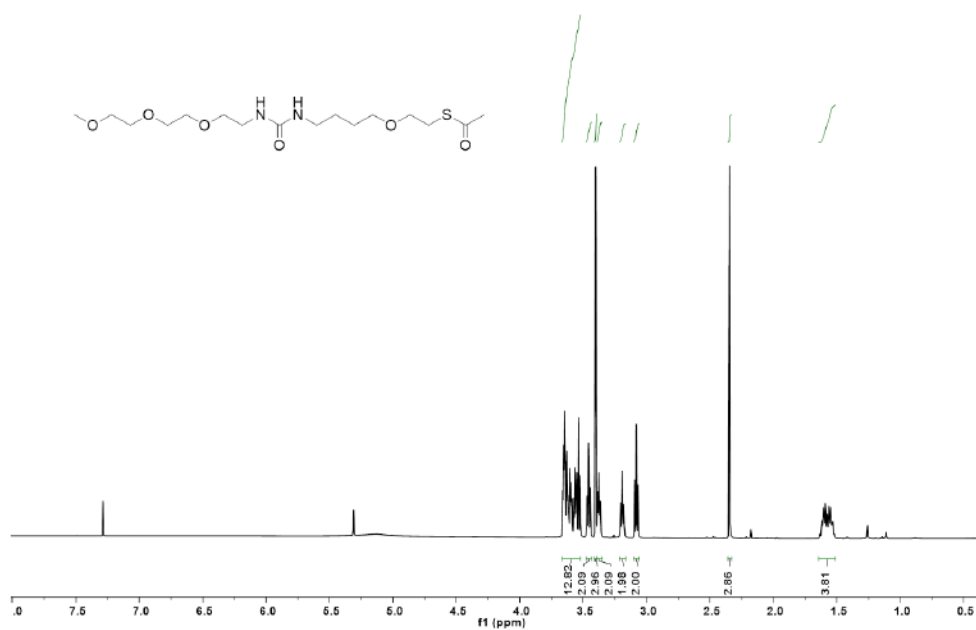
Figure A69. ^{1}H NMR spectrum of compound C28.
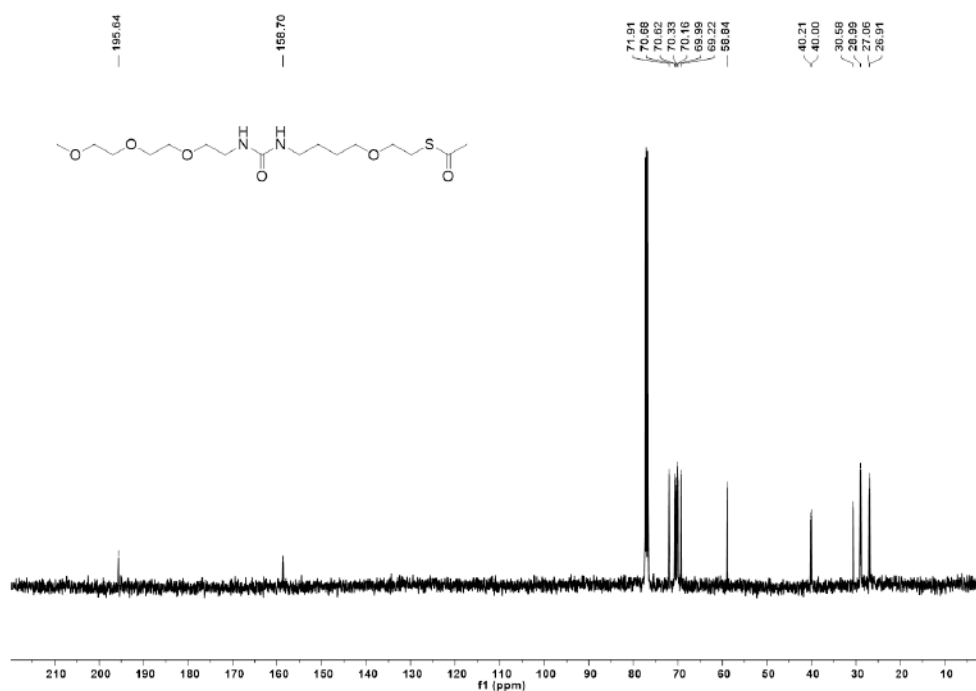
Figure A70. ^{13}C NMR spectrum of compound C28.
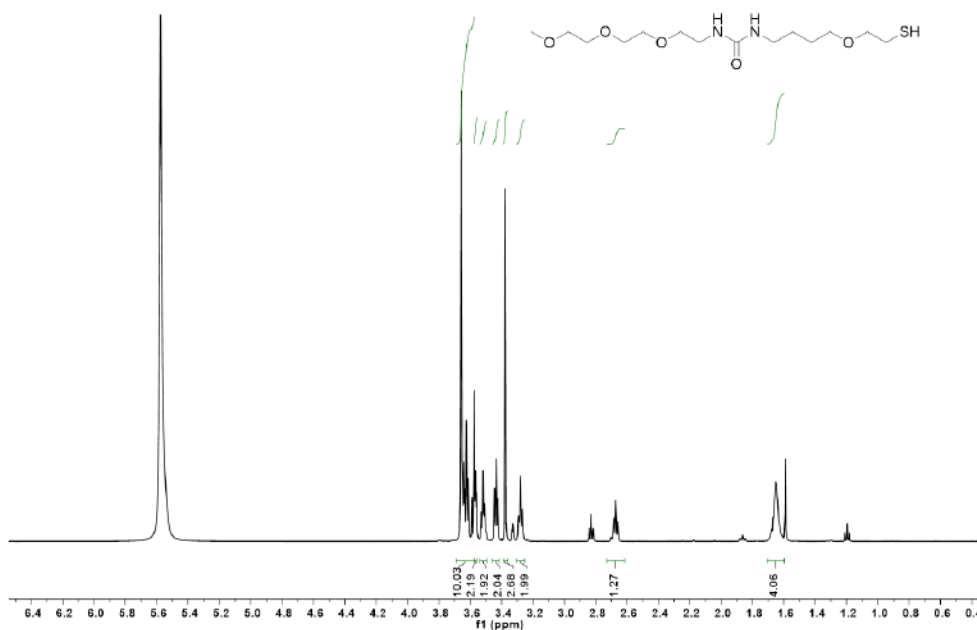
Figure A71. ^{1}H NMR spectrum of thiol 14.
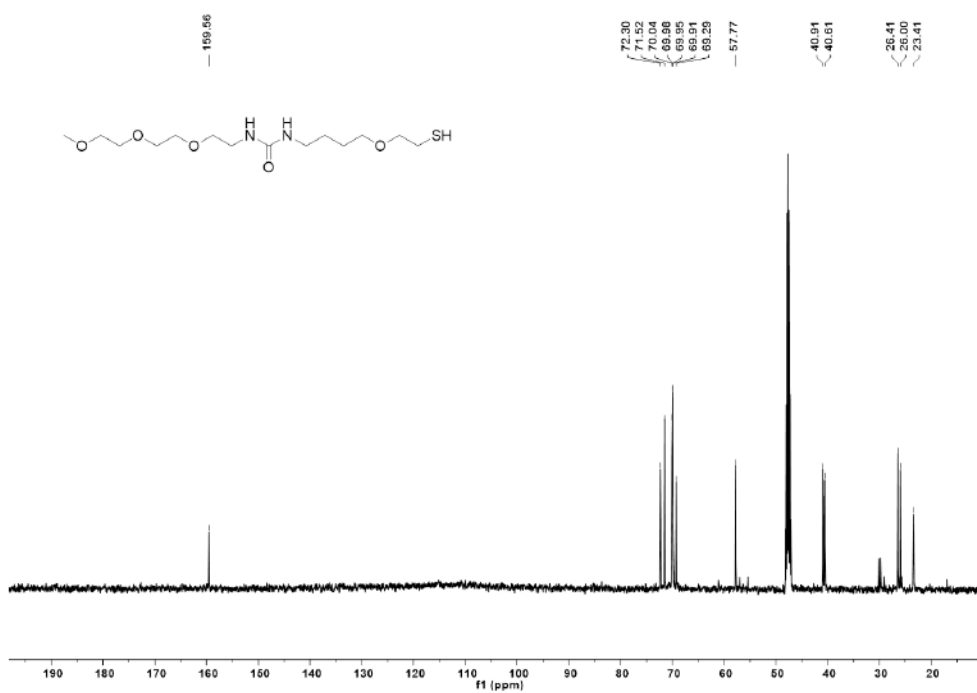
Figure A72. ^{13}C NMR spectrum of thiol 14.
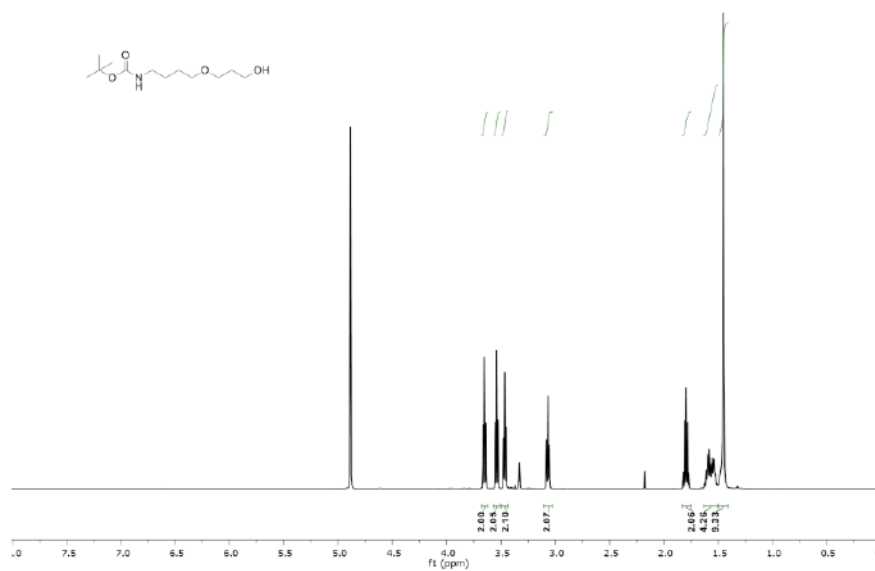
Figure A73. ^{1}H NMR spectrum of C29.
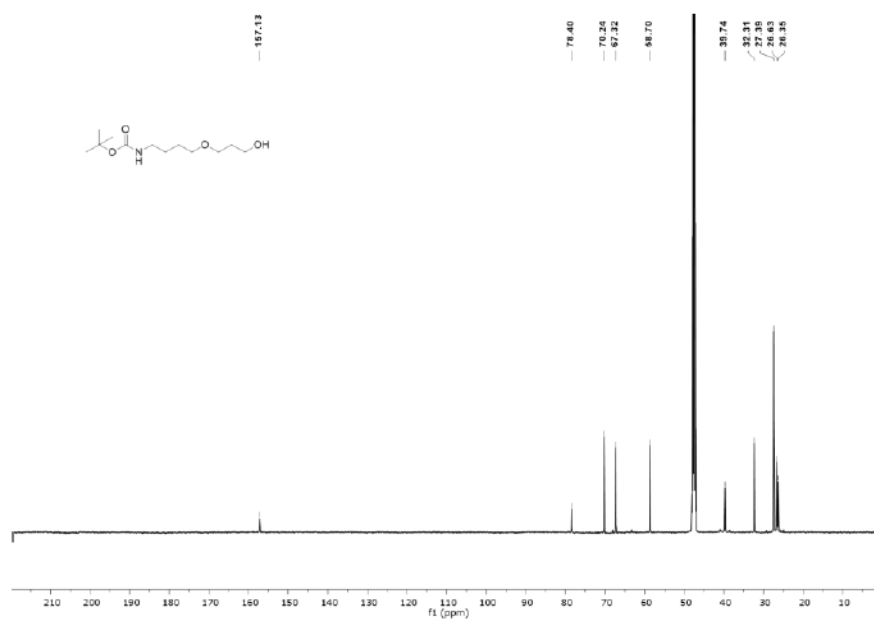
Figure A74. ^{13}C NMR spectrum of compound C29.

196
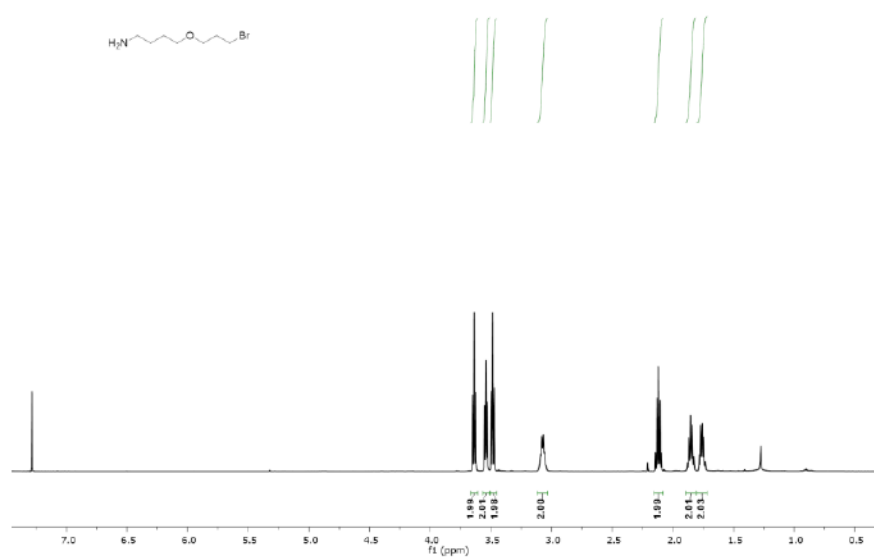
Figure A75. ^{1}H NMR spectrum of C31.
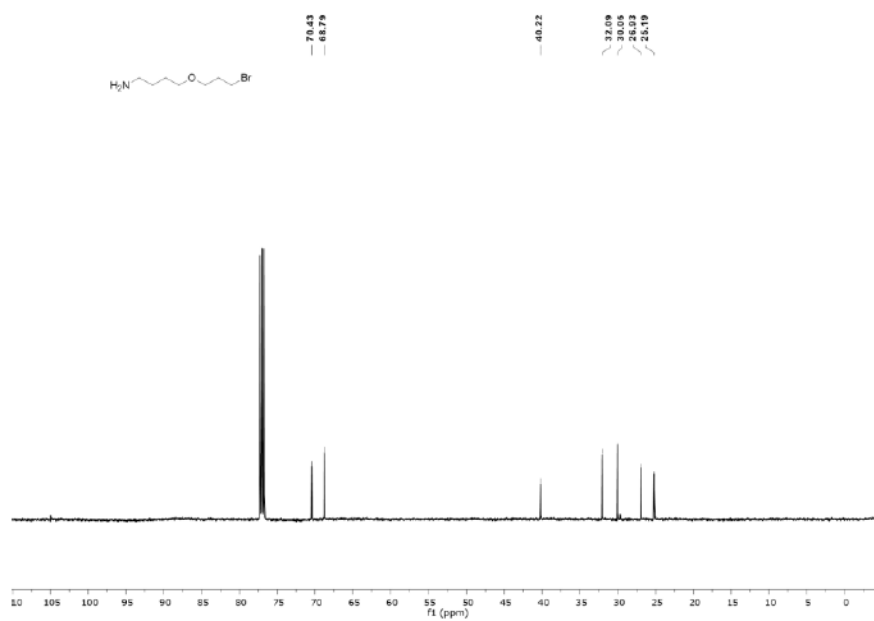
Figure A76. ^{13}C NMR spectrum of C31.
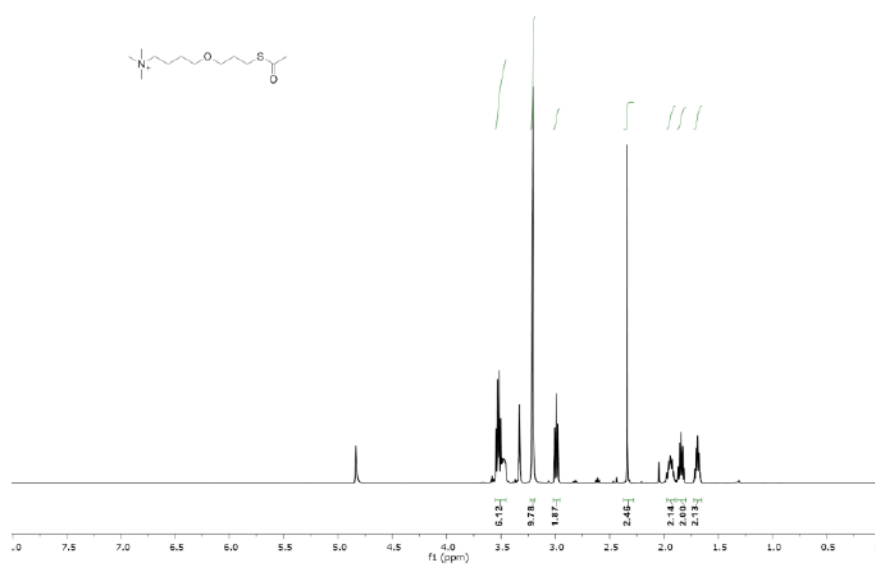
Figure A77. ^{1}HNMR spectrum of compound C33.
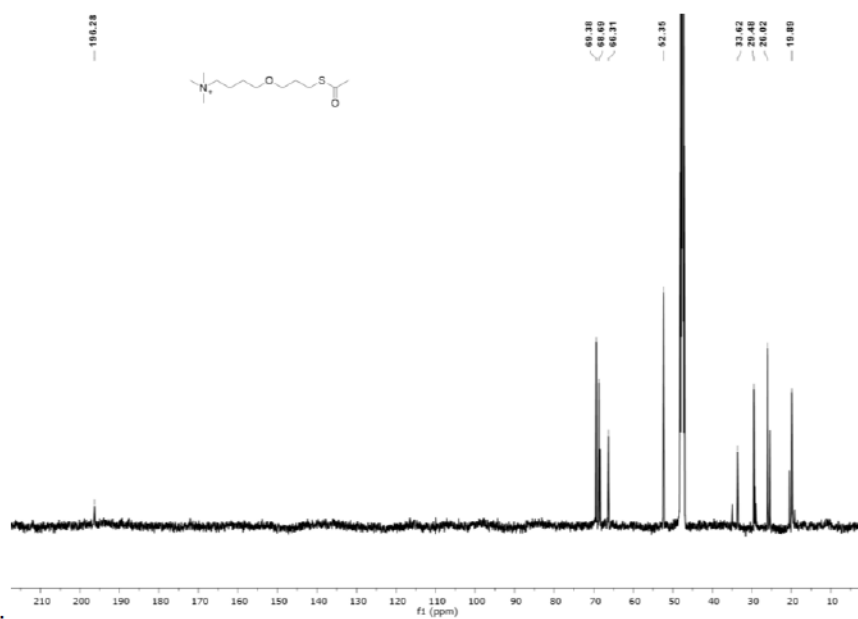
Figure A78. ^{13}C NMR spectrum of C33.
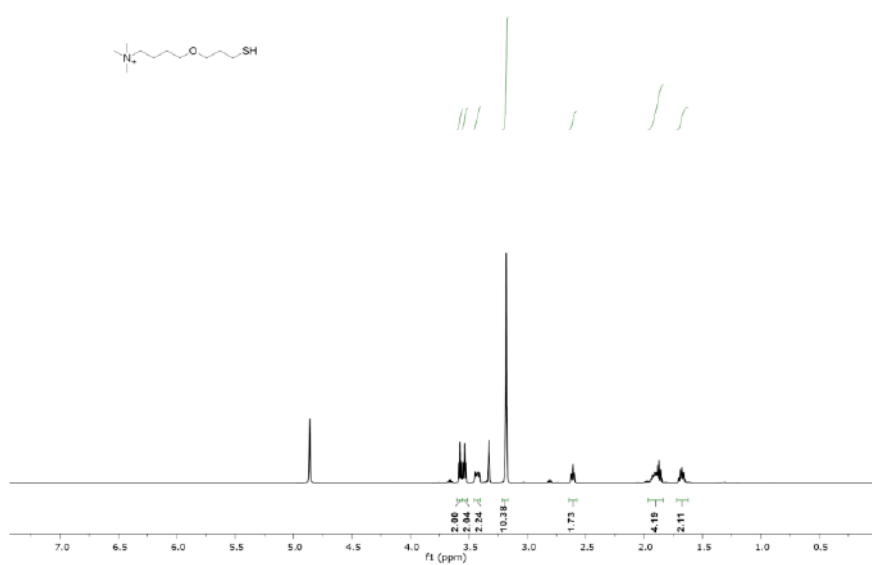
Figure A79. ^{1}HNMR spectrum of thiol 17.
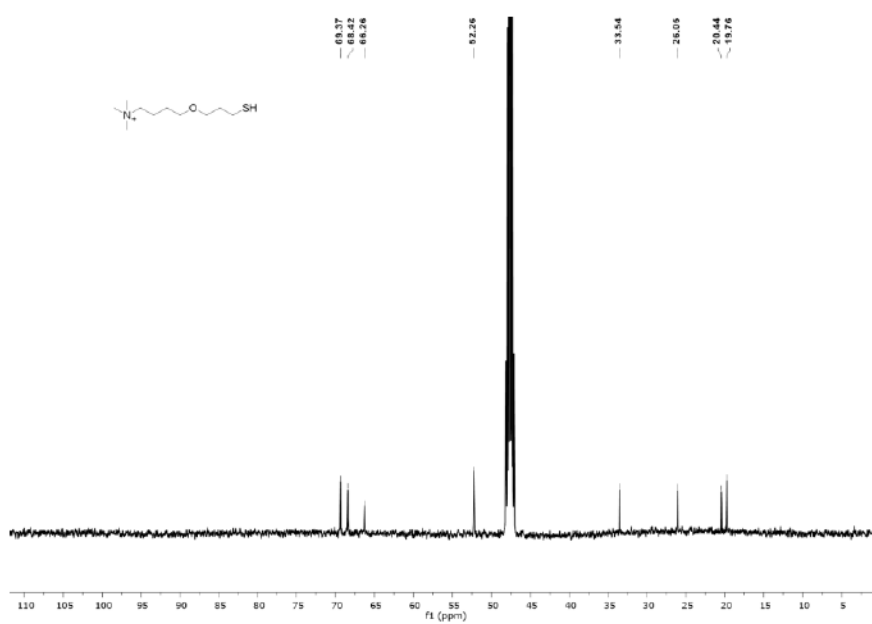
Figure A80. ^{13}C NMR spectrum of thiol 17.
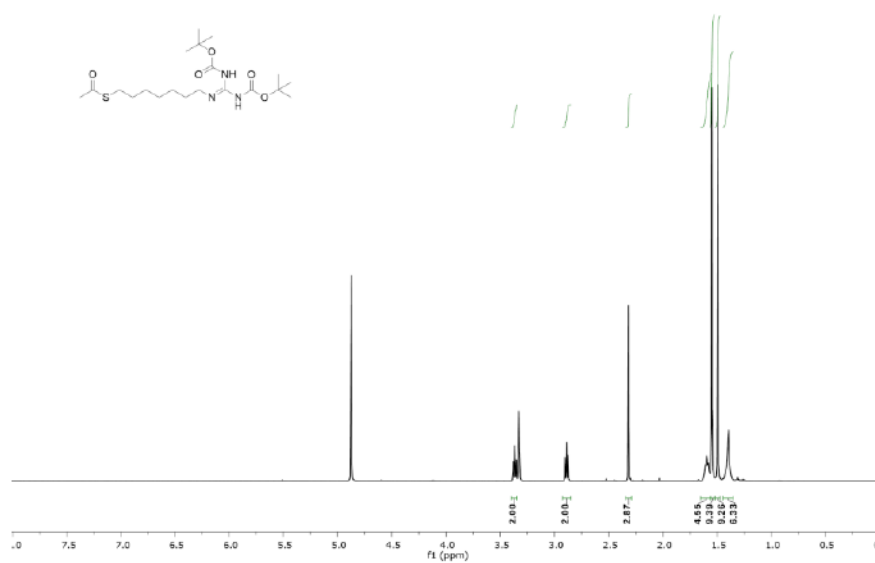
Figure A81. ^{1}HNMR spectrum of C35.
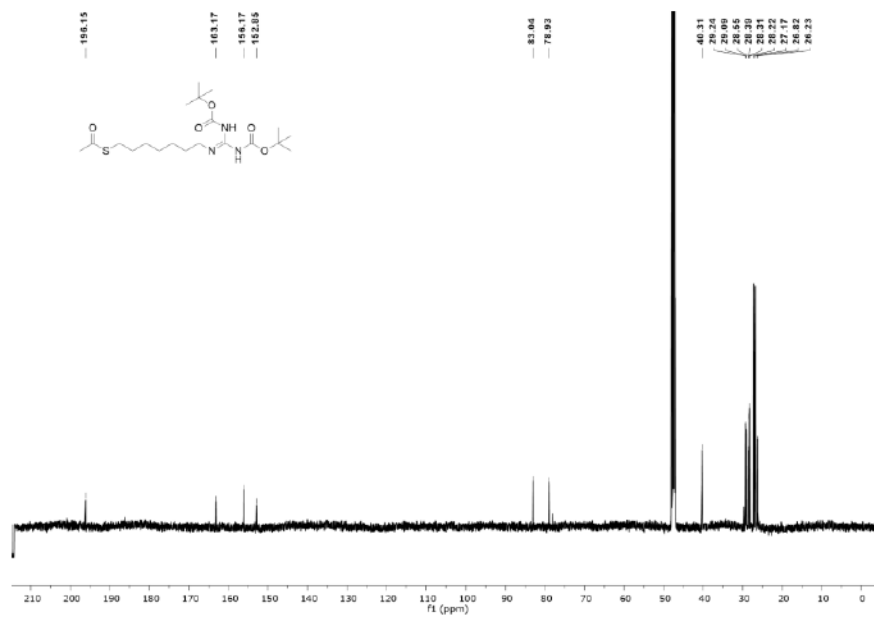
Figure A82. ^{13}C NMR spectrum of C35.
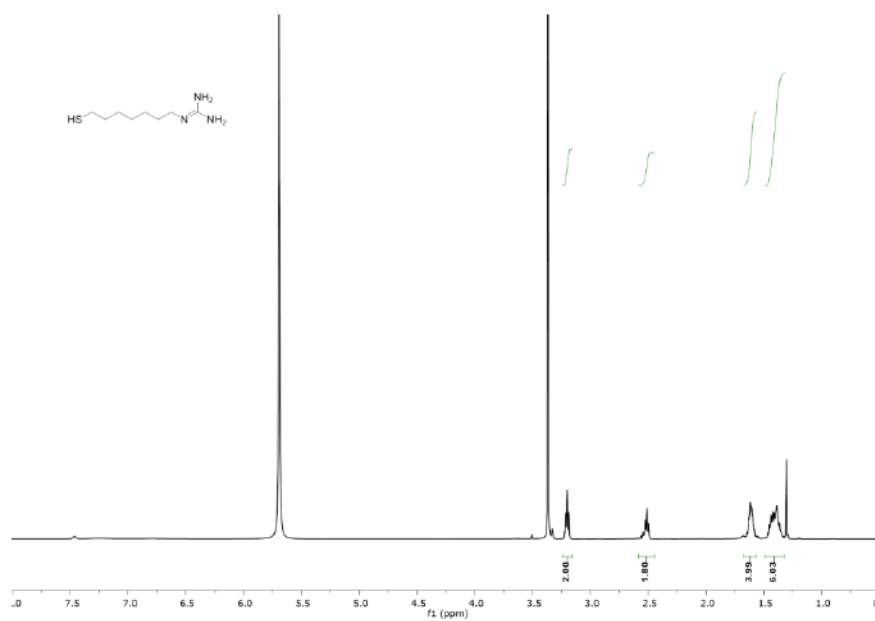
Figure A83. ^{1}HNMR spectrum of thiol **18**.
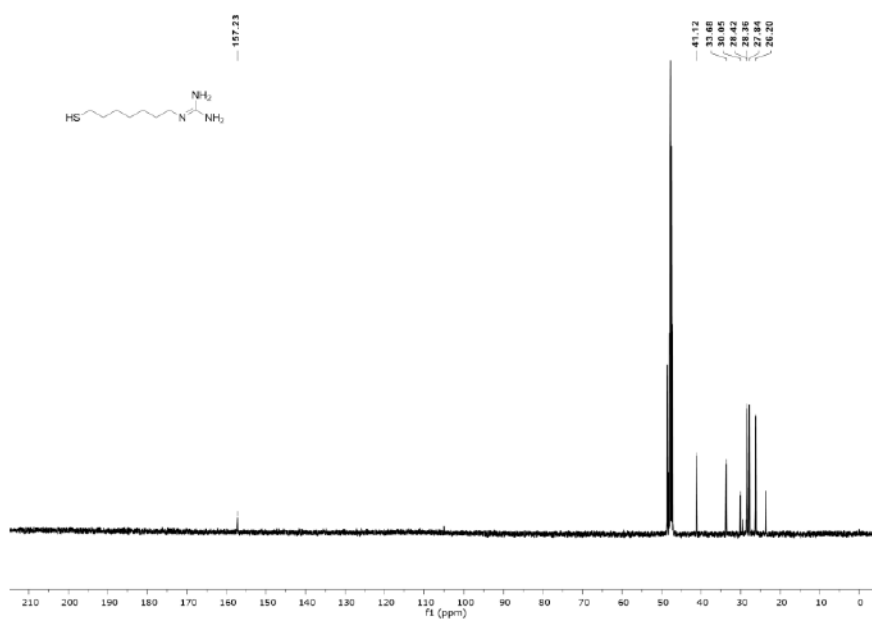
Figure A84. ^{13}C NMR spectrum of thiol **18**.
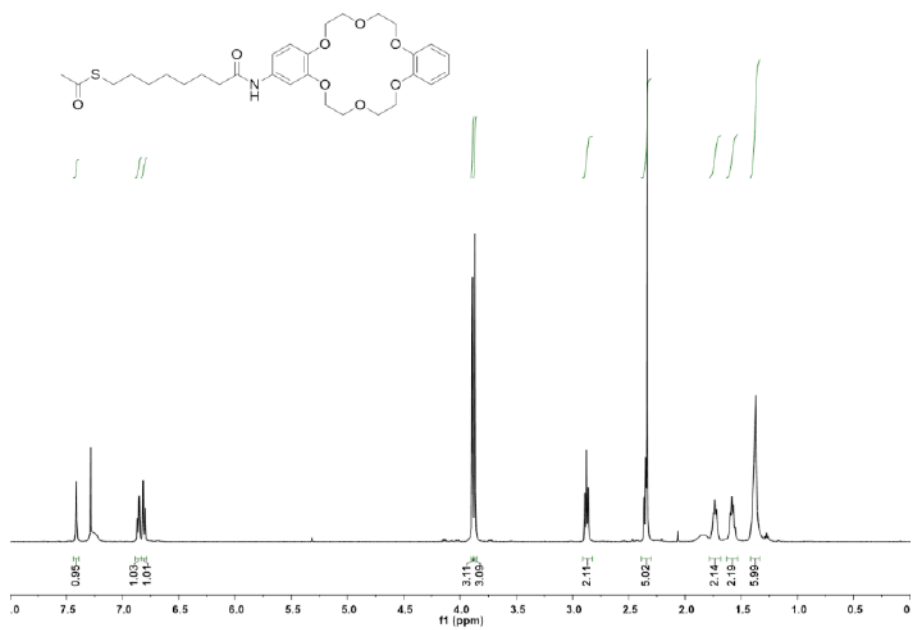
Figure A85. ^{1}H NMR spectrum of C36.
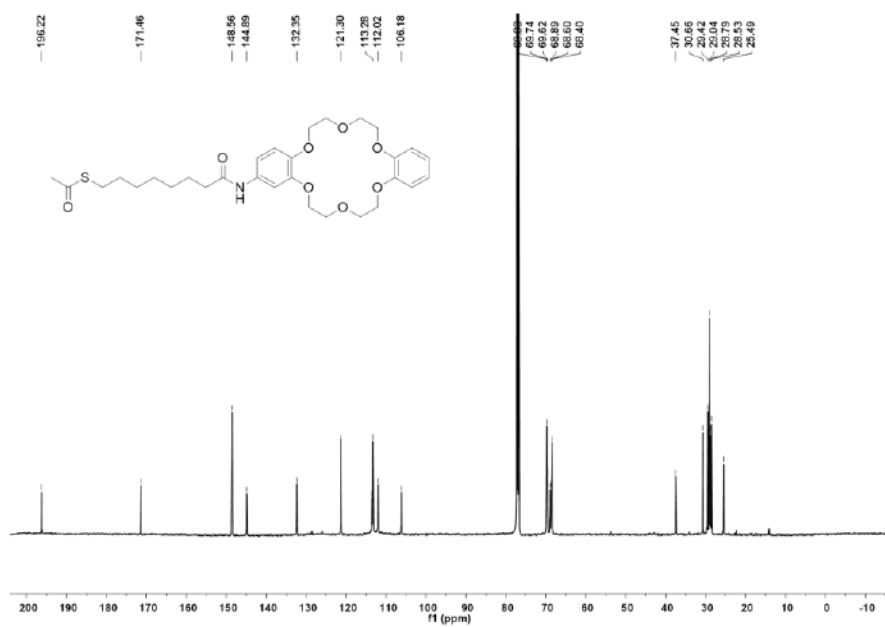
Figure A86. ^{13}C NMR spectrum of C36.
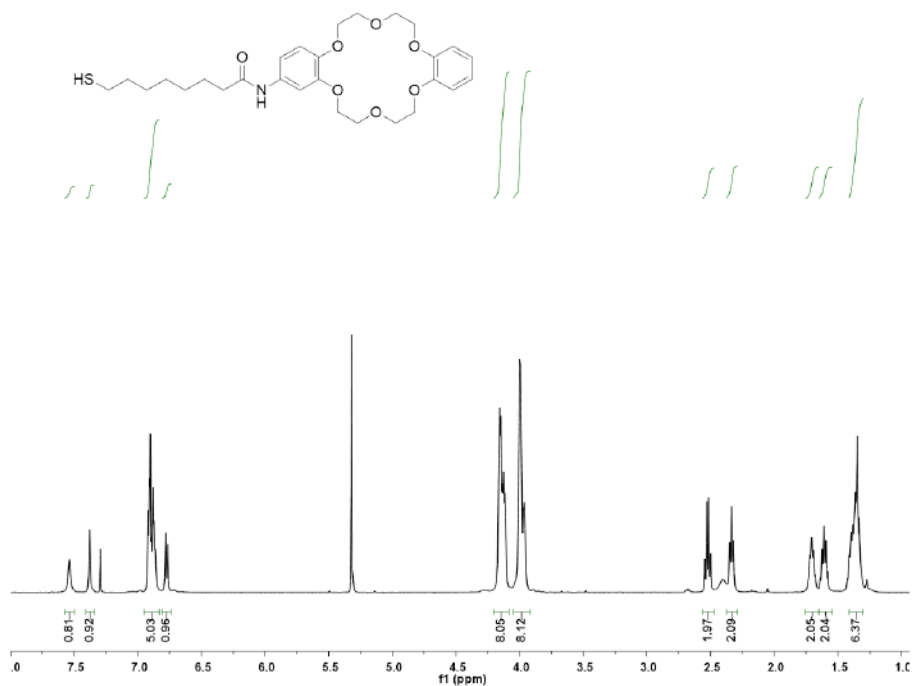
Figure A87. ¹H NMR spectrum of thiol 19.
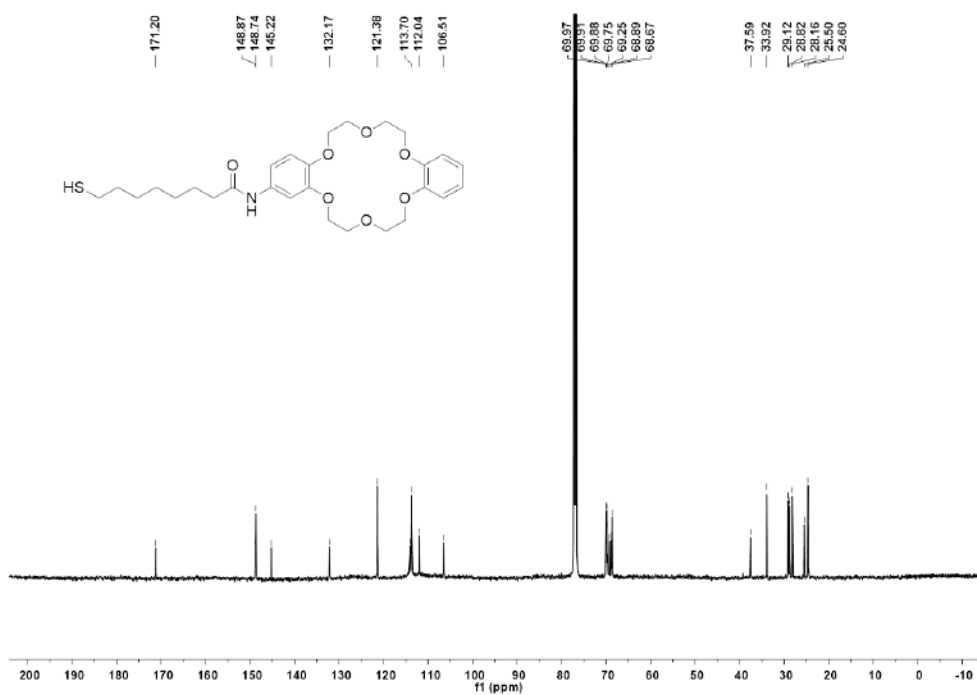
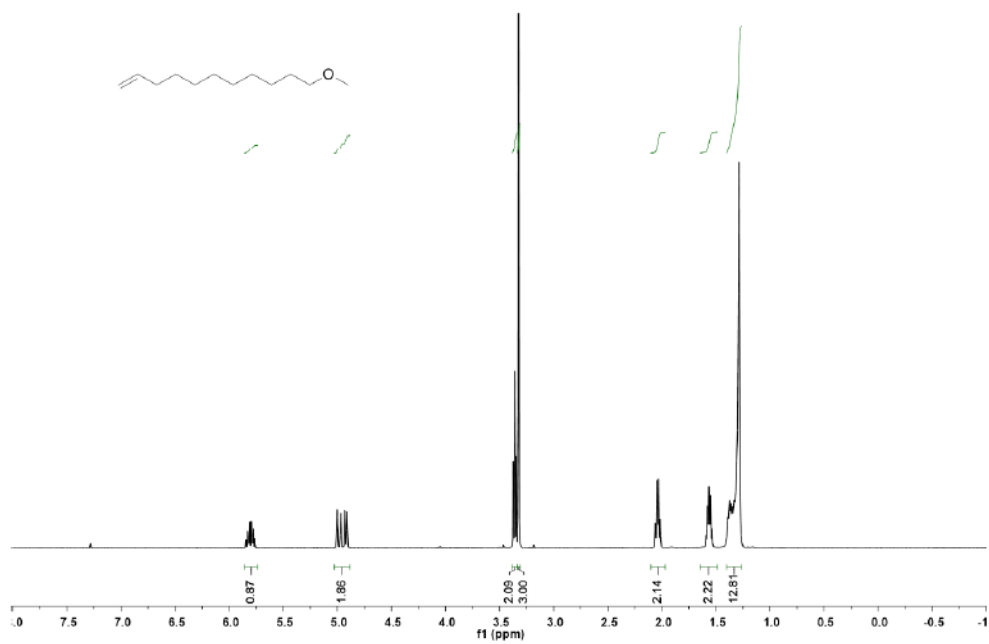**Figure A88.** ¹³C NMR spectrum of thiol 19.
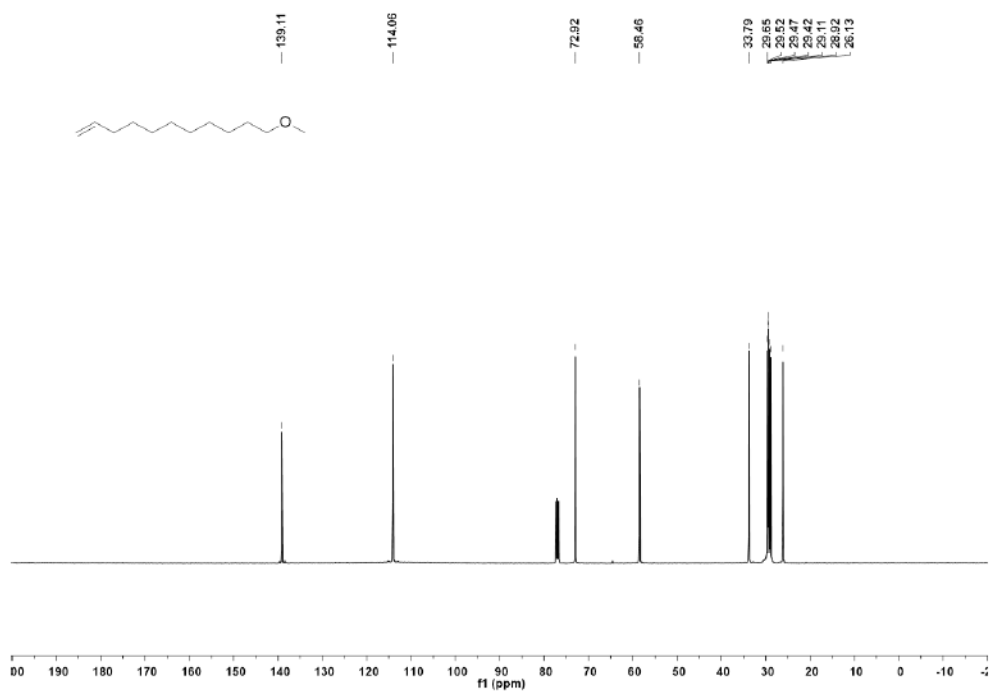
Figure A89. ^{1}H NMR spectrum of C37.

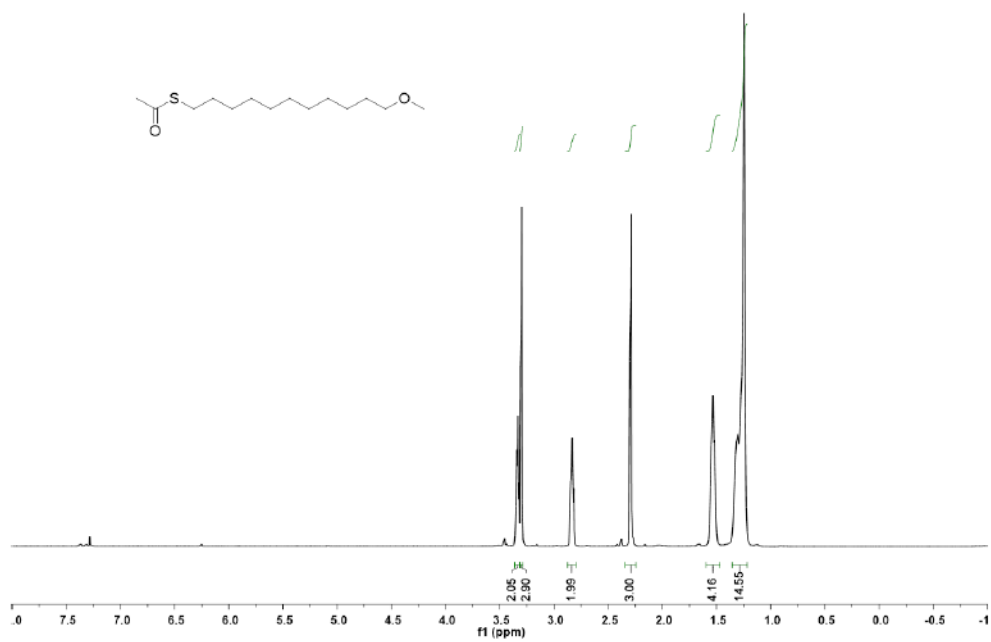**Figure A90.** ^{13}C NMR spectrum of C37.

Figure A91. ^{1}H NMR spectrum of C38.
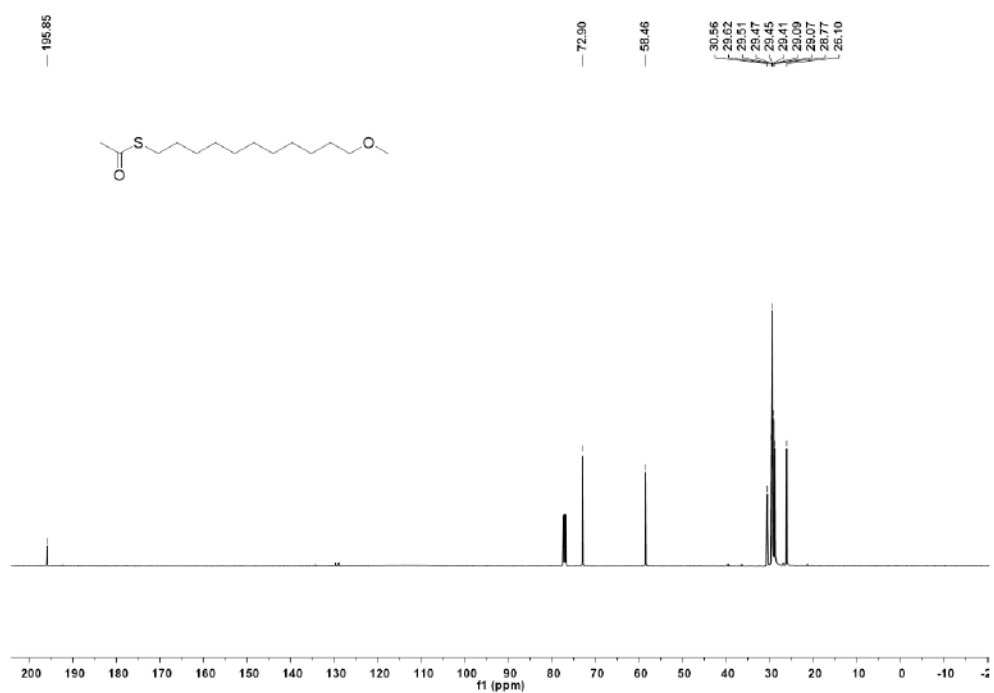
Figure A92. ^{13}C NMR spectrum of C38.
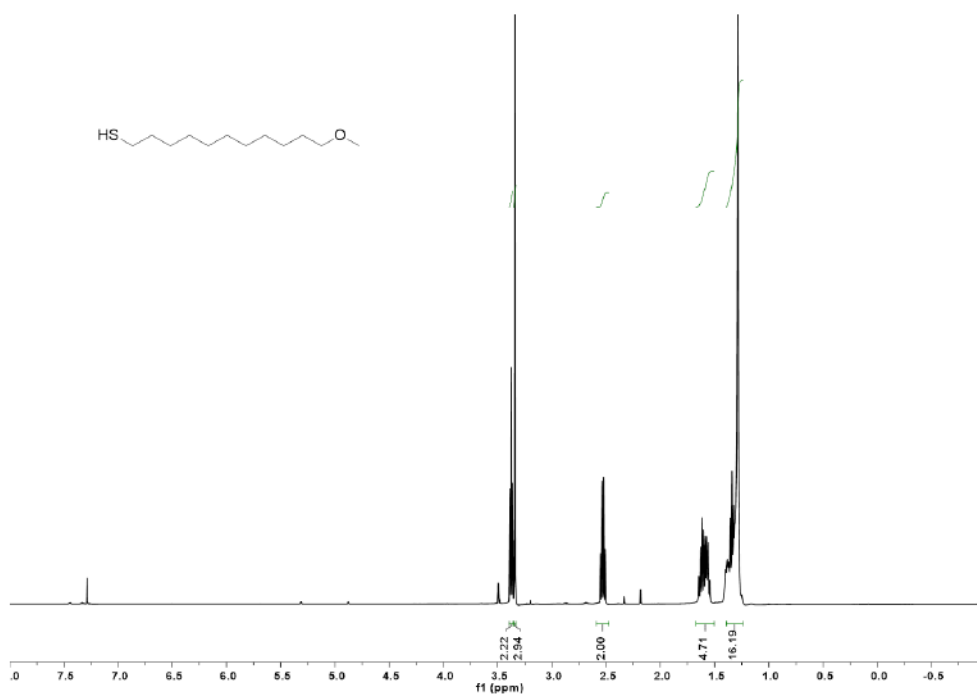
Figure A93. ^{1}H NMR spectrum of thiol 20.
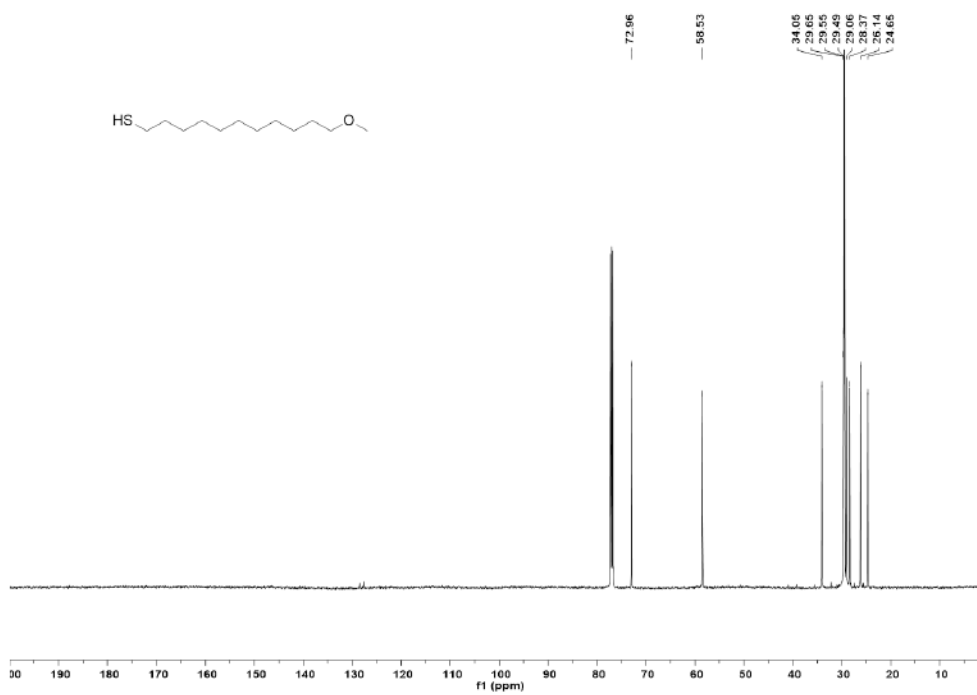
Figure A94. ^{13}C NMR spectrum of thiol 20.
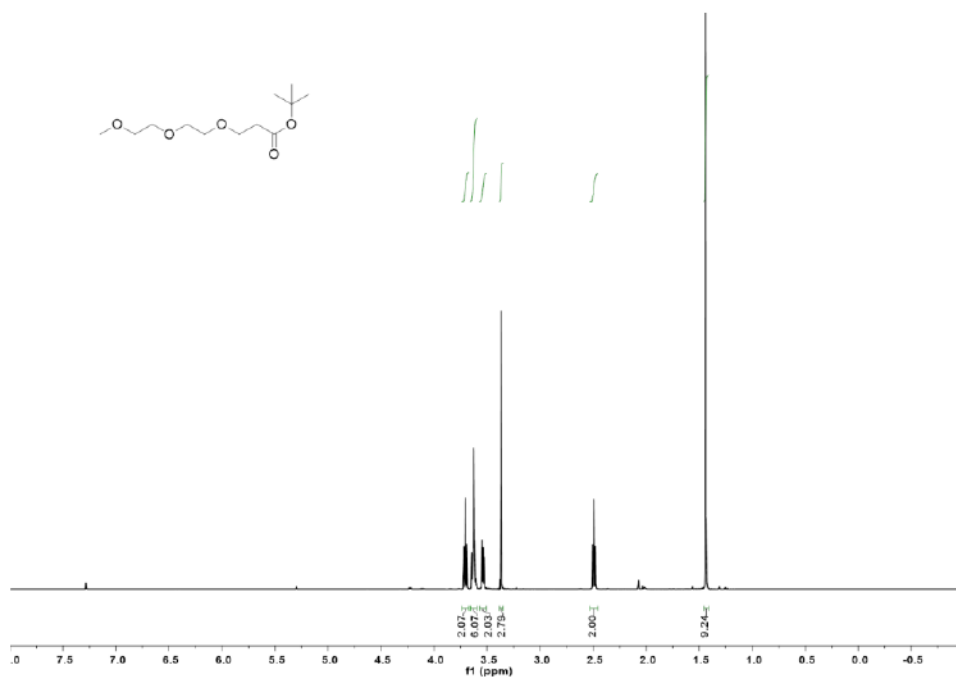
Figure A95. ^{1}H NMR spectrum of C39.
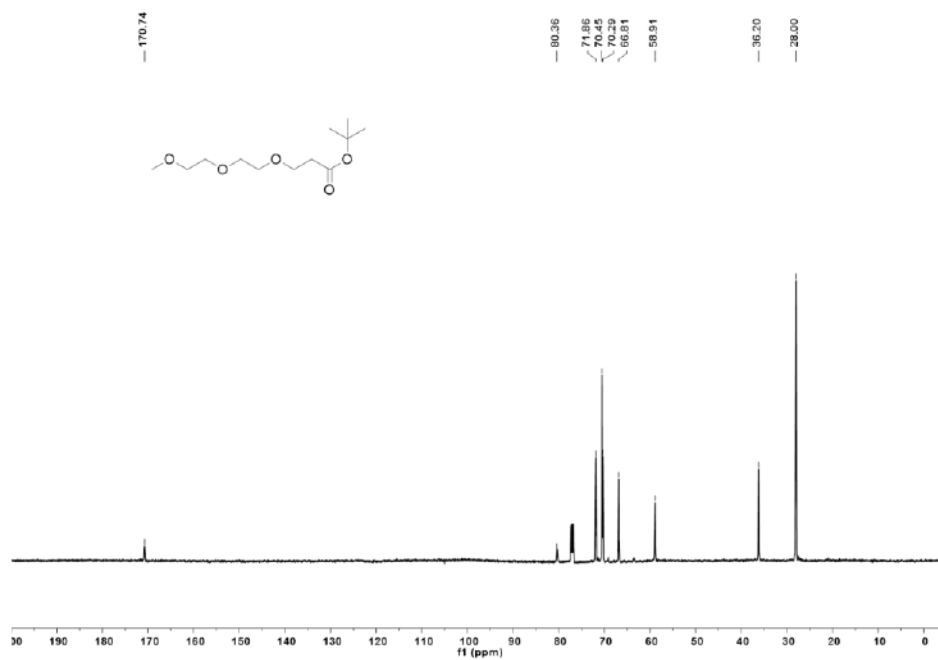
Figure A96. ^{13}C NMR spectrum of C39.
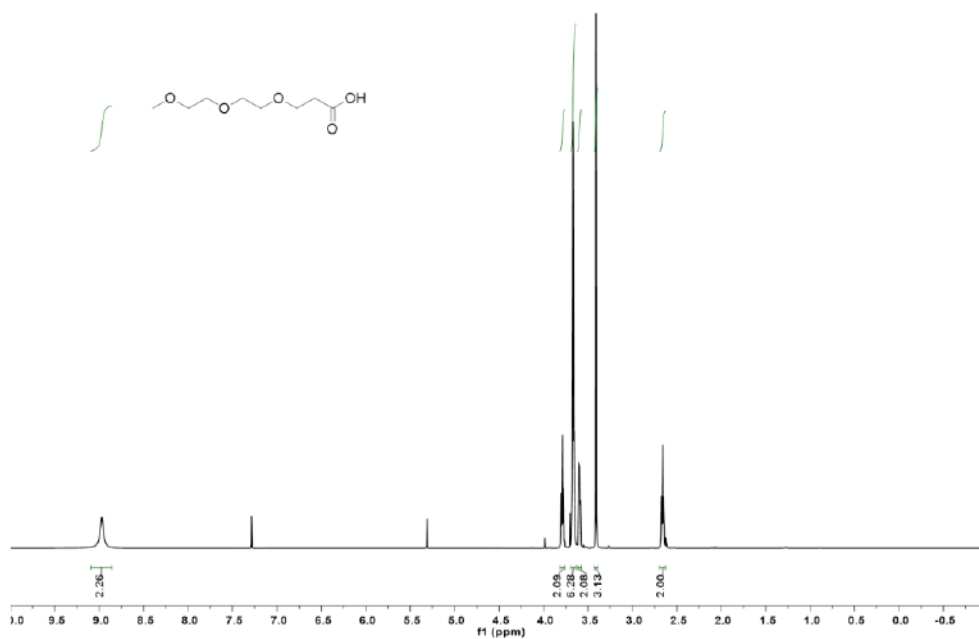
Figure A97. ^{1}H NMR spectrum of C40.
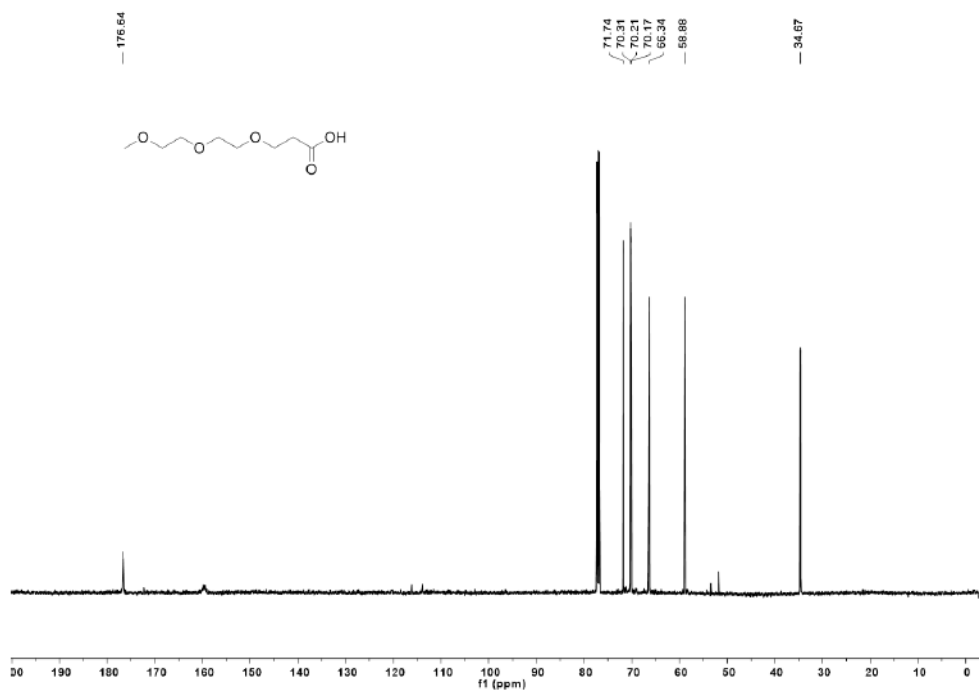
Figure A98. ^{13}C NMR spectrum of C40.

Figure A99. ^{1}H NMR spectrum of C41.
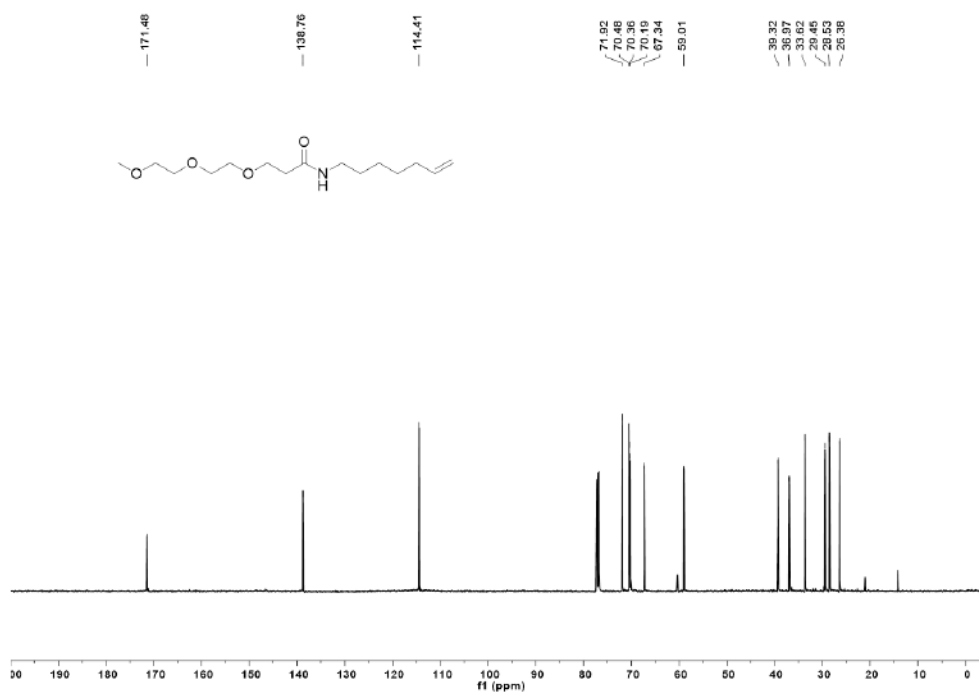
Figure A100. ^{13}C NMR spectrum of C41.
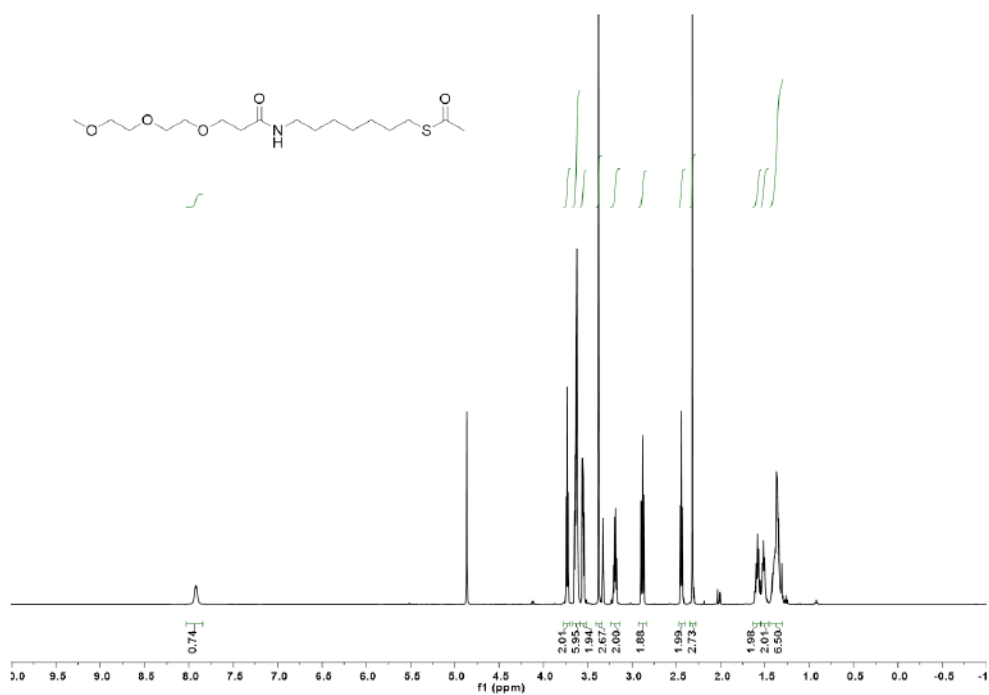
Figure A101. ^{1}H NMR spectrum of C42.

Figure A102. ^{13}C NMR spectrum of C42.
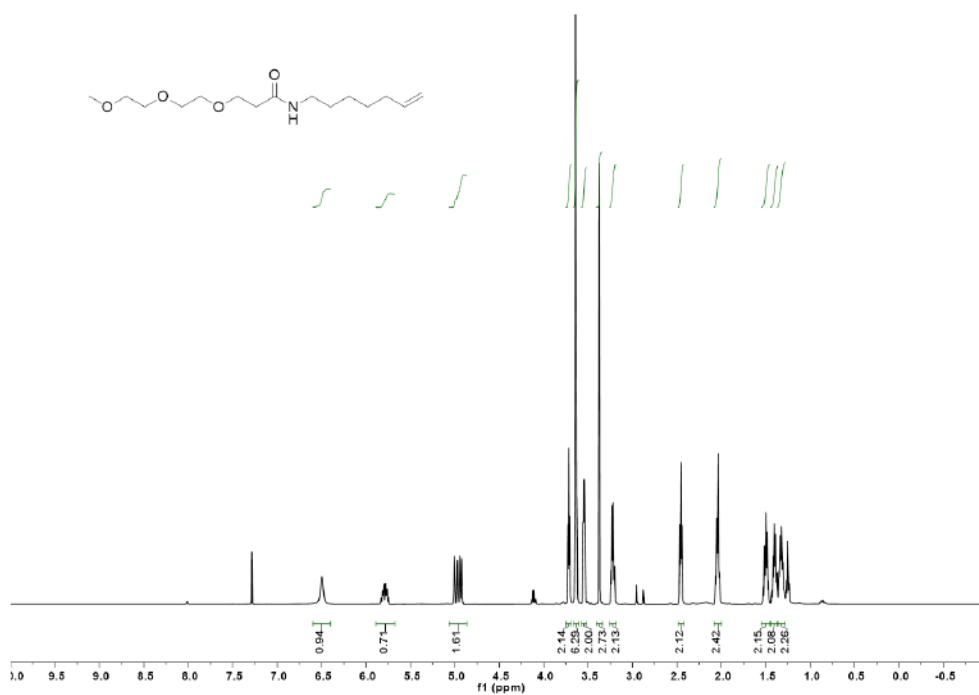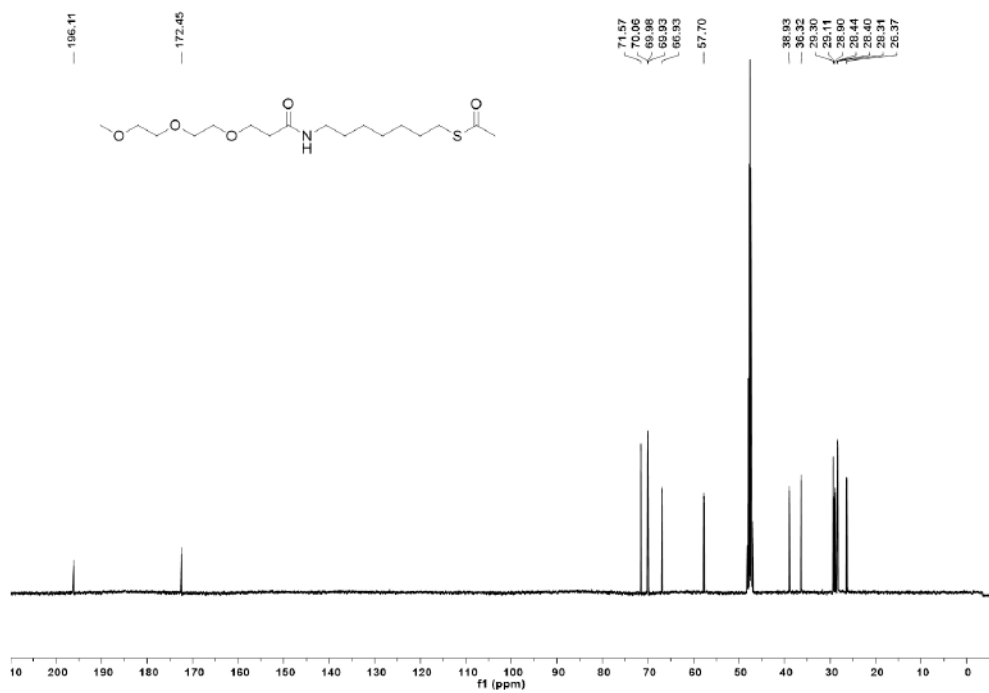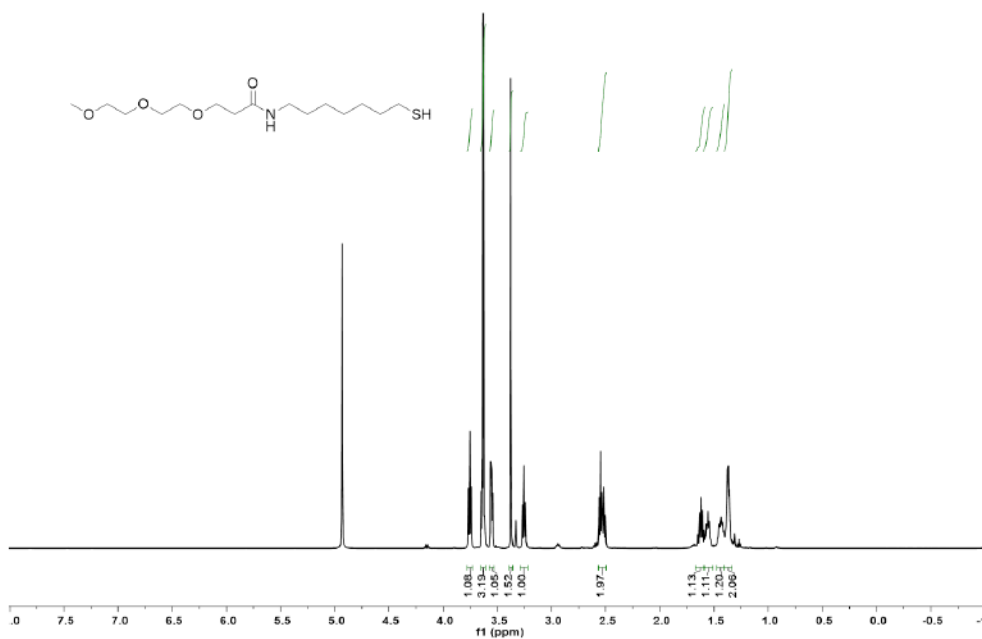
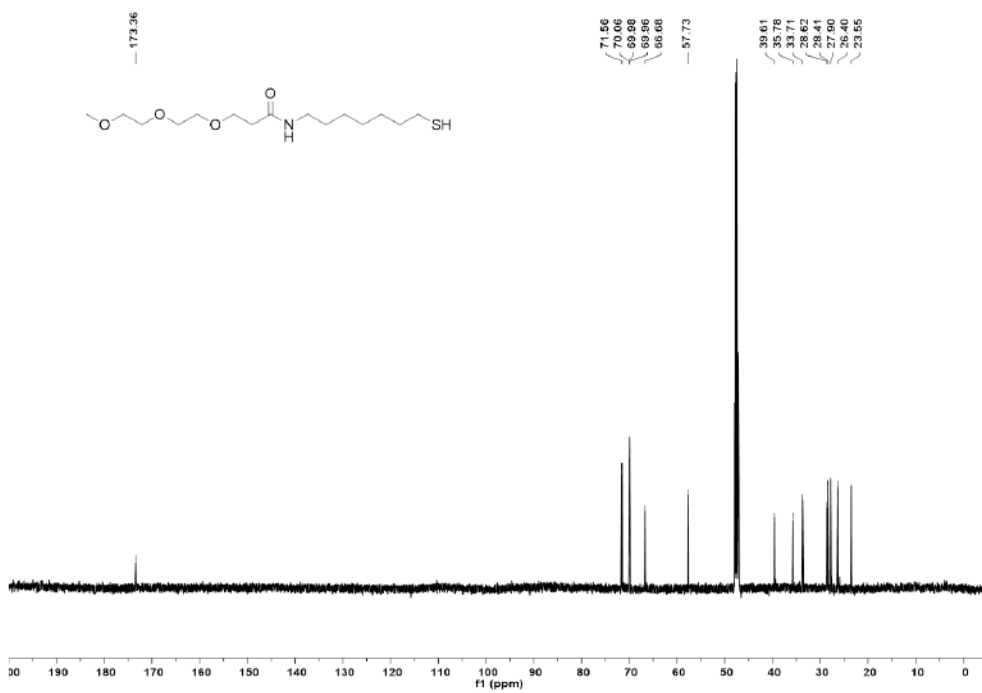**Figure A103.** ^{1}H NMR spectrum of thiol 23.

Figure A104. ^{13}C NMR spectrum of thiol 23.

References

1. S. H. Gellman, *Chem. Rev.*, 1997, **97**, 1231-1232.
2. E. Persch, O. Dumele and F. Diederich, *Angew. Chem. Int. Edit.*, 2015, **54**, 3290-3327.
3. M. Karplus, *J. Mol. Recognit.*, 2010, **23**, 102-104.
4. K. Saha, S. S. Agasti, C. Kim, X. N. Li and V. M. Rotello, *Chem. Rev.*, 2012, **112**, 2739-2779.
5. X. H. Liu, Y. Wang, P. Chen, Y. S. Wang, J. L. Mang, D. Aili and B. Liedberg, *Anal. Chem.*, 2014, **86**, 2345-2352.
6. S. W. Zeng, D. Baillargeat, H. P. Ho and K. T. Yong, *Chem. Soc. Rev.*, 2014, **43**, 3426-3452.
7. S. Yapar, M. Oikonomou, A. H. Velders and S. Kubik, *Chem. Commun.*, 2015, **51**, 14247-14250.
8. A. Kyrychenko, G. V. Karpushina, D. Syechkarev, D. Kolodezny, S. I. Bogatyrenko, A. P. Kryshtal and A. O. Doroshenko, *J. Phys. Chem. C.*, 2012, **116**, 21059-21068.
9. O. R. Miranda, X. N. Li, L. Garcia-Gonzalez, Z. J. Zhu, B. Yan, U. H. F. Bunz and V. M. Rotello, *J. Am. Chem. Soc.*, 2011, **133**, 9650-9653.
10. M. Brust and G. J. Gordillo, *J. Am. Chem. Soc.*, 2012, **134**, 3318-3321.
11. C. W. Chu, J. S. Na and G. N. Parsons, *J. Am. Chem. Soc.*, 2007, **129**, 2287-2296.
12. M. C. Daniel and D. Astruc, *Chem. Rev.*, 2004, **104**, 293-346.
13. E. A. Hauser and J. E. Lynn, *Experiments in colloid chemistry*, McGraw-Hill: New York, 1940.
14. J. Turkevich, P. C.Stevenson and J. Hiller, *Discuss. Faraday Soc.*, 2018, **514**, 528-533.
15. M. Wuithschick, A. Birnbaum, S. Witte, M. Sztucki, U. Vainio, N. Pinna, K. Rademann, F. Emmerling, R. Kraehnert and J. Polte, *ACS. Nano.*, 2015, **9**, 7052-7071.
16. N. E. Larm, J. B. Essner, K. Pokpas, J. A. Canon, N. Jahed, E. I. Iwuoha and G. A. Baker, *J. Phys. Chem. C.*, 2018, **122**, 5105-5118.
17. R. Sardar, A. M. Funston, P. Mulvaney and R. W. Murray, *Langmuir*, 2009, **25**, 13840-13851.
18. F. Manea, C. Bindoli, S. Polizzi, L. Lay and P. Scrimin, *Langmuir*, 2008, **24**, 4120-4124.
19. S. Kubowicz, J. Daillant, M. Dubois, M. Delsanti, J. M. Verbavatz and H. Mohwald, *Langmuir*, 2010, **26**, 1642-1648.
20. M. Zheng and X. Y. Huang, *J. Am. Chem. Soc.*, 2004, **126**, 12047-12054.
21. A. Centrone, Y. Hu, A. M. Jackson, G. Zerbi and F. Stellacci, *Small*, 2007, **3**, 814-817.
22. R. Bonomi, A. Cazzolaro and L. J. Prins, *Chem. Commun.*, 2011, **47**, 445-447.
23. G. H. Woehrle and J. E. Hutchison, *Inorg. Chem.*, 2005, **44**, 6149-6158.
24. Y. C. Yeh, B. Creran and V. M. Rotello, *Nanoscale*, 2012, **4**, 1871-1880.
25. W. J. Sommer and M. Weck, *Langmuir*, 2007, **23**, 11991-11995.
26. J. Gil-Tomas, L. Dekker, N. Narband, I. P. Parkin, S. P. Nair, C. Street and M. Wilson, *J. Mater. Chem.*, 2011, **21**, 4189-4196.
27. M. Oroval, C. Coll, A. Bernardos, M. D. Marcos, R. Martinez-Manez, D. G. Shchukin and F. Sancenon, *ACS. Appl. Mater. Inter.*, 2017, **9**, 11332-11336.
28. S. L. Pilicer, P. R. Bakhshi, K. W. Bentley and C. Wolf, *J. Am. Chem. Soc.*, 2017, **139**, 1758-1761.
29. J. F. Teichert, D. Mazunin and J. W. Bode, *J. Am. Chem. Soc.*, 2013, **135**, 11314-11321.
30. D. J. Wales, J. Grand, V. P. Ting, R. D. Burke, K. J. Edler, C. R. Bowen, S. Mintova and A. D. Burrows, *Chem. Soc. Rev.*, 2015, **44**, 4290-4321.
31. M. E. Kyriazi, D. Giust, A. H. El-Sagheer, P. M. Lackie, O. L. Muskens, T. Brown and A. G. Kanaras, *ACS. Nano.*, 2018, **12**, 3333-3340.
32. Y. R. Kim, R. K. Mahajan, J. S. Kim and H. Kim, *ACS. Appl. Mater. Inter.*, 2010, **2**, 292-295.
33. R. A. Potyrailo, *Chem. Soc. Rev.*, 2017, **46**, 5311-5346.

References

34. Z. Xu, C. Liu, S. Zhao, S. Chen and Y. Zhao, *Chem. Rev.*, 2018. DOI: 10.1021/acs.-chemrev.8b00202.

35. G. Nestor, T. Anderson, S. Oscarson and A. M. Gronenborn, *J. Am. Chem. Soc.*, 2017, **139**, 6210-6216.

36. M. C. Tourell, T. S. Ali, H. J. Hugo, C. Pyke, S. Yang, T. Lloyd, E. W. Thompson and K. I. Momot, *Magn. Reson. Med.*, 2018, **80**, 1243-1251.

37. R. R. Ernst, *Biosci. Rep.*, 1992, **12**, 143-187.

38. K. Wuthrich, *Angew. Chem. Int. Ed.*, 2003, **42**, 3340-3363.

39. Y. C. Zhao and T. M. Swager, *J. Am. Chem. Soc.*, 2015, **137**, 3221-3224.

40. A. Sarkar, I. E. Biton, M. Neeman and A. Datta, *Inorg. Chem. Commun.*, 2017, **78**, 21-24.

41. J. Axthelm, S. H. C. Askes, M. Elstner, G. U. Reddy, H. Gorls, P. Bellstedt and A. Schiller, *J. Am. Chem. Soc.*, 2017, **139**, 11413-11420.

42. L. Gabrielli, M. Carril, D. Padro and F. Mancin, *Chem. Eur. J.*, 2018, **24**, 13036-13042.

43. B. Perrone, S. Springhetti, F. Ramadori, F. Rastrelli and F. Mancin, *J. Am. Chem. Soc.*, 2013, **135**, 11768-11771.

44. M. V. Salvia, F. Ramadori, S. Springhetti, M. Diez-Castellnou, B. Perrone, F. Rastrelli and F. Mancin, *J. Am. Chem. Soc.*, 2015, **137**, 886-892.

45. M. V. Salvia, G. Salassa, F. Rastrelli and F. Mancin, *J. Am. Chem. Soc.*, 2015, **137**, 11399-11406.

46. O. Soubias and K. Gawrisch, *J. Am. Chem. Soc.*, 2005, **127**, 13110-13111.

47. L. Gabrielli, D. Rosa-Gastaldo, M. V. Salvia, S. Springhetti, F. Rastrelli and F. Mancin, *Chem. Sci.*, 2018, **9**, 4777-4784.

48. A. Kapur, F. Aldeek, X. Ji, M. Safi, W. T. Wang, A. Del Cid, O. Steinbock and H. Mattoussi, *Bioconjugate Chem*, 2017, **28**, 678-687.

49. L. Y. Chen, C. W. Wang, Z. Q. Yuan and H. T. Chang, *Anal. Chem.*, 2015, **87**, 216-229.

50. C. C. Huang and H. T. Chang, *Anal. Chem.*, 2006, **78**, 8332-8338.

51. J. Chen, Y. Huang, S. L. Zhao, X. Lu and J. N. Tian, *Analyst*, 2012, **137**, 5885-5890.

52. T. Y. Wang, C. Y. Chen, C. M. Wang, Y. Z. Tan and W. S. Liao, *ACS. Sensors.*, 2017, **2**, 354-363.

53. K. Das, S. Sarkar and P. K. Das, *ACS. Appl. Mater. Inter.*, 2016, **8**, 25691-25701.

54. B. Dubertret, M. Calame and A. J. Libchaber, *Nat. Biotechnol.*, 2001, **19**, 365-370.

55. C. Pezzato, D. Zaramella, M. Martinelli, G. Pieters, M. A. Pagano and L. J. Prins, *Org. Biomol. Chem.*, 2015, **13**, 1198-1203.

56. T. Minami, Y. Liu, A. Akdeniz, P. Koutnik, N. A. Esipenko, R. Nishiyabu, Y. Kubo and P. Anzenbacher, Jr, *J. Am. Chem. Soc.*, 2014, **136**, 11396-11401.

57. E. V. Anslyn, *J. Org. Chem.*, 2007, **72**, 687-699.

58. S. Rana, A. K. Singla, A. Bajaj, S. G. Elci, O. R. Miranda, R. Mout, B. Yan, F. R. Jirik and V. M. Rotello, *ACS. Nano.*, 2012, **6**, 8233-8240.

59. O. R. Miranda, H. T. Chen, C. C. You, D. E. Mortenson, X. C. Yang, U. H. F. Bunz and V. M. Rotello, *J. Am. Chem. Soc.*, 2010, **132**, 5285-5289.

60. B. Y. Li, X. Z. Li, Y. H. Dong, B. Wang, D. Y. Li, Y. M. Shi and Y. Y. Wu, *Anal. Chem.*, 2017, **89**, 10639-10643.

61. R. L. Phillips, O. R. Miranda, C. C. You, V. M. Rotello and U. H. F. Bunz, *Angew. Chem. Int. Edit.*, 2008, **47**, 2590-2594.

62. U. H. F. Bunz and V. M. Rotello, *Angew. Chem. Int. Ed.*, 2010, **49**, 3268-3279.

63. C. Pezzato, B. Lee, K. Severin and L. J. Prins, *Chem. Commun.*, 2013, **49**, 469-471.

64. M. Lucarini, P. Franchi, G. F. Pedulli, P. Pengo, P. Scrimin and L. Pasquato, *J. Am. Chem. Soc.*, 2004, **126**, 9326-9329.

65. C. A. Mirkin, R. L. Letsinger, R. C. Mucic and J. J. Storhoff, *Nature*, 1996, **382**, 607-609.

66. K. Aslan, J. R. Lakowicz and C. D. Geddes, *Anal. Biochem.*, 2004, **330**, 145-155.

67. G. F. Wang, H. Y. Park and R. J. Lipert, *Anal. Chem.*, 2009, **81**, 9643-9650.

References

68. S. Kim, T. H. Kim, J. Huh, J. Bang and S. H. Choi, *ACS. Macro. Lett.*, 2015, **4**, 417-421.
69. J. J. Kuna, K. Voitchovsky, C. Singh, H. Jiang, S. Mwenifumbo, P. K. Ghorai, M. M. Stevens, S. C. Glotzer and F. Stellacci, *Nat. Mater.*, 2009, **8**, 837-842.
70. A. Centrone, E. Penzo, M. Sharma, J. W. Myerson, A. M. Jackson, N. Marzari and F. Stellacci, *P. Natl. Acad. Sci.,* 2008, **105**, 9886-9891.
71. A. Hung, S. Mwenifumbo, M. Mager, J. J. Kuna, F. Stellacci, I. Yarovsky and M. M. Stevens, *J. Am. Chem. Soc.*, 2011, **133**, 1438-1450.
72. A. Verma, O. Uzun, Y. H. Hu, Y. Hu, H. S. Han, N. Watson, S. L. Chen, D. J. Irvine and F. Stellacci, *Nat. Mater.*, 2008, **7**, 588-595.
73. A. Ghosh, S. Basak, B. H. Wunsch, R. Kumar and F. Stellacci, *Angew. Chem. Int. Edit.*, 2011, **50**, 7900-7905.
74. Y. Yi, L. Sanchez, Y. Gao and Y. Yu, *Analyst*, 2016, **141**, 3526-3539.
75. Q. K. Ong, J. Reguera, P. J. Silva, M. Moglianetti, K. Harkness, M. Longobardi, K. S. Mali, C. Renner, S. De Feyter and F. Stellacci, *ACS. Nano.*, 2013, **7**, 8529-8539.
76. M. Moglianetti, Q. K. Ong, J. Reguera, K. M. Harkness, M. Mameli, A. Radulescu, J. Kohlbrecher, C. Jud, D. I. Svergun and F. Stellacci, *Chem. Sci.*, 2014, **5**, 1232-1240.
77. Q. Ong, Z. Luo and F. Stellacci, *Acc. Chem. Res.*, 2017, **50**, 1911-1919.
78. X. Liu, M. Yu, H. Kim, M. Mameli and F. Stellacci, *Nat. Commun.*, 2012, **3**, 1-9.
79. G. Guarino, F. Rastrelli, P. Scrimin and F. Mancin, *J. Am. Chem. Soc.*, 2012, **134**, 7200-7203.
80. G. M. Clore and J. Iwahara, *Chem. Rev.*, 2009, **109**, 4108-4139.
81. K. M. Harkness, A. Balinski, J. A. McLean and D. E. Cliffel, *Angew. Chem. Int. Edit.*, 2011, **50**, 10554-10559.
82. A. P. Gies, D. M. Hercules, A. E. Gerdon and D. E. Cliffel, *J. Am. Chem. Soc.*, 2007, **129**, 1095-1104.
83. C. Gentilini, P. Franchi, E. Mileo, S. Polizzi, M. Lucarini and L. Pasquato, *Angew. Chem. Int. Edit.*, 2009, **48**, 3060-3064.
84. C. Vilain, F. Goettmann, A. Moores, P. Le Floch and C. Sanchez, *J. Mater. Chem.*, 2007, **17**, 3509-3514.
85. C. Singh, P. K. Ghorai, M. A. Horsch, A. M. Jackson, R. G. Larson, F. Stellacci and S. C. Glotzer, *Phys. Rev. Lett.*, 2007, **99**, 226106.
86. L. Marchetti and M. Levine, *ACS. Catal.*, 2011, **1**, 1090-1118.
87. J. Lee, Y. M. Lee and W. J. Kim, *Chem. Mater.*, 2016, **28**, 3961-3967.
88. J. Krishnan, *Ind. Eng. Chem. Res.*, 2011, **50**, 13236-13243.
89. W. Hatanaka, M. Kawaguchi, X. Z. Sun, Y. Nagao, H. Ohshima, M. Hashida, Y. Higuchi, A. Kishimura, Y. Katayama and T. Mori, *Bioconjugate Chem.*, 2017, **28**, 296-301.
90. F. Biedermann, W. M. Nau and H. J. Schneider, *Angew. Chem. Int. Edit.*, 2014, **53**, 11158-11171.
91. M. R. Mackiewicz, H. L. Hodges and S. M. Reed, *J. Phys. Chem. B.*, 2010, **114**, 5556-5562.
92. L. Riccardi, L. Gabrielli, X. H. Sun, F. De Biasi, F. Rastrelli, F. Mancin and M. De Vivo, *Chem.*, 2017, **3**, 92-109.
93. C. Pezzato, P. Scrimin and L. J. Prins, *Angew. Chem. Int. Edit.*, 2014, **53**, 2104-2109.
94. A. Badia, S. Singh, L. Demers, L. Cuccia, G. R. Brown and R. B. Lennox, *Chem. Eur J.*, 1996, **2**, 359-363.
95. A. Badia, W. Gao, S. Singh, L. Demers, L. Cuccia and L. Reven, *Langmuir*, 1996, **12**, 1262-1269.
96. A. K. Boal and V. M. Rotello, *J. Am. Chem. Soc.*, 2000, **122**, 734-735.
97. C. C. Lin, Y. C. Yeh, C. Y. Yang, C. L. Chen, G. F. Chen, C. C. Chen and Y. C. Wu, *J. Am. Chem. Soc.*, 2002, **124**, 3508-3509.
98. D. A. Giljohann, D. S. Seferos, W. L. Daniel, M. D. Massich, P. C. Patel and C. A. Mirkin, *Angew. Chem. Int. Edit.*, 2010, **49**, 3280-3294.

References

99. E. C. Dreaden, A. M. Alkilany, X. H. Huang, C. J. Murphy and M. A. El-Sayed, *Chem. Soc. Rev.*, 2012, **41**, 2740-2779.

100. C. Pezzato, S. Maiti, J. L. Y. Chen, A. Cazzolaro, C. Gobbo and L. J. Prins, *Chem. Commun.*, 2015, **51**, 9922-9931.

101. S. Su, X. L. Zuo, D. Pan, H. Pei, L. H. Wang, C. H. Fan and W. Huang, *Nanoscale*, 2013, **5**, 2589-2599.

102. P. Pengo, S. Polizzi, M. Battagliarin, L. Pasquato and P. Scrimin, *J. Mater. Chem.*, 2003, **13**, 2471-2478.

103. M. Lucarini and L. Pasquato, *Nanoscale*, 2010, **2**, 668-676.

104. R. H. Terrill, T. A. Postlethwaite, C. H. Chen, C. D. Poon, A. Terzis, A. D. Chen, J. E. Hutchison, M. R. Clark, G. Wignall, J. D. Londono, R. Superfine, M. Falvo, C. S. Johnson, E. T. Samulski and R. W. Murray, *J. Am. Chem. Soc.*, 1995, **117**, 12537-12548.

105. M. J. Hostetler, J. E. Wingate, C. J. Zhong, J. E. Harris, R. W. Vachet, M. R. Clark, J. D. Londono, S. J. Green, J. J. Stokes, G. D. Wignall, G. L. Glish, M. D. Porter, N. D. Evans and R. W. Murray, *Langmuir*, 1998, **14**, 17-30.

106. A. Piserchia, M. Zerbetto, M. V. Salvia, G. Salassa, L. Gabrielli, F. Mancin, F. Rastrelli and D. Frezzato, *J. Phys. Chem. C.*, 2015, **119**, 20100-20110.

107. W. D. Luedtke and U. Landman, *J. Phys. Chem.*, 1996, **100**, 13323-13329.

108. C. Briggs, T. B. Norsten and V. M. Rotello, *Chem. Commun.*, 2002, 1890-1891.

109. H. Schmitt, A. Badia, L. Dickinson, L. Reven and R. B. Lennox, *Adv. Mater.*, 1998, **10**, 475-480.

110. K. Stott, J. Keeler, Q. N. Van and A. J. Shaka, *J. Magn. Reson.*, 1997, **125**, 302-324.

111. L. Devesse, I. Smirnova, R. Lonneborg, U. Kapp, P. Brzezinski, G. A. Leonard and C. Dian, *Mol. Microbiol.*, 2011, **81**, 354-367.

112. M. Lucarini, P. Franchi, G. F. Pedulli, C. Gentilini, S. Polizzi, P. Pengo, P. Scrimin and L. Pasquato, *J. Am. Chem. Soc.*, 2005, **127**, 16384-16385.

113. V. Oleinikovas, G. Saladino, B. P. Cossins and F. L. Gervasio, *J. Am. Chem. Soc.*, 2016, **138**, 14257-14263.

114. C. K. Kim, P. Ghosh, C. Pagliuca, Z. J. Zhu, S. Menichetti and V. M. Rotello, *J. Am. Chem. Soc.*, 2009, **131**, 1360-1361.

115. A. K. Boal and V. M. Rotello, *J. Am. Chem. Soc.*, 1999, **121**, 4914-4915.

116. Y. L. Liu, T. Minami, R. Nishiyabu, Z. Wang and P. Anzenbacher, *J. Am. Chem. Soc.*, 2013, **135**, 7705-7712.

117. A. Chmielewska, L. Konieczna, A. Plenis, M. Bieniecki and H. Lamparczyk, *Biomed. Chromatogr.*, 2006, **20**, 119-124.

118. B. Yilmaz and U. Ciltas, *J. Phar. Anal.*, 2015, **5**, 153-160.

119. C. H. Hsu, Y. J. Cheng, B. Singco and H. Y. Huang, *J. Chromatogr. A.*, 2011, **1218**, 350-358.

120. A. Hlavacek, Z. Farka, M. Hubner, V. Hornakova, D. Nemecek, R. Niessner, P. Skladal, D. Knopp and H. H. Gorris, *Anal. Chem.*, 2016, **88**, 6011-6017.

121. M. Ben Haddada, M. Huebner, S. Casale, D. Knopp, R. Niessner, M. Salmain and S. Boujday, *J. Phys. Chem. C.*, 2016, **120**, 29302-29311.

122. T. T. K. Nguyen, T. T. Vu, G. Anquetin, H. V. Tran, S. Reisberg, V. Noel, G. Mattana, Q. V. Nguyen, T. D. Lam, M. C. Pham and B. Piro, *Biosens. Bioelectron.*, 2017, **97**, 246-252.

123. G. Salassa and T. Burgi, *Nanoscale Horiz.*, 2018, **3,** 457-463.

124. P. Anzenbacher, P. Lubal, P. Bucek, M. A. Palacios and M. E. Kozelkova, *Chem. Soc. Rev.*, 2010, **39**, 3954-3979.

125. Y. L. Liu and M. Bonizzoni, *J. Am. Chem. Soc.*, 2014, **136**, 14223-14229.

126. M. A. Palacios, Z. Wang, V. A. Montes, G. V. Zyryanov and P. Anzenbacher, *J. Am. Chem. Soc.*, 2008, **130**, 10307-10314.

References

127.   E. G. Shcherbakova, B. Zhang, S. Gozem, T. Minami, P. Y. Zavalij, M. Pushina, L. D. Isaacs and P. Anzenbacher, *J. Am. Chem. Soc.*, 2017, **139**, 14954-14960.

128.   T. Minami, N. A. Esipenko, A. Akdeniz, B. Zhang, L. Isaacs and P. Anzenbacher, *J. Am. Chem. Soc.*, 2013, **135**, 15238-15243.

129.   Z. Luo, J. Hou, L. Menin, Q. K. Ong and F. Stellacci, *Angew. Chem. Int. Edit.*, 2017, **56**, 13521-13525.

130.   R. P. Carney, G. A. DeVries, C. Dubois, H. Kim, J. Y. Kim, C. Singh, P. K. Ghorai, J. B. Tracy, R. L. Stiles, R. W. Murray, S. C. Glotzer and F. Stellacci, *J. Am. Chem. Soc.*, 2008, **130**, 798-799.

131.   Y. Cheng, A. C. Samia, J. D. Meyers, I. Panagopoulos, B. W. Fei and C. Burda, *J. Am. Chem. Soc.*, 2008, **130**, 10643-10647.

132.   S. Neri, S. G. Martin, C. Pezzato and L. J. Prins, *J. Am. Chem. Soc.*, 2017, **139**, 1794-1797.

133.   M. Szewczyk, G. Sobczak and V. Sashuk, *ACS. Catal.*, 2018, **8**, 2810-2814.